

CHARACTERIZATION OF POLYVINYLDENE FLUORIDE  
TRIFLUOROETHYLENE/ZINC OXIDE QUANTUM DOTS  
COMPOSITE THIN FILMS FOR PYROELECTRIC  
NANOGENERATOR APPLICATIONS

NURAZLIN BINTI AHMAD

FACULTY OF SCIENCE  
UNIVERSITI MALAYA  
KUALA LUMPUR

2023

**CHARACTERIZATION OF POLYVINYLDENE  
FLUORIDE TRIFLUOROETHYLENE/ZINC OXIDE  
QUANTUM DOTS COMPOSITE THIN FILMS FOR  
PYROELECTRIC NANOGENERATOR APPLICATIONS**

**NURAZLIN BINTI AHMAD**

**THESIS SUBMITTED IN FULFILMENT OF THE  
REQUIREMENTS FOR THE DEGREE OF DOCTOR OF  
PHILOSOPHY**

**DEPARTMENT OF PHYSICS  
FACULTY OF SCIENCE  
UNIVERSITI MALAYA  
KUALA LUMPUR**

**2023**

**UNIVERSITI MALAYA**

**ORIGINAL LITERARY WORK DECLARATION**

Name of Candidate: **NURAZLIN BINTI AHMAD**

Matric No: **SHC140069**

Name of Degree: **DOCTOR OF PHILOSOPHY**

Title of Thesis ("this Work"):

**CHARACTERIZATION OF POLYVINYLIDENE FLUORIDE  
TRIFLUOROETHYLENE/ZINC OXIDE QUANTUM DOTS COMPOSITE THIN  
FILMS FOR PYROELECTRIC NANOGENERATOR APPLICATIONS**

Field of Study: **PHYSICS**

I do solemnly and sincerely declare that:

- (1) I am the sole author/writer of this Work;
- (2) This Work is original;
- (3) Any use of any work in which copyright exists was done by way of fair dealing and for permitted purposes and any excerpt or extract from, or reference to or reproduction of any copyright work has been disclosed expressly and sufficiently and the title of the Work and its authorship have been acknowledged in this Work;
- (4) I do not have any actual knowledge nor do I ought reasonably to know that the making of this work constitutes an infringement of any copyright work;
- (5) I hereby assign all and every rights in the copyright to this Work to the University of Malaya ("UM"), who henceforth shall be owner of the copyright in this Work and that any reproduction or use in any form or by any means whatsoever is prohibited without the written consent of UM having been first had and obtained;
- (6) I am fully aware that if in the course of making this Work I have infringed any copyright whether intentionally or otherwise, I may be subject to legal action or any other action as may be determined by UM.

Candidate's Signature

Date:

Subscribed and solemnly declared before,

Witness's Signature

Date:

Name:

Designation:

# CHARACTERIZATION OF POLYVINYLIDENE FLUORIDE TRIFLUOROETHYLENE/ZINC OXIDE QUANTUM DOTS COMPOSITE THIN FILMS FOR PYROELECTRIC NANOGENERATOR APPLICATIONS

## ABSTRACT

In the first part of this study, the copolymer P(VDF-TrFE) thin films prepared by sol-gel method were annealed in the range of Curie temperature up to the melting point [80 °C – 140 °C] to increase their crystallinity. A remnant polarization,  $P_r$  of 76.7 mCm<sup>-2</sup>, which gives a pyroelectric coefficient of 31 μCm<sup>-2</sup>K<sup>-1</sup> and a figure of merit (FOM)  $F_D$  of 86 μCm<sup>-2</sup>K<sup>-1</sup> (1 kHz) was obtained for the sample annealed at 100 °C, where the phase was about to transit from ferroelectric to paraelectric. In the second part, a novel P(VDF-TrFE) / ZnO QDs nanocomposite films stabilized with organic ligands (TEA) were fabricated using a spin-coating technique with fillers composition; 0, 0.15, 0.25, 0.35 and 0.50 wt%. Particle size analysis with UV-Vis and TEM confirmed that the QDs size is in the range ~2.5 - 3 nm. Incorporation of 0.15 wt% ZnO QDs into copolymer achieved optimum ferroelectric, dielectric and pyroelectric properties which gives the highest value of remnant polarization ( $P_r = 10.02 \mu\text{C}/\text{cm}^2$ ), dielectric constant ( $\epsilon' = 13.9$ ) and pyroelectric coefficient (49 μC/m<sup>2</sup>K). The significant enhancement of these properties is because of the morphological structure of P(VDF-TrFE) which demonstrates higher distribution of micelle-like crystallite and growth of elongated rod-like crystallite. Including ZnO QDs in the polymer matrix induces local dipole moment due to its polar character giving rise to spontaneous polarization. Further measurement of the ferroelectric hysteresis loop leads to energy storage density,  $U_e$  is 8.2 J/cm<sup>3</sup> and from pyroelectric activity, energy harvesting Figure of merit (FOM),  $F_E$  is 19.5 Jm<sup>-3</sup>K<sup>2</sup> obtained at 1 kHz for 0.15 wt%. The polarization of the non-centrosymmetric crystal structure of ZnO interacts synergistically with the P(VDF-TrFE) polymer host which contributes to the increase in ferroelectric and pyroelectric properties up to 0.15 wt%

composition. The addition of ZnO QDs of more than 0.25 wt% in P(VDF-TrFE) degrades the ferroelectric properties due to excessive leakage current density and the emergence of saturated agglomeration as micelle-like hole structure on the surface of Si substrate, which cause the energy harvesting and storage performance to deteriorate. The Thermally Stimulated Current (TSC) study was performed to investigate the molecular motions of the crystalline copolymer P(VDF-TrFE) and its polymer composite P(VDF-TrFE) / ZnO QDs. The TSC measurement mainly revealed three depolarization peaks, which are known as the  $\beta$ ,  $\alpha$  and Curie mode ( $\rho$ ) peaks in P(VDF-TrFE). The TSC spectrum's relaxation peaks revealed spontaneous polarization or a switching characteristic of P(VDF-TrFE) observed at a specific temperature of  $T_g$  and the Curie mode. The involvement of space charges injection at the polymer/semiconductor interface and molecular-ions deep traps during the poling process of TSC can result in the decomposition the of TSC spectrum with high activation energy at most relaxation peaks of P(VDF-TrFE) / ZnO QDs. The pyroelectric nanogenerator developed in this research can be exploited to robust its performance in energy storage and energy harvesting applications.

**Keywords:** Polarization, P(VDF-TrFE), Ferroelectric, Pyroelectric, Thermally Stimulated Current (TSC)

# **PENCIRIAN FILEM NIPIS KOMPOSIT POLIVINILIDENA FLORIDA TRIFLOROETILENA/TITIK KUANTUM ZINK OKSIDA UNTUK APLIKASI NANOGENERATOR PIROELEKTRIK**

## **ABSTRAK**

Pada bahagian pertama kajian ini, filem nipis kopolimer P(VDF-TrFE) disediakan menggunakan kaedah pemprosesan sol-gel yang disepuhlindapkan dalam julat suhu Curie sehingga takat lebur [80 °C – 140 °C] untuk meningkatkan kehablurannya. Pengutuban remanen ialah 76.7 mCm<sup>-2</sup>, yang memberikan pekali piroelektrik 31 μCm<sup>-2</sup>K<sup>-1</sup> dan angka merit (FOM)  $F_D$  86 μCm<sup>-2</sup>K<sup>-1</sup> (1 kHz), diperoleh daripada sampel yang disepuhlindapkan pada 100 °C, di mana fasa akan beralih daripada ferroelektrik kepada paraelektrik. Dalam bahagian kedua kajian, filem nanokomposit novel P(VDF-TrFE) / ZnO QDs yang distabilkan dengan ligan organik (TEA) telah dihasilkan melalui teknik salutan putaran dengan mengubah komposisi pengedopan; 0, 0.15, 0.25, 0.35 dan 0.50 wt%. Analisis saiz zarah dengan UV-Vis dan TEM mengesahkan saiz QDs adalah dalam julat ~2.5 - 3 nm. Penggabungan 0.15 wt% ZnO QDs ke dalam kopolimer mencapai sifat ferroelektrik, dielektrik dan piroelektrik optimum yang menghasilkan nilai tertinggi untuk pengutuban remanen ( $P_r = 10.02 \mu\text{C}/\text{cm}^2$ ), pemalar dielektrik ( $\epsilon' = 13.9$ ) dan pekali piroelektrik (49 μC/m<sup>2</sup>K). Peningkatan ketara sifat-sifat ini adalah kerana struktur morfologi P(VDF-TrFE) yang menunjukkan penyebaran kristal seperti misel dan pengembangan kristal seperti batang memanjang yang lebih tinggi. Penggabungan ZnO QDs dalam matriks polimer mendorong momen dipol tempatan kerana sifat kutubnya yang menimbulkan polarisasi spontan. Pengukuran lanjut gelung histerisis ferroelektrik membawa kepada ketumpatan penyimpanan tenaga,  $U_e$  sebanyak 8.2 J/cm<sup>3</sup> dan daripada aktiviti piroelektrik, penuaian tenaga angka merit (FOM),  $F_E$  ialah 19.5 Jm<sup>-3</sup>K<sup>2</sup> yang diperolehi pada 1 kHz untuk 0.15 wt%. Polarisasi struktur hablur tak simetri pusat ZnO berinteraksi secara sinergistik dengan hos polimer P(VDF-TrFE) yang menyumbang kepada

peningkatan sifat ferroelektrik dan piroelektrik sehingga komposisi 0.15 wt%. Peningkatan ZnO QDs selanjutnya, melebihi 0.25 wt% dalam P(VDF-TrFE) merosotkan sifat ferroelektrik disebabkan oleh ketumpatan arus bocor yang terlalu tinggi dan kemunculan aglomerasi tepu sebagai struktur lubang seperti misel pada permukaan substrat Si, di mana akan menyebabkan prestasi penuaian dan penyimpanan tenaga merosot. Kajian Arus Terangsang Terma (TSC) telah dijalankan untuk menyiasat pergerakan molekul kopolimer kristal P(VDF-TrFE) dan komposit polimernya P(VDF-TrFE) / ZnO QDs. Pengukuran TSC mendedahkan terutamanya tiga puncak depolarisasi, yang dikenali sebagai puncak  $\beta$ ,  $\alpha$  dan mod Curie ( $\rho$ ) dalam P(VDF-TrFE). Puncak kelonggaran spektrum TSC mendedahkan fenomena polarisasi spontan atau ciri pensuisan P(VDF-TrFE) yang diperhatikan pada suhu tertentu  $T_g$  dan mod Curie. Penglibatan suntikan cas ruang pada antara muka polimer / semikonduktor dan perangkap dalam ion molekul semasa proses poling TSC boleh mengakibatkan penguraian spektrum TSC dengan tenaga pengaktifan tinggi pada kebanyakan puncak kelonggaran P(VDF-TrFE) / ZnO QD. Penjana nano piroelektrik yang dibangunkan dalam penyelidikan ini boleh dieksploitasi untuk memperkukuh prestasinya dalam aplikasi penyimpanan tenaga dan penuaian tenaga.

**Kata kunci:** Pengutuban, P(VDF-TrFE), Ferroelektrik, Piroelektrik, Arus Terangsang Terma (TSC)

## ACKNOWLEDGEMENTS



### **In the Name of Allah, The Most Gracious, The Most Merciful**

Essentially, I would like to praise Allah the Almighty, the Most Gracious, and the Most Merciful for His blessing. Who is giving me this chance, the vigour, the fortitude and permitting me to complete this thesis in spite of all the glitches and challenges. My humblest gratitude to the Holy Prophet Muhammad (peace be upon him), his family and his companions.

The research presented in this dissertation was carried out under the supervision of Professor Dr. Wan Haliza Abd. Majid and Professor Ts. Dr. Norhana Abd. Halim. I owe them my sincere gratitude for their guidance, understanding, patience and most importantly, their positive encouragement and warm spirit in completing this thesis. It has been a great pleasure and honour to have them as my supervisors. Many parties and individuals assisted me extensively in the years leading up to the publication of this research. I wish to acknowledge my helpful colleagues from the Ferroelectrics and OLED groups, particularly Ms. Nurul Izzah, Ms. Mardhiah, Dr. Nurain, Ms. Hannah, Dr. Gan Wee Chen, Dr. Rahman, Dr. Selvi, Mr. Kelvin, Mr. Suffian, Dr. Rohul, Ms. AinFatin and Dr. Arif for the extensive scientific discussions and support during the experimental work.

Special thanks to Assoc. Professor Dr. Zul Hazrin from the Center of Ionic, Department of Physics, Faculty of Science, University Malaya for allowing me to conduct TSC experiments in his laboratory and for encouraging me to complete my PhD. I am also indebted to my research colleague, Mr. Abhishek Sasmal from the Indian Institute of Technology Madras for his assistance in the present work.

During these difficulties, I was fortunate to have fantastic friends like Dr. Azuraida, Mrs. Noor Fadhilah, Dr. Hidayati and Mrs. Fatin Amirah. In addition, special thanks, honors and appreciation are due to them, as well as all professionals, colleagues (Physics Department, Universiti Pertahanan Nasional Malaysia), family members, friends and all those whose names are not mentioned here, who have contributed significantly to the successful completion of the study. May Allah shower the above individuals with success and honour in their lives.



My ultimate thanks are dedicated to my parents, Maznah Mat and Hj. Ahmad Abd. Rahman, and mother and father-in-law, Asmah Hj. Ali and Kamarul Zambree Ali Othman, for their endless support, love, and prayer. I also would like to thank my sisters and brother, Azalia, Akmal and Aizuddin who have given me plentiful help and support in completing this thesis.

Finally, yet importantly, my heartfelt thanks and love goes to my husband, Yeop Adzlan Kamarul Zambree, and my lovely children, Nurul Danisha, Nurul Safrina and Yusuf Aryan, who have continuously inspired and supported me in all walks of life. Their genuine love has been with me throughout all my struggle and has assisted me overcome the obstacles that lie ahead. May Allah bless us all with success, health, happiness, patience and strength.

Universiti Malaysia

## TABLE OF CONTENTS

<b>ABSTRACT.....</b>	<b>iii</b>
<b>ABSTRAK.....</b>	<b>v</b>
<b>ACKNOWLEDGEMENTS.....</b>	<b>vii</b>
<b>LIST OF FIGURES .....</b>	<b>xiii</b>
<b>LIST OF TABLES .....</b>	<b>xix</b>
<b>LIST OF SYMBOLS AND ABBREVIATIONS .....</b>	<b>xx</b>
 <b>CHAPTER 1: INTRODUCTION.....</b>	 <b>1</b>
1.1 Introduction .....	1
1.2 Historical backgrounds .....	2
1.3 Research objectives .....	5
1.4 Dissertation outline .....	6
 <b>CHAPTER 2: LITERATURE REVIEW .....</b>	 <b>9</b>
2.1 Introduction .....	9
2.2 Ferroelectric materials .....	9
2.2.1 Polyvinylidene fluoride Trifluoroethylene P(VDF-TrFE) Polymer.....	12
2.2.2 Zinc oxide quantum dots (ZnO QDs) .....	19
2.2.3 Ferroelectric composites .....	23
2.3 Dielectric properties .....	26
2.4 Ferroelectric properties .....	36
2.5 Pyroelectric properties .....	39
2.6 Thermally Stimulated Current (TSC) .....	45
2.7 Summary .....	51

<b>CHAPTER 3: EXPERIMENTAL METHODOLOGY .....</b>	<b>53</b>
3.1 Introduction .....	53
3.2 Sample preparation .....	53
3.2.1 P(VDF-TrFE) copolymer thin films .....	53
3.2.2 P(VDF-TrFE) copolymer thick films .....	54
3.2.3 ZnO Quantum Dots stabilized with organic ligand TEA .....	55
3.2.4 P(VDF-TrFE) / ZnO QDs thin nanocomposite films .....	57
3.2.5 P(VDF-TrFE) / ZnO QDs thick nanocomposite films .....	59
3.2.6 Annealing process .....	60
3.2.7 Poling process .....	61
3.3 Structural analysis .....	62
3.3.1 X-ray diffraction .....	62
3.3.2 Fourier transform infrared spectroscopy .....	63
3.3.3 Differential scanning calorimetry .....	64
3.3.4 High-resolution transmission electron microscopy .....	64
3.3.5 Field emission scanning electron microscopy .....	65
3.4 Optical analysis .....	65
3.4.1 Ultraviolet-visible spectroscopy .....	65
3.4.2 Photoluminescence spectroscopy .....	66
3.5 Electrical measurements .....	66
3.5.1 Dielectric measurements .....	66
3.5.2 Ferroelectric measurements .....	67
3.5.3 Pyroelectric measurements .....	67
3.5.4 Thermally Stimulated Current (TSC) measurements .....	69
3.6 Summary .....	72

<b>CHAPTER 4: STRUCTURAL AND OPTICAL ANALYSIS OF COPOLYMER P(VDF-TrFE), ZnO QDs AND NANOCOMPOSITE THIN FILMS P(VDF-TrFE) / ZnO QDs .....</b>	<b>73</b>
4.1 Introduction .....	73
4.2 Copolymer P(VDF-TrFE) at different annealing temperatures .....	73
4.2.1 XRD analysis and determination of percentage of crystallinity .....	73
4.2.2 FTIR analysis .....	77
4.2.3 DSC analysis .....	78
4.2.4 FESEM analysis .....	80
4.3 Ligand stabilized zinc oxide quantum dots ZnO / TEA .....	84
4.3.1 XRD analysis .....	84
4.3.2 UV-Vis analysis and determination of ZnO / TEA bandgap .....	85
4.3.3 PL analysis .....	88
4.3.4 FESEM and EDX analysis .....	89
4.3.5 TEM analysis .....	92
4.4 Nanocomposite films with various weightage percentage of ZnO QDs .....	94
4.4.1 XRD analysis .....	94
4.4.2 FTIR analysis .....	95
4.4.3 FESEM and EDX analysis .....	96
4.5 Conclusion .....	101
<b>CHAPTER 5: FERROELECTRIC PROPERTIES OF COPOLYMER P(VDF-TrFE) AND NANOCOMPOSITE THIN FILMS P(VDF-TrFE) / ZnO QDs .....</b>	<b>103</b>
5.1 Introduction .....	103
5.2 Ferroelectric of copolymer at different annealing temperatures .....	103
5.3 Ferroelectric and energy storage performance of composite films P(VDF-TrFE) / ZnO QDs .....	107
5.4 Leakage current analysis of composite films .....	112
5.5 Conclusion .....	113

<b>CHAPTER 6: DIELECTRIC AND PYROELECTRIC PROPERTIES OF COPOLYMER P(VDF-TrFE) AND NANOCOMPOSITE THIN FILMS P(VDF-TrFE) / ZnO QDs .....</b>	<b>115</b>
6.1 Introduction .....	115
6.2 Dielectric of copolymer P(VDF-TrFE) at different annealing temperature .....	115
6.3 Pyroelectric coefficient of copolymer P(VDF-TrFE) at different annealing temperatures .....	119
6.4 Energy harvesting and sensor Figure of Merit (FOM) of copolymer films .....	122
6.5 Dielectric of composite P(VDF-TrFE) / ZnO QDs .....	124
6.6 Room temperature dielectric models .....	130
6.7 Pyroelectric activity of composite P(VDF-TrFE) / ZnO QDs .....	134
6.8 Energy harvesting and sensor Figure of Merit (FOM) of nanocomposite films P(VDF-TrFE) / ZnO QDs .....	136
6.9 Conclusion .....	138
 <b>CHAPTER 7: THERMALLY STIMULATED CURRENT (TSC) OF COPOLYMER P(VDF-TrFE) AND COMPOSITE THICK FILMS P(VDF-TrFE) / ZnO QDs .....</b>	 <b>140</b>
7.1 Introduction .....	140
7.2 TSC analysis of copolymer P(VDF-TrFE) at different annealing temperatures	140
7.3 Decomposition on TSC peaks of As-cast and Anneal P(VDF-TrFE) at 100 °C .....	148
7.4 TSC analysis of composite P(VDF-TrFE) / ZnO QDs .....	153
7.5 Decomposition of composite P(VDF-TrFE) / ZnO QDs .....	155
7.6 Conclusion .....	166
 <b>CHAPTER 8: CONCLUSION .....</b>	 <b>168</b>
8.1 Conclusion .....	168
8.2 Future work .....	171
<b>REFERENCES .....</b>	<b>173</b>
<b>LIST OF PUBLICATIONS .....</b>	<b>190</b>

## LIST OF FIGURES

<b>Figure 1.1</b>	: Research methodology flow chart .....	8
<b>Figure 2.1</b>	: The interrelationship of ferroelectric and subgroups based on symmetry .....	12
<b>Figure 2.2</b>	: (a) unit, (b) molecule and (c) crystal structures of PVDF .....	14
<b>Figure 2.3</b>	: The three chain conformations of PVDF in different polymorphs: (a) TTT planar zigzag, (b) TGTG' and (c) TTTGTTTG'. Green, yellow and grey colours indicate the fluorine, hydrogen and carbon atom, respectively .....	15
<b>Figure 2.4</b>	: The three crystal structures of PVDF in different polymorphs (a) TTT planar zigzag, (b) TGTG' and (c) TTTGTTTG'.....	17
<b>Figure 2.5</b>	: Schematic diagram of crystallization transformation among polymorphs of PVDF due to electrical, mechanical and thermal treatments .....	18
<b>Figure 2.6</b>	: Dipole orientation of monomer TrFE .....	19
<b>Figure 2.7</b>	: The density of states in different confinement configurations: (a) bulk, (b) quantum well, (c) quantum wire and (d) quantum dots ...	20
<b>Figure 2.8</b>	: Zinc oxide crystal structure (a) cubic rock salt, (b) cubic zinc blende and (c) hexagonal wurtzite. Red and black color indicate the oxygen and zinc atom, respectively .....	21
<b>Figure 2.9</b>	: Lattice structure of wurtzite ZnO. The direction of the dipole is illustrated with a vector P .....	22
<b>Figure 2.10</b>	: Different types of polarization as a function of frequency in polymers together with relaxations and resonance regimes following the EM spectrum .....	28
<b>Figure 2.11</b>	: Schematic illustrations of electronic, orientation, ionic and space charge polarization mechanism .....	29
<b>Figure 2.12</b>	: The real, $\epsilon'$ (black line) and imaginary, $\epsilon''$ (red line) part of the complex dielectric function for a copolymer P(VDF-TrFE) 75/25 relaxation process at -20°C .....	34
<b>Figure 2.13</b>	: Typical <i>P-E</i> ferroelectric hysteresis loop. Circles with arrows represent the polarization state of the material at the indicated field	39
<b>Figure 2.14</b>	: Pyroelectric sample with dipoles and polarization vector: (a) spontaneous polarization without electrodes, (b) with two conductive electrodes and connected to an ammeter at a constant temperature, (c) while being heated, and (d) while cooling .....	41

<b>Figure 2.15</b>	: The relationships between the thermal (temperature), mechanical (strain) and electrical (field) properties of a crystal .....	43
<b>Figure 2.16</b>	: Ideal rectangular short-circuited pyroelectric current spectra in response to triangular temperature wave .....	44
<b>Figure 2.17</b>	: Schematic configuration of typical electrets with aligned dipoles and space charges .....	46
<b>Figure 2.18</b>	: Schematic illustration of typical TSC result for PMMA. The symbols $\gamma$ , $\beta$ , $\alpha$ and $\rho$ indicate relaxation peaks in the material .....	48
<b>Figure 3.1</b>	: MIM structure of P(VDF-TrFE) thin films .....	54
<b>Figure 3.2</b>	: Fabrication flowchart of the spin coating polymer thin films .....	54
<b>Figure 3.3</b>	: P(VDF-TrFE) cast films via solution casting .....	55
<b>Figure 3.4</b>	: ZnO QDs (a) synthesized using reflux method (b) final solution (c) after precipitation and centrifuge process .....	56
<b>Figure 3.5</b>	: Flowcharts of ZnO / TEA QDs synthesis by sol-gel method .....	57
<b>Figure 3.6</b>	: Solutions of nanocomposite viewed under UV lamp 365 nm with different weightage percentage. From right, 0, 0.15, 0.25, 0.35 and 0.50 wt% of P(VDF-TrFE) / ZnO QDs .....	58
<b>Figure 3.7</b>	: Fabrication flowchart of the polymer / quantum dots nanocomposite thin films .....	59
<b>Figure 3.8</b>	: Thin film configuration of P(VDF-TrFE) / ZnO QDs composite films on a glass substrate (a) real picture (b) schematic diagram ...	59
<b>Figure 3.9</b>	: The P(VDF-TrFE) / ZnO QDs thick nanocomposite film .....	60
<b>Figure 3.10</b>	: A beam of parallel X-ray penetrating atomic planes in a crystalline material .....	63
<b>Figure 3.11</b>	: Schematic drawing of the pyroelectric measurement .....	68
<b>Figure 3.12</b>	: Schematic drawing of the TSC principle .....	70
<b>Figure 3.13</b>	: The experimental setup of TSC system .....	71
<b>Figure 4.1</b>	: XRD patterns of P(VDF-TrFE) films annealed at 80 °C to 140 °C with 10 °C temperature increments .....	75
<b>Figure 4.2</b>	: Peak fitting and deconvolution of XRD curve for P(VDF-TrFE) thin films at different annealing temperature (a) 80 °C (b) 90 °C (c) 100 °C (d) 110 °C (e) 120 °C (f) 130 °C (g) 140 °C .....	76

<b>Figure 4.3</b>	: Dependence of the percentage of the crystalline structure as a function of annealing temperature .....	77
<b>Figure 4.4</b>	: FTIR absorbance spectra of P(VDF-TrFE) at the different annealing temperatures .....	78
<b>Figure 4.5</b>	: Differential scanning calorimetry (DSC) thermogram of annealed P(VDF-TrFE) 72/25 at 80 °C .....	79
<b>Figure 4.6</b>	: Differential scanning calorimetry (DSC) thermogram of as-cast and annealed P(VDF-TrFE) 72/25 .....	80
<b>Figure 4.7</b>	: FESEM microstructure of (a) as-cast and (b)-(e) annealed P(VDF-TrFE) at different temperature from 80 °C to 140 °C at magnification and resolution (i) 5 k, 1 $\mu$ m (ii) 50 k, 100nm and (iii) 200 k, 100 nm .....	83
<b>Figure 4.8</b>	: X-ray diffraction pattern of wurtzite crystalline ZnO QDs on a glass substrate .....	85
<b>Figure 4.9</b>	: Optical absorption spectra for ZnO quantum dots capped with TEA .....	86
<b>Figure 4.10</b>	: Determination of the band gap as the intercept between the photon energy and the extrapolation of the linear region of the square of the absorption .....	88
<b>Figure 4.11</b>	: PL spectra of ZnO QDs capped with TEA .....	89
<b>Figure 4.12</b>	: FESEM images of (i) as-cast ZnO QDs and (ii) anneal ZnO QDs at 100 °C spin coat on Si wafer at different magnification and resolution .....	90
<b>Figure 4.13</b>	: EDX spectra of (i) as-cast ZnO QDs and (ii) anneal ZnO QDs ....	91
<b>Figure 4.14</b>	: TEM micrograph (a) and (c) and histogram (b) and (d) of particle size distribution for ZnO QDs and (e) the lattice fringe of ZnO QDs wurtzite plane .....	93
<b>Figure 4.15</b>	: XRD pattern of P(VDF-TrFE) and nanocomposite films with various concentrations of ZnO QDs .....	95
<b>Figure 4.16</b>	: FTIR spectra of copolymer P(VDF-TrFE), ZnO QDs and nanocomposite thin films .....	96
<b>Figure 4.17</b>	: FESEM images of P(VDF-TrFE) / ZnO QDs films anneal at 100 °C spin coat on Si wafer (a) 0.15 wt% (b) 0.25 wt% (c) 0.35 wt% and (d) 0.50 wt% with magnification and resolution of (i) 5 k, 10 $\mu$ m (ii) 50 k, 1 $\mu$ m (iii) 100 k, 500 nm .....	98
<b>Figure 4.18</b>	: EDX spectra of P(VDF-TrFE) / ZnO QDs films at (a) 0.15 wt% (b) 0.25 wt% (c) 0.35 wt% and (d) 0.50 wt% .....	100



<b>Figure 5.1</b>	: Hysteresis of the polarization of P(VDF-TrFE) copolymer thin films at room temperature as a function of the electric poling field	105
<b>Figure 5.2</b>	: <i>D-E</i> hysteresis loops of P(VDF-TrFE) copolymer thin films as measured at room temperature for various annealing temperatures at 60 V applied voltage .....	106
<b>Figure 5.3</b>	: Dependence of remnant polarization with the percentage of film's crystallinity on the various annealing temperature .....	107
<b>Figure 5.4</b>	: (a) <i>D-E</i> hysteresis loops at 100 Hz and (b) Remnant polarization of P(VDF-TrFE) / ZnO QDs composite films with various compositions .....	108
<b>Figure 5.5</b>	: (a) <i>D-E</i> hysteresis loops at 100 Hz and (b) Energy discharge and charging density of P(VDF-TrFE) / ZnO QDs composite films with various compositions .....	110
<b>Figure 5.6</b>	: Leakage current curve of P(VDF-TrFE) / ZnO QD composite film	113
<b>Figure 6.1</b>	: Room temperature dielectric frequency spectra of P(VDF-TrFE) films at various annealing temperatures .....	116
<b>Figure 6.2</b>	: Dielectric frequency spectra for the P(VDF-TrFE) thin film annealed at 100 °C and measured at a temperature step size of 10 °C from room temperature (RT) to 120 °C .....	118
<b>Figure 6.3</b>	: Dielectric constant of P(VDF-TrFE) film annealed at 100 °C as a function of temperature with a step size of 10 °C .....	118
<b>Figure 6.4</b>	: (a) Change in pyroelectric current with time and temperature of the P(VDF-TrFE) thin film and (b) graph of $I_p$ versus rate of temperature change, $dT/dt$ for poled P(VDF-TrFE) thin film annealed at 100 °C .....	120
<b>Figure 6.5</b>	: Pyroelectric coefficient, $P_i$ of P(VDF-TrFE) thin films plotted together with their respective remnant polarization and percentage crystalline for various annealing temperatures .....	121
<b>Figure 6.6</b>	: Dependence of pyroelectric coefficient with two figures of merit (FOMs), $F_D$ and $F_E$ on various annealing temperatures of P(VDF-TrFE) thin films .....	124
<b>Figure 6.7</b>	: Real ( $\epsilon'$ ) and imaginary ( $\epsilon''$ ) dielectric spectra of P(VDF-TrFE) / ZnO QDs (a) 0 wt% (b) 0.15 wt% (c) 0.25 wt% (d) 0.35 wt% and (e) 0.50 wt% .....	126
<b>Figure 6.8</b>	: Frequency dependence of dielectric spectra, real ( $\epsilon'$ ) and imaginary ( $\epsilon''$ ) of P(VDF-TrFE) / ZnO QDs composites with different filler contents at room temperature. ....	128
<b>Figure 6.9</b>	: Temperature dependence of real ( $\epsilon'$ ) and imaginary ( $\epsilon''$ ) for various dielectric spectra wt% of ZnO at 1 kHz .....	129

<b>Figure 6.10</b>	: Various models of the effective dielectric permittivity ( $\epsilon'$ ) as a function of the weightage of ZnO QDs ( $\phi$ ) at room temperature and 1 kHz .....	132
<b>Figure 6.11</b>	: Schematic diagram of polymer/filler composite materials consisting of filler particle, interphase and matrix .....	133
<b>Figure 6.12</b>	: The pyroelectric coefficient ( $P_i$ ) with a respective filler content (wt%) of nanocomposite films. The inset figure shows the pyroelectric current waveform .....	136
<b>Figure 6.13</b>	: Dependence of pyroelectric coefficient ( $P_i$ ) with energy harvesting figure of merit ( $F_E$ ) and detectivity figure of merit ( $F_D$ ) on various of of P(VDF-TrFE) / ZnO QDs nanocomposite films .....	137
<b>Figure 7.1</b>	: TSC complex spectrum of P(VDF-TrFE) 72/25 for 100 °C anneal films at (a) vary poling temperatures (b) varied times of poling .....	142
<b>Figure 7.2</b>	: TSC complex spectrum of P(VDF-TrFE) 72/25 for as-cast film and all anneal films at various setting parameters (a) $T_p = 60$ °C, $t_p = 2$ min, $E = 5$ MV/m (b) $T_p = 60$ °C, $t_p = 10$ min, $E = 10$ MV/m and (c) $T_p = 60$ °C, $t_p = 20$ min, $E = 20$ MV/m .....	143
<b>Figure 7.3</b>	: DSC (endothermic process) and TSC measurements for the (a) as-cast and, (b)-(e) Anneal P(VDF-TrFE) films .....	148
<b>Figure 7.4</b>	: Decomposition of the TSC spectrum of the as-cast P(VDF-TrFE) film for $\alpha_1$ , $\alpha_2$ and $\rho$ relaxation peaks .....	151
<b>Figure 7.5</b>	: Decomposition of the TSC spectrum of the annealed P(VDF-TrFE) at 100 °C for $\beta$ , $\alpha_1$ , $\alpha_2$ and $\rho$ relaxation peaks .....	152
<b>Figure 7.6</b>	: TSC complex spectrum of (a) copolymer P(VDF-TrFE) (b) nanocomposite P(VDF-TrFE) / ZnO QDs, at different thickness .....	154
<b>Figure 7.7</b>	: Decomposition of the TSC spectrum of the 0 wt% P(VDF-TrFE) / ZnO QDs films .....	156
<b>Figure 7.8</b>	: Decomposition of the TSC spectrum of the 0.15 wt% P(VDF-TrFE) / ZnO QDs films .....	157
<b>Figure 7.9</b>	: Decomposition of the TSC spectrum of the 0.25 wt% P(VDF-TrFE) / ZnO QDs films .....	158
<b>Figure 7.10</b>	: Decomposition of the TSC spectrum of the 0.35 wt% P(VDF-TrFE) / ZnO QDs films .....	159
<b>Figure 7.11</b>	: Decomposition of the TSC spectrum of the 0.50 wt% P(VDF-TrFE) / ZnO QDs films .....	161

<b>Figure 7.12</b>	: Schematic representation of the image charges on electrodes released by depolarization of dipoles, space charges and homocharges within the electrets .....	164
--------------------	---	-----

Universiti Malaya

## LIST OF TABLES

<b>Table 2.1</b>	: Symbol of the 32-point groups on crystallography. Remarks: (*) implies that piezoelectric effect may be exhibited and (+) implies that pyroelectric and ferroelectric effects may be exhibited .....	11
<b>Table 2.2</b>	: Ferroelectric studies of polymer nanocomposite films embedded with quantum dot. ....	25
<b>Table 2.3</b>	: Pyroelectric properties of thin polymer and nanocomposite films observed at frequency 1 kHz .....	45
<b>Table 4.1</b>	: Distribution of structures observed in nanocomposite films of P(VDF-TrFE) / ZnO .....	98
<b>Table 5.1</b>	: Ferroelectric studies of polymer nanocomposite films embedded with quantum dots .....	111
<b>Table 6.1</b>	: The PVDF and P(VDF-TrFE) based composite systems .....	138
<b>Table 7.1</b>	: TSC parameters of copolymer films .....	145
<b>Table 7.2</b>	: TSC peak positions and activation energy of copolymer and composite films through the decomposition technique presented in this work .....	162

## LIST OF SYMBOLS AND ABBREVIATIONS

$A$	:	Area
$C$	:	Capacitance
$C_o$	:	Capacitive component
$D$	:	Electric displacement
$d$	:	Crystallite size
$E$	:	Electric field
$E_c$	:	Coercive field
$E_o$	:	Amplitude of electric field
$F$	:	Force
$f$	:	Frequency
$f_t$	:	Resonance frequency
$hkl$	:	Diffraction peak at half-maximum intensity
$I$	:	Current
$I_c$	:	Capacitive component of the current
$I_p$	:	Pyroelectric current
$I_R$	:	Resistive component of the current
$J$	:	Current density
$k$	:	Scherrer constant / Shape factor
$L$	:	Inductance
$\vec{P}$	:	Polarization
$P_r$	:	Remnant polarization
$P_s$	:	Spontaneous polarization
$\vec{p}$	:	Dipole moment
$p_{ primary\ effect }$	:	Primary pyroelectric

$P_{\text{secondary effect}}$	:	Secondary pyroelectric
$q$	:	Charge
$T_c$	:	Curie transition temperature
$T_d$	:	Depolarization temperature
$T_m$	:	Maximum temperature
$T_0$	:	Curie-Weiss temperature
$t$	:	Thickness
$V$	:	Volume
$v$	:	Domain wall motion
$X$	:	Curie constant
$Z$	:	Impedance
$\beta$	:	Inverse dielectric constant
$\delta$	:	Phase lag
$\epsilon'$	:	Real permittivity
$\epsilon''$	:	Imaginary permittivity
$\epsilon^*$	:	Complex dielectric permittivity
$\epsilon_s$	:	Instantaneous relative permittivity
$\epsilon$	:	Strain
$\Delta\epsilon$	:	Dielectric strength
$\Delta P_s$	:	Change in spontaneous polarization
$\Delta T$	:	Change of temperature
$dT/dt$	:	Heating rate
$P_i$	:	Pyroelectric coefficient
$\tau$	:	Relaxation time
$\mu$	:	Dipole moment per unit volume

$\vartheta$	:	Mobility of the domain wall
$\omega$	:	Angular frequency
$\theta$	:	Bragg diffraction angle in X-ray diffraction
$\lambda$	:	Wavelength
$\rho$	:	Density
$\sigma^*$	:	Complex conductivity
$\phi$	:	Volume fractions
wt%	:	Weight percentage
DSC	:	Differential scanning calorimetry
FESEM	:	Field emission scanning electron microscopy
FTIR	:	Fourier transform infrared spectroscopy
HRTEM	:	High-resolution transmission electron microscope
MEK	:	Methyl ethyl ketone
MIM	:	Metal-insulator-metal structure
PL	:	Photoluminescence spectroscopy
PVDF	:	Polyvinylidene fluoride
P(VDF-TrFE)	:	Polyvinylidene fluoride trifluoroethylene
QDs	:	Quantum dots
TEA	:	Triethanolamine
TrFE	:	Trifluoroethylene
TSC	:	Thermally Stimulated Current
UV-Vis	:	Ultraviolet-visible spectroscopy
XRD	:	X-ray diffraction
ZnO	:	Zinc oxide

## CHAPTER 1: INTRODUCTION

### 1.1 Introduction

The development of smart materials with superior properties, lower cost and smaller dimensions is vital in designing energy harvesting nanogenerators. Researchers' interest in energy conversion has grown over the past decade to harness the waste of many forms of energy sources in the environment. Many energy conversion mechanisms are exploited, including piezoelectric, pyroelectric, triboelectric and others. The ability of a material to produce a temporal voltage corresponds to the temperature fluctuation, which is based on polarization, which is called the pyroelectric effect. This effect is commonly observed in polymeric materials. To fabricate a thermal or infrared sensor, it is essential that a material has a high pyroelectric constant, low dielectric loss, and low specific heat and thermal conductivity (Gan & Majid, 2015; Jayalakshmy & Philip, 2015; Zhang et al., 2017). Recently, Yang et al. (2012) reported a ZnO nanowire array for a pyroelectric nanogenerator with the pyroelectric current and voltage coefficients of  $\sim 1.2 - 1.5 \text{ nC/cm}^2\text{K}$  and  $\sim 2.5 - 4.0 \times 10^4 \text{ V/mK}$ , respectively. The development of hybrid materials consisting of polymers (organic) and nanoparticles (inorganic) as efficient energy harvesters and energy storage devices is of critical importance nowadays. The polymer nanocomposites are categorized as hybrid materials which contain nanofillers embedded into the polymer matrix. Spin-coating is a common approach in the deposition of nanocomposite thin films before energy harvesting and energy storage applications.

The quasi-hexagonal symmetry structure of P(VDF-TrFE)  $\beta$  phase crystal exhibits the most crystalline phase with the greatest spontaneous polarization in the unit cell and is a good feature in electrical properties (Furukawa, 1989). In this study, the copolymer P(VDF-TrFE) with great characteristics such as stable polarization and short switching time is favourable as a polymer matrix in the fabrication of polymer nanocomposite devices. Semiconductor



quantum dots (QDs) or nanocrystals were used as nanofillers in a copolymer host to develop polymer nanocomposite devices. Because of their tunable physical dimensions and good optoelectronic capabilities due to size confinement and anisotropic geometry, QDs have received a lot of attention as nanofillers.

## **1.2 Historical backgrounds**

Polyvinylidene fluoride (PVDF) and its copolymer with trifluoroethylene (TrFE) are ideal candidates for ferroelectric polymers because of their superior ferroelectric performance and ease of processing into thin films. It was around 1970 when Kawai discovered PVDF in the form of electret (Kawai, 1969). Poling the polymer PVDF with a high electric field induces orientation of the permanent dipoles and possibly creates a space charge by injection of free charge carriers between the electrodes to robust the electrical properties of a polymer. Soon after, Bergman reported the discovery of pyroelectricity and non-linear optical properties of PVDF in 1971 (Bergman et al., 1971). Lando and Doll proposed in 1968 that direct crystallization of polar PVDF can be induced by incorporating a small amount of trifluoroethylene (TrFE) and tetrafluoroethylene (TeFE) into PVDF from melt crystallization (Doll & Lando, 1970).

Current research focuses on the inclusion of nanocrystals into polymer matrix for various applications; indium phosphide (InP) QDs in polydimethylsiloxane (PDMS) for solar energy harvesting (Sadeghi et al., 2020), CsPbBr<sub>3</sub> QDs-NOA63 NC with PDMS as a passivation layer for piezoelectric nanogenerator (Lee et al., 2021) and carbon dots (C-dots) in conducting polymers (polypyrrole (PPy) and polyaniline (PANI)) for energy storage applications (Devadas & Imae, 2018). Sadeghi et al. (2020) in his work, copper doping of a zinc carboxylate-passivated InP core and nanoengineering of the ZnSe shell; were used to produce a high in-device quantum efficiency of QDs of more than 80%. Polymer nanocomposites, on the other hand, exhibit high reabsorption and low external quantum efficiency in host materials, making them unsuitable for electro-optical measurements. Moreover, the cost of

the polymer host (PDMS) and QD synthesis chemicals may limit large-scale production. According to Lee et al., (2021), CsPbBr<sub>3</sub> QDs-NOA63 polymer nanocomposites have a higher output voltage of piezoelectric nanogenerators (PENGs), which is ascribed to the very high piezoelectric coupling between the QDs and the polymer matrix. Embedment of CsPbBr<sub>3</sub> QDs into NOA63 polymer matrix avoided the formation of pinholes on the surface of the polymer nanocomposites while also increasing the thickness of the piezoelectric layer. It has also been reported that the specific capacity and long-term stability of carbon-dot (C-dot) polymer nanocomposites in conducting polymers of polypyrrole (PPy) and polyaniline (PANI) increase due to the synergistic effect of polymers and C-dots (Devadas & Imae, 2018). The limited mechanical stability and cycle life of conducting polymers, which results in poor charge/discharge capabilities, has been overcome in this case by embedding C-dots in the conducting polymer matrix.

From the literature review thus far, no research work on zinc oxide QDs acting as a zero-dimensional nanofiller in a ferroelectric polymer host such as polyvinylidene difluoride (PVDF) or its copolymer P(VDF-TrFE) has been reported, with a focus on the electrical properties related to the energy storage performance of the polymer nanocomposite. It is of great interest to investigate ZnO QDs-P(VDF-TrFE) due to the particle size effect on its structural and physical properties, which will impact its electrical properties and energy storage performance.

Three main issues must be addressed for any polymer nanocomposite to be useful as an energy harvester: the agglomeration of quantum dots (QDs), toxicity and energy harvesting performance. Surface modification using a capping agent is essential for controlling the as-synthesized QD size and preventing rapid agglomeration due to the high surface energy. Ligand-stabilized ZnO QDs have been thoroughly investigated to control their electrical and optical properties. Adnan et al. have demonstrated the ability to synthesise monodisperse ZnO QDs stabilised using triethanolamine (TEA) with an average size of 2.4 nm (Adnan et al., 2017). TEA ligands tend to encapsulate the surface of ZnO and hence result in smaller QDs.

TEA is also highly soluble in polar solvents like ethanol. Among the II-VI binary compound semiconductors, ZnO QDs are of particular interest due to their distinctive properties, which include a wide direct energy gap of  $\sim 3.4$  eV at room temperature, a large exciton binding energy of 60 meV, and nontoxicity (Alim et al., 2005). ZnO QDs are known as green materials, with low-cost and stable synthesis (Fu et al., 2007). Broadband metal oxide semiconductors like ZnO offer unique characteristics such as a wide bandgap, high electron mobility, and appropriate light absorption. As a result, they are suitable for high-temperature and high-power electrical devices, as well as UV optoelectronics (Galdámez-Martínez et al., 2020). Furthermore, due to the noncentral symmetry in the wurtzite of ZnO QDs, this material exhibits pyroelectric and piezoelectric characteristics and is frequently utilized in piezoelectric sensors, mechanical actuators, and QD solar cells (Mohamed et al., 2021). ZnO's hexagonal wurtzite crystal structure is the thermodynamically stable phase under ambient conditions. Recently, pyroelectric thin films with spherically symmetric PbS QDs that have an asymmetric ligand shell called Janus-ligand shell showed a pyroelectric coefficient,  $P_i$  of  $1.97 \times 10^{-7}$  C/m<sup>2</sup>K (Huang et al., 2021; Kołodziejczak-Radzimska et al., 2012). These materials, however, include lead, which causes major environmental pollution. Exposure to environmental pollution should be avoided using nontoxic or lead-free pyroelectric materials. For piezoelectric energy harvesting devices, ZnO nanorods (NRs) and nanowires (NWs) are well-known non-toxic materials that are frequently produced by hydrothermal synthesis (Bhadwal et al., 2023). ZnO nanorods have demonstrated a great deal of promise in the field of energy harvesting; however, it is important to remember that many factors can affect how well they work, including the nanorods' dimensions, orientation, crystal structure, surface treatments, and passivation (He et al., 2012; AbuBakar et al., 2023; Obreja et al., 2019; Jalali et al., 2013). The ZnO NRs or NWs' pyroelectric response may depend on their dimensions, including length, diameter, and aspect ratio (Consonni et al., 2021). Li et al. (2015) reported that reducing the diameter size of the nanowires from 7  $\mu\text{m}$  to 1.5  $\mu\text{m}$  improved the piezoelectric coefficient from 18.2 to 46.9 pmV<sup>-1</sup> (Bhadwal et al., 2023). The increase of

polarization per unit volume as the diameters of the NWs reduced is responsible for the improvement of the piezoelectric coefficient. By reducing surface defects, the stability and performance of ZnO NWs or NRs could be enhanced by surface treatments and passivation layers (Sánchez-Godoy et al., 2022). Therefore, incorporating ZnO QDs as fillers in the fabrication of polymer nanocomposites device is a feasible strategy due to its nontoxicity. There are several chemical routes for preparing ZnO QDs, such as the sol-gel method, spray pyrolysis, precipitation, vapour phase transport process (VPT), thermal decomposition, hydrothermal synthesis, and electrochemical growth. Among these techniques, the sol-gel method has received particular interest due to its simplicity, inexpensiveness, and easy scalability.

### **1.3 Research objectives**

The initial phase of the research work is to study the effect of thermal annealing of the copolymer P(VDF-TrFE) through the thermally stimulated current (TSC) method and to explore the relations of the observed TSC spectra with the structural, morphological, ferroelectric, dielectric and pyroelectric properties as parameters for the energy harvesting figure of merit. Later, in this study, the inclusion of ZnO QDs as a filler in the optimally annealed P(VDF-TrFE) copolymer films was developed as potential energy storage and energy harvesting nanogenerators. It is hypothesised that adding nanocrystal ZnO nanofillers to the copolymer matrix will boost polarisation and hence the current generated by pyroelectric activities. The energy storage ability of the P(VDF-TrFE) / ZnO QD nanocomposite and its prospective application as an energy harvesting device, will be evaluated using the ferroelectric hysteresis loop and pyroelectric activities. Therefore, the specific objectives of this research are:

- [1] To increase the crystallinity and polarization of P(VDF-TrFE) and to obtain the optimum remnant polarization,  $P_r$ , dielectric constant and pyroelectric coefficient,  $P_i$  of P(VDF-TrFE).
- [2] To investigate the effects of annealing treatment on the polarization of copolymer P(VDF-TrFE) free films by Thermal Stimulated Current (TSC).
- [3] To determine the size of synthesized ZnO QDs and to investigate the effect of semiconductive filler ZnO QDs in P(VDF-TrFE) matrix on ferroelectric, dielectric and pyroelectric properties together the performance energy storage and energy harvesting nanogenerator of P(VDF-TrFE) / ZnO QDs device.
- [4] To investigate the relaxations revealed by Thermal Stimulated Current (TSC) for nanocomposite P(VDF-TrFE) / ZnO QDs films.

#### **1.4 Dissertation outline**

In Chapter 1, a brief introduction to ferroelectric materials and semiconducting quantum dots and their potential application is given. This chapter also includes the historical development of ferroelectric materials. It is followed by the research objectives, which emphasise the importance of understanding the structure and electrical properties of the copolymer P(VDF-TrFE) and ZnO quantum dots to improve the performance of ferroelectric materials.

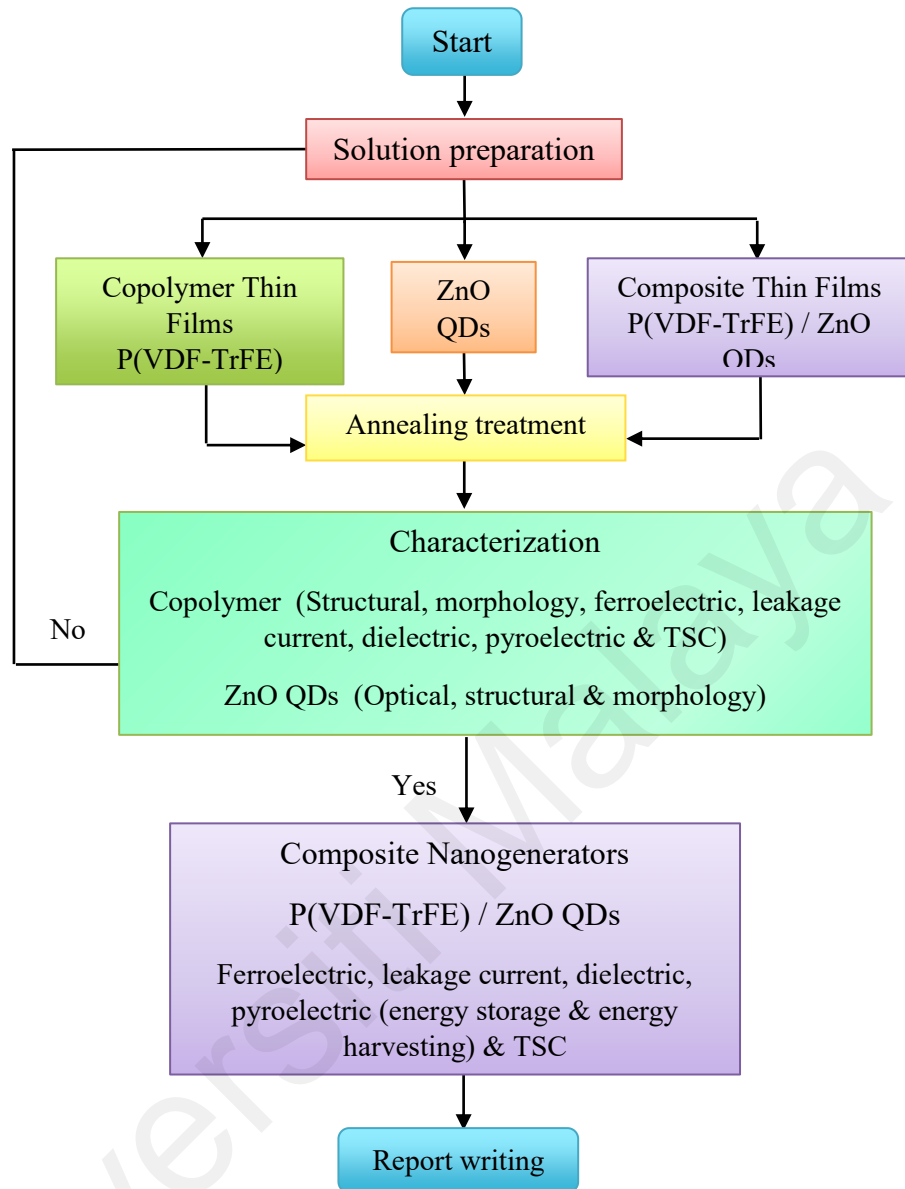
Chapter 2 of this thesis gives a comprehensive overview of the background of the materials, including the ferroelectric polymer P(VDF-TrFE), semiconductor ZnO nanocrystals or quantum dots and composites. The mechanism involved in the polarization of dielectric, ferroelectric, and pyroelectric materials, including the thermally stimulated current, is also discussed. Chapter 3 outlines the methodology and theoretical aspects of the experiment. The annealing treatment of the copolymer films, the synthesis of ZnO QDs using the sol-gel method, the fabrication of nanocomposites, and the preparation of the samples for electrical

and TSC measurements are discussed in detail. The principle and equipment setup for the electrical and TSC measurement used in this study were also explained.

In Chapter 4, the structural and morphological of copolymer P(VDF-TrFE), ZnO QDs and nanocomposite films of P(VDF-TrFE) embedded with less than 1 wt% nanofiller ZnO QDs are elaborated. The optical studies of ligand-stabilized quantum dots are explained in detail. The copolymer P(VDF-TrFE) was annealed at various annealing temperatures during the initial phase of research to study the relationship between the structure and crystallinity of the sample. In the fabrication of polymer nanocomposite nanogenerators, the best-annealed copolymer films are used as polymer hosts. Chapter 5 discusses the physical functional properties (ferroelectric and leakage current) of the copolymer and the polymer nanocomposite. The hysteresis loop obtained in the ferroelectric measurement was further analyzed to investigate the performance of P(VDF-TrFE) / ZnO QDs nanogenerators in energy storage.

Chapter 6 focuses on the dielectric (room temperature and temperature dependence measurement) and pyroelectric of the annealed copolymer and polymer nanocomposite. The study also examined P(VDF-TrFE) films and P(VDF-TrFE) / ZnO QDs nanogenerators for energy harvesting and sensor figure of merit based on the dielectric and pyroelectric properties of the samples. The ferroelectric, dielectric and pyroelectric properties are strongly influenced by the degree of crystallinity.

Chapter 7 discussed the Thermal Stimulated Current study of P(VDF-TrFE) and P(VDF-TrFE) / ZnO QDs. Both samples were analyzed using a decomposition technique that reveals some well-known relaxation phenomena such as space charge, dipole group and segmental relaxations with their respective activation energies. Finally, chapter eight summarises the findings of the overall study in this thesis and suggests several possible research works that can be explored in the future. Figure 1.1 shows the flow chart of the research methodology in this work.



**Figure 1.1: Research methodology flow chart.**

## CHAPTER 2: LITERATURE REVIEW

### 2.1 Introduction

This chapter presents the origin and history of ferroelectric materials such as polymer, semiconductor filler and polymer-semiconductor composites. The theoretical mechanism that plays role in the polarization of ferroelectric, dielectric and pyroelectric are discussed in this chapter. Basic principles and theoretical background of Thermally Stimulated Current will be elucidated as well.

### 2.2 Ferroelectric materials

The terms dielectric, ferroelectric and pyroelectric are frequently mentioned in this dissertation. All the above terms originate from the asymmetry of the crystal structure. The structural symmetry of a crystal depends on its lattice structure and it affects geometrically the structure and physical properties of the crystal such as dielectric, mechanical, piezoelectric, ferroelectric, nonlinear optical properties, etc (Xu, 2013). The lattice structure is described by the Bravais unit cell of the crystal. There are only thirty-two macroscopic symmetry types of crystals (32-point groups) that exist as illustrated in Table 2.1, among thousands of crystals in nature. In a point group, the eight symmetry elements (excluding translation symmetry) consist of rotation axes such as 1 (without rotation), 2 (rotation diad), 3 (rotation triad), 4 (rotation tetrad), 6 (rotation hexad),  $\bar{4}$  (rotation-inversion tetrad axis),  $I$  (inversion centre) and  $m$  (reflection mirror), respectively (Xu, 2013).

According to Neumann's principle, the symmetry group of the physical properties in a crystal refers generally to the 32-point groups derived from the crystal forms. Thus, if a crystal has a physical parameter subjected to a symmetrical operation, the value of this physical parameter should remain unchanged. Among the 32-point groups, 11-point groups are centrosymmetry with a symmetry centre. A symmetric crystal does not have any polarity and

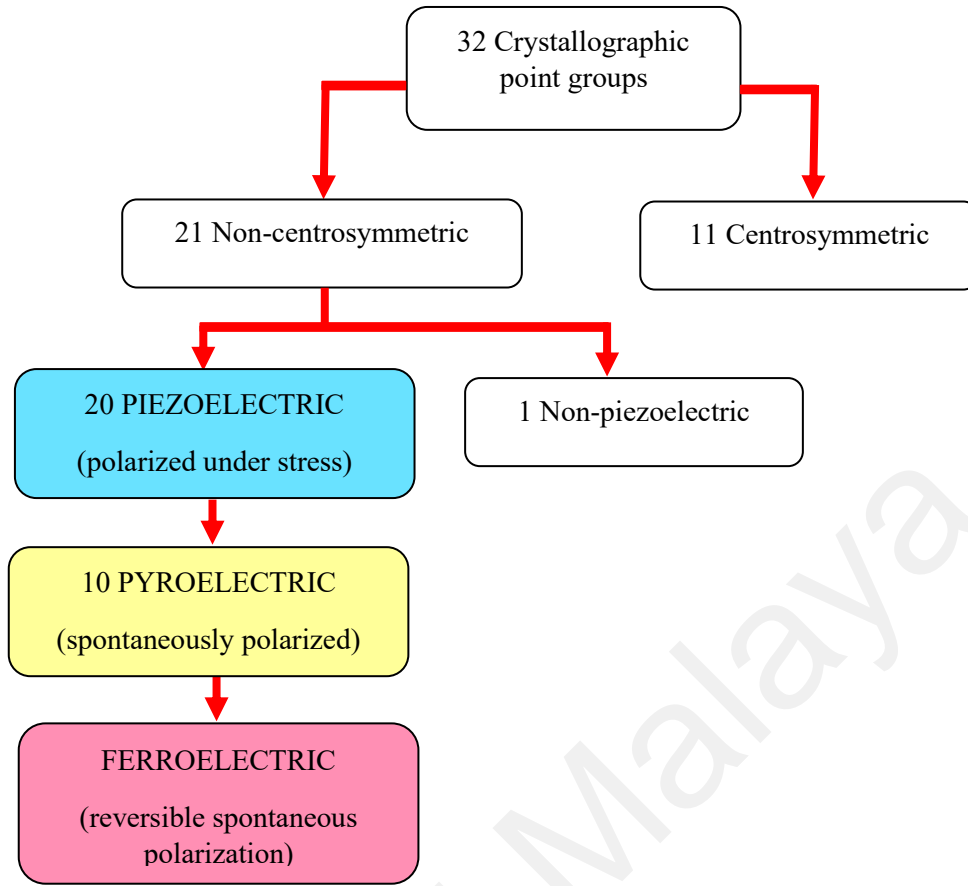


possesses one or more crystallographically unique direction axis. Among these, 20-point groups (\*) exhibit piezoelectricity, while 10-point groups (\*+) have only one unique direction axis. A crystal with point-group symmetry has a unique rotation axis but does not have any mirror perpendicular to this axis. Along a unique rotation axis, the atomic arrangement at one end is different from the other opposite end. These crystals are called polar crystals and exhibit spontaneous polarization.

Polar crystals that have at least two equilibrium orientations for the spontaneous polarization vector in the absence of an external electric field and that can have their spontaneous polarization switched between these two equilibrium orientations by an applied external electric field are regarded as ferroelectric materials. The ferroelectric crystal is also defined as a dielectric material that has a net dipole moment even in the absence of an external electric field. This net dipole moment is due to the centre of the positive charge in the crystal not coinciding with the centre of the negative charge due to its crystalline structure, which is referred to as spontaneous polarization,  $P_s$  (Xu, 2013). Based on the crystallographic point groups, all ferroelectrics are pyroelectric, and all pyroelectrics are piezoelectric, which generally belong to the dielectric. However, not all piezoelectrics are pyroelectric, and not all pyroelectrics are ferroelectric (Batra & Aggarwal, 2013). The relationship between ferroelectric, pyroelectric and piezoelectric together with their subgroups based on symmetry are summarized in Figure 2.1.

**Table 2.1: Symbol of the 32-point groups on crystallography. Remarks: (\*) implies that the piezoelectric effect may be exhibited and (+) implies that pyroelectric and ferroelectric effects may be exhibited (adapted from Xu, 2013)**

Crystal system	International notation	Scönflies' notation	Remarks
Triclinic	1	$C_1$	*+
	$\underline{1}$	$C_1(S_2)$	-
Monoclinic	2	$C_2$	*+
	$m(\underline{2})$	$C_s(C_{1h})$	*+
	$2/m$	$C_{2h}$	-
Orthorhombic	2mm	$C_{2v}$	*+
	222	$D_2(V)$	*
	$mmm$	$D_{2h}(V_h)$	-
Tetragonal	4	$C_4$	*+
	$\underline{4}$	$S_4$	*
	$\underline{4}2m$	$D_{2d}(V_d)$	*
	422	$D_4$	*
	$4mm$	$C_{4v}$	*+
	$4/m$	$C_{4h}$	-
	$4/mmm$	$D_{4h}$	-
Trigonal (Rhombohedral)	3	$C_3$	*+
	$\underline{3}$	$C_{3i}(S_6)$	-
	$3m$	$C_{3v}$	*+
	32	$D_3$	*
	$\underline{3}m$	$D_{3d}$	-
Hexagonal	6	$C_6$	*+
	$\underline{6}$	$C_{3h}$	*
	$6mm$	$C_{6v}$	*+
	$6/m$	$C_{6h}$	-
	622	$D_6$	*
Hexagonal	$\underline{6}m2$	$D_{6h}$	*
	$6/mmm$	$D_{6h}$	-
Cubic	23	$T$	*
	$\underline{4}3m$	$T_d$	*
	$m3$	$T_h$	-
	432	$O$	-
	$m3m$	$O_h$	-



**Figure 2.1: The interrelationship of ferroelectric and subgroups based on symmetry.**

### 2.2.1 Polyvinylidene fluoride Trifluoroethylene P(VDF-TrFE) Polymer

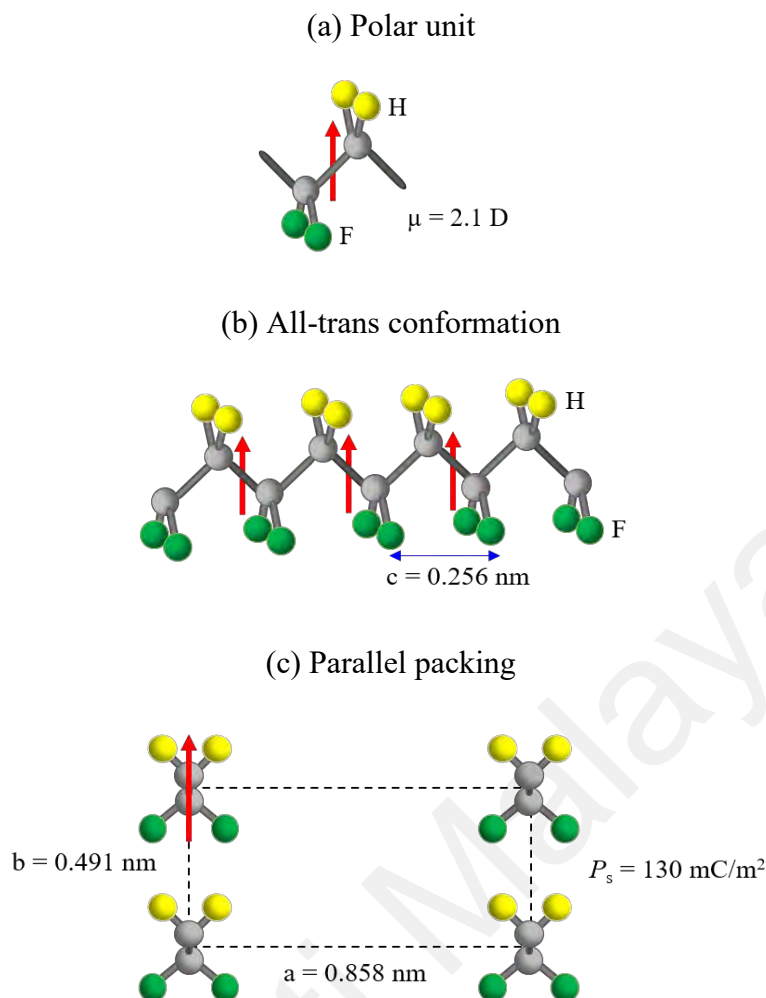
Ferroelectric polymers such as aromatic polyamides (Liu et al., 2014; Murata et al., 1993), polyureas (Tasaka et al., 1992; Yanaka et al., 2020), polyurethane (Dai et al., 2021; Tasaka et al., 1994) and polyvinylidene fluoride have gained great interest since last four decades due to their high functional materials suitable for energy storage and transducer (Alkan et al., 2012; Ren et al., 2020).

Polyvinylidene fluoride (PVDF) and its copolymer with trifluoroethylene (TrFE) are an ideal candidate for ferroelectric polymers because of their superior ferroelectric performance and ease of processing into thin films (Mai et al, 2015). Polyvinylidene fluoride (PVDF) was discovered by Kawai in 1969 (Fukada, 1989). It is a fluorocarbon polymer, which results from the polymerization of vinylidene fluoride (VDF) monomers with a chemical formula  $(-\text{CH}_2-\text{CF}_2-)$ . This  $(-\text{CH}_2\text{CF}_2-)$  monomer is built up from positively charged H-atoms and

negatively charged F-atoms which are aligned in one direction and perpendicular to the chain axis (backbone). A dipole moment in PVDF perpendicular to the chain in each monomer originating from its high electronegativity of a fluorine atom and hydrogen atom and has a vacuum dipole moment of  $\mu_v = 7 \times 10^{-30}$  Cm (2.1 Debyes). The dipole moment orientation is subjected to the conformation and packing of molecules as shown in Figure 2.2 for the polar unit, all-trans chain conformations and parallel packing of PVDF structure (Furukawa, 1997; Zhu et al., 2008). Arrows indicate the dipole direction normal to carbon chains. If the molecule emerges as  $\beta$  phase (Form I) which has an all-trans (TTT) planar zigzag chain conformations (refer to Figure 2.2(b)) with a parallel packing (see Figure 2.2(c)), the dipoles are aligned in one direction, perpendicular to the carbon chain.  $\beta$  phase crystals arranged in a parallel packing, also known as a quasi-hexagonal-symmetry structure (Figure 2.2(c)), exhibit the greatest spontaneous polarization in the unit cell and are hence of particular importance for electrical properties. Higher spontaneous polarization,  $P_s$  reflects greater ferroelectric behaviour which can be experimentally determined by  $D$ - $E$  hysteresis measurements. The lattice constants of such a quasi-hexagonal-symmetry unit cell are  $a = 0.850$  nm,  $b = 0.491$  nm, and  $c = 0.256$  nm (Furukawa, 1997; Zhu et al., 2008). The sum of dipole moment over a unit volume,  $\mu_v$  yields a large crystalline polarization,  $P_s$ .

$$P_s = \frac{2\mu_v}{abc} = 130 \text{ mC/m}^2 \quad (2.1)$$

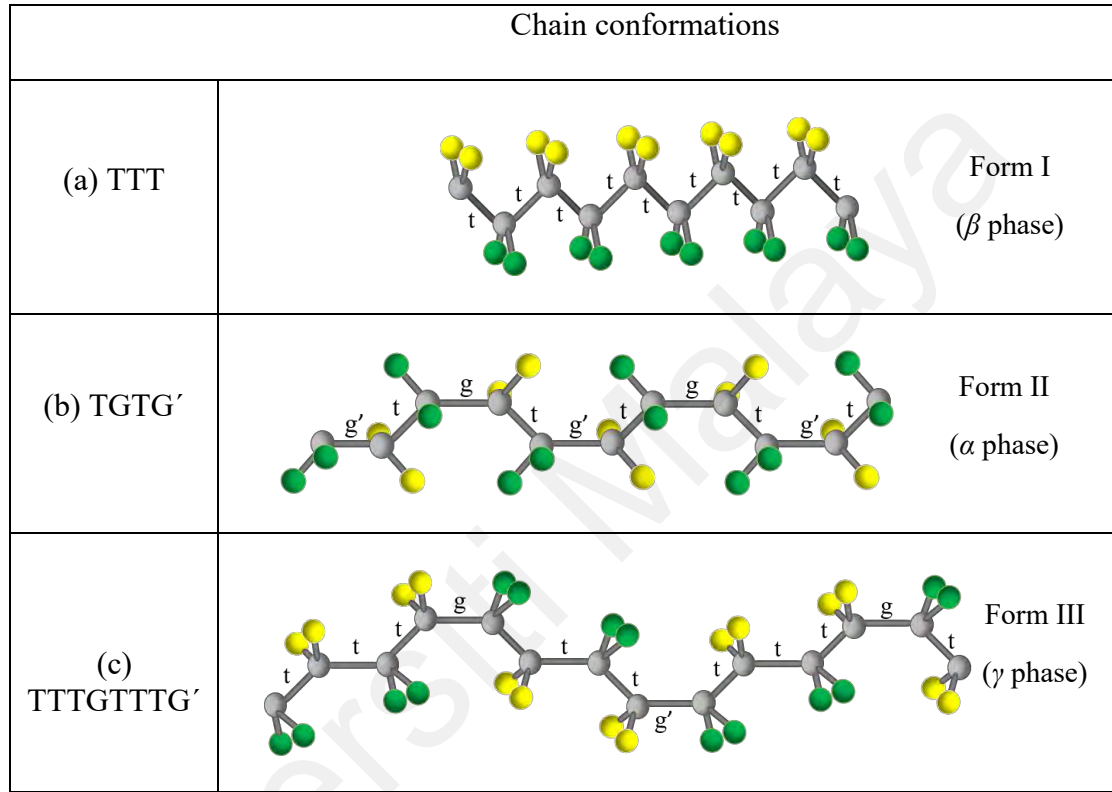
where  $a$ ,  $b$  and  $c$  are the lattice constants with  $a = 0.858$  nm,  $b = 0.491$  nm and  $c = 0.256$  nm, respectively. The dipoles in the  $\beta$  phase conformation are switchable by applying an electric field, thus the  $\beta$  phase is responsible for the PVDF's ferroelectricity (Furukawa, 1997).



**Figure 2.2: (a) unit, (b) molecule and (c) crystal structures of PVDF (Furukawa, 1997).**

PVDF is a semicrystalline polymer that consists of 50% crystallinity and coexists with an amorphous phase. PVDF exhibits four crystalline polymorphs; Form I ( $\beta$  phase), Form II ( $\alpha$  phase), Form III ( $\gamma$  phase) and Form IV ( $\delta$  phase), which are related to the molecular chain conformations as shown in Figure 2.3 (Li & Wang, 2016; Lovinger, 1983; Shepelin et al., 2019; Wu et al., 2020). Their packing fashions play a dominant role in the overall polarity of the PVDF crystalline phase. The  $\alpha$  phase of PVDF has a trans-gauche (TGTG') molecule packed in an antiparallel packing (Figure 2.4(b)), and among the four polymorphs, only this phase is nonpolar, while the remaining three are polar crystalline. The dipole components in the  $\alpha$  phase neutralize each other due to antiparallel packing and hence no polarity is found in this phase. The macromolecular chains of the  $\gamma$  phase have a TTTGTTTG' conformation and an intermediate between the  $\alpha$  and  $\beta$  phases, which form a polar crystalline due to its parallel

packing. Form IV polymorph or  $\delta$  phase is a different packing structure of  $\alpha$  phase which consist of parallel packing of TGTG'. The parallel and antiparallel molecular packing is related to the dipole orientation in the direction perpendicular to the chain axis. From a vector sum of the constituent dipoles, the spontaneous polarization,  $P_s$  of the  $\gamma$  and  $\delta$  is around one-half of the  $\beta$  phase.

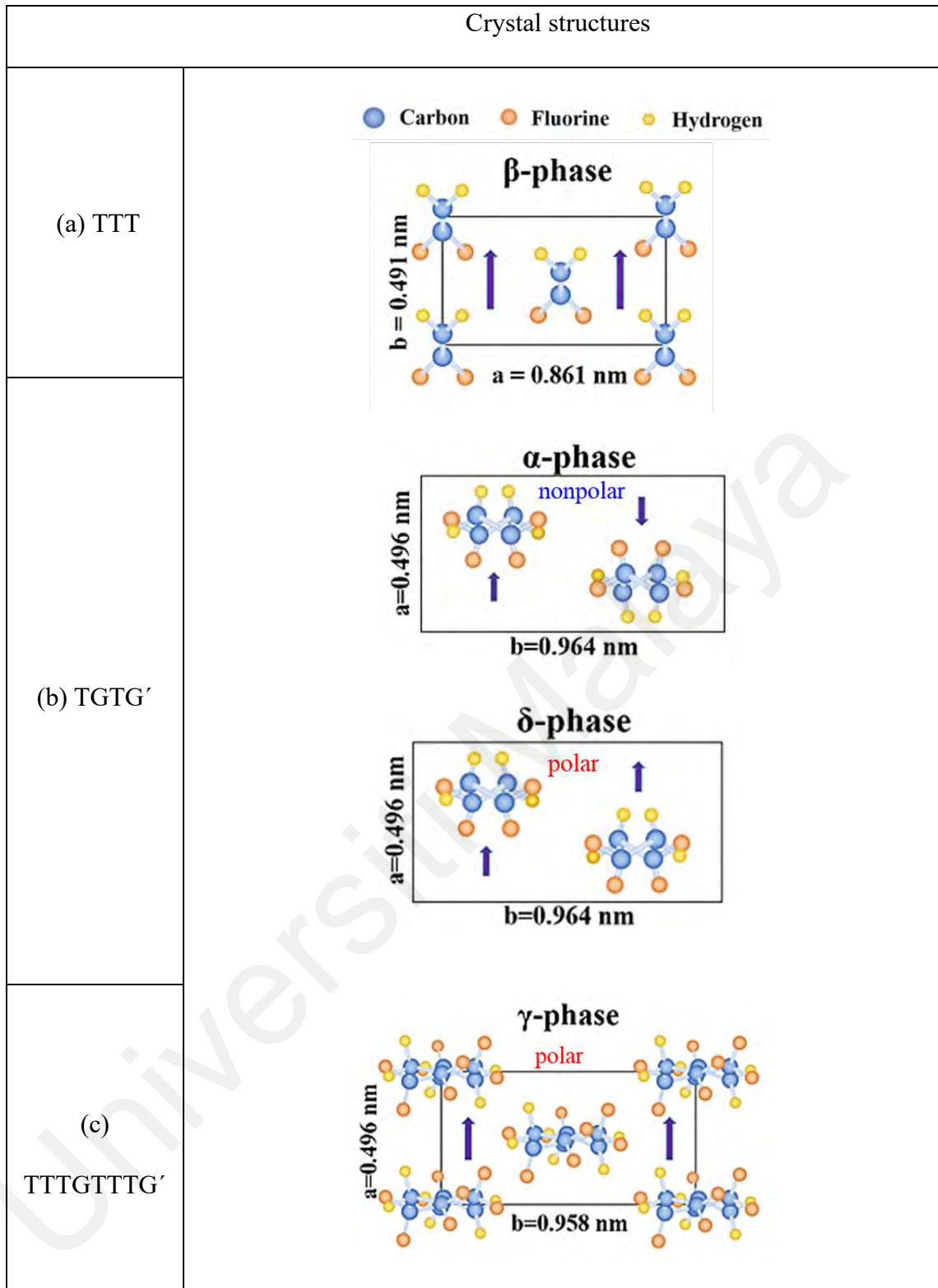


**Figure 2.3: The three chain conformations of PVDF in different polymorphs: (a) TTT planar zigzag, (b) TGTG' and (c) TTTGTTTG'. Green, yellow and grey colours indicate the fluorine, hydrogen and carbon atom, respectively.**

Ferroelectric behaviour observed in PVDF polymer is closely related to the alignment and orientation of its crystalline polymorph crystals. The  $\alpha$  phase is the most common polymorph of PVDF mainly attained during crystallization from the melt at moderate or high supercooling (Jurczuk et al., 2015). Besides that, the crystal structure of a ferroelectric material can be transformed into another crystal structure by applying appropriate stress, heat or electric field. Special treatments like high-pressure crystallization and ultra-drawing could increase the crystallinity of the  $\beta$  phase and  $P_r$  to 100 mC/m<sup>2</sup>. Figure 2.5 shows the phase transformation schemes of crystalline polymorph PVDF. The thermal, mechanical and electrical treatments

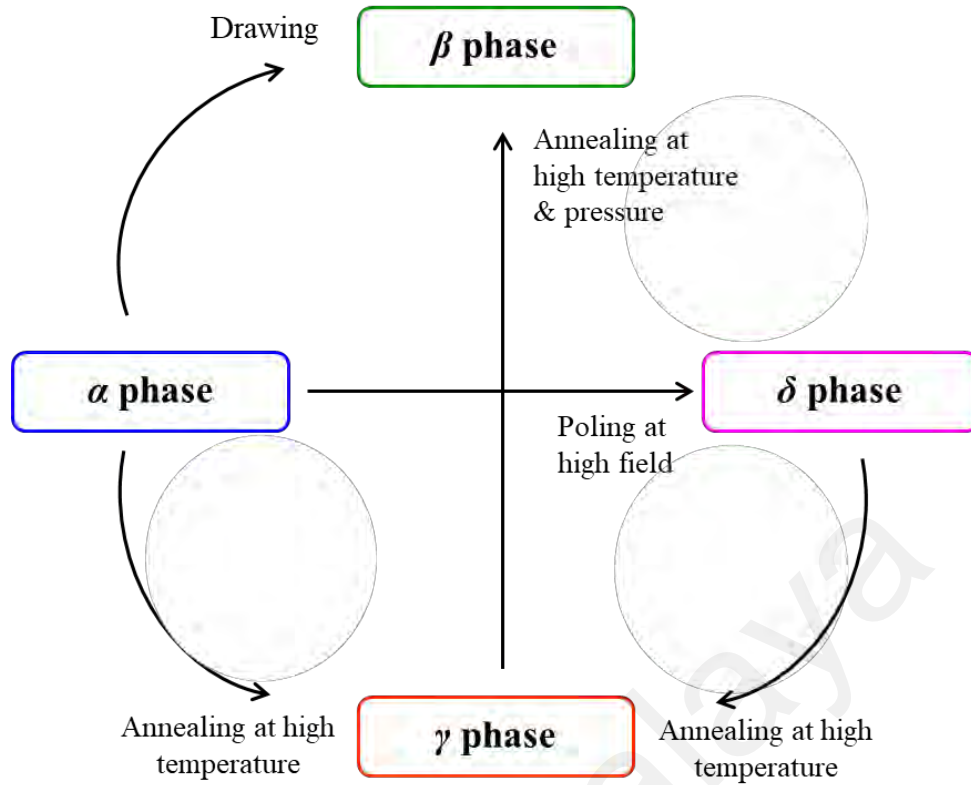
produce a specific crystalline polymorph of PVDF (Furukawa, 1989). Melt-crystallization produces the  $\alpha$  phase film as the most stable polymorph. Annealing of the  $\alpha$  phase film at an appropriate temperature induces transformation to the  $\gamma$  phase. Mechanical drawing stretches the chain molecules and thus causes the conversion of  $\alpha$  phase to  $\beta$  phase, where the chain elongates from TGTG' conformation extend to all-trans conformation. Annealing under high pressure and temperature causes the conversion of the  $\gamma$  phase into the  $\beta$  phase due to the close packing of the molecules. Whilst the transformation of the  $\alpha$  phase into its polar,  $\delta$  phase is obtained by applying a high electric field, greater than 500 MV/m (Matsushige et al., 1980). Further increase in applied electric fields will induce additional conversion into the  $\beta$  phase via the  $\gamma$  phase (Das Gupta & Doughty, 1977; Davis et al., 1978). The  $\delta$  phase is obtained by polarizing  $\alpha$  phase crystals at a high electric field, 500 MV/m (Furukawa, 1989).

Londo and Doll in 1968 suggested that the introduction of a small amount of trifluoroethylene (TrFE) and tetrafluoroethylene (TeFE) into PVDF induces direct crystallization into the polar  $\beta$  phase from the melt crystallization (Londo & Doll, 1968). The dipole moment of the TrFE monomer is reduced by half of PVDF  $\sim 1.05$  Debyes as shown in Figure 2.6. Therefore, the dipole moment per unit cell reduces as TrFE content increases (Li et al., 2014). Like PVDF, P(VDF-TrFE) has been reported to crystallize into four types of crystalline phases which are  $\beta$ ,  $\alpha$ ,  $\gamma$  and  $\delta$ . Overall, P(VDF-TrFE) exhibits a much higher crystalline  $\beta$  phase compared to that of the pure PVDF and thus it tends to crystallize in the polar  $\beta$  phase by annealing at a temperature between the Curie transition temperature ( $T_c$ ) and the melting temperature ( $T_m$ ) without the need for mechanical stretching (Furukawa, 1989; Weber et al., 2010). As PVDF-TrFE content is higher than 20 mol%, then it can directly be crystallized into the polar  $\beta$  phase (Jia et al., 2017).



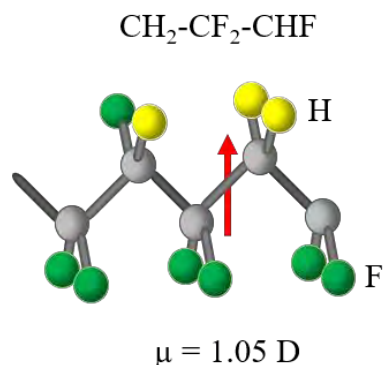
**Figure 2.4:** The three crystal structures of PVDF in different polymorphs (a) TTT planar zigzag, (b) TGTG' and (c) TTTGTTTG' (Li et al., 2021).





**Figure 2.5: Schematic diagram of crystallization transformation among polymorphs of PVDF due to electrical, mechanical and thermal treatments.**

Through this research, P(VDF-TrFE) is selected as a polymer matrix to form a layer film of polymer nanocomposite deposited onto glass substrates with the ZnO quantum dots as nanofillers since it easily forms the  $\beta$  phase conformation compared to PVDF (Takeo Furukawa, Nakajima, & Takahashi, 2006). Films prepared with a low evaporation rate and a high boiling point solvents such as dimethylformamide (DMF), dimethyl sulfoxide (DMSO) and polar solvent of diethyl carbonate (DEC) and methyl ethyl ketone (MEK) are favourable to form the polar  $\beta$  phase PVDF. Therefore, MEK was chosen due to rapid dissolving in PVDF-TrFE.

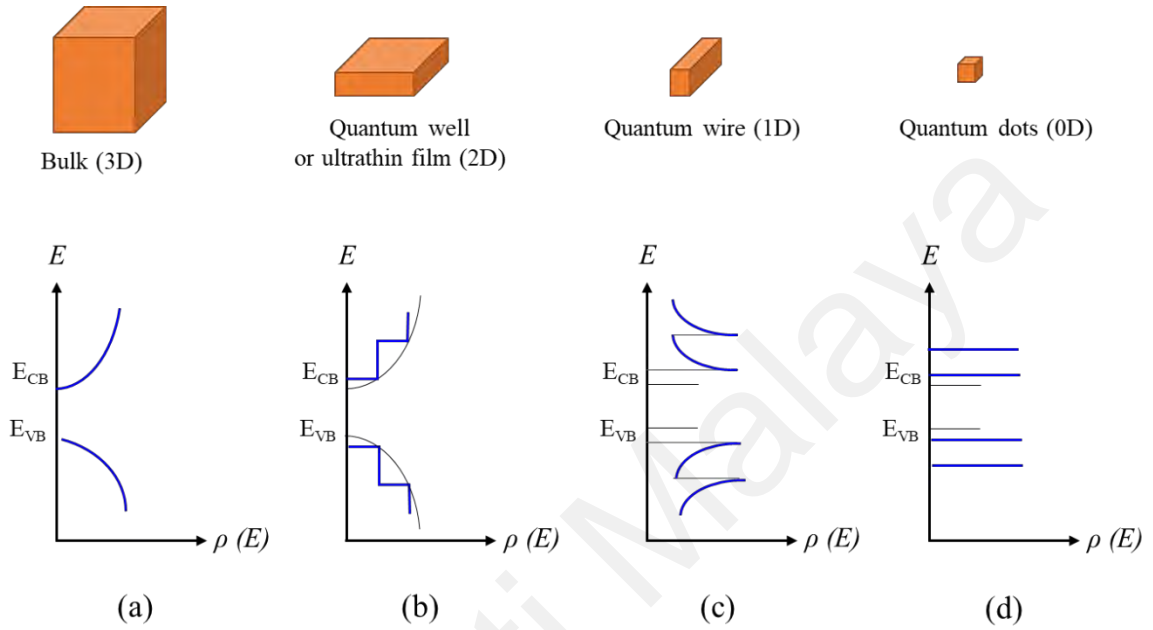


**Figure 2.6: Dipole orientation of monomer TrFE.**

### 2.2.2 Zinc oxide quantum dots (ZnO QDs)

The quantum dots (QDs) are initially discovered in the early 1980s by Brus, Efros, and Ekimov and their discovery is recognized by the Optical Society of America (Ekimov & Onushchenko, 1981; Wagner et al., 2019). Because of their tunable physical dimensions and good optoelectronic capabilities due to size confinement and anisotropic geometry, QDs have received a lot of attention as nanofillers. A quantum dot is a zero-dimensional relative to the bulk and the limited number of electrons results in discrete quantized energies in the density of states (DOS) for nonaggregate zero-dimensional structures. The density of states,  $\rho$  is the number of states per interval of energy at each energy level that can be occupied by electrons. The density of states as a function of energy is illustrated in Figure 2.7 for bulk materials, quantum wells, quantum wires and QDs. When the length of a semiconductor is reduced to the same order as the exciton radius, for example, to a few nanometers, the quantum confinement effect occurs and the exciton properties are modified. Depending on the dimension of the confinement, three kinds of confined structures are defined: quantum well (2D), quantum wire (1D) and quantum dot (0D). The energy band gap is separated between the finite energy level of conduction and the valance band. When an electron from the valance band achieves sufficient energy to overcome the energy gap, due to thermal excitation or absorption of a photon, and it goes to the conduction band, a hole is created on the left behind of the valance band. The combination of the electron and hole pair leads to the formation of

excitons. Due to the different polarity charges and the Coulomb force exchange interaction, the attractive connection between the electron-hole pair is called a quasiparticle which is named exciton (Ramalingam et al., 2020). Thus, excitons are coupled of electron-hole pairs via Coulomb attraction in semiconductor nanomaterials.

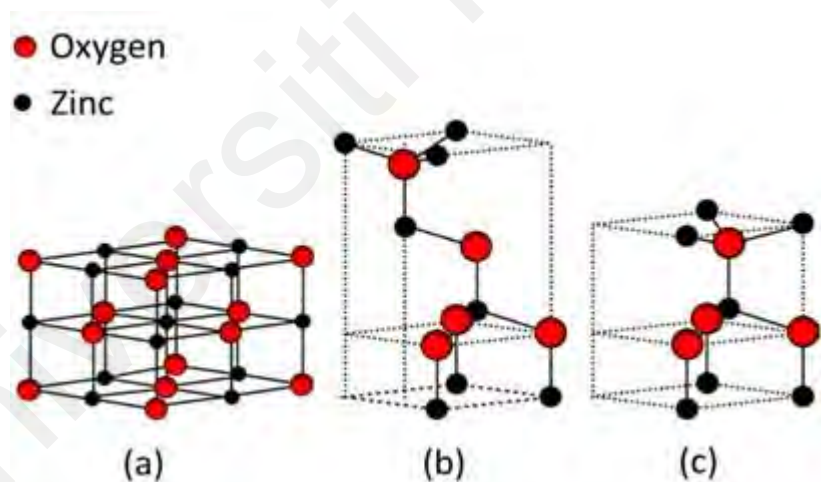


**Figure 2.7: The density of states in different confinement configurations: (a) bulk, (b) quantum well, (c) quantum wire and (d) quantum dots (Sahu, 2019).**

Semiconductor quantum dots with a particle size similar to that of the exciton Bohr radius has attracted significant attention to nanotechnology research nowadays because of their unique size-dependent optical and electronic properties. Among the II-VI binary compound semiconductors, ZnO QDs are of great importance due to their prominent features such as a wide direct energy gap  $\sim 3.4$  eV at room temperature, a large exciton binding energy of 60 meV and non-toxicity (Alim et al., 2005). ZnO QDs is well known for its green, low-cost, simple and stable synthesis (Fu et al., 2007; Singh et al., 2018) with excellent optical, electrical and electronic properties for a wide range of applications from optoelectronic to healthcare (Kamruzzaman, 2020; Park et al., 2020). Further increase in energy band gap leads to a

smaller particle size of QDs. The extensive applications of ZnO QDs are contributed from its piezoelectricity, chemical stability and biocompatibility (Schoenhalz et al., 2010).

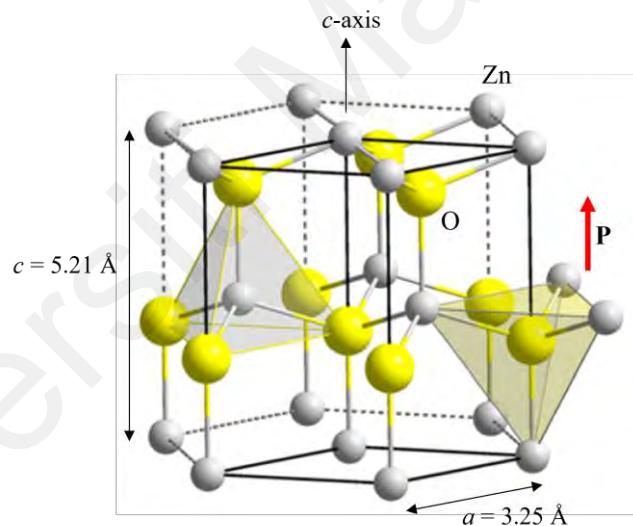
The crystal structures that emerged by ZnO are rock salt (or Rochelle salt), zinc blende and wurtzite as illustrated in Figure 2.8. The thermodynamically stable phase under ambient conditions is wurtzite symmetry. ZnO with the wurtzite hexagonal crystal structure is formed in this work. The wurtzite ZnO structure is composed of two interpenetrating hexagonal close-packed (hcp) sublattices and made up of alternating planes of  $\text{Zn}^{2+}$  and  $\text{O}^{2-}$  ions that are tetrahedrally coordinated along the threefold  $c$ -axis in fractional coordinates. Zinc has the electron configuration  $(1s)^2(2s)^2(2p)^6(3s)^2(3p)^6(3d)^{10}(4s)^2$ ; the oxygen configuration is  $(1s)^2(2s)^2(2p)^4$ . The ZnO binding in its crystal lattice involves a  $sp^3$  hybridization of the electron states, leading to four equivalent orbitals, directed in a tetrahedral geometry. In the resulting semiconducting crystal, the bonding  $sp^3$  states constitute the valence band, while the conduction band originates from its antibonding counterpart (Geurts, 2010).



**Figure 2.8: Zinc oxide crystal structure (a) cubic rock salt, (b) cubic zinc blende and (c) hexagonal wurtzite. Red and black colour indicates the oxygen and zinc atoms, respectively (Özgür et al., 2005).**

The wurtzite structure consists of a hexagonal unit cell with two lattice parameters  $a = 3.25 \text{ \AA}$  and  $c = 5.21 \text{ \AA}$ . This lattice type is classified by its point group 6 mm (international notation) or  $C_{6v}$  (Schoenflies notation) and the space group  $C_{6v}^4$  in the Schoenflies notation and  $P6_3mc$  in the Hermann–Mauguin notation (Morkoç & Özgür, 2008). The space group

$P6_3mc$  is non-centrosymmetric and is allowed to exhibit ferroelectricity, although no polarization-electric field ( $D$ - $E$ ) loop has been observed until the melting point. Each zinc ion is surrounded by a tetrahedron of four oxygen ions and similarly, each oxygen ion is coordinated by a tetrahedron of four zinc ions (see Figure 2.9). The arrangement of this tetrahedral coordination exhibits ZnO as a polar character, giving rise to spontaneous electric polarization,  $P_s$  (Rahman, 2019). The orientation of axes and faces in a wurtzite lattice is denoted by four-digit Miller indices  $hkl$ . The  $c$ -axis direction is referred to as  $[0001]$ , and the surface perpendicular to the  $c$ -axis is the hexagonal  $(0001)$  plane (Geurts, 2010). ZnO QDs have distinguishable pyroelectric and piezoelectric properties due to the non-centre-symmetry in the wurtzite, which is used in piezoelectric sensors, mechanical actuators, and QD solar cells (Mohamed et al., 2021).



**Figure 2.9: Lattice structure of wurtzite ZnO. The direction of the dipole is illustrated with a vector P (Photo sourced from [https://en.wikipedia.org/wiki/Zinc\\_oxide](https://en.wikipedia.org/wiki/Zinc_oxide)).**

Several chemical routes for preparing ZnO QDs, such as the sol-gel method, spray pyrolysis, precipitation, vapour phase transport process (VPT), thermal decomposition, hydrothermal synthesis, and electrochemical growth. Among these techniques, the sol-gel method received particular interest due to its simplicity, inexpensiveness, and scalability (Asok et al., 2012; Chen et al., 2011). In recent years, surface modification with a capping agent is crucial to control the as-synthesized quantum dots size as well as an attempt to prevent

rapid agglomeration due to the high surface energy. The surface ligands such as organic ligands or inorganic shells act as stoppers to control the QD growth and surface-passivating ligands prohibit the formation of dangling bonds which would lead to broadband of surface states just below the conduction band-edge. The commonly used head groups of the ligands are carboxyl, amino, thiol, phosphate group, etc (Shang & Ning, 2017; Shi et al., 2011). Recently, Adnan et al. (2017) were able to synthesize monodisperse ZnO QDs stabilized with triethanolamine (TEA) with an average size of 2.4 nm. TEA ligands tend to encapsulate the surface of ZnO and therefore result in a smaller size of QDs. TEA also shows high solubility in polar solvents like ethanol which is used as a solvent to synthesize QDs in this work (Jacob & Thomas, 2014).

### **2.2.3 Ferroelectric Composites**

Significant attention to research on the production and development of hybrid materials consisting of polymer (organic) and nanoparticles (inorganic) is essential in assembling superior multifunctional properties for broad spectrums of application. The polymer nanocomposites are categorized as hybrid materials which contain nanofillers embedded into the polymer matrix. The unique combination feature of a polymer such as flexibility, easy processing; and nanofillers such as high thermal stability, chemical stability, high refractive index; have potentially emerged in a wide range of applications including memory devices, integrated capacitors, full cells and optical devices (Adnan et al., 2018).

The development of hybrid materials as efficient energy harvesters and energy storage devices is of critical importance nowadays. Spin-coating is a common approach in the deposition of nanocomposite thin films before energy harvesting and energy storage applications. Spin-coating provides an easy way to coat a monolayer of either polymers or nanoparticles or complete dissolution of both materials onto a clean surface of a substrate using a spin-coater machine. The thickness of the coated components can be controlled by adjusting the coating speed.

Polymer composites comprising of ferroelectric particles embedded in polymer materials with different connectivity have generated great interest among known pyroelectric infrared detecting materials such as lead titanate (PT), lead zirconate titanate (PZT), barium titanate (BT) and triglycine sulfate (TGS) with poly-vinylidene fluoride (PVDF) or polyvinylidene fluoride-trifluoroethylene P(VDF-TrFE) as polymer host (Dias & Das-Gupta, 1996). The properties of these composites depend on the following factors; (i) the properties of its constituents, (ii) the volume fraction of each constituent, (iii) the polarizability of particles and (iv) the nature of inter-connecting these particles (Guggilla & Batra, 2011). Ferroelectric polymers are highly flexible but with low density and weak piezoelectric properties. The desirable combination of both components (i.e., polymer and nanofillers) by coupling them in the right manner will maximize the characteristic advantages of composite.

Recently, a group of researchers headed by Ojha et al., has developed a flexible device called a piezoelectric nanogenerator (PENG) using ZnO microrods blended with polyvinylidene fluoride (PVDF) through the supersonic spraying method (Ojha et al., 2023). The PENG was applied to various body parts, including the elbows, palms, knees, and feet. The device's performance and electric signals were measured using a periodic tapping test with a tapping force of 20 N at 5 Hz. The ZP5-based PENG demonstrated good performance as an LED lighting and touch sensor, achieving a maximum power of 112.5  $\mu\text{W}$  at 0.08 M $\Omega$ . The PENG has a power density of 12.5  $\mu\text{Wcm}^{-2}$  with an area of 3 cm  $\times$  3 cm. According to the study, ZnO microrods can act as a nucleating agent to create strong local interactions with PVDF on the contact surface, thereby promoting PVDF's  $\beta$  phase transformation. The PVDF/ZnO composite could therefore be used to power tiny electronic devices (Ojha et al., 2023; Zhang et al., 2023).

On the other hand, the introduction of zero-dimensional nanofiller into ferroelectric polymer hosts is of great interest nowadays to investigate the particle size's effect on their structural and physical properties. Nevertheless, the studies on the effect of embedding QDs into the ferroelectric polymer for energy storage and energy harvesting purposes are

considered new due to the lack of reported works (as listed in Table 2.2). Table 2.2 remarks an electrical output of several composite films embedded with quantum dots filler. The filler aspect ratio, filler dispersion, filler alignment and orientation, polymer-polymer interaction, polymers and filler interaction, and the poling status are the key variables that determine the attributes of the ferroelectric nanocomposite. The extensive surface area of the filler may present benefits or limitations for such a system. The covalent bonding between the chains of capping ligands and the surface of quantum dots may lead to steric hindrance which can provide essential stability to the nanocomposite (Javed et al., 2020).

In this study, ZnO quantum dots capped with organic ligand TEA synthesized by the sol-gel method will be embedded into copolymer P(VDF-TrFE) with various concentrations to form nanocomposite films. The functional electrical properties of the nanocomposite films P(VDF-TrFE) / ZnO QDs will be thoroughly investigated.

**Table 2.2: Ferroelectric studies of polymer nanocomposite films embedded with quantum dots.**

Material	Method	Remark	Reference
CdSe QDs/P(VDF-TrFE)	Langmuir-Blodgett	Exhibit approximately $6 \mu\text{Cm}^{-2}$ for 60 nm composite films through <i>D-E</i> hysteresis loop	(Korlacki et al., 2011)
PMMA/carbon quantum dots (CDs)/PEDOT: PSS	Spin coating	Enlargement of memory window with obvious $I_{sc}$ and $V_{oc}$ values in hysteretic I-V characteristic is due to the increment of dipole moment and spatial ordering in sandwiched multilayer which further increased the polarization electric field.	(Zhang et al., 2016)
CdSe/ZnS quantum dots/PVC	Solution casting	The lowest concentration of CdSe/ZnS in PVC (0.083 wt%) had the highest value of the dielectric constant compared with the concentration.	(Ahmed & Morsi, 2017)
$\text{Cd}_{1-x}\text{Zn}_x\text{Se}_{1-y}\text{S}_y$ nanodots/ P(VDF-HFP)	Solution casting	Largest discharged energy density, $U_e \sim 26 \text{ Jcm}^{-3}$ among reported works so far in the polymer nanocomposites with low filler contents.	(Li et al., 2020)



### 2.3 Dielectric properties

There are two types of dielectrics which are polar and non-polar. The polar dielectrics have permanent dipole moments while the non-polar dielectrics do not possess any permanent dipole moment. Dielectrics are insulating materials that do not conduct electric current due to the very low density of free charge carriers. Molecules or particles exhibit dipole moment if the electric centres of gravity of positive and negative charges do not match. As an example, for a system with a positive charge  $+q$  and negative charge  $-q$  being separated by distance  $\vec{r}$  with the dipole moment of  $\vec{p} = q\vec{r}$ . For any distribution of density chargers  $\rho_e(\vec{r})$ , the dipole moment can be expressed by (Kremer & Schönhal, 2002):

$$\vec{p} = \int_{volume} \vec{r} \rho_e(\vec{r}) d^3 \vec{r} \quad (2.2)$$

Electric polarization denotes an occurrence of the relative displacement of the negative and positive charges of atoms or molecules, the orientation of existing dipoles toward the direction of the field, or the separation of mobile charge carriers at the interfaces of impurities or other defect boundaries, caused by an external electric field (Chi, 2004). Figure 2.10 shows the dependence of each polarization mechanism which contributes to the overall polarization of materials on the frequency of the applied electric field. The polarization (dipole moment per unit volume) of a dielectric material arises from four different mechanisms:

i. *Electronic polarization*

Electronic polarization exists in all dielectric materials. It originates from the displacement of the negatively charged electron shell against the positively charged core under the influence of an external field.

ii. *Ionic polarization*

Both electronic and ionic polarization occurs in the resonance regime above the infrared frequencies. An ionic polarization occurs in ionic materials such as NaCl. The

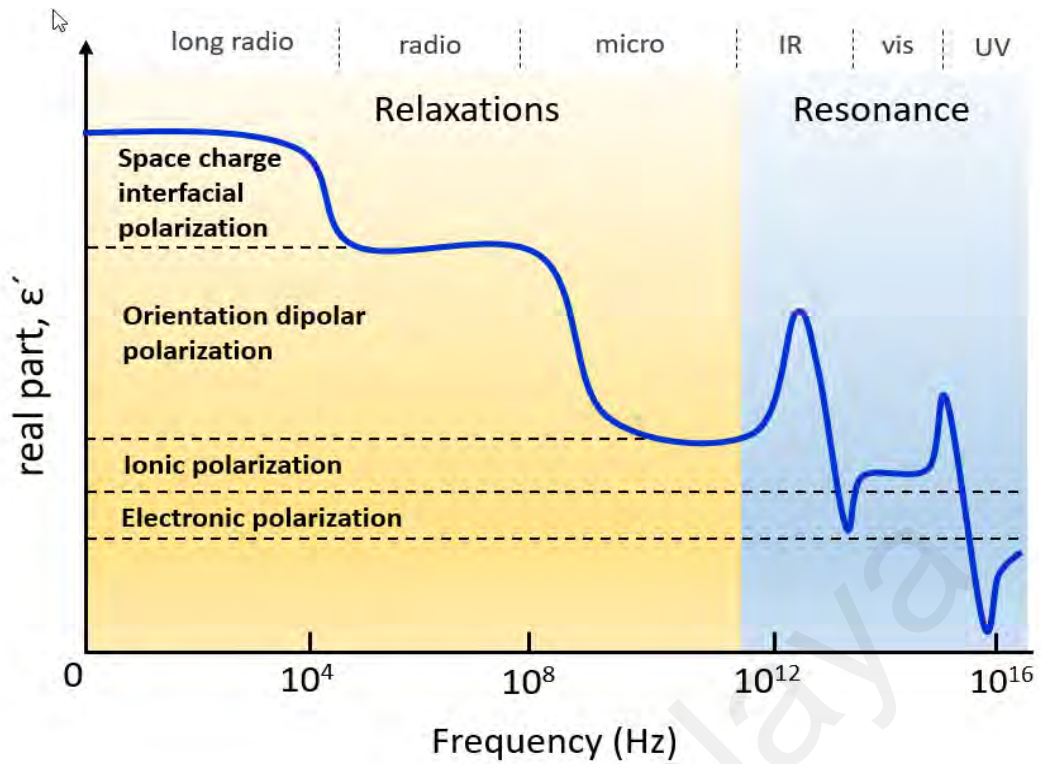
application of an external electric field leads to small displacements of ions from their equilibrium positions which consequently increase the net dipole moment.

*iii. Orientation dipolar polarization*

Orientation polarization describes the rotation of permanent dipoles as a function of the applied electric field. The orientation polarization is exhibited only in materials that possess permanent dipole moments. It results in a dielectric relaxation phenomenon that is associated with the molecular motion of the material. The dielectric constant of orientation dipolar polarization is affected by the phase structures. For example, the dipole orientation of polyvinylidene fluoride, and PVDF derivatives leads to the formation of a  $\beta$  phase, thereby increasing the dielectric constant.

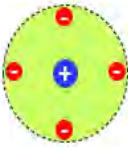
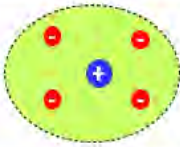
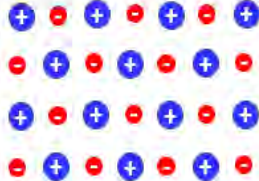



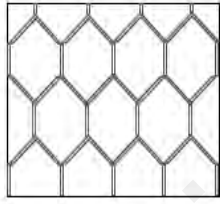
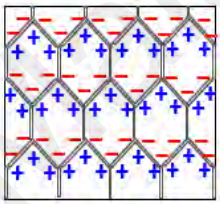
*iv. Space charge interfacial polarization*

Space charge interfacial polarization also called the Maxwell-Wagner effect, appears at low frequencies due to the low mass of the electron. It is related to the confined motions of charges resulting in an accumulation of charge at the interfaces of a multi-component system which creates space-charge separations under an applied electric field. It exists due to the space charges that are trapped in electrodes and at the heterogeneous structure of grain boundaries.



**Figure 2.10: Different types of polarization as a function of frequency in polymers together with relaxations and resonance regimes following the EM spectrum (Zhu & Wang, 2012).**

The schematic structure of electrical polarization due to electrons, ions, dipoles and space charges with the applied field is illustrated in Figure 2.11. Electronic polarization originates from minor shifts in electron clouds from any atom within the dielectric corresponding to its positive nucleus. It is also occurring due to the polarization of localized electrons. Ionic polarization is caused by an electrical field that deforms the atomic nuclei arrangement or distortion of atomic position in a molecule or lattice. In the case of dipolar polarization, there is a tendency for permanent dipole to align by the electric field to give a net polarization in that direction. Space charge polarization can occur at the interface of metal to the dielectric, at grain boundaries in ceramics and domain walls in ferroelectrics and is induced by migration charge carriers.

Polarization Mechanisms			
	Unpolarized state ( $E = 0$ )	Polarized state $\longrightarrow E$	Originate
Electronic			polarization of localized electrons
Ionic			displacement of ions
Orientation Dipolar			reorientation of polar molecules
Space Charge Interfacial			long range of charge migration

**Figure 2.11: Schematic illustrations of electronic, orientation, ionic and space charge polarization mechanisms.**

The total electric polarization of dielectric material is equal to the sum of electronic, ionic and orientation (if there are some influences of impurities in the system) polarizations. The average polarization,  $\vec{P}$  is resulted from  $N$  amounts of electric dipole moments,  $\vec{p}$  which are all aligned per unit volume,  $V$  can be described by (Kremer & Schönhal, 2002):

$$\vec{P} = \frac{1}{V} \sum_{i=0}^N \vec{p}_i \quad (2.3)$$

where  $i$  is the number of dipole moments in the system.

Investigation of the dielectric properties of a presented material provides beneficial information for understanding the mechanism of electric polarization and the relaxation phenomenon of the system. Dielectric properties are generally denoted by a dielectric constant (represents polarization) and dielectric loss (represents relaxation). Both dielectric constant

and dielectric loss of substances vary with frequency. A dielectric relaxation phenomenon is observed in the orientation polarization or molecular fluctuation of dipoles due to the molecules. When an external electric field is applied to the substance, it causes a lag in attaining an equilibrium state. The dielectric relaxation phenomenon is due to the exponential decay of the polarization with time, with the removal of the external electric field in a dielectric substance. Meanwhile, a resonance effect is found in electronic or ionic polarization.

Orientation polarization of molecular dipoles is a much more languid process seen at the lower range frequency range compared to electronic and atomic polarization. To obtain equilibrium maximum orientation polarization, sufficient time is required to permit the applied electric field to be realized in the dielectric material. Should a sufficient duration elapses during the measurement (at low frequency), then the relative permittivity is known as static dielectric permittivity,  $\epsilon_s$  will be observed. Conversely, should polarization be measured instantaneously when the field is applied, then a low magnitude of instantaneous relative permittivity,  $\epsilon_\infty$  will be produced.

The polarization phenomenon is scrutinized by considering the applied alternating electric field,  $E$  with an amplitude,  $E_0$ , angular frequency,  $\omega$  and time,  $t$  across a dielectric material.

The applied electric field,  $E$  is given as:

$$E = E_0 \cos \omega t \quad (2.4)$$

Polarization emerges when the frequency reaches a certain threshold. The orientation of any dipoles will ineluctably lag the applied field. The phase lag in the electric displacement,  $D$  can be expressed as:

$$D = D_0 \cos (\omega t - \delta) \quad (2.5)$$

where  $\delta$  is the phase lag. The electric displacement can be rewritten as:

$$D = D_1 \cos \omega t - D_2 \sin \omega t \quad (2.6)$$

where  $D_1 = D_0 \cos \delta$  and  $D_2 = D_0 \sin \delta$ .

Hence, the real permittivity,  $\epsilon'$  and imaginary permittivity,  $\epsilon''$  can be obtained as:

$$\epsilon' = \frac{D_1}{\epsilon_0 E_0} \quad \text{and} \quad \epsilon'' = \frac{D_2}{\epsilon_0 E_0} \quad (2.7)$$

The dispersion of the dielectric response of each contribution leads to dielectric losses of the substance which can be mathematically expressed by a complex dielectric permittivity:

$$\epsilon^* = \epsilon' - i\epsilon'' \quad (2.8)$$

Therefore, the tangent loss can also relate as:

$$\delta = \frac{\epsilon''}{\epsilon'} \sim \frac{\text{the energy dissipated per cycle}}{\text{energy per cycle}} \quad (2.9)$$

The real and imaginary parts will be much profound understood when considering material in a capacitor, where  $\epsilon'$  is the real part which indicates relative permittivity used for calculation of capacitance,  $\epsilon''$  is the imaginary part that represents the energy loss in the dielectric medium and  $\epsilon_0$  is the permittivity of free space. The current,  $I$  flow in the external circuit due to applied alternating voltage is given by the real part of  $V$  ( $V = V_0 e^{i\omega t}$ ), is evaluated from the complex relative permittivity:

$$I = \epsilon^* C_0 \frac{dV}{dt} = i\omega \epsilon^* C_0 V = \omega C_0 (\epsilon'' + i\epsilon') V \quad (2.10)$$

a capacitive component of the current leads the voltage by  $90^\circ$  is given by:

$$I_c = i\omega C_0 \varepsilon' V \quad (2.11)$$

where a resistive component is in phase with the voltage:

$$I_R = \omega C_0 \varepsilon'' V \quad (2.12)$$

The relaxation time,  $\tau$  is defined as the duration of the reduction of the polarization value to  $1/e$  of its initial value, where  $e$  is the natural logarithm base. It is a measure of the time when the dipoles become oriented with the electric field. The relaxation time,  $\tau$  is expressed by:

$$f(\tau) = \frac{1}{e} \quad (2.13)$$

For the maximum loss factor, the angular frequency,  $\omega_m$  is written as:

$$\omega_m = \frac{1}{\tau} \quad (2.14)$$

Materials in solid and liquid form which were initially in a condensed molecular state experienced restricted movement in the presence of an electric field. Constant collisions of molecules cause internal friction; thus, the molecules turn slowly and exponentially approach the final state of the orientation polarization with a relaxation time constant. When the electric field becomes zero, the sequence is reversed and random distribution is restored at the same time constant. The critical frequency,  $f_m$  can be expressed in terms of angular frequency,  $\omega_m$  as:

$$f_m = \frac{\omega_m}{2\pi} = \frac{1}{2\pi\tau} \quad (2.15)$$

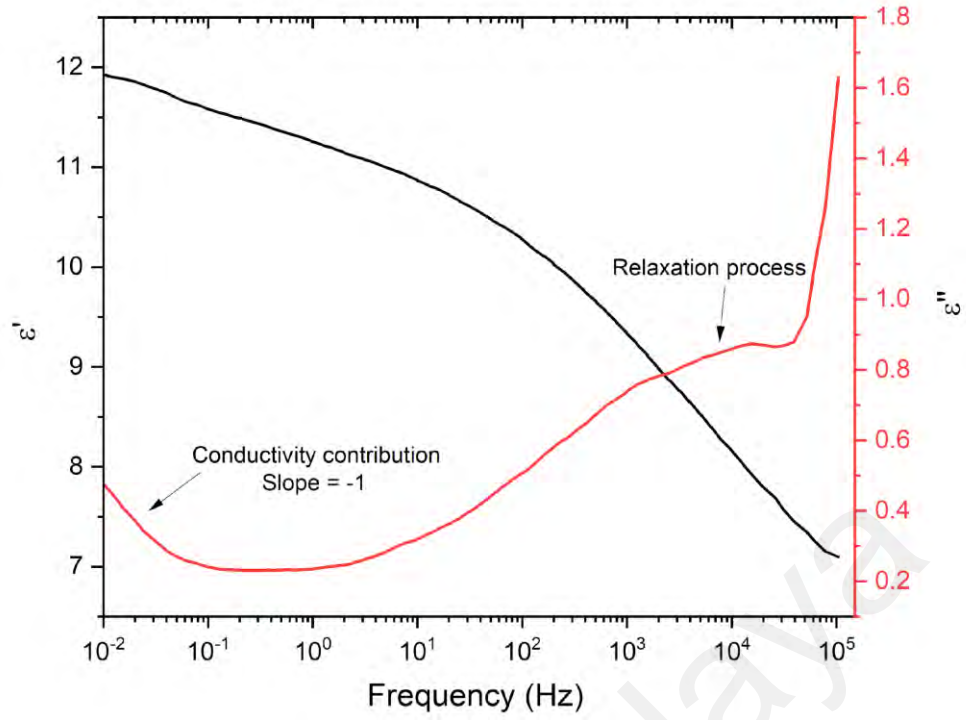
The complex dielectric permittivity,  $\varepsilon^*$  is introduced to allow for dielectric losses due to the friction accompanying polarization and orientation of electric dipoles. It is dependent on the frequency and temperature. The emergence is contributed by different processes such as microscopic fluctuations of molecular dipoles (rotational diffusion), the propagation of mobile

charge carriers (translational diffusion of electrons, holes or ions), and the separation of charges at interfaces, which gives rise to additional polarizations (Kremer & Schönhal, 2002).

One of the important elements in dielectric spectroscopy is an investigation of the relaxation process of a material. Relaxation processes are due to rotational fluctuations of molecular dipoles and are characterized by a peak in the imaginary part,  $\epsilon''$  and a step-like decrease of the real part,  $\epsilon'$  of the complex dielectric permittivity,  $\epsilon^*$  (refer Equation 2.8) with increasing frequency, as shown in Figure 2.12). Conversely, as the imaginary part of the dielectric function increases with decreasing frequency, hence conduction phenomenon can be observed. The real part of a complex dielectric function for pure ohmic conduction is independent of frequency while the imaginary part increases with decreasing frequency.

At a low-frequency regime, the alternating electric field is slow enough so that the dipoles can move smoothly with the field variations. The dielectric loss,  $\epsilon''$  is directly proportional to the frequency if the polarization is fully established. As the frequency increases, dielectric loss,  $\epsilon''$  keep increasing. However, the storage of the real part of the dielectric constant,  $\epsilon'$  starts to decrease because of the phase lag between the dipole alignment and the electric field. At a high-frequency regime, which is above the relaxation frequency, the  $\epsilon'$  and  $\epsilon''$  decrease as the electric field is too fast to influence the dipole rotation and eventually, the orientation polarization disappears. The dielectric spectrum of 75/25 mol ratio of P(VDF-TrF)E observed in this work as shown in Figure 2.12, is equivalent to other reported work (Furukawa & Johnson, 1981; Kremer & Schönhal, 2002).





**Figure 2.12: The real,  $\epsilon'$  (black line) and imaginary,  $\epsilon''$  (red line) part of the complex dielectric function for a copolymer P(VDF-TrFE) 75/25 relaxation process at -20 °C.**

Dielectric relaxation processes are usually analyzed using several model functions. Debye function is a fundamental theoretical function where both the frequency and the time domain have been suggested to describe the experimentally observed spectra. The Debye function for the frequency dependence of  $\epsilon^*$  is written as:

$$\epsilon^* = \epsilon_\infty + \frac{\Delta\epsilon}{1+i\omega\tau_D} \quad (2.16)$$

where  $\Delta\epsilon = \epsilon_S - \epsilon_\infty$  is the dielectric relaxation strength, where  $\epsilon_S$  is the static dielectric permittivity,  $\epsilon_\infty$  is the infinite relative dielectric and  $\tau_D$  is the Debye relaxation time where the maximal loss occurs. The relaxation peaks are asymmetrical and display a high-frequency tail where its half-width of measured loss peaks is much broader as predicted by the Debye function and it is referred to as a non-Debye (non –ideal) relaxation behaviour. As a result, the broadening of the dielectric function can be described by the Cole-Cole function (Kremer & Schönhal, 2002):

$$\varepsilon^* = \varepsilon_\infty + \frac{\Delta\varepsilon}{1+(i\omega\tau_{cc})^\alpha} \quad (2.17)$$

where  $\alpha$  denotes the symmetrical broadening of the relaxation peaks. In the Debye function,  $\alpha = 1$  while in the Cole-Cole function  $\alpha$  is  $0 < \alpha \leq 1$ . The Cole-Cole relaxation time,  $\tau_{cc}$  denotes the position of a maximal loss by  $\omega = 1/\tau_{cc}$ .

The complex dielectric function can have an asymmetric broadening peak and depicted by the Cole-Davidson function (Kremer & Schönhal, 2002):

$$\varepsilon^* = \varepsilon_\infty + \frac{\Delta\varepsilon}{(1+i\omega\tau_{CD})^\beta} \quad (2.18)$$

The parameter  $\beta(0 < \beta \leq 1)$  describes an asymmetric broadening for the relaxation function. The Debye function is obtained when  $\beta = 1$ . It should be noted that the characteristic relaxation time of this asymmetric model function like the Cole- Davidson function does not coincide with the relaxation time which is related to the position of maximal loss. The relationship of both quantities depends on the shape parameter.

A more general model was then introduced by Havriliak and Negami (HN-function) which is an incorporation of the Cole-Cole and the Cole-Davidson function (Kremer & Schönhal, 2002):

$$\varepsilon^* = \varepsilon_\infty + \frac{\Delta\varepsilon}{(1+(i\omega\tau_{CD})^\alpha)^\beta} \quad (2.19)$$

For the fractional shape parameters  $\alpha$  and  $\beta$  which represent the symmetric and asymmetric broadening of the complex dielectric function, where  $0 < \alpha, \alpha\beta \leq 1$  holds. The parameters  $\alpha$  and  $\beta$  are related to the limiting behaviour of the complex dielectric function at low and high frequencies. The HN function provides a better fitting scheme for a complete description of the isolated regions involved in the system. Analysis study on the frequency and temperature dependence of the complex permittivity allows the dielectric strength, phase transition, transition temperature and frequency relaxation involved in the system to be determined.

## 2.4 Ferroelectric properties

Ferroelectricity is a property of materials that have a spontaneous electric polarization that can be reversed by the application of an external electric field. A crystal is composed of a definite chemical composition in which the molecules are made up of positive ions and negative ions occupying lattice sites to constitute a crystal structure lattice. The smallest repeating unit of the lattice is called the unit cell and the specific symmetry of the unit cell identifies whether the crystal exhibits ferroelectric, piezoelectric, pyroelectric or electro-optic effects (Kao, 2004). Ferroelectric materials have received intensive investigation nowadays in exploring the uniqueness of their structural transformation phenomena. Generally, ferroelectric crystals possess one or more ferroelectric phases. The ferroelectric phase is a state that exhibits spontaneous polarization,  $P_s$  in a certain temperature range and the direction of the spontaneous polarization can be reoriented by an external electric field. Meanwhile, spontaneous polarization is defined by the value of the dipole moment per unit volume, or the value of the charge per unit area on the surface perpendicular to the axis of the spontaneous polarization or also referred to as the crystal axis. A spontaneous polarization can be written as:

$$P_s = \frac{(\iiint \mu \, dV)}{\text{volume}} \quad (2.20)$$

where  $\mu$  is the dipole moment per unit volume. Ferroelectricity usually vanishes above a certain temperature called Curie or transition temperature,  $T_c$ . At the  $T_c$ , the crystal undergoes a phase transition from the polar state to the non-polar state. Above the transition temperature  $T_c$ , the crystal is said to be in the paraelectric state.

The uniform alignment of electric dipoles or uniform polarization regions is called ferroelectric domains. The interface between the two domains is known as the domain wall. The orientation of the dipoles usually coincides with the direction of the spontaneous polarization. The ferroelectric domain structure depends on the structure of the ferroelectric crystal. A ferroelectric crystal generally consists of regions called domains of homogeneous

polarization, within each of which the polarization is in the same direction, but in the adjacent domains, the polarization is in different directions so that the net polarization of the specimen is equal to zero in the beginning when no electric field is applied. However, a strong field may reverse the spontaneous polarization of the domain and this phenomenon is known as domain switching. When an electric field,  $E$  is applied, the velocity of the domain wall motion  $v$  can be written as:

$$v = \vartheta E \quad (2.21)$$

where  $\vartheta$  is the mobility of the domain wall. The motion of the domain wall is contributed by the stress distribution, space charges and defects in the crystal (Xu, 1991).

Ferroelectrics are the most typical nonlinear dielectrics with switchable spontaneous polarization. The switching ability of the ferroelectric polarization can be observed by measuring the dielectric displacement current in response to a cyclic electric field which gives rise to a hysteresis loop (see Figure 2.13), the designation of ferroelectricity. At large signals, both the electric displacement,  $D$  and the polarization,  $P$  are nonlinear functions of the electric field,  $E$  was given as the linear equation below:

$$D = P + \varepsilon_0 E \quad (2.22)$$

where  $\varepsilon_0$  is the permittivity of free space ( $8.85 \times 10^{-12}$  C/Vm). For most ferroelectric materials, the second term on the right-hand side in the above equation is negligible, and a  $D$ - $E$  and  $P$ - $E$  loop becomes interchangeable.

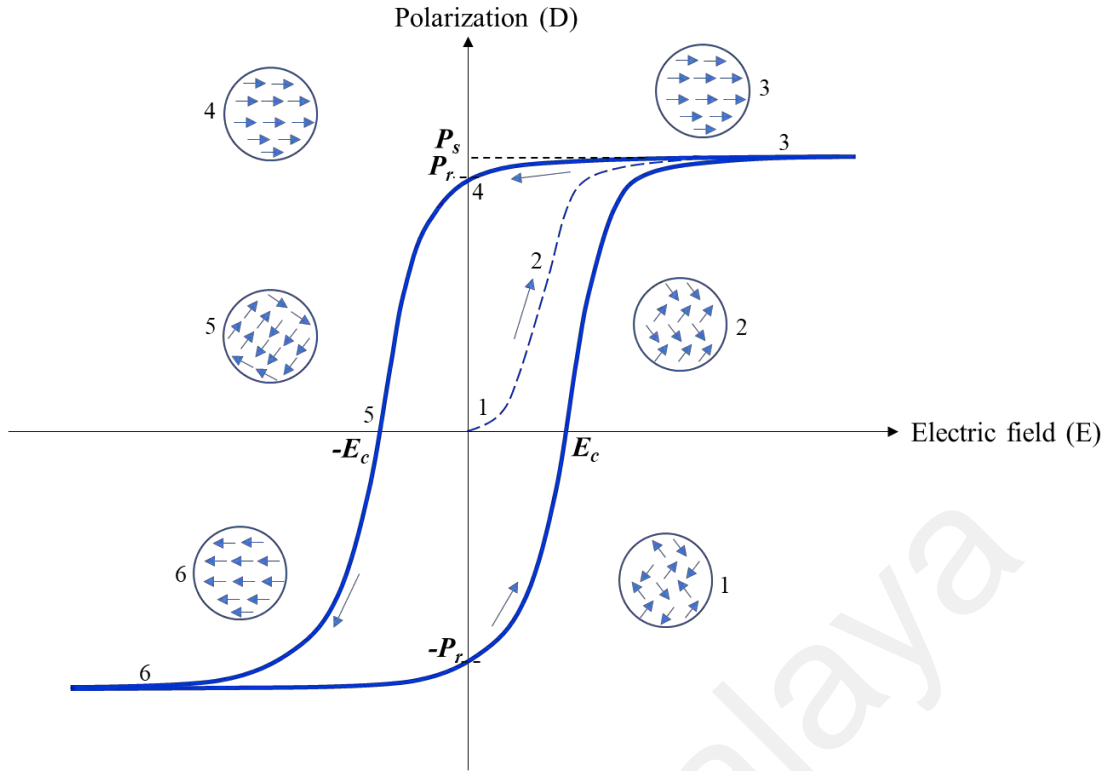
Applying a small amount of electric field on the ferroelectric crystal will exhibit only a linear relationship of  $P$  and  $E$  since the applied field is not enough to switch any domain or dipoles and the ferroelectric crystal will behave as a normal dielectric material (paraelectric). When the electric field is increasing, the dipoles begin to line up with the field (points 1 to 3 in Figure 2.13). Eventually, the field aligns all of the dipoles until all the domains are aligned

in the positive direction and the maximum polarization is obtained. This state is the saturation state in which the crystal is composed of just a single domain.

As the electric field strength decrease and reduce to zero, the polarization will generally decrease (at point 4) but does not return to zero, because some of the domains will remain aligned in the positive direction and the crystal will exhibit a remanent polarization,  $P_r$ . The ability to retain polarization permits the ferroelectric material to retain information, making the material useful in computer circuitry. The extrapolation of the linear line from point 3 back to the polarization axis (zero electric fields at point E) represents the value of the spontaneous polarization,  $P_s$ . When the electric field is applied in the opposite direction, the dipoles are reversed. A coercive field,  $E_c$  must be applied to remove the polarization and randomize the dipoles (point 5). Switching of ferroelectric polarization from one state to another can be achieved by applying an electric field higher than a threshold value, commonly known as the coercive field,  $E_c$ . It is also defined as the strength of the electric field required to reduce polarization to zero. Further increase of the electric field in the negative direction will cause saturation to occur in the opposite polarization (point 6). Thus, the cycle of the hysteresis loop can be completed by reversing the electric field direction once again.

As an electric field is applied to a ferroelectric crystal in an isothermal cycle, Joule heating disposes of the electrical flow to the system. The energy dissipated ( $W$ ) per unit volume ( $V$ ) of the ferroelectric crystal is equal to the area enclosed by the  $D$ - $E$  schematic of the hysteresis loop which can be utilized for energy harvesting purposes (Batra & Aggarwal, 2013):

$$\frac{W}{V} = \oint dDE \quad (2.23)$$



**Figure 2.13: Typical  $P$ - $E$  ferroelectric hysteresis loop. Circles with arrows represent the polarization state of the material at the indicated fields (Askeland, 1996).**

## 2.5 Pyroelectric properties

A pyroelectric phenomenon is the transformation of the temperature dependence of spontaneous polarization on a single crystal or poly-crystalline aggregates. As the temperature of the material fluctuates, the internal polarization of the material changes, which generates a flow of charges across the surface of the material. The pyroelectric effect was first discovered in tourmaline by Teophrast (Lang, 1974). Pyroelectric materials are dielectric materials that possess spontaneous electrical polarization and appear even in the absence of an applied electrical field or stress. All ferroelectric materials exhibit pyroelectricity but not all pyroelectric materials exhibit ferroelectricity. The pyroelectricity of a material is measured by the pyroelectric coefficient,  $P_i$ . A small change in temperature,  $\Delta T$  in the crystal, results in the change in the spontaneous polarization vector,  $\Delta P_s$  and can be written as:

$$\Delta P_s = P_i \Delta T \quad (2.24)$$

The pyroelectric coefficient,  $P_i$  is a vector with three components and describes the change in the electrical charge per unit surface area during heating or cooling. The unit of a pyroelectric coefficient is represented by  $C/m^2K$  or  $\mu C/m^2K$  (Furukawa et al., 1984).

The generation of charges or pyroelectric current during heating and cooling in a pyroelectric sample is graphically shown in Figure 2.14. In general, a homogeneous pyroelectric material with a constant pyroelectric coefficient throughout the temperature at any time is uniform, the electric current generated (see Figure 2.14(c)(d)) from the pyroelectric effect is expressed as (Bowen et al., 2014):

$$i_p = \frac{dQ}{dt} = P_i A \frac{dT}{dt} \quad (2.25)$$

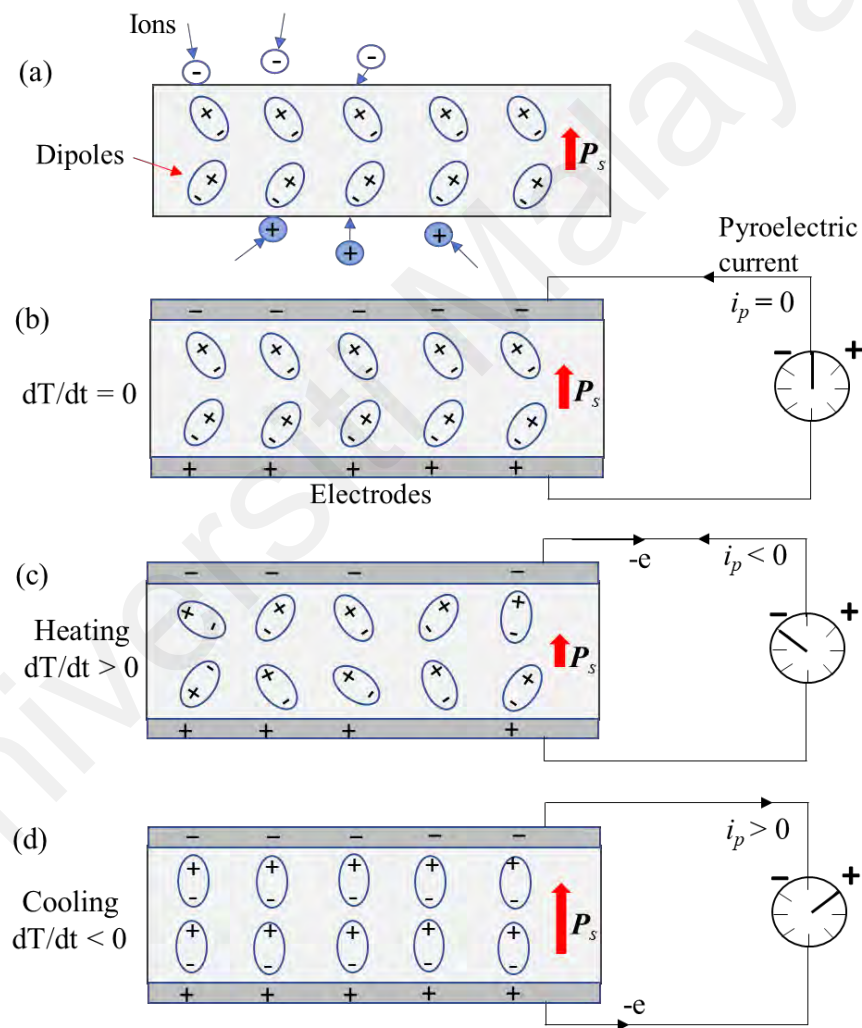
where the equation above denotes pyroelectric charge (Q), pyroelectric current ( $i_p$ ), rate of temperature change ( $dT/dt$ ), the surface area of the pyroelectric material (A) and pyroelectric coefficient ( $P_i$ ).

The arrangement of polarization due to the pyroelectric effect in a pyroelectric material is explained by the following conditions (Batra & Aggarwal, 2013):

1. Before the attachment of electrodes: Pyroelectric sample consists of dipole moments that add up in the direction perpendicular to the flat surfaces which bestow spontaneous polarization. Spontaneous polarization of the pyroelectric sample attracts free charges (ions that are represented as positive and negative circles) to the material's surface, thereby masking the charges (Figure 2.14(a)).
2. Sample as attached to electrodes and connected to an ammeter for measuring current: The temperature of the pyroelectric sample with electrodes is held constant, so the spontaneous polarization is constant and no current flows through the external circuit (Figure 2.14(b)).
3. Heating pyroelectric sample: As the sample with electrodes is heated, the spontaneous polarization is reduced (shown by  $P_s$  arrow length). A reduction in dipole movement

toward polar alignment caused a decrease in the number of bound charges at the electrodes. Therefore, redistribution of free charges to compensate for the change in bound charge leads to ejection of bound charges which emerges as the current flowing through the external circuit and is termed as pyroelectric current,  $i_p$  (Figure 2.14(c)).

4. Cooling pyroelectric sample: Spontaneous polarization is increased if the sample with the electrodes is cooled, engaging ambient charges to the surface of the electrodes, which leads to a current generation in the circuit with opposite signs (Figure 2.14(d)).



**Figure 2.14: Pyroelectric sample with dipoles and polarization vector: (a) spontaneous polarization without electrodes, (b) with two conductive electrodes and connected to an ammeter at a constant temperature, (c) while being heated, and (d) while cooling (Batra & Aggarwal, 2013; Bowen et al., 2015).**



Based on the thermodynamic diagram (Lang, 2005) in Figure 2.15 illustrates the thermodynamic reversible interactions that may occur among the thermal, mechanical, and electrical properties of a crystal. Variables  $S$ ,  $D$ , and  $\varepsilon$  in the inner circles denote entropy, dielectric displacement, and strain, respectively. Pyroelectricity is a coupled effect where a change in temperature causes a change in electric displacement,  $D$  (C/m<sup>2</sup>). There are two routes to the pyroelectric effect. The primary route is shown by a solid red line and the second route is indicated by a dotted red line. In the first route, the primary pyroelectric effect is caused by a change in temperature, which leads to a change in the electric displacement in a crystal under constant strain  $\sigma$ , rigidly clamped to prevent expansion or contraction (in other words, the shape and size of a crystal held fixed during heating). The primary pyroelectric effect signifies direct coupling between polarization and temperature. In the second route, the secondary pyroelectric effect is a result of crystal deformation which means that the crystal may be in free form, thus the thermal expansion occurs freely. The total pyroelectric coefficient mechanically free condition is given as (Kishore & Priya, 2018):

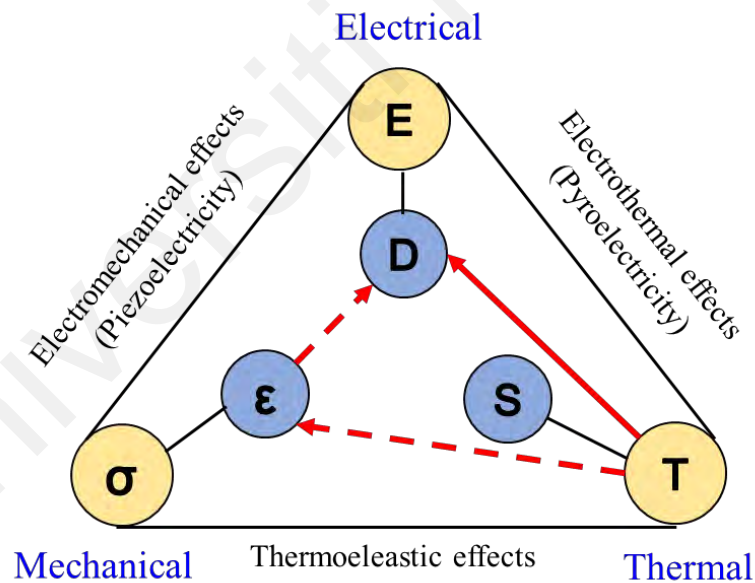
$$p^{\sigma,E} = p^{\varepsilon,E} + d_{ij}e_{ij}^E\lambda_i^E \quad (2.26)$$

where the first term on the right-hand side of the equation shows the primary pyroelectric coefficient under constant strain conditions while the second term represents the secondary pyroelectric coefficient, which tensors  $d_{ij}$ ,  $e_{ij}^E$  and  $\lambda_i^E$  are the piezoelectric coefficient, elastic constant and thermal expansion coefficient, respectively. When  $\partial\sigma = 0$ , the above equation could further be written as:

$$\begin{array}{cc} \text{primary} & \text{secondary} \\ \left(\frac{\partial D}{\partial T}\right)_{\sigma} = \left(\frac{\partial D}{\partial T}\right)_{\varepsilon} + \left(\frac{\partial D}{\partial \varepsilon}\right)_T \left(\frac{\partial \varepsilon}{\partial T}\right)_{\sigma} \end{array} \quad (2.27)$$

This equation shows the measured effect divided by primary and secondary pyroelectric effects. In the first term,  $\left(\frac{\partial D}{\partial T}\right)_{\varepsilon}$  in the system refers to the primary (true) pyroelectric effect at

constant strain when the crystal is under the clamped condition as explained in Equation (2.26). This phenomenon is related to the crystal lattice reconstruction (without any deformation of the crystal) due to the temperature change. The second term is the secondary pyroelectric effect, which describes both thermal expansion and piezoelectric effects. The term of  $\left(\frac{\partial \varepsilon}{\partial T}\right)_\sigma$  is defined as the pyroelectric effect measured at constant stress when the crystal is free to change its shape. Another pyroelectric effect obtained from the pyroelectricity arises from the path  $T \rightarrow \varepsilon \rightarrow D$  as shown in Figure 2.15. As a result, when the crystal is free to deform or expand, an electrical displacement,  $D$  obtained from thermal expansion. This causes a strain ( $T \rightarrow \varepsilon$ ), which in turn by the piezoelectric path ( $\varepsilon \rightarrow D$ ) contributes to the electrical displacement,  $D$ . This is called the pseudo pyroelectric effect or false pyroelectric of the first kind. Temperature changes in lattice constant are related to the changes of elementary dipole moments, consequently resulting in polarization (Tichý et al., 2010).

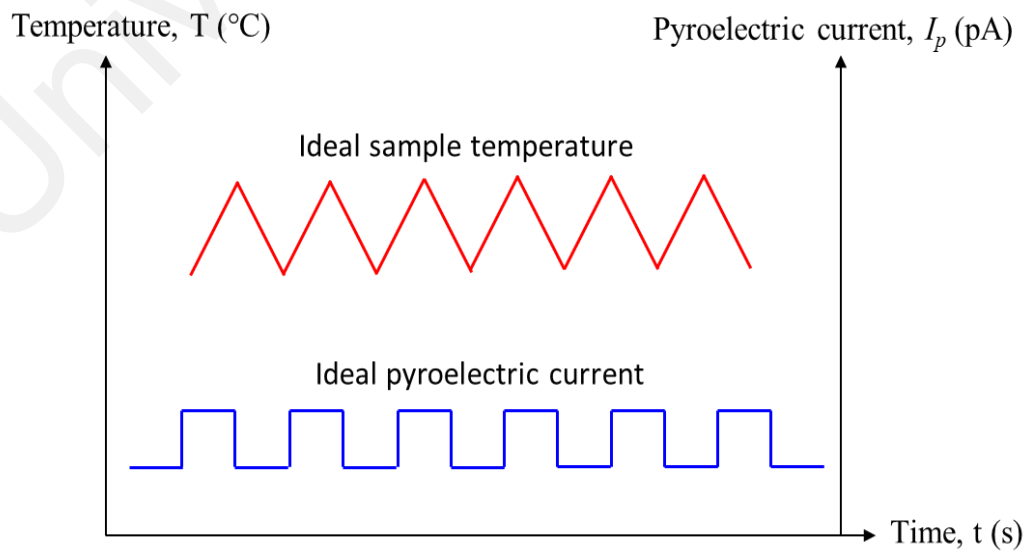


**Figure 2.15: The relationships between the thermal (temperature), mechanical (strain) and electrical (field) properties of a crystal (Tichý et al., 2010).**

A typical temperature and pyroelectric current wave profile versus time obtained during heating and cooling of the pyroelectric sample at a linear rate is shown in Figure 2.16. The

rate of temperature change is calculated from the gradient of the triangular wave of the sample temperature, while the pyroelectric current can be obtained from the amplitude of the square wave profile (Majid et al., 2000).

Pyroelectric properties of polymer and nanocomposite materials such as pyroelectric coefficient ( $P_f$ ), dielectric constant ( $\epsilon'$ ), tangent loss ( $\tan \delta$ ) and detectivity of the figure of merit,  $F_D$  are listed in Table 2.2. The composite film of P(VDF-TrFE)–BNT–BKT–BT (Mahdi & Majid, 2016) shows the highest pyroelectric coefficient and significant performance of  $F_D$  among all reported works in Table 2.2. Although ceramic fillers like BNT exhibit high pyroelectric properties as indicated in Table 2.2, it is essential to study quantum size effects like ZnO QDs on the electrical (ferroelectric, dielectric and pyroelectric) performance of energy harvesting and storage devices. In this work, 0.15 wt% of ZnO QDs in P(VDF-TrFE) could contribute about half of the pyroelectric coefficient reported by Mahdi & Majid (2016) with a QDs size in the range of  $\sim 2.5 - 3$  nm. It is believed that varying the quantum dots' size may open the possibility to control the pyroelectric properties of polymer nanocomposites. Hence, in the future, the investigation of the quantum size effect of ZnO QDs in different size ranges on P(VDF-TrFE) is necessary to explore their potential ferroelectric, dielectric and pyroelectric properties.



**Figure 2.16: Ideal rectangular short-circuited pyroelectric current spectra in response to triangular temperature wave (WC & Majid, 2009).**

**Table 2.3: Pyroelectric properties of thin polymer and nanocomposite films observed at frequency 1 kHz.**

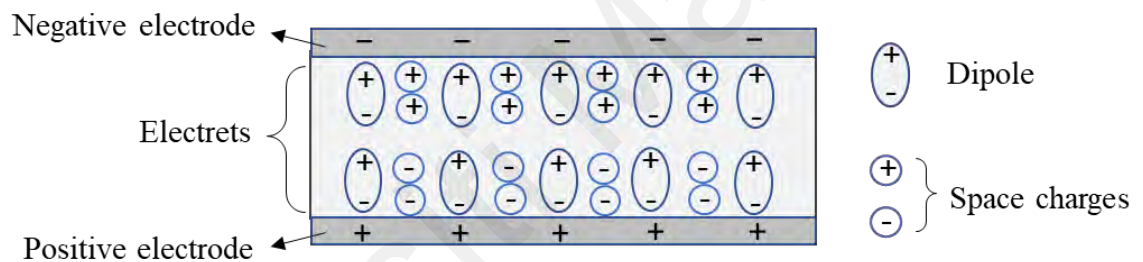
Material	Volume fraction, $\phi$ or weight percentage, wt%	$P_i$ ( $\mu\text{Cm}^{-2}\text{K}^{-1}$ )	$\epsilon'$	Tan $\delta$	$F_D$ ( $\mu\text{Cm}^{-2}\text{K}^{-1}$ )	Ref.
P(VDF–TrFE)/ZnO QDs	0.15 wt%	49	13.9	0.02	93	This work
P(VDF–TrFE)–BNT–BKT–BT	$\phi = 0.20$	95	$\sim 20$	-	137.99	(Mahdi & Majid, 2016)
PVDF/ $\text{La}_2\text{O}_3$	3.0 wt%	42	$\sim 8$	-	86	(Gan & Majid, 2015)
$\Phi\text{SBN}-(1-\Phi)\text{PVDF}$	$\phi = 0.3$	13.5	28	0.016	20.13	(Kumar & Kumar, 2013)

## 2.6 Thermally Stimulated Current (TSC)

Thermally stimulated current, TSC measurement is extensively studied in diverse fields, i.e., physics, electronics, electrical engineering, chemistry, ceramics and biology. TSC is a method to investigate the molecular relaxations phenomena of dielectric and semiconducting materials which are generally involving the study of thermally activated charge, electron trap and activation energy of a material. TSC operates as short-circuit current that flows during heating due to the displacement of positive and negative charges (e.g., electrons, holes, ions) as well as to the rotational motion of permanent dipoles in samples, due to the phase transition of materials (e.g., the glass transition phase, Curie point, etc.) (Iwamoto & Taguchi, 2018). TSC study was able to show a close correlation between the carrier detrapping process and molecular motion in a polymer (Ito & Nakakita, 1980).

TSC measurement involves the emergence of temporal thermoelectrets. An electret is defined as a piece of dielectric material having quasi-permanent electrical charges. A piece of the poled ferroelectric material can also be considered an electret. The term quasi-permanent is regarding the charges decay time which the process is very slow and takes much longer than

the time in which studies are performed with the electret (Kao, 2004). There are various ways to form electrets in a dielectric material either by the application of an electric field between metallic electrodes, or by the application of a strong static magnetic field, or simply by a thermal process without both fields and also by the application of mechanical pressure to the dielectric material. The sources of electrets are commonly from both dipole polarization and space charges. These kinds of charges can be trapped within the materials or with time they may form layers of surface charges (see Figure 2.17). An electret also could be formed as a carrier that is transferred in a molecular or domain structure throughout the dielectric. The trapped positive and negative carriers may be formed as layers of space charges which are often positioned close to the two surfaces of the electrets (Van Turnhout, 1971).



**Figure 2.17: Schematic configuration of typical electrets with aligned dipoles and space charges (Van Turnhout, 1971)**

Reliable mechanisms for TSC include several processes that contribute to the discharge of electrets, where restoration of charge neutrality is essentially a driving force for all the processes. These processes can be classified into two main categories (Belana et al., 1981; Van Turnhout, 1971):

1. Disorientation of dipoles

By redistributing all dipoles at random, this technique tends to eradicate persistent dipole polarization. It entails the rotation of a couple of positive and negative charges, which necessitates the expenditure of a specific quantity of energy known as activation energy. It could be a few eV per dipole in a solid dielectric. Dipole disorientation is

thus a thermally induced phenomenon that can be increased by heating. The activation energy of each dipole in electrets is generally different from one another. As a result, as illustrated in Figure 2.18, current–temperature plots reveal several relaxation peaks. At low temperatures, dipoles with low activation energy will disorient. Those polarized dipoles with high activation energy, on the other hand, will disorient at a higher temperature. The peaks associated with dipoles include the following:

(a)  $\gamma$  and  $\beta$  peaks

The disorientation of dipoles at low temperatures is represented by these peaks. Individual peaks might overlap and merge into a broad peak due to small changes in activation energy.  $\beta$  peak is a term used in polymers to describe a broad peak. Depolarization activities by polar side groups with continuous distribution activation energies is attributed to this peak.

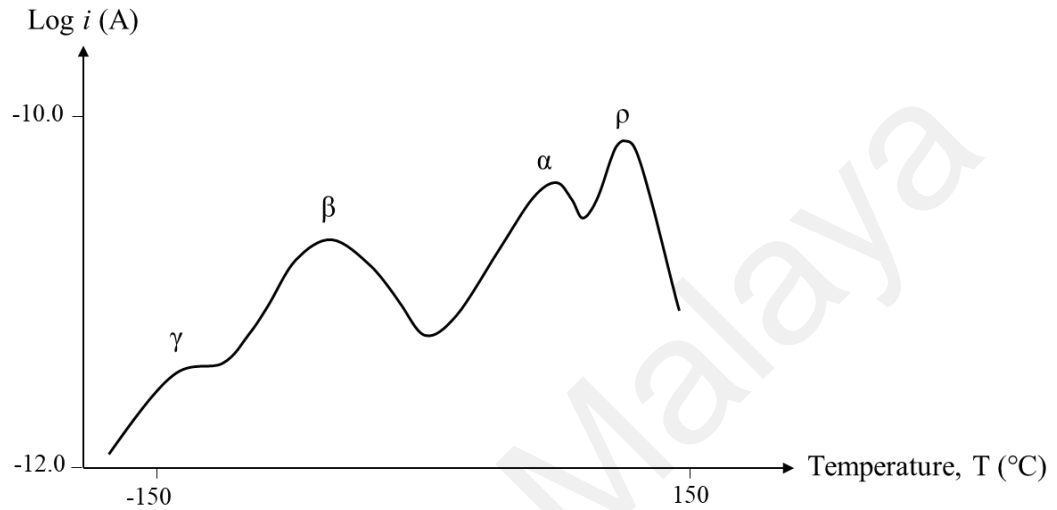
(b)  $\alpha$  peak

This is another broad peak that has formed because of overlapping peaks. The origin, on the other hand, identifies this relaxation peak, with small variations in dipole rotational mass causing the peak to arise. When polymers are heated to their softening temperature, for example. The mobility of major chain segments within the polymers causes the dipoles to become disoriented. The  $\alpha$  peak in Figure 2.18 is produced by disorientation by various dipoles, and it is positioned at the glass-rubber transition temperatures  $T_g$  of the polymers.

2. Space charges -  $\rho$  peak

In electrets, immobilized space charges are stored in a non-uniform manner and are frequently seen around electrodes. The heating process, on the other hand, gives energy to these carriers, allowing them to migrate and neutralize at the electrodes and within the electrets. The recombination of charges with opposite signs is involved in these neutralization processes. The drift in the local electric field and diffusion, which tends to remove the charge concentration gradient, are the driving forces. The emergence of

$\rho$  peaks in Figure 2.18 characterizes this relaxation effect. When compared to the temperatures of  $\beta$  and  $\alpha$  peaks, it appears at a higher temperature. This is because dipole disorientation only requires local rotation. The neutralization of space charges, on the other hand, necessitates their transit over many atomic distances. As a result, space charges should have sufficient energy to operate at a higher temperature.



**Figure 2.18: Schematic illustration of typical TSC result for PMMA. The symbols  $\gamma$ ,  $\beta$ ,  $\alpha$  and  $\rho$  indicate relaxation peaks in the material (Van Turnhout, 1980).**

Bucci and Fieschi (Vanderschueren & Gasiot, 1979) developed the first consistent theory on dipolar processes in the TSC technique in 1964. It was based on several studies on crystalline materials with dipolar ionic defects. They discovered that dipole reorientation in materials strictly follows the first-order kinetic theory. It means that charge recombination, rather than retrapping, dominated depolarizations within an electret system. Bucci and his coworker used the Debye relaxation model (Van Turnhout, 1980; Vanderschueren & Gasiot, 1979) to describe the system, which assumed electrets were composed of non-interacting dipoles with a single relaxation time. The polarization process performed on these dipoles by the applied electric field  $F_p$  at temperature  $T_p$  during time  $t$  results in the accumulation of polarization density  $P$  in unit volume, which gives:

$$P(t) = P_e \left[ 1 - \exp\left(\frac{-t}{\tau}\right) \right] \quad (2.28)$$

where  $P_e$  is the equilibrium or steady-state polarisation and  $\tau$  is the dipolar relaxation time. According to *Langevin* function for all cases except the lowest temperature and highest field (Vanderschueren et al., 1980);

$$P_e = \frac{sN_d p_\mu^2 \kappa F_p}{kT_p} \quad (2.29)$$

Geometrical factor  $s$  in this relation depends on the possible dipolar orientation. Where for free rotating dipoles  $s = 1/3$ , while for nearest-neighbour face-centred vacancy within ionic crystal  $s = 2/3$ .  $N_d$  represents the concentration of dipoles, where  $p_\mu$  is the electrical moment,  $k$  for Boltzmann's constant and  $\kappa F_p$  for the local DC electrical field that operates on the dipoles. Assuming that the relaxation times for both polarization and depolarization processes on dipoles are the same, the decay of polarization after field removal at  $t = \infty$  is given by:

$$P(t) = P_e \exp\left(\frac{-t}{\tau}\right) \quad (2.30)$$

The first order kinetic equation that governs the process thus describes the corresponding depolarization current as follow,

$$J(t) = -\frac{dP(t)}{dt} = \frac{P(t)}{\tau} \quad (2.31)$$

where  $h = dT/dt$  is the heating rate; and rewriting Equation (2.31) will give

$$P(t) = P_e \left[ \exp\left(-\int_0^t \frac{dt}{\tau}\right) \right] \quad (2.32)$$

This equation is based on some postulate, which are:

- a) this relation also holds for varying temperature
- b) the initially frozen-in polarization  $P(T_o)$  is equal to the equilibrium polarization reach at the polarizing temperature  $P_e(T_p)$



c) the temperature variation of  $\tau$  is given by an Arrhenius-type equation

$$\tau = \tau_o \exp\left(\frac{E}{kT}\right) \quad (2.33)$$

where  $\tau_o$  is the relaxation time at infinite temperature and  $E$  is the activation energy for dipolar orientation and disorientation. It is to be noted that  $f_o = 1/\tau_o$  is the characteristic frequency factor or natural frequency and normally associated to the vibrational frequency of a material. The current density  $J_D$  from TSC measurement which represents an asymmetrical curve or peak in TSC thermogram is given by (Kitis et al., 1998; Mudarra, Belana et al., 1998):

$$J_D(T) = \frac{P_e(T_p)}{\tau_o} \exp\left(\frac{-E}{kT}\right) \exp\left[-\frac{1}{h\tau_o} \int_{T_o}^T \exp\left[\frac{-E}{kT'}\right] dT'\right] \quad (2.34)$$

At low temperatures, the first exponential dominates and is responsible for the initial rise in current with temperature, whereas, at high temperatures, the second exponential dominates and eventually slows down the current growth. As a result, the generated current rapidly diminishes, especially when the activation energy is high. It then generates a relaxation peak, the shape of which is strongly influenced by the heating rate  $h$ , frequency factor  $f_o$ , and activation energy  $E$ . Differentiating Equation (2.34) yields an equation that depicts their effects on a peak's maximum temperature.

$$T_m = \left[\frac{E}{k} h \tau_o \exp\left(\frac{E}{kT_m}\right)\right]^{\frac{1}{2}} \quad (2.35)$$

The activation energy  $E$ , relaxation time  $\tau$  and frequency factor  $f_o$  can be calculated mathematically and used to show relaxation effects in TSC data. Furthermore, the information gleaned from these parameters will be useful in deducing putative mechanisms underlying the formation of TSC peaks, such as high activation energy, which is frequently greater than 4 eV, implying that space charge release is involved in TSC peak formation.

Decomposition analysis can reveal some known relaxation phenomena such as space charge (Curie mode,  $\rho$ ) [0.85 eV, 1.1 eV] (Yamada et al. , 1982), segmental relaxations ( $T_g$  peak) [1.0 – 2.9 eV] (Capsal et al., 2013; Teyssedre & Lacabanne, 1995) and dipole group ( $\beta$  peak) [0.18 eV, 1.17 eV] (Eliasson, 1985; Mizutani et al., 1981) with their respective activation energies. The respective values of activation energy are referred for PVDF and its copolymer P(VDF-TrFE) as reported by others. The value of activation energy  $E$  can be estimated via a technique known as the initial rise method. The initial rise method which was introduced by Garlick and Gibson focuses on the initial currents that form a TSC peak (Garlick & Gibson, 1948). It is because the integrals term in the  $J_D(T)$  function (Equation 2.34) is negligible at  $T \ll T_{max}$ . The first exponential thus dominates the temperature rise of the initial current, so that at the beginning of a peak the TSC current becomes.

$$J_D(T) = \frac{P_e(T_p)}{\tau_o} \exp\left(\frac{-E}{kT}\right) \quad (2.36)$$

where  $P_e$  is equilibrium polarization reach at the polarizing temperature,  $T_p$ .

or

$$\ln J_D(T) \approx \text{const.} \left[ \frac{-E}{kT} \right] \quad (2.37)$$

Therefore, the activation energy  $E$  values can be estimated by plotting the Arrhenius type equation with the  $\ln J_D(T)$  against  $(1/T)$ .

## 2.7 Summary

Most investigations on organic ferroelectric P(VDF-TrFE) were primally focused on the  $\beta$  phase due to its excellent electrical properties for various application purposes. A brief description of various physical quantities related to ferroelectric, dielectric and pyroelectric effects in polymer and composite materials is presented in this chapter. In the present work, the ferroelectric switching characteristics, dielectric and pyroelectric properties of highly crystalline P(VDF-TrFE) films and the effect of ZnO quantum dots embedded into copolymer

matrix prepared by the spin-coating technique are investigated. TSC measurement takes place to investigate the relaxation behaviour of P(VDF-TrFE) and through TSC analysis, the correlation between the surface morphologies, phase transition, crystallinity and so forth, can be achieved. To date, no details of ferroelectric, dielectric and pyroelectric analysis on ZnO QDs doped with P(VDF-TrFE) nanocomposite film has been reported and thus this thesis provides detailed information in fundamental structural and electrical properties of the composite thin films with potential application in energy harvesting devices.

Universiti Malaysia

## CHAPTER 3: EXPERIMENTAL METHODOLOGY

### 3.1 Introduction

This chapter provides a detailed overview of the experimental and sample preparation techniques used for the study. It comprises three main sections. The sample preparation of copolymer P(VDF-TrFE) thin and cast films treated with annealing process, the sol-gel method for synthesizing ZnO QDs and the fabrication of P(VDF-TrFE) / ZnO QDs nanocomposite in thin or cast films are briefly described. In order to produce composite materials with a polymer matrix, the P(VDF-TrFE) films prepared at the first stage need to go through the annealing process to find their optimum properties as a pyroelectric material before they can be used as a polymer host. The structural analysis and surface morphology of the samples are presented in Section 3.3. Details of the electrical measurement including Thermally Stimulated Current measurement and the experimental set-up of the samples to serve as pyroelectric energy harvesting materials are discussed in Section 3.4 of this chapter.

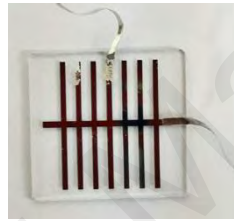
### 3.2 Sample preparation

#### 3.2.1 P(VDF-TrFE) copolymer thin films

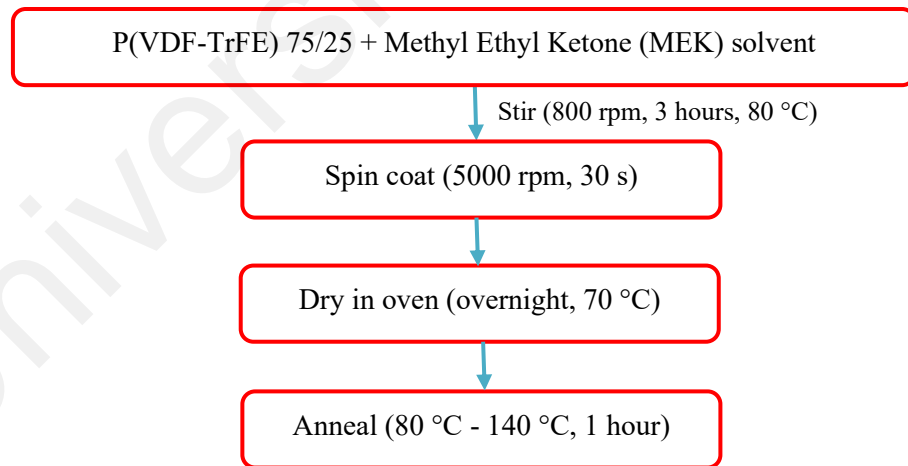
Copolymer P(VDF-TrFE) with a molar ratio of 75/25 in powder form was supplied by Kureha Corporation, Japan. The polar solvent for the polymer used in this experiment is Methyl Ethyl Ketone (MEK, 99 %) from Sigma-Aldrich.

The P(VDF-TrFE) powders were dissolved in MEK to form polymer solutions of 5 wt%. The solutions undergo a stirring process at 800 rpm and 80 °C for 3 hours using a magnetic stirrer. Solutions of P(VDF-TrFE) were dropped onto the Aluminium (Al) coated glass substrate surface using a pipette and then spin-coated with a speed of 5,000 rpm for 30 s. The spin-coated films were dried in the oven overnight at 70 °C to remove the residual solvent. Then, the as-deposited films were subjected to an annealing treatment at various temperatures

in the range of 80 °C to 140 °C each for 1 hour purposely for increasing the film crystallinity by using a hot plate. The films were annealed at different temperatures before the deposition of the top electrodes. Finally, (1 × 1) mm<sup>2</sup> area aluminium electrodes were then coated onto the films by thermal evaporation method through a metal mask to produce a metal-insulator-metal (MIM) thin-film device (see Figure 3.1) prior to electrical characterizations such as dielectric, ferroelectric and pyroelectric of copolymer films. The thickness of the thin films was measured using a KLA Tencor P-6 mechanical profiler which can measure films with thickness in the range of 200 - 300 nm. The flow chart showing the procedure for preparing PVDF-TrFE thin films is depicted in Figure 3.2.



**Figure 3.1: MIM structure of P(VDF-TrFE) thin films.**



**Figure 3.2: Fabrication flowchart of the spin coating polymer thin films.**

### 3.2.2 P(VDF-TrFE) copolymer thick films

Synthesis protocol as mentioned in earlier work (Section 3.2.1) was followed to obtain 5 wt% of copolymer PVDF-TrFE solution. Films of P(VDF/TrFE) were cast from 5 wt% MEK

solution onto glass Petri dishes. The annealing and drying process for cast films are similar to the thin films as described in Figure 3.2 above. Subsequently, the films were peeled off from the glass petri dish at room temperature. Freestanding copolymer films with an average thickness of 30  $\mu\text{m}$  and 2 cm  $\times$  2 cm dimensions were prepared as shown in Figure 3.3 as a requirement for Thermal Stimulated Current (TSC) measurement.



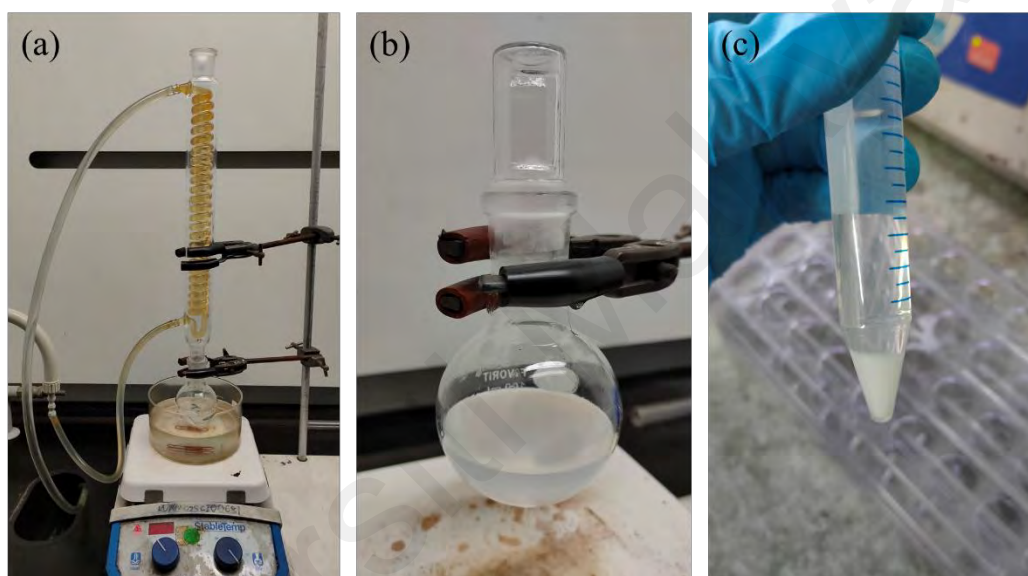
**Figure 3.3: P(VDF-TrFE) cast films via solution casting.**

### **3.2.3 ZnO Quantum Dots stabilized with organic ligand TEA**

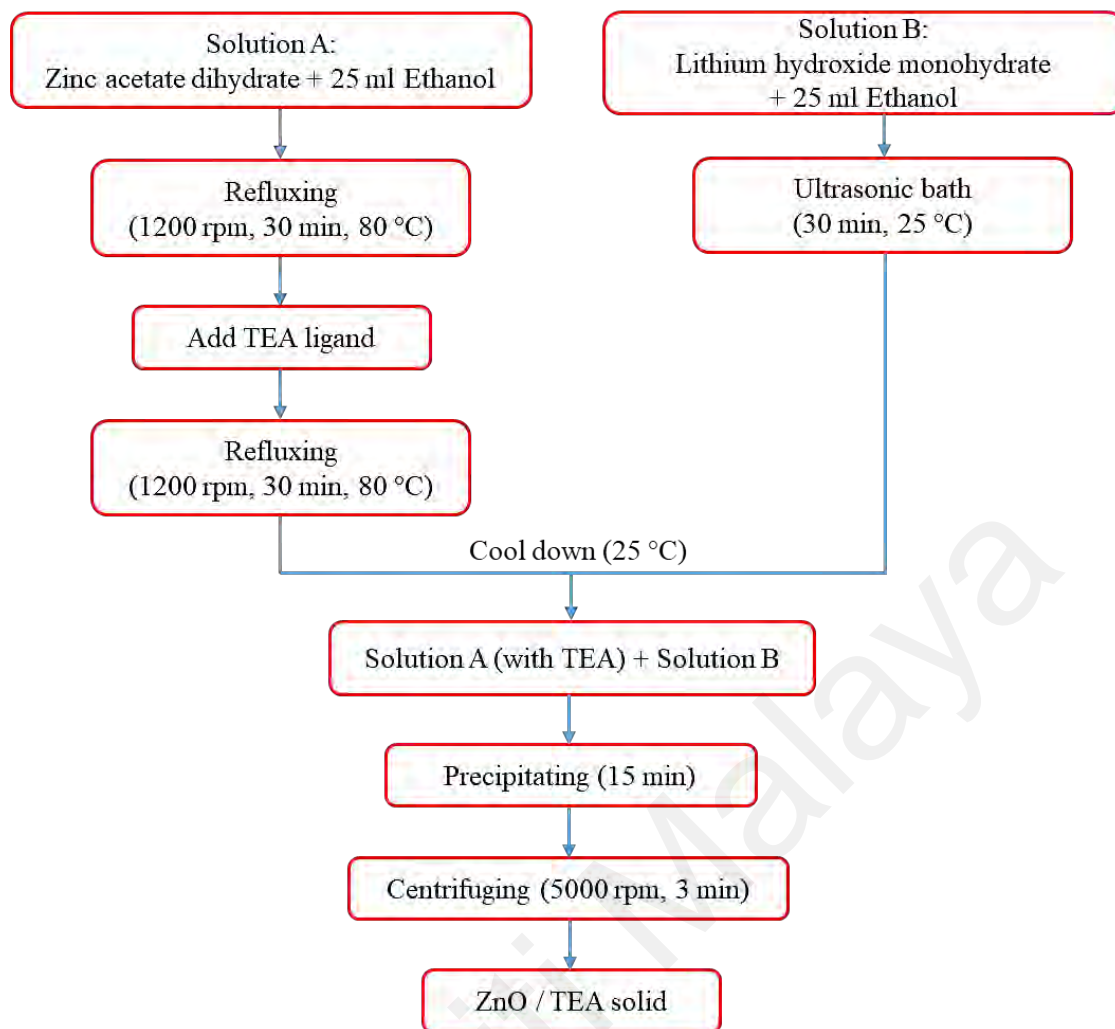
Zinc acetate dihydrate ( $\text{Zn}(\text{OAc})_2 \cdot 2\text{H}_2\text{O}$ ) was sourced from Sigma–Aldrich. Lithium hydroxide monohydrate ( $\text{LiOH} \cdot \text{H}_2\text{O}$ ) and acetone (99.5 %) were supplied by Friendemann Schmidt. Triethanolamine (TEA) of 99 % purity was purchased from Merck, while Ethanol (99.9 %) was purchased from J. Kollin Chemicals.

ZnO QDs were prepared according to the reported synthesis by Adnan et al. (2017). The raw material,  $\text{Zn}(\text{OAc})_2 \cdot 2\text{H}_2\text{O}$  (0.5488 g) was dissolved in 25 mL ethanol using the refluxing method at 80 °C for 30 minutes at speed 1200 rpm. Afterwards, a specific amount (66.3  $\mu\text{L}$ ) of Triethanolamine (TEA) was added to the  $\text{Zn}^{2+}$  precursor solution and then allowed to reflux (see Figure 3.4(a)) for another 30 minutes. Meanwhile,  $\text{LiOH} \cdot \text{H}_2\text{O}$  (0.2623 g) was dissolved in 25 mL ethanol using an ultrasonic bath at room temperature for 30 minutes. The two

solutions were then cooled down to room temperature (refer to Figure 3.4(b)). The LiOH solution was added rapidly to the  $\text{Zn}^{2+}$  precursor solution and then the mixture was stirred vigorously at 1200 rpm for 10 minutes to form ZnO / TEA QDs. The ZnO / TEA QDs were eventually collected by precipitating with acetone and centrifuging process at 5000 rpm for 3 minutes, as shown in Figure 3.4(c). Then, the solid ZnO QDs were kept in the freezer at -20 °C for future use. The flow chart showing the procedure for synthesizing ZnO QDs is shown in Figure 3.5.



**Figure 3.4: ZnO QDs (a) synthesised using reflux method (b) final solution (c) after precipitation and centrifuge process.**



**Figure 3.5: Flowcharts of ZnO / TEA QDs synthesis by sol-gel method.**

### 3.2.4 P(VDF-TrFE) / ZnO QDs thin nanocomposite films

The starting material was copolymer P(VDF-TrFE) with a molar ratio of 75/25 powder form was purchased from Kureha Corporation, Japan. Methyl Ethyl Ketone (MEK, 99 %, Sigma-Aldrich) was used as the polar solvent for the polymer.

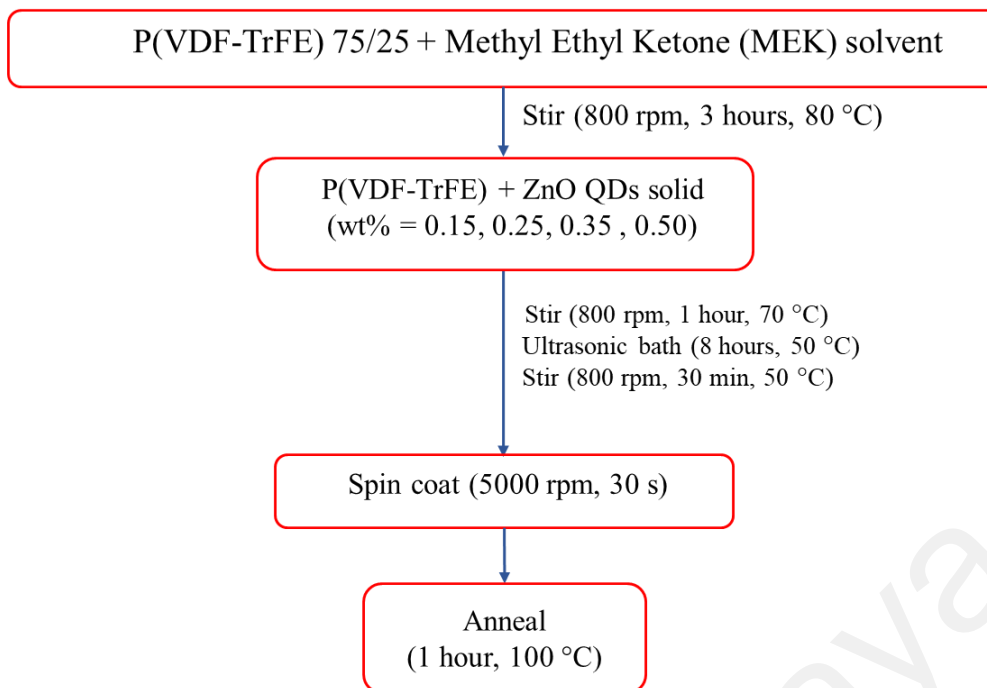
Before forming nanocomposite film, ZnO QDs produced from Section 3.2.3 were dried using purified nitrogen gas. The P(VDF-TrFE) and ZnO QDs powders were dispersed at different weightage percentages from 0.15 to 0.50 with 5 wt% of MEK (refer to Figure 3.6). Figure 3.7 shows the fabrication flowchart of the P(VDF-TrFE) / ZnO QDs nanocomposite thin films. Nanocomposites of P(VDF-TrFE) / ZnO QDs were prepared by dispersing the ceramic powder in a solution of polymer for 1 hour at 70 °C using a magnetic stirrer.



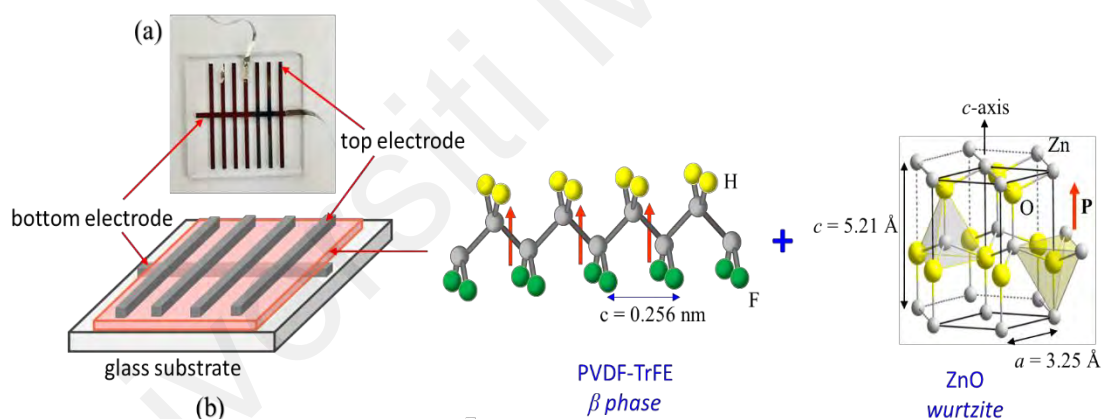
Subsequently, the final solution was agitated for up to 8 hours at 50 °C by ultrasonic bath until complete polymer dissolution. The solution was stirred for another 30 minutes at 50 °C using a magnetic stirrer to ensure complete mixing and dissolution of the solutions. The compositions were varied as 0, 0.15, 0.25, 0.35 and 0.50 wt%, and spin-coated at 5000 rpm for 30 seconds onto a clean glass which initially evaporated with Al electrode. To remove residual solvent, the films were dried overnight in a 70 °C oven. The thin films were then annealed for 1 hour at 100 °C to induce higher crystallinity structures of P(VDF-TrFE). Finally, the top electrode with effective ( $1 \times 1$ ) mm<sup>2</sup> is deposited on the thin films prior to electrical measurement, using the thermal evaporation method to produce a metal-insulator-metal (MIM) thin-film device (refer to Figure 3.8). The thickness of the thin film was measured using KLA Tencor P-6 mechanical profiler. The thickness of the films was in the range of 250 to 300 nm.



**Figure 3.6: Solutions of nanocomposite viewed under UV lamp 365 nm with different weightage percentage. From right, 0, 0.15, 0.25, 0.35 and 0.50 wt% of P(VDF-TrFE) / ZnO QDs.**



**Figure 3.7: Fabrication flowchart of the polymer / quantum dots nanocomposite thin films.**

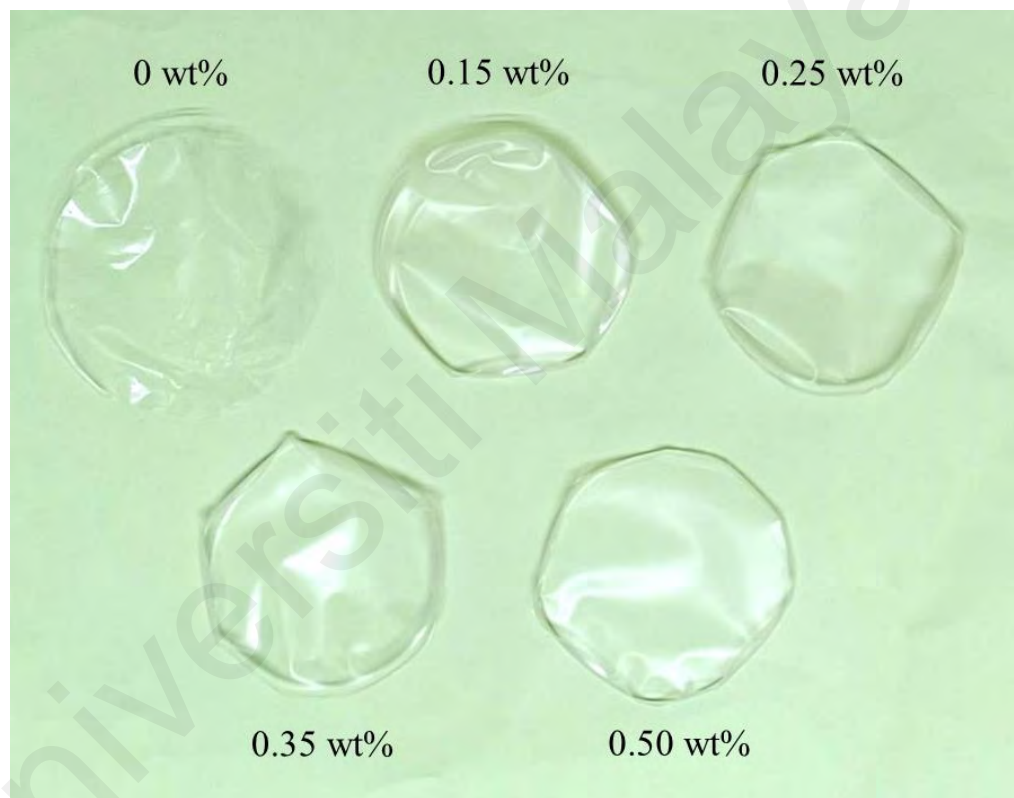


**Figure 3.8: Thin-film configuration of P(VDF-TrFE) / ZnO QDs composite films on a glass substrate (a) real picture (b) schematic diagram.**

### 3.2.5 P(VDF-TrFE) / ZnO QDs thick nanocomposite films

These composite films were also prepared for Thermal Stimulated Current (TSC) measurement for the purpose of investigating their molecular ability of both the amorphous and crystalline phase. The free-standing films of the P(VDF-TrFE) / ZnO QDs nanocomposite were prepared for the TSC measurement. P(VDF-TrFE) powders were dissolved in 5 wt% MEK solvents. The selected compositions and synthesis procedure are the same as the

preparation of thin nanocomposite films as mentioned in Section 3.2.4. The resulting composite solutions were poured into an open glass container and dried in the oven for one day at 70 °C. The bulk composites were annealed at 100 °C for one hour to enhance the crystallinity of the polymer. Prior to TSC characterization, the films with a thickness of  $\sim 30 \mu\text{m}$  were then peeled off from the glass petri dish at room temperature and were evenly cut with dimensions of  $2 \times 2 \text{ cm}^2$ . Figure 3.9 shows the P(VDF-TrFE) / ZnO QDs thick nanocomposite film with various weightage percentages.



**Figure 3.9: The P(VDF-TrFE) / ZnO QDs thick nanocomposite film.**

### **3.2.6 Annealing process**

The pyroelectric behaviour of a material is caused by the contribution of the most crystalline phase of PVDF with a strong dipole moment, which is referred to as the  $\beta$  phase. The dipole arrangement is perpendicular to the direction of the polymer chain axis, resulting in a highly polar conformation recognized as the all-trans (TTTT) conformation, which was discussed in detail in the previous chapter. Many efforts have been undertaken to increase the crystallinity

of copolymer P(VDF-TrFE) films, such as by applying a poling process to (Roggero et al., 2017; Viola et al., 2018), applying an annealing treatment to (Mahdi et al., 2014; Spampinato et al., 2018) or mechanically stretching (Khoon-Keat et al., 2018; Ma et al., 2018) the polymer. To form the desired  $\beta$  phase crystalline films, the prepared films in this work are subjected to an annealing treatment at specific temperatures for a specific duration of processing. Copolymer P(VDF-TrFE) can be directly crystallized into the  $\beta$  phase by heat treatment at a temperature between the Curie transition temperature ( $T_c$ ) and the melting temperature ( $T_m$ ) (Nan Jia et al., 2017). In the first phase of the study, copolymer films are subjected to various annealing temperature,  $T_a$  where  $T_c < T_a < T_m$ . The selected annealing temperatures are 80 °C, 90 °C, 100 °C, 110 °C, 120 °C, 130 °C and 140 °C. All copolymer films are annealed for one hour which is sufficient to obtain high  $\beta$  phase fraction (Mahdi et al., 2014). At the second stage of study, the best annealed copolymer films which gives an optimum pyroelectric coefficient, better remnant polarization and dielectric constant is chosen to act as a polymer matrix to be embedded with semiconductive filler, ZnO QDs to form nanocomposite device films.

### 3.2.7 Poling process

A poling process is an essential procedure prior to the observation of the ferroelectric and pyroelectric activity of the samples. The poling process is needed to obtain a greater ferroelectric domain, which is a microscopic area within the material where all the electric dipoles are oriented in the same direction as a result of the applied electric field. It can be achieved via placing a crystal inside a continuing force field that can interact with all dipoles in uniform alignment. As a result of the poling process, the polar axes of the dipoles are realigned in the direction of the applied electric field. When the electric field is removed, the dipoles remain aligned to some extent. The field necessary to facilitate the alignment of dipoles is called the coercive field,  $E_c$ . It should also be noted that the degree of alignment of the dipoles decreases with time after polling. In this dissertation, an electric field of 200 MV/m was applied to the P(VDF-TrFE) films (applied to all P(VDF-TrFE) at various annealing

temperatures) for 10 minutes at room temperature using a DC power supply. Meanwhile, the composite films were poled at 166 MV at the same temperature and duration of polling. It is important to note that the samples treated under a high electric field during the polling process led to dielectric breakdown. To avoid permanent damage to the samples by arcs or dielectric breakdowns, the samples were immersed in the silicone oil bath. Samples are short-circuited and discharged immediately after the polling process to eliminate excessive loads.

### 3.3 Structural analysis

#### 3.3.1 X-ray diffraction

X-ray diffraction (XRD) characterization utilizes an X-ray beam that is projected onto the sample. X-ray diffraction measurement was carried out to examine the phase and crystalline structure of copolymer, semiconductive filler ZnO QDs and its polymer composite. XRD measurement was carried out using a PANalytical-Empryean diffractometer with CuK $\alpha$  radiation ( $\lambda = 1.54060 \text{ \AA}$ ) over a wide range of  $2\theta$  ( $5^\circ$  to  $70^\circ$ ) with a step size of  $0.02^\circ$ . The crystallite size of the ZnO QDs was determined through X-ray line broadening method using Scherrer equation:

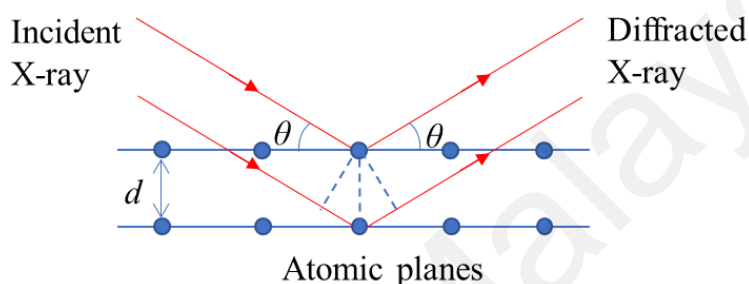
$$d = k\lambda / \beta_{hkl} \cos \theta \quad (3.1)$$

where  $d$  is the crystallite size in nanometers,  $\lambda$  is the wavelength of the radiation,  $k$  is the shape factor ( $k = 0.89$ ),  $\beta_{hkl}$  is the broadening of the  $hkl$  diffraction peak at half-maximum intensity (in radians) and  $\theta$  is the Bragg diffraction angle. When a crystal is bombarded with X-rays of a fixed wavelength (corresponding to the spacing of the atomic-scale crystal lattice planes) and at certain incident angles, intense reflected X-rays are produced when the wavelengths of the scattered X-rays constructively interfere. The differences in the travel path must be integer multiples of the wavelength for the waves to interfere constructively. When this constructive interference occurs, an X-ray diffracted beam leaves the crystal at the same angle as the

incident beam as illustrated in Figure 3.10. The fundamental principle described above is based on Bragg's law:

$$n\lambda = 2d \sin \theta \quad (3.2)$$

whereby  $\lambda$  is the incident wavelength,  $\theta$  is the angle of incident and  $d$  is the inter-planar spacing of atomic planes. The crystallite size obtained through XRD measurement is also compared with the value obtained from the TEM characterization.



**Figure 3.10: A beam of parallel X-ray penetrating atomic planes in a crystalline material.**

### 3.3.2 Fourier transform infrared spectroscopy

Fourier transform infrared (FTIR) spectroscopy is the study of matter interacting with electromagnetic fields in the infrared radiation (IR) region as a function of photon frequency. IR radiation comprises a broad electromagnetic spectrum from visible to microwave regions, with wavenumbers ranging from 4000 to 400  $\text{cm}^{-1}$ . This method can identify the chemical bonding of the organic and inorganic materials through molecular vibration in the wavelength of the infrared absorption spectrum. When a material is exposed to infrared radiation, the sample molecules absorb radiation of a certain wavelength causing a change in the dipole moment of the molecules. Some of the infrared radiation is transmitted by the sample and part of it is absorbed. As a result, the vibrational energy level of the sample molecule shifts from the ground state to the excited state. The molecular chemical bonds have the characteristic absorption frequency from the wavelength of the infrared absorption spectrum. Therefore, the resulting spectrum of FTIR shows the transmission and absorption of sample molecules which

generates a molecular fingerprint of the chemical bonds in the sample. In this study, Perkin Elmer 2000 FTIR spectroscopy system has been employed to ascertain the chemical bonding of the P(VDF-TrFE) and nanocomposite thin films in the transmission mode.

### **3.3.3 Differential scanning calorimetry**

Differential scanning calorimetry (DSC) is an analytical technique to determine the thermal properties of a material. DSC thermograms were recorded using a Mettler Toledo 822 instrument to analyze the thermal transitions of the copolymer and nanocomposite films. About 5 mg sample was encapsulated in an aluminium pan before the measurement. The P(VDF-TrFE) (75/25) cast film was subjected to spectroscopy DSC analysis by raising the temperature from -40 °C to 200 °C and then reducing it back to -40 °C. The heating and cooling rates were performed at  $\pm 10$  °C/min. It is operated under a nitrogen gas atmosphere to reduce thermo-oxidative degradation. The Curie point,  $T_c$  and crystalline melting point,  $T_m$  of the polymer were examined through this technique.

### **3.3.4 High-resolution transmission electron microscope**

The high-resolution transmission electron microscope (HRTEM) is a powerful tool to characterize the microstructures of materials at a very high spatial resolution. HRTEM is used to observe the crystal structures, interfaces and defects in crystalline materials such as dislocations, stacking faults and grain boundaries (Möbus, 2003). TEM incorporates a high-energy electron beam that passes through an ultra-thin sample, then the transmitted part of the electron beam is focused and magnified by an electromagnetic lens to form a diffraction pattern or image. TEM images of ZnO QDs were captured using a Hitachi HT-7700 TEM operating at 120 kV and statistical analysis was performed by measuring particles from various areas on the Formvar with carbon coating on a 300 mesh Cu grid. Prior to HRTEM measurement, a copper grid was dipped into a very dilute ZnO QDs solution and dried at room temperature.

### **3.3.5 Field emission scanning electron microscopy**

The morphological characteristics of copolymer at different annealing temperatures and nanocomposite films at various weightage percentages were viewed in a field electron scanning electron microscopy, FESEM. In the present work, the microscope was operated at high vacuum mode using a Hitachi (SU8220) field electron scanning electron microscopy and provided images from resolutions of 1  $\mu\text{m}$  to 300 nm. A field emission cathode in the electron gun generates electrons that are supplied to the sample surface in FESEM. The sample surface produces lower energy secondary electrons. The surface image of the sample is constructed by measuring the secondary electron intensity as a function of the position of the primary scanning electron beam. Using the Image J software, the average size of the particles is calculated from the surface morphology image of the samples. Moreover, energy dispersive X-ray spectrometry was performed to determine the presence of ZnO QDs in composite films.

## **3.4 Optical analysis**

### **3.4.1 Ultraviolet-visible spectroscopy**

Ultraviolet-visible (UV-Vis) spectroscopy is an analytical technique that determines the number of discrete wavelengths of UV or visible light absorbed or transmitted by a sample. To promote electrons in a substance to a higher energy state, which is detected as absorption, a specific amount of energy is required. Electrons in different bonding environments in a substance require a different amount of energy to be promoted to a higher energy state. Thus, light absorbs at different wavelengths in different substances. Optical absorption measurements within the UV-visible range of ZnO QDs dispersed in ethanol were performed at room temperature using Perkin Elmer Lambda 750 UV-vis spectrometer. The wavelength range used in the experiment was 200 to 400 nm. The observed spectrum from UV-visible spectroscopy can be displayed as a graph of absorbance, optical density or transmittance



versus wavelength. Moreover, the UV-visible absorption measurement was further used to determine the bandgap using the Tauc plot equation:

$$(\alpha h\nu)^2 = A(h\nu - E_g) \quad (3.3)$$

where  $\alpha$  is the absorption coefficient near the absorption edge,  $h$  is a Plank's constant,  $\nu$  is a frequency vibration,  $A$  is the edge-width parameter and  $E_g$  is the optical band-gap energy.

### 3.4.2 Photoluminescence spectroscopy

Photoluminescence (PL) spectroscopy involves a form of light emission spectroscopy as a result of a process known as photoexcitation. When light is directed onto a sample, the energy is absorbed by the electrons within the material and becomes excited, a process called excitation. When electrons return to their equilibrium states from excited states, energy can be released in the form of light and is called the relaxation process. In this work, photoluminescence studies were carried out on dried films of ZnO QDs dispersed in ethanol. The photoluminescence spectra were recorded using Perkin Elmer LS 50B luminescence spectrometer.

## 3.5 Electrical measurements

### 3.5.1 Dielectric measurements

The impedance analyzer is equipped with an integrated system to measure the real and imaginary parts of an impedance vector of the samples. In this study, the dielectric properties of the copolymer P(VDF-TrFE) and the nanocomposites were measured using Impedance Analyzer (Agilent 4294A) at the frequency range of 40 Hz to 110 MHz. The dielectric results were expressed in terms of either the complex permittivity:

$$\varepsilon^* = \varepsilon' - i \varepsilon'' \quad (3.4)$$

or the complex conductivity:

$$\sigma^* = \sigma' + i \sigma'' \quad (3.5)$$

The free relative dielectric permittivity,  $\varepsilon'$  is defined as the ratio of the material permittivity to the permittivity of free space while the imaginary permittivity,  $\varepsilon''$  is calculated from the equation below:

$$\varepsilon'' = \tan \varepsilon' \tan \delta \quad (3.6)$$

where  $\tan \delta$  is the dissipation factor. The measurements were carried out in the temperature dependence for copolymer to investigate the Curie point at different annealing temperatures and to observe the effect of ZnO QDs filler in composite films.

### 3.5.2 Ferroelectric measurements

The ferroelectric hysteresis loop was characterized using Radiant Technology Precision LC Analyzer at room temperature. The  $P$ - $E$  hysteresis loop is observed by a Sawyer-Tower circuit. The ferroelectric  $D$ - $E$  hysteresis loops were measured with step amplitude of an applied electric field at 100 Hz or with a pulse width of 10 ms for all samples. The voltage step size was gradually increased for each 5 V for P(VDF-TrFE) and its nanocomposite films.

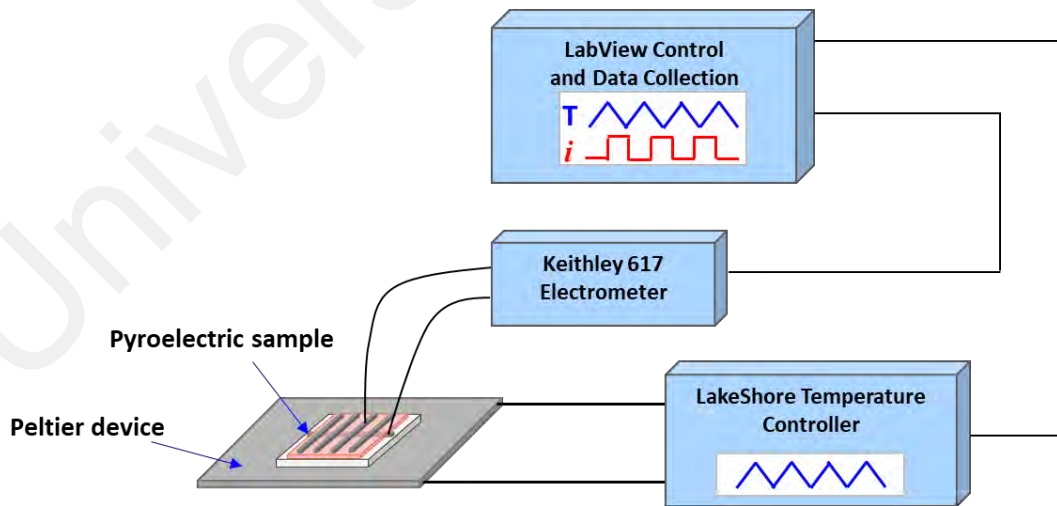
### 3.5.3 Pyroelectric measurements

Due to the non-centrosymmetric crystalline structure of the copolymer P(VDF-TrFE) thin film, dipole polarization can be spontaneous and temperature-dependent. Therefore, the pyroelectric effect of copolymers was also investigated in this work. The pyroelectric coefficient of the annealed copolymer and its nanocomposite P(VDF-TrFE) / ZnO QDs thin films were measured using the quasi-static measurement method. The sample was mounted on a Peltier heater that was connected to the temperature controller. The temperature of the thin films was measured with a highly sensitive silicon diode sensor. Triangular temperature waveforms with five heating rates utilized in this experiment by a Lakeshore 331 temperature

controller were  $0.01\text{ }^{\circ}\text{Cs}^{-1}$ ,  $0.015\text{ }^{\circ}\text{Cs}^{-1}$ ,  $0.02\text{ }^{\circ}\text{Cs}^{-1}$ ,  $0.025\text{ }^{\circ}\text{Cs}^{-1}$  and  $0.03\text{ }^{\circ}\text{Cs}^{-1}$  at a temperature in the range of  $26\text{ }^{\circ}\text{C}$  to  $29\text{ }^{\circ}\text{C}$ . While the heating rates and temperature range for nanocomposite variants are as follows;  $0.02\text{ }^{\circ}\text{Cs}^{-1}$ ,  $0.025\text{ }^{\circ}\text{Cs}^{-1}$ ,  $0.03\text{ }^{\circ}\text{Cs}^{-1}$ ,  $0.035\text{ }^{\circ}\text{Cs}^{-1}$ ,  $0.04\text{ }^{\circ}\text{Cs}^{-1}$ , and  $0.05\text{ }^{\circ}\text{Cs}^{-1}$  at a temperature of  $26\text{ }^{\circ}\text{C}$  to  $30\text{ }^{\circ}\text{C}$ . Pyroelectric system equipped with LAB VIEW 12 software for data acquisition and the IEE-488 GPIB interface was used to enable the computer to control and receive data from the two instruments (temperature controller and electrometer). The schematic representation of the experimental setup for the quasi-static pyroelectric measurement is shown in Figure 3.11. The resulting pyroelectric short-circuited current,  $I_p$  was measured with a Keithley 617 Electrometer and then was evaluated using the equation below:

$$I_p = P_i A \frac{\Delta T}{\Delta t} \quad (3.7)$$

where  $I_p$  is the peak-to-peak pyroelectric current,  $P_i = \frac{\Delta P}{\Delta T}$  is the pyroelectric coefficient,  $A$  is the area of the sample and  $\frac{\Delta T}{\Delta t}$  is the temperature gradient.



**Figure 3.11: Schematic drawing of the pyroelectric measurement.**

### 3.5.4 Thermally Stimulated Current measurements

Thermally stimulated current (TSC) studies of polar materials such as polyvinylidene fluoride (PVDF) and its copolymer poly(vinylidene fluoride-co-trifluoroethylene), P(VDF-TrFE) materials have received a lot of attention because they exhibit highly polarized behaviour when subjected to an electric field, with the positive end of the dipole aligned with the negative charges. In the present work, the TSC technique was carried out to investigate the molecular motions of the crystalline copolymer P(VDF-TrFE) and its nanocomposites. Generally, in TSC, the spectrum monitored is the electric current that is generated from the depolarization process in a sample, previously frozen in after an electric field polarizing process. The principles employed in the TSC system are sketched in Figure 3.12 and explained as follows (Van Turnhout, 1980):

#### 1. Polarization

The sample is initially heated above its glass transition temperature,  $T_g$ , to form an artificial thermoelectret. It follows with polarization by applying direct current D.C electrical field  $E_p$  for  $t_p$  minutes.

#### 2. Quenching

Polarized charges are then frozen by cooling the sample in the polarization field,  $E_p$  to lower temperature,  $T_o$ . These charges are considered to be practically stationary at this temperature.

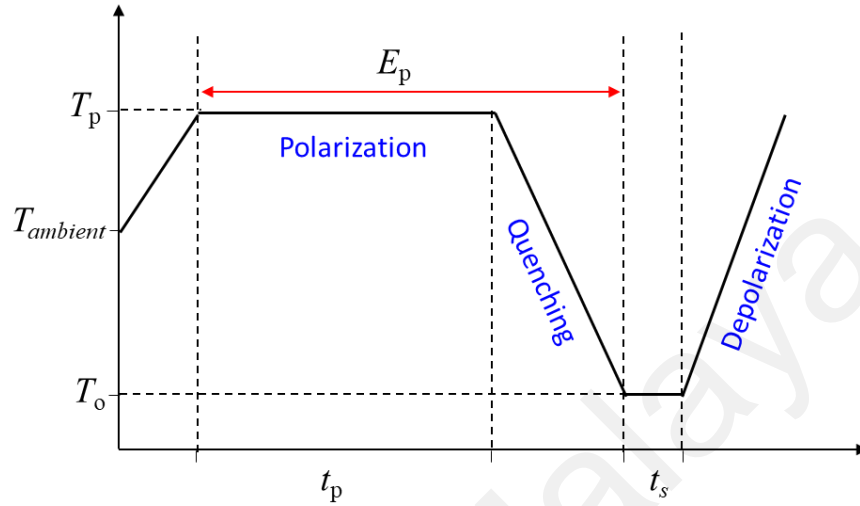
#### 3. Removal of electric field

For this process, the poling electric field  $E_p$  at  $T_o$  is typically reduced to  $0 \text{ Vm}^{-1}$ . The sample is now stabilized for  $t_s$  minutes at  $T_o$  temperature. The electret charges that emerged in the sample are converted into a thermoelectret.

#### 4. Depolarization

Finally, the electrets sample is short-circuited and reheated at a constant rate, such as at  $1 \text{ }^\circ\text{C/min}$ . The resultant dipole relaxation is observed and it is detected as a depolarization current as a function of temperature. As an outcome, the depolarization

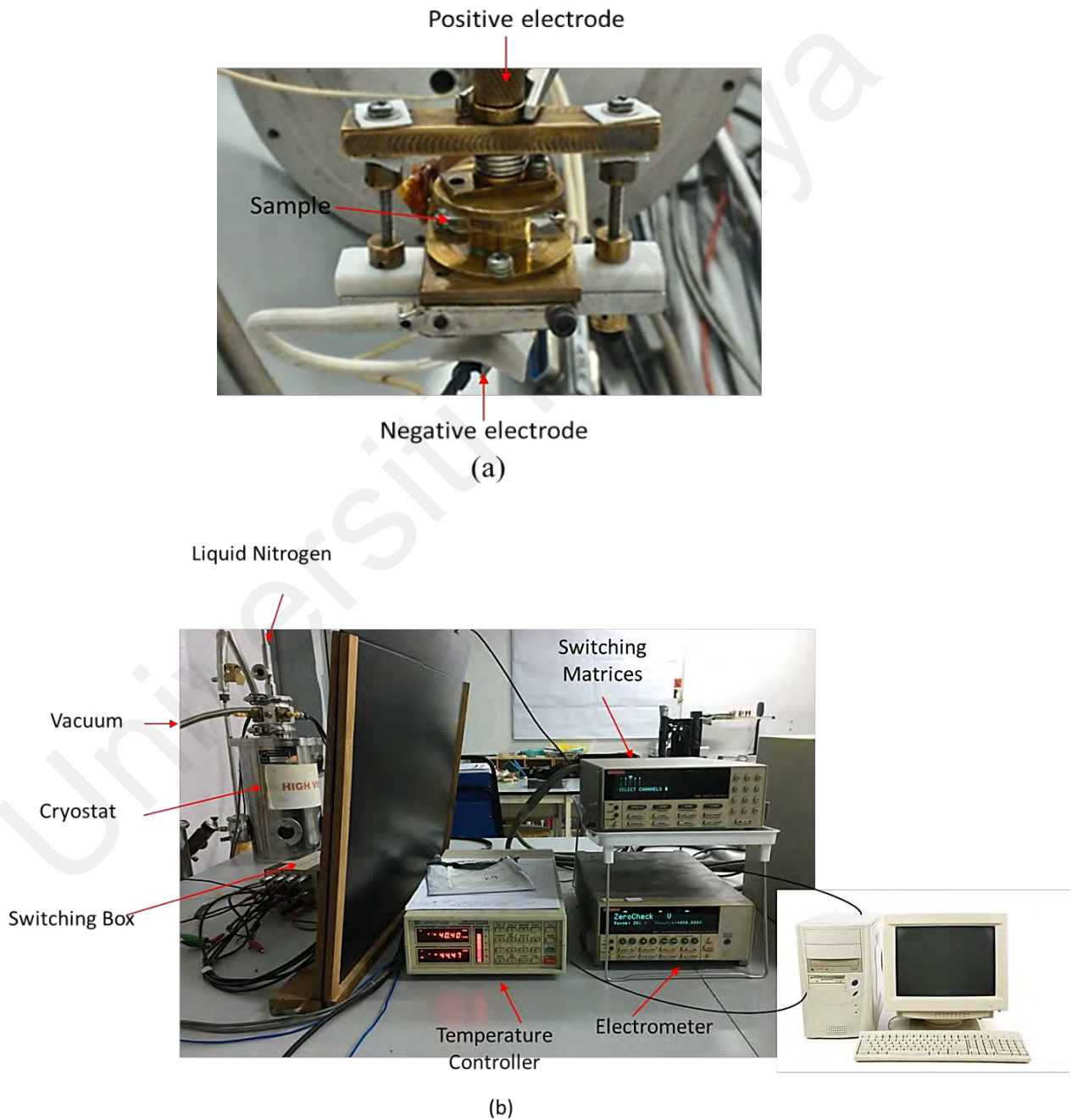
process of the activated electret charges produces the discharge current. TSC, or thermally stimulated current, is measured with an electrometer and recorded as a function of temperature by a computer.



**Figure 3.12: Schematic drawing of the TSC principle.**

TSC measurements were conducted in a laboratory-developed by Abdul Halim (2010). Inside the cryostat or vacuum chamber, a sample of (P(VDF-TrFE) cast film with an average thickness of 30  $\mu\text{m}$  and dimensions of  $2 \times 2 \text{ cm}^2$  was clamped between a pair of electrodes (see Figure 3.13(a)). This cryostat can be evacuated via a special opening that is directly connected to a vacuum pump. It also comes with a nozzle on the top that is linked to a liquid nitrogen tank. On the side of the nozzle, there is a special opening for pressure relief from liquid nitrogen. Firstly, the sample was heated to a poling temperature  $T_p$ , which must be higher than the glass transition temperature  $T_g$  of the copolymer, to eliminate the surface and volume charges. The sample was then subjected to an electric field, called a poling field, of 20 MV/m for 20 minutes ( $t_p$ ) to allow orientation of molecular dipoles and charge polarization. Next, the sample was quenched (rapidly cooled) with liquid nitrogen to a minimum temperature,  $T_{\min} = -140^\circ\text{C}$  and the polarizations were thus frozen in. After that, both electrodes were short-circuited for 5 minutes to remove any stray charges. Polarization decay

was induced by gradually increasing the temperature from the minimum to the maximum temperature,  $T_{\max} = 130\text{ }^{\circ}\text{C}$ , at a constant rate of  $dT/dt = 5\text{ }^{\circ}\text{C}/\text{min}$ . An ammeter connected in series to a Keithley 6517 electrometer was used to measure the depolarization current as a function of temperature. The LakeShore TC330 temperature controller is used in this system and it comes with an IEEE-488 interface card that allows it to be integrated into a computer system. The entire functioning TSC system is shown in Figure 3.13(b).



**Figure 3.13: The experimental setup of TSC system.**

### 3.6 Summary

The sample preparation of copolymer P(VDF-TrFE) thin and cast films annealed at various temperatures, the sol-gel method for synthesizing ZnO QDs and the fabrication of P(VDF-TrFE) / ZnO QDs nanocomposite in thin or cast films were discussed and the characterization techniques used were explained. The annealing procedure for all samples is compulsory to enhance the film's crystallinity and robust electrical performance of the device. Observations revealed that the presence of a nearby object close to TSC setup can interfere with the measurement of the TSC current, which is significantly low, ranging from  $10^{-15}$  to  $10^{-9}$  A. This effect may be related to the electric field produced by the human body (Abdul Halim, 2010).

## **CHAPTER 4: STRUCTURAL AND OPTICAL ANALYSIS OF COPOLYMER P(VDF-TrFE), ZnO QDs AND NANOCOMPOSITE THIN FILMS P(VDF-TrFE) / ZnO QDs**

### **4.1 Introduction**

The poling process (Roggero et al., 2017; Viola et al., 2018), the annealing treatment (Mahdi et al., 2014; Spampinato et al., 2018) and the mechanical stretching (Khoon-Keat et al., 2018; Ma et al., 2018) of the copolymer have all been employed to increase the crystallinity of the copolymer  $\beta$  phase. Among the initiatives, thermal annealing is the easiest, direct and efficient to alter molecules arrangement and therefore enhance the  $\beta$  phase domains. Heat treatments were applied in between the Curie transition temperature ( $T_c$ ) and the melting temperature ( $T_m$ ). In this chapter, copolymer P(VDF-TrFE) thin films were prepared via spin coating and meanwhile cast films via drop-casting method. The copolymer structure and the electrical properties which include ferroelectric, dielectric, pyroelectric and Thermal Stimulated Current (TSC) were thoroughly analyzed and reported. The optimum annealed P(VDF-TrFE) film which shows the highest remnant polarization and pyroelectric coefficient was chosen as a polymer host to form nanocomposite films with ZnO QDs.

### **4.2 Copolymer P(VDF-TrFE) at different annealing temperatures**

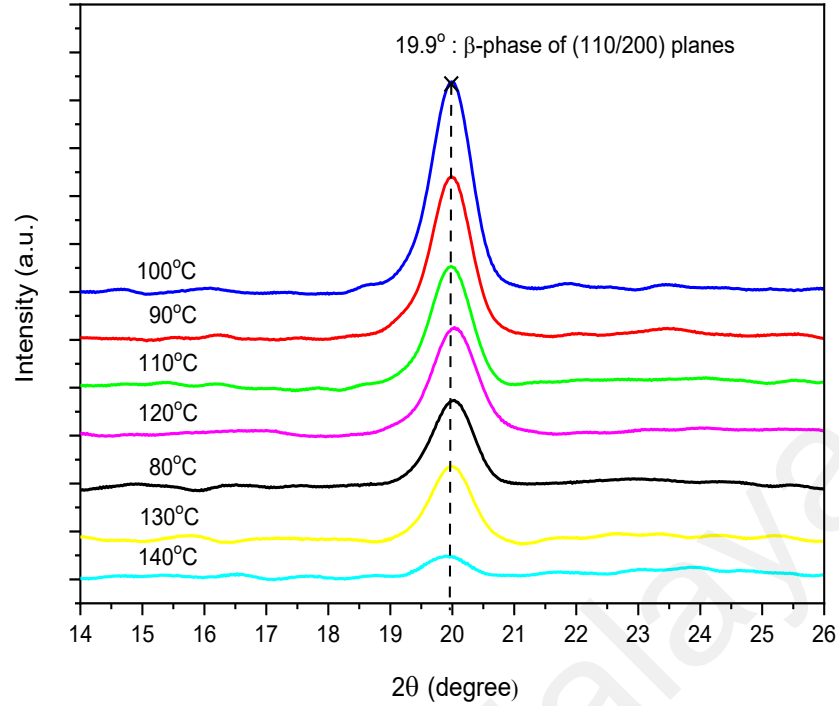
The copolymer thin films were annealed at various temperatures 80 °C, 90 °C, 100 °C, 110 °C, 120 °C, 130 °C and 140 °C using a hot plate. Spin coating films deposited on Si wafer prior to structural and morphological measurement were annealed using the same procedure.

#### **4.2.1 XRD analysis and determination of percentage of crystallinity**

At the atomic scale, XRD is used to observe the crystal structure and identify the phases of P(VDF-TrFE) thin film. The diffraction angle represents the inter-planar spacing and orientation of the crystal planes, while the diffraction intensity represents the quantity of the



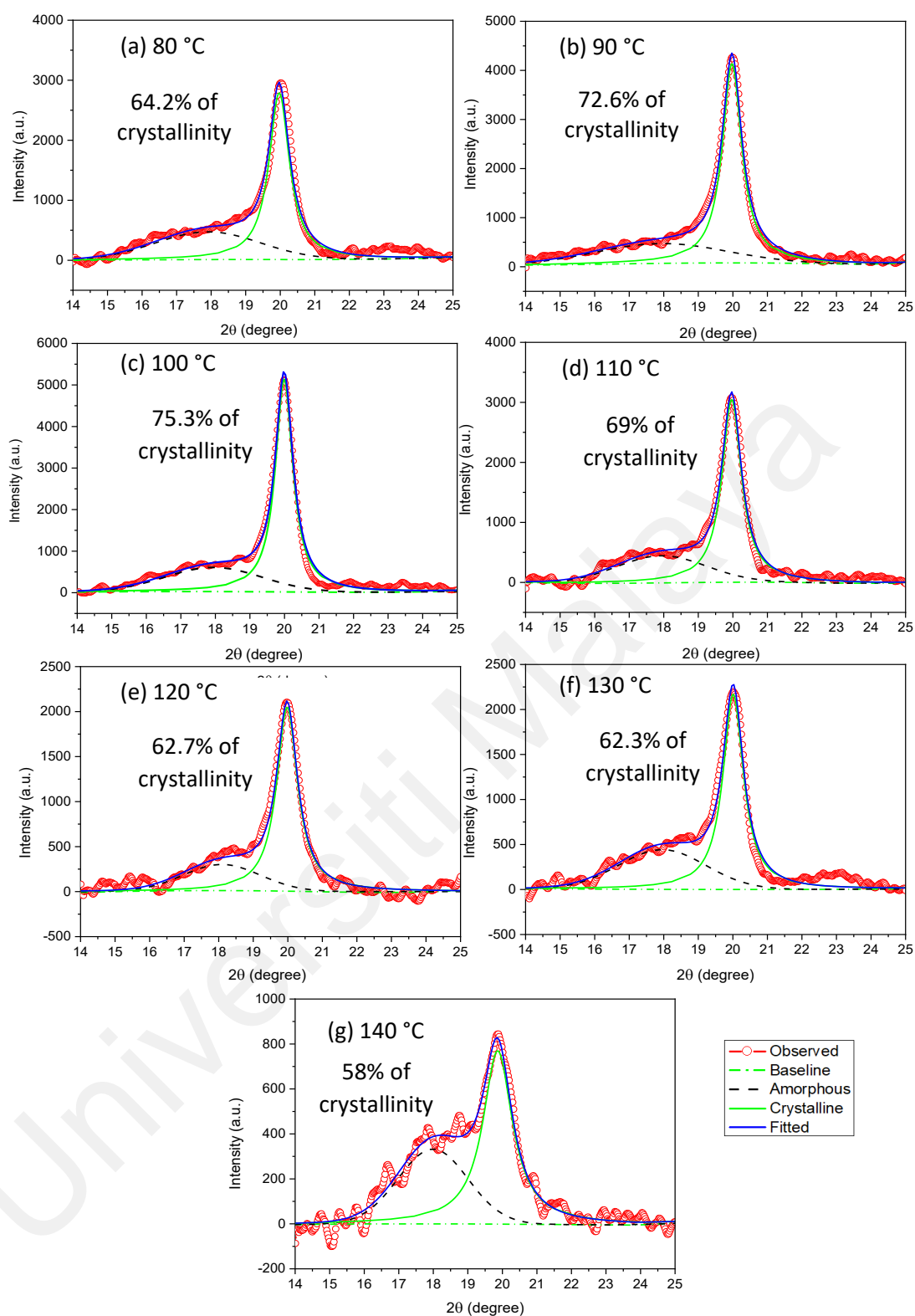
corresponding crystal planes, which is related to the degree of crystallinity. The crystal structure of P(VDF-TrFE) is normally affected by the annealing process (Mao et al., 2011). Figure 4.1 depicts the X-ray diffraction patterns of 75/25 copolymer P(VDF-TrFE) films deposited on silicon substrates at various annealing temperatures. In all crystalline samples, the (110)/(200) peak at  $2\theta = 19.9^\circ$  corresponds to the  $\beta$  phase orientation planes remains conspicuous (Cheon et al., 2018; J. Choi et al., 2000; Choi et al., 2010; Fu et al., 2016). The unit cell in the  $\beta$  crystal phase of P(VDF-TrFE) is orthorhombic, which has an all-*trans* (TTT) planar zigzag chain conformations perpendicular to the carbon chain. Each beta phase chain is aligned and packed with the CF<sub>2</sub> groups parallel to the b-axis. In P(VDF-TrFE) copolymer thin films, the intensity of a diffraction peak in Figure 4.1 is directly proportional to the degree of crystallinity of the  $\beta$  phase. The diffraction peaks become noticeably sharper as the thermal annealing temperature rises to 100 °C. However, when the annealing temperature reaches 120 °C, the absorption intensity decreases, implying that there is an optimal range of thermal annealing temperature for crystallization of P(VDF-TrFE) copolymer films. Therefore, X-ray diffraction techniques demonstrated that the annealing temperature has a strong influence on the crystallisation of P(VDF-TrFE) films. The increase in the ferroelectric  $\beta$  phase content of P(VDF-TrFE) thin film was further verified using the deconvolution technique.



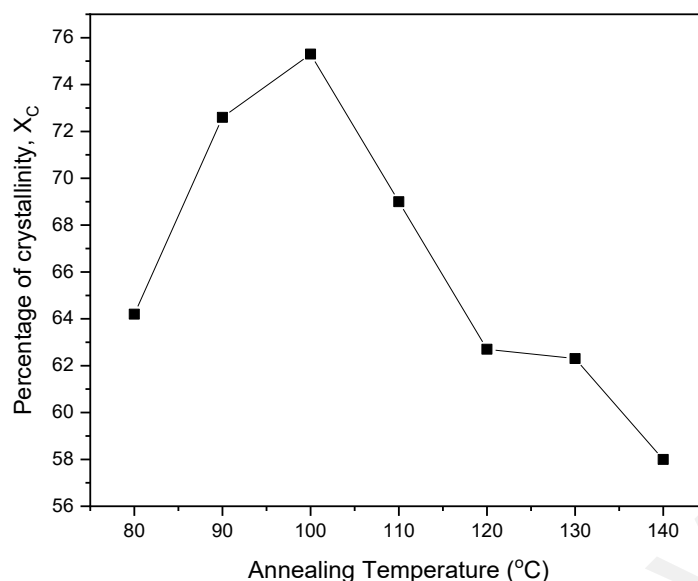
**Figure 4.1: XRD pattern of P(VDF-TrFE) films annealed at 80 °C to 140 °C with 10 °C temperature increments.**

Deconvolution of the peak for all annealing temperatures was carried out by fitting to a superposition of Gaussian functions, which made it possible to determine the integrated peak area and to refine the peak position. Figure 4.2(a)-(g) represents the deconvolution of XRD spectra for annealed P(VDF-TrFE) films at temperatures ranging from 80 °C to 140 °C. The patterns of deconvolution spectra were consistent across all annealing temperatures.

The results of the deconvolution analysis were extracted and shown in Figure 4.3. This indicates that the percentage of crystallinity,  $X_c$ , was high in the annealing temperature ranges of 90 °C to 10 °C, which is close to the Curie point. However, above the annealing temperature of 100 °C, the  $\beta$  phase crystallization is retarded, with  $X_c$  decreasing dramatically as the annealing temperature rises. The optimal annealing temperature is around 100 °C, which produces a crystallinity of 75.3% in the P(VDF-TrFE) thin film. Therefore, the annealing temperature has a significant influence on the crystallization of the  $\beta$  phase, which is consistent with other reported work (Fu et al., 2016).



**Figure 4.2: Peak fitting and deconvolution of XRD curve for P(VDF-TrFE) thin films at different annealing temperature (a) 80 °C (b) 90 °C (c) 100 °C (d) 110 °C (e) 120 °C (f) 130 °C (g) 140 °C.**

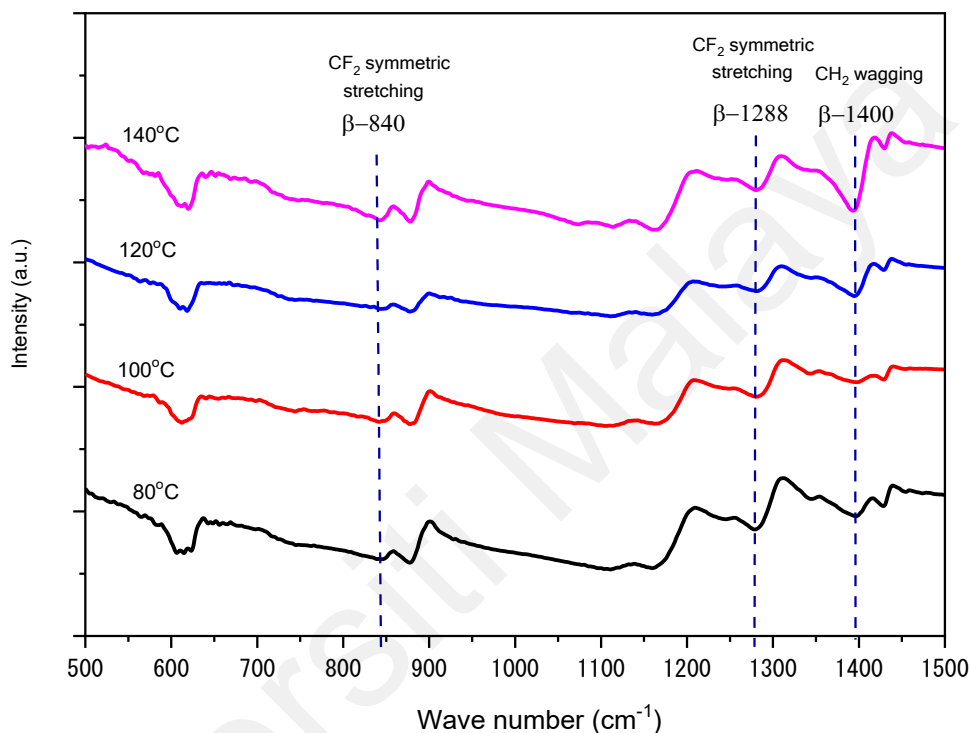


**Figure 4.3: Dependence of the percentage of the crystalline structure as a function of annealing temperature.**

#### 4.2.2 FTIR analysis

FTIR studies were carried out to investigate the  $\beta$  phase formation due to the chosen annealing temperature. Infrared spectroscopy reveals the fact that the molecule's electrical dipole moment changes during rotation or vibration at certain frequencies that correspond to discrete energy levels. A change in the bond length (stretching) or the bond angle (bending) causes the molecules to vibrate. Some bonds can stretch in-phase (symmetrical stretch) or out of phase (asymmetrical stretch). As shown in Figure 4.4, three characteristic absorption bands of the crystalline  $\beta$  phase or the all-trans ferroelectric phase together with vibrational modes were identified at  $840\text{ cm}^{-1}$ ,  $1288\text{ cm}^{-1}$  and  $1400\text{ cm}^{-1}$ . The bands of  $840\text{ cm}^{-1}$  and  $1288\text{ cm}^{-1}$  are assigned to the  $\text{C-F}$  symmetrical stretching with dipole moments parallel to the polar b-axis in the orthorhombic unit cell (Arshad et al., 2019); while the band at  $1400\text{ cm}^{-1}$  is assigned to the  $\text{C-C}$  stretching and wagging vibration of  $\text{CH}_2$  with the dipole moment along the c-axis (Valiyaneerilakkal et al., 2017). When the copolymer thin films were annealed at  $80\text{ }^\circ\text{C}$  and  $100\text{ }^\circ\text{C}$ , the high thermal energy allowed the polymer chains to reorient and align parallel to the substrate, as indicated by the IR absorption at  $840\text{ cm}^{-1}$  and  $1288\text{ cm}^{-1}$ . However,

when the thin films were annealed at elevated temperatures of 120 °C and 140 °C, which is closer to the melting point, the intensity of the IR absorption at 1400 cm<sup>-1</sup> increases, suggesting that the polymer chains are starting to rotate and partially align themselves normally to the substrate. The rotation has resulted in a decrease in the  $\beta$  phase crystalline region of P(VDF-TrFE) copolymer films (Mao et al., 2011).

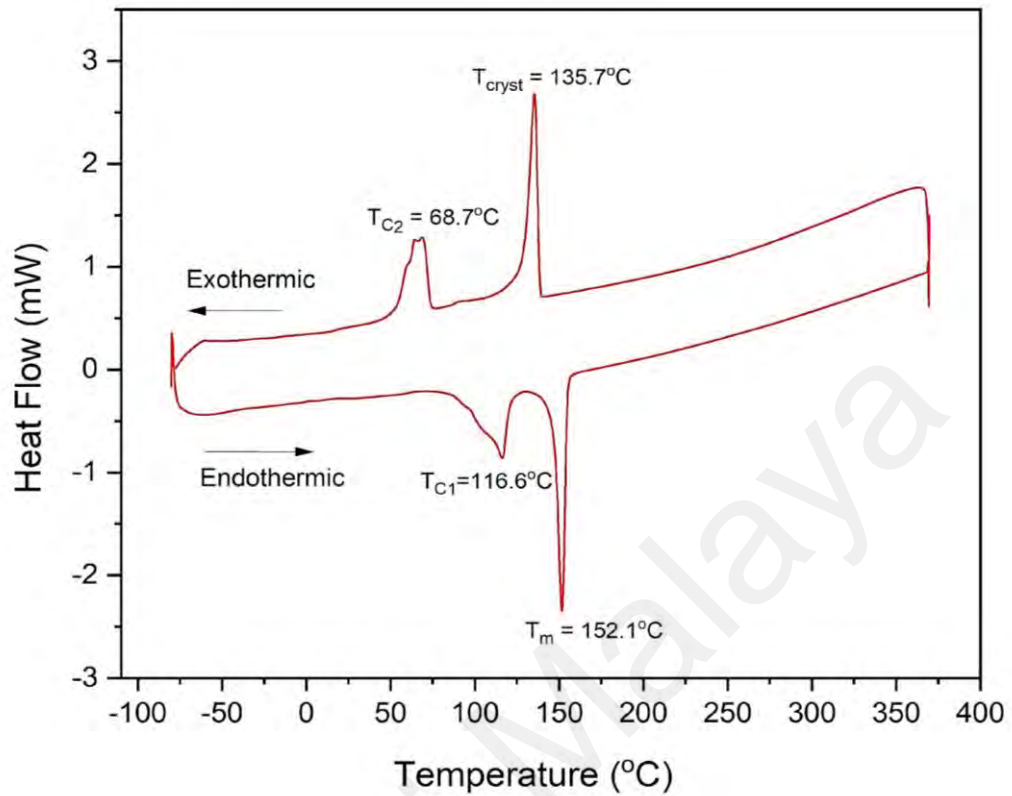


**Figure 4.4: FTIR absorbance spectra of P(VDF-TrFE) at the different annealing temperatures.**

### 4.2.3 DSC analysis

The DSC analysis of the cast film made of P(VDF-TrFE) (75/25) was carried out by increasing the temperature from -40 °C to 200 °C and then decreasing it again to -40 °C. Both the heating and cooling rates were  $\pm 10$  °C/min. The influence of the annealing temperature on the ferroelectric-paraelectric transition and the melting behaviour of the samples were investigated and shown in Figure 4.5. Initially, the film annealed at 80 °C was subjected to DSC measurement up to its minimum temperature of -100 °C in order

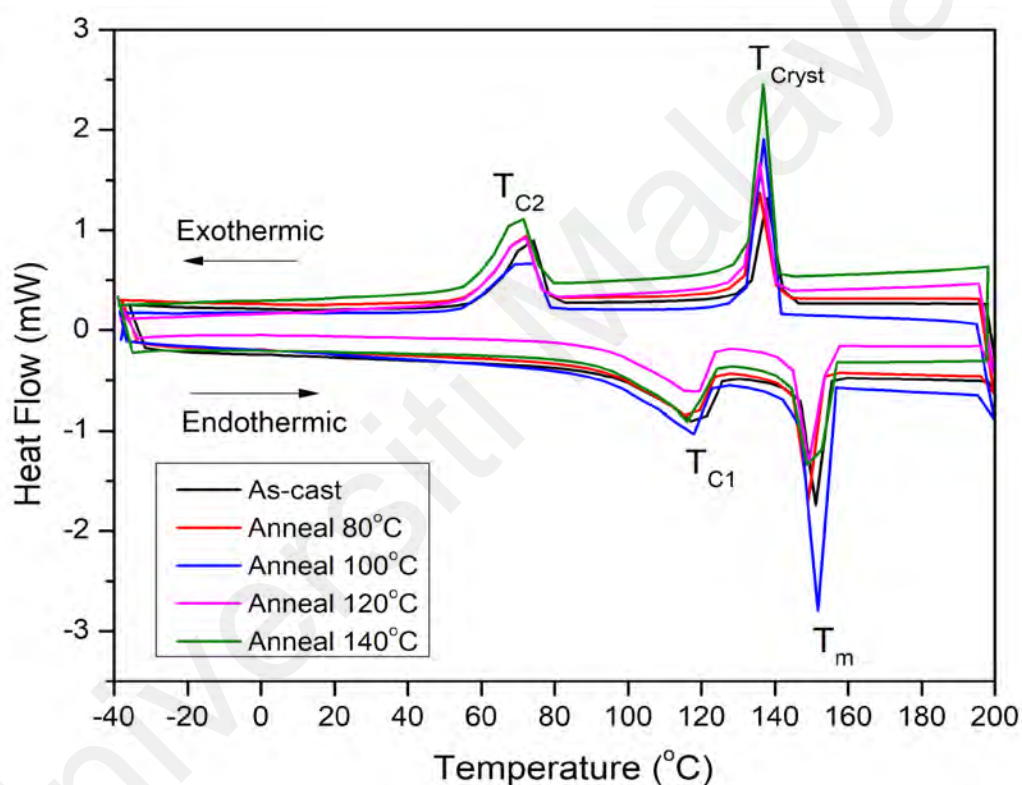
to observe  $T_g$  but no peak appeared during the endothermic process as shown in Figure 4.5. Therefore, the DSC scan was set to a minimum temperature of -40 °C for all other samples.



**Figure 4.5: Differential scanning calorimetry (DSC) thermogram of annealed P(VDF-TrFE) 72/25 at 80 °C.**

For all films, two endothermic peaks are identified during the heating (endothermic) process, ranging from 116.8 °C to 121.4 °C and 148.7 °C to 152.9 °C, respectively (refer Figure 4.6). The lower temperature peak corresponds to the Curie temperature  $T_{C1}$ , at which the copolymers showed a Curie transition from the ferroelectric (FE) phase to the paraelectric (PE) phase. The higher temperature peak corresponds to the melting temperature  $T_m$ . This FE-PE phase transition is associated with the crystalline phase change from the polar phase to the non-polar phase and the copolymer conformation changes from all-trans to trans-gauche (Bharti & Zhang, 2001; Poulsen & Ducharme, 2010). During the cooling (exothermic) the P(VDF-TrFE) films showed peaks at  $\sim 138.1$  °C to  $135.8$  °C and  $\sim 74.6$  °C to  $67.7$  °C, which is the crystallization temperature  $T_{cryst}$  and the Curie temperature  $T_{C2}$  (Arifin & Ruan, 2018; Roggero et al., 2017). The  $T_{C2}$  peak represents the PE-FE phase transition. Figure 4.6 also

shows that the FE-PE phase transition occurred at a higher temperature when heated than the PE-FE phase transition when cooling, which Furukawa (1997) stated as the first-order transition (Furukawa, 1997). When the annealing temperature is increased to a higher value up to 100 °C, the intensity of the Curie and melting peaks increases due to the increase in the crystallinity of the thin films. Both cast and all annealed P(VDF-TrFE) films show no obvious glass transition in the DSC thermogram, hence the glass transition temperature  $T_g$  cannot be determined from these spectra.



**Figure 4.6: Differential scanning calorimetry (DSC) thermogram of as-cast and annealed P(VDF-TrFE) 72/25.**

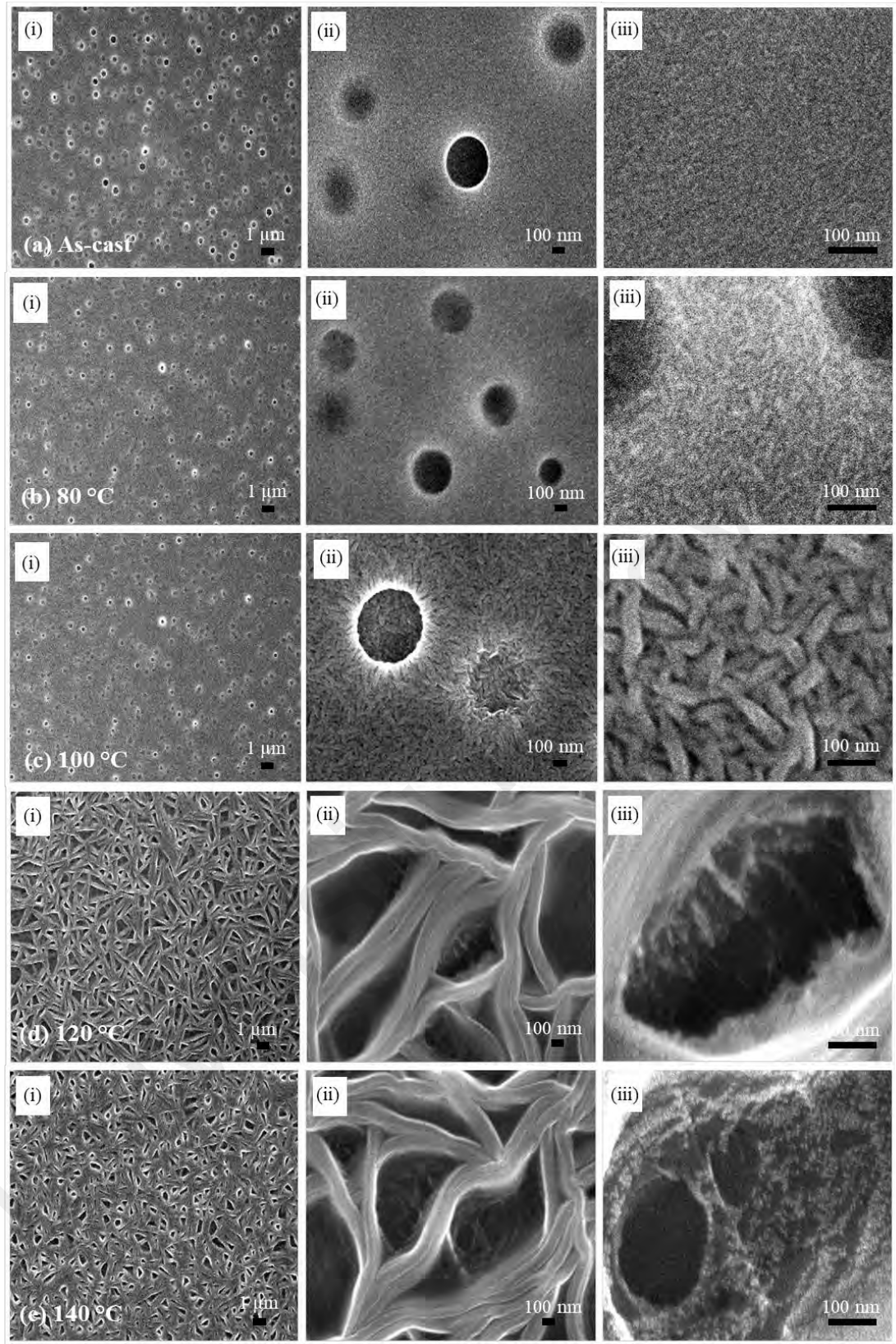
#### 4.2.4 FESEM analysis

The morphology of the copolymer was investigated using FESEM technology with a magnification of 5 k to 200 k and a resolution of 1  $\mu\text{m}$  to 100 nm. Figure 4.7(a) to (e)((i), (ii) and (iii)) show the FESEM surface images of the cast (without annealing treatment) and annealed copolymer P(VDF-TrFE) layers on Si substrates. The surface morphology of the film annealed at 80 °C and 100 °C was covered by spherical crystalline micelles embedded in

the elongated rod-shaped structures, as shown in Figure 4.7(b)(iii) and (c)(iii). The observed micellar crystalline structure of P(VDF-TrFE) as shown in Figure 4.7(a)(ii) to (c)(ii), recently reported by others works with TEM measurements (Meereboer et al., 2019; Terzic et al., 2018). The diameter of the spherical micelle-like structure increases with increasing annealing temperature from  $0.29 \pm 0.07 \mu\text{m}$  to  $0.5 \pm 0.1 \mu\text{m}$ . The distribution of the micelle-like structure is uniform in the thin film, which indicates that the polymer is completely dissolved in a very homogeneous manner since it can be observed that the micelle-like crystallites expand and grow as a function of the temperature of the heat treatment. The image observed in Figure 4.7(a)(iii) shows the high resolution of the undefined crystallite structures of the as-cast copolymer thin film. The film annealed at  $80^\circ\text{C}$  as shown in Figure 4.7(b)(iii) showed very small grains of crystallite structures, and the size was not measurable from the FESEM image. However, when the annealing temperature was raised to  $100^\circ\text{C}$ , the elongated rod-shaped crystallite structure with an average size of  $95.1 \pm 0.1 \text{ nm}$  long and  $33 \text{ nm}$  wide can be observed, as shown in Figure 4.7(c)(iii) (El Hami et al., 2001). The elongated crystallite rod-like structures are tightly packed together. They are ascribed to the  $\beta$  phase crystallites of P(VDF-TrFE). The copolymer thin film received more thermal energy when annealed at  $100^\circ\text{C}$  than when not annealed or annealed at  $80^\circ\text{C}$ . This allowed the molecular chains to reorient and align parallel to the substrate, resulting in an all-trans (TTTT) conformation. When the copolymer thin film is annealed at  $120^\circ\text{C}$ , the micelle-like crystallite disappears and the acicular crystallite is observed, as shown in Figure 4.7(d)(i). For the copolymer thin film annealed at this temperature ( $120^\circ\text{C}$ ), the average size of the acicular crystallite increases to  $1.5 \mu\text{m}$ . As the micelle-like and elongated rod-like crystallites begin to coalesce, several different structures emerge. At this  $120^\circ\text{C}$  annealing temperature, which is above the Curie point, the films were in the transition phase from ferroelectric to paraelectric, therefore the small needle-like crystallite appears in the edge-on of the large acicular crystallite structure (Lau, Liu, Chen, & Withers, 2013). The small needle-like structure can be clearly seen in the high-resolution image of Figure 4.7(d)((ii) and (iii)). When the copolymer thin film was



annealed at the higher temperature of 140 °C, as shown in Figure 4.7(e)((i)-(iii)), the length of the crystallite gradually increased to 1.8  $\mu\text{m}$  and the area in which the needle-like crystallite formed increased as the annealing temperature approaches the melting point of the copolymer. At this stage, the thermal energy absorbed by the thin film was sufficient to cause the chain axis of the molecular structure to be reoriented perpendicular to the substrate surface, and consequently the flexibility of movement increases. The existence of the micelle-like crystallites embedded on the elongated rod-like crystallites contributed to the favourable electrical properties in the copolymer thin films and this will be explained in more detail in the next section. The morphological structure of the as-cast and annealed P(VDF-TrFE) are agreeable with the results obtained from XRD, FTIR and DSC.



**Figure 4.7: FESEM microstructure of (a) as-cast and (b)-(e) annealed P(VDF-TrFE) at different temperature from 80 °C to 140 °C at magnification and resolution (i) 5 k, 1  $\mu\text{m}$  (ii) 50 k, 100 nm and (iii) 200 k, 100 nm.**

### 4.3 Ligand stabilized zinc oxide quantum dots ZnO / TEA.

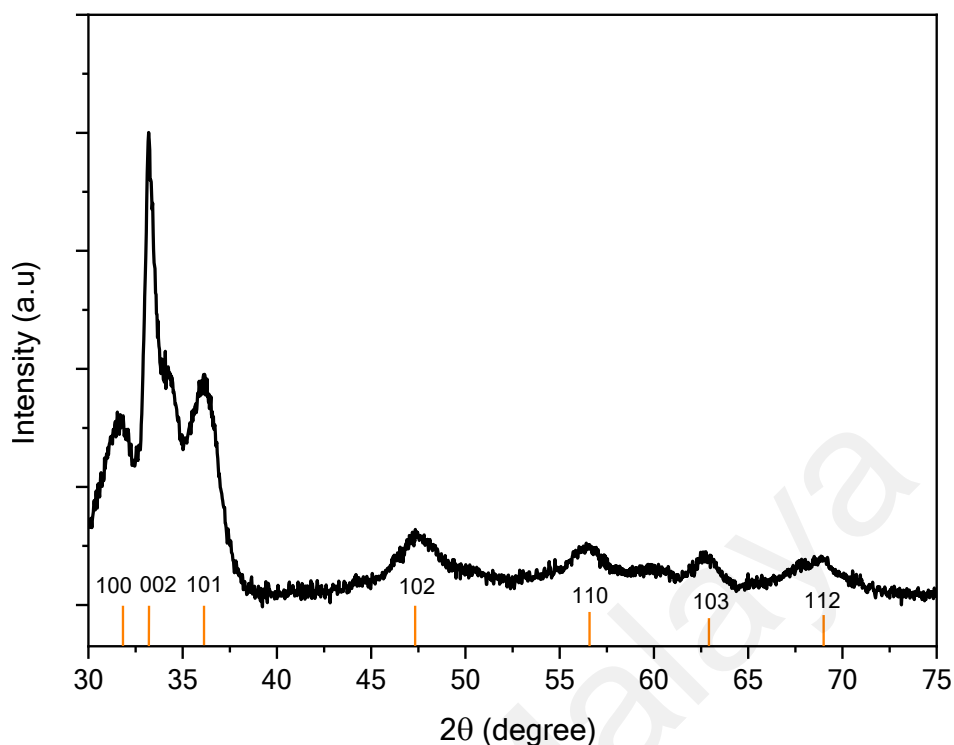
Recently, monodisperse ZnO QDs stabilized with triethanolamine (TEA) were produced with an average size of 2.4 nm (Adnan et al., 2017). TEA ligands tend to encapsulate the surface of ZnO, resulting in a smaller size of QDs. TEA also shows high solubility in polar solvents such as ethanol. The synthesized ZnO QDs were evaluated with XRD, UV–Vis and TEM for particle size analysis.

#### 4.3.1 XRD analysis

The X-ray diffraction patterns of the as-grown ZnO QD films are shown in Figure 4.8 demonstrating that all the diffraction peaks can be indexed as typical hexagonal wurtzite ZnO crystal structures. The diffraction peaks of hexagonal wurtzite ZnO at scattering angles ( $2\theta$ ) correspond to (100), (002), (101), (102), (110), (103) and (112) crystal planes. According to Debye–Scherrer formula (4.1),

$$D = \frac{K\lambda}{(\beta \cos \theta)} \quad (4.1)$$

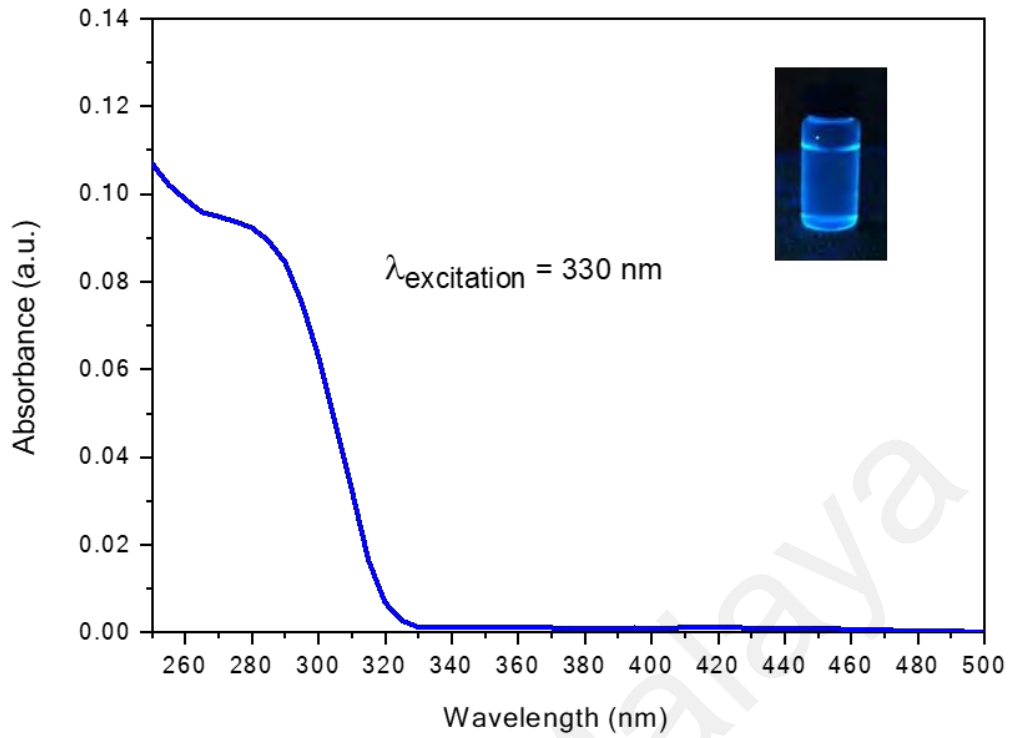
where  $D$  is the crystallite size,  $K$  is Scherrer's coefficient equal to 0.89,  $\lambda$  is the wavelength of X-rays (1.54056 Å),  $\beta$  is the full width at half maximum and  $\theta$  is the Bragg's angle. The average crystallite size,  $D$  of synthesized ZnO QDs using the Scherrer equation at crystal planes (002), (101) and (103), respectively, is  $2.0 \pm 0.5$  nm which was further verified by the TEM image. The wurtzite ZnO structure is composed of two interpenetrating hexagonal close-packed (hcp) sublattices and made up of alternating planes of  $\text{Zn}^{2+}$  and  $\text{O}^{2-}$  ions that are tetrahedrally coordinated along the threefold  $c$ -axis in fractional coordinates (Geurts, 2010). The wurtzite structure consists of a hexagonal unit cell with two lattice parameters  $a = 3.25$  Å and  $c = 5.21$  Å.



**Figure 4.8: X-ray diffraction pattern of wurtzite crystalline ZnO QDs on a glass substrate.**

#### **4.3.2 UV-Vis analysis and determination of ZnO / TEA bandgap**

The UV-Vis absorption spectra of ZnO QDs capped with TEA and dispersed in ethanol is presented in Figure 4.9. It shows that the optical absorption spectra of ZnO have an absorption edge 321 nm in the ultraviolet region with the absorption maxima at 281 nm. The inset in Figure 4.9 is the photograph of the as-synthesized ZnO QDs capped with TEA under a UV lamp (365 nm). The blue luminescence light (the inset figure in Figure 4.9) is observed, which is simultaneously evidenced by the blue-shifted absorption edge at 321 nm in Figure 4.9 assigned to the ZnO QDs compared to the bulk material at 370 nm (Farzana et al., 2018).



**Figure 4.9: Optical absorption spectra for ZnO quantum dots capped with TEA. The inset figure is the photoemission color of the as-synthesized ZnO QDs capped with TEA under a UV lamp.**

For a direct bandgap semiconductor of ZnO, the bandgap energy can be expressed by Equation (4.2),

$$(\alpha h\nu)^2 = A(h\nu - E_g) \quad (4.2)$$

where the absorption coefficient ( $\alpha$ ) near the absorption edge is related to the excitation energy ( $h\nu$ ),  $A$  is the edge-width parameter and  $E_g$  is the optical bandgap energy. The band gap was calculated using an extrapolating method (Tauc approach) which requires the absorption spectra of ZnO QDs. Figure 4.10 depicts the extrapolation of the linear part in the  $(\alpha h\nu)^2$  vs  $h\nu$  curves of the sample and the intersection of the dashed line with the  $h\nu$  axis gives the value of the optical energy bandgap. The obtained bandgap is 3.81 eV. The energy bandgap is comparable with the results presented by Asok et al. (2012) at a particular range of the molar ratio of ZnO / LiOH. The band gap increases with decreasing particle size due to nanoscale electron confinement, the so-called quantum size effect. When the particle size reaches the

nanoscale, where each particle consists of only a very small number of atoms or molecules, the number of overlaps of orbitals or energy levels decreases, and the width of the band becomes narrower. This leads to an increase in the energy gap between the valence and conduction bands.

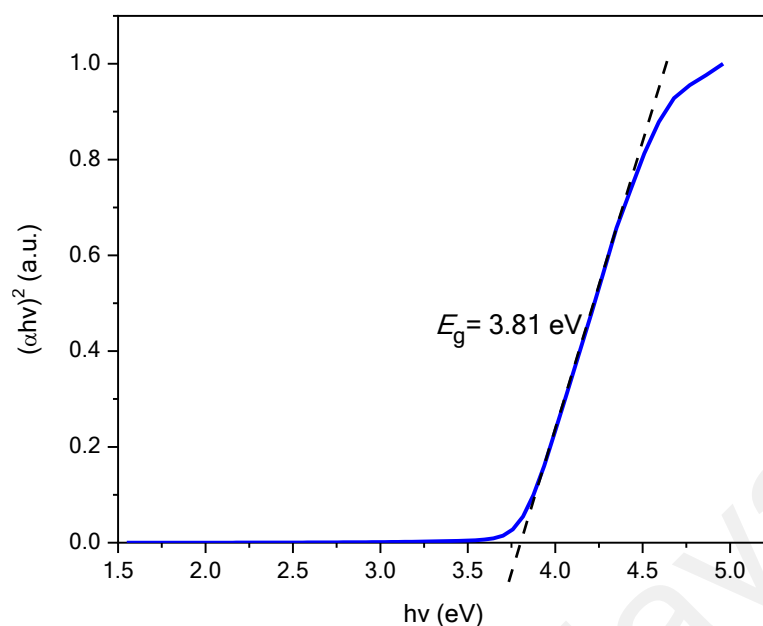
The average particle size can be determined from the absorption onset of UV-Vis absorption spectra (Figure 4.9) by using effective mass model (Brus 1986; Berger, 1996) where the bandgap  $E^*$  can be approximated by Equation (4.3):

$$E^* = E_{g,bulk} + \frac{h^2\pi^2}{2er^2} \left( \frac{1}{m_e^*m_o} + \frac{1}{m_h^*m_o} \right) - \frac{1.8e}{4\pi\epsilon\epsilon_0r} - \frac{0.124e^3}{h^2(4\pi\epsilon\epsilon_0)^2} \left( \frac{1}{m_e^*m_o} + \frac{1}{m_h^*m_o} \right)^{-1} \quad (4.3)$$

where  $E_{g,bulk}$  is the bulk bandgap in eV,  $h$  is Planck's constant,  $r$  is a particle radius,  $m_e^*$  is the electron effective mass,  $m_h^*$  is the hole effective mass,  $m_o$  is free electron mass,  $e$  is the electron charge,  $\epsilon$  is the relative permittivity and  $\epsilon_o$  is the permittivity of free space. Due to relatively small effective masses ( $m_e^* = 0.26$ ,  $m_h^* = 0.59$ ) of ZnO, bandgap enlargement is expected for particles with radii less than about 4 nm (Oskam, Hu, Penn, Pesika, & Searson, 2002). Therefore, the average particle size of the nanoparticles can be determined by using the mathematical model of the effective mass approximation Equation (4.4) (Singh & Vishwakarma, 2015):

$$r(nm) = \frac{-0.3049 + \sqrt{-26.23012 + \frac{10240.72}{\lambda_p}}}{-6.3829 + \frac{2483.2}{\lambda_p}} \quad (4.4)$$

where  $r$  is radius of the particle and  $\lambda_p$  is the peak absorbance wavelength for monodispersed ZnO nanoparticles. The absorbance peak of the prepared ZnO QDs is at 281 nm, indicating that the calculated radius of ZnO quantum dots is 1.18 nm. Hence the particle size estimated as 2R is 2.36 nm. The obtained value is in line with XRD analysis and HRTEM analysis in Section 4.3.5.

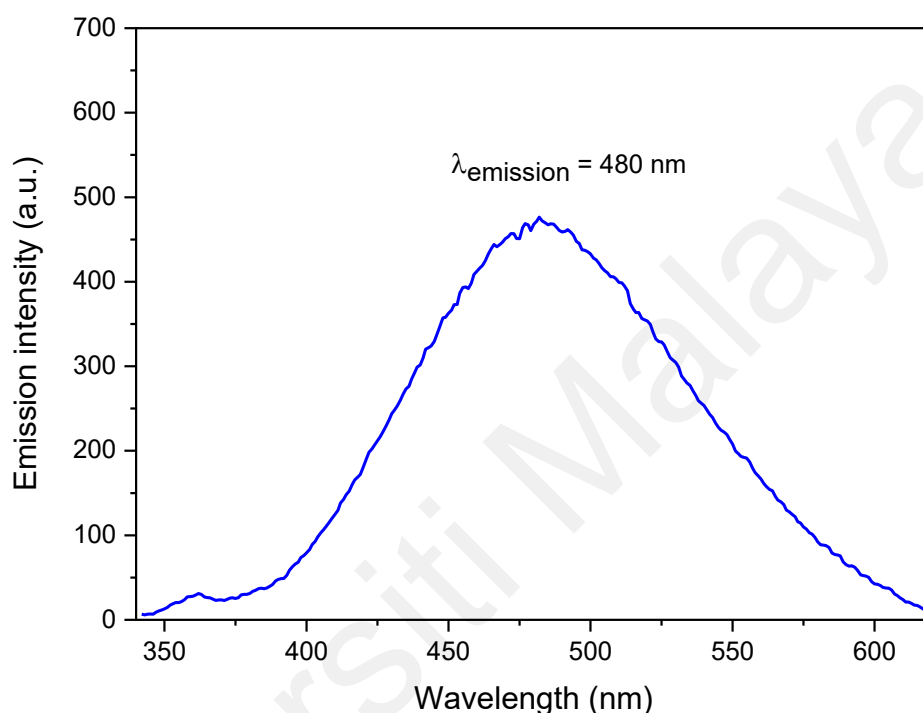


**Figure 4.10: Determination of the bandgap as the intercept between the photon energy and the extrapolation of the linear region of the square of the absorption.**

### 4.3.3 PL analysis

The photoluminescence spectra of ZnO QDs capped with TEA is shown in Figure 4.11. The emission band centred at 480 nm is obtained under the 330 nm excitation band confirming the blue luminescence obtained from the ZnO QDs prepared in this work. The origin of visible emission of ZnO QDs present in this work can be ascribed by surface oxygen vacancies which are agreed with other reported work (Asok et al., 2012). Surface defects, such as a high surface to volume ratio and surface passivation, are caused by the binding of TEA molecules on the surface of ZnO quantum dots. Blue emission has been reported and attributed to electron transfer from the shallow donor level of the oxygen vacancies ( $E_g = \sim 2.8 \text{ eV}$ ) and the zinc interstitial ( $E_g = \sim 2.7 \text{ eV}$ ) to the valence band (Oliva et al., 2015). In addition, the introduction of TEA induced a higher emission intensity. Furthermore, the presence of LiOH precursors and amino alcohol ligands promotes the formation of oxygen vacancies. The Coulomb interactions between the partial charge of the ZnO dangling bonds at the surface of ZnO QDs and the TEA ligand hinder  $\text{Zn}^{2+}$  from diffusing through the ligands to the surface of ZnO

(Adnan et al., 2017; Schoenhalz et al., 2010). Therefore, the particle size can be controlled through surface passivated ligands. A low intensity UV emission peak appeared near 360 nm is originated from the recombination of free excitons in near-band-edge (NBE) of ZnO (Li et al., 2017). This peak is frequently attributed to the direct recombination of electrons in the conduction band and holes in the valence band (Panigraphy et al., 2012).



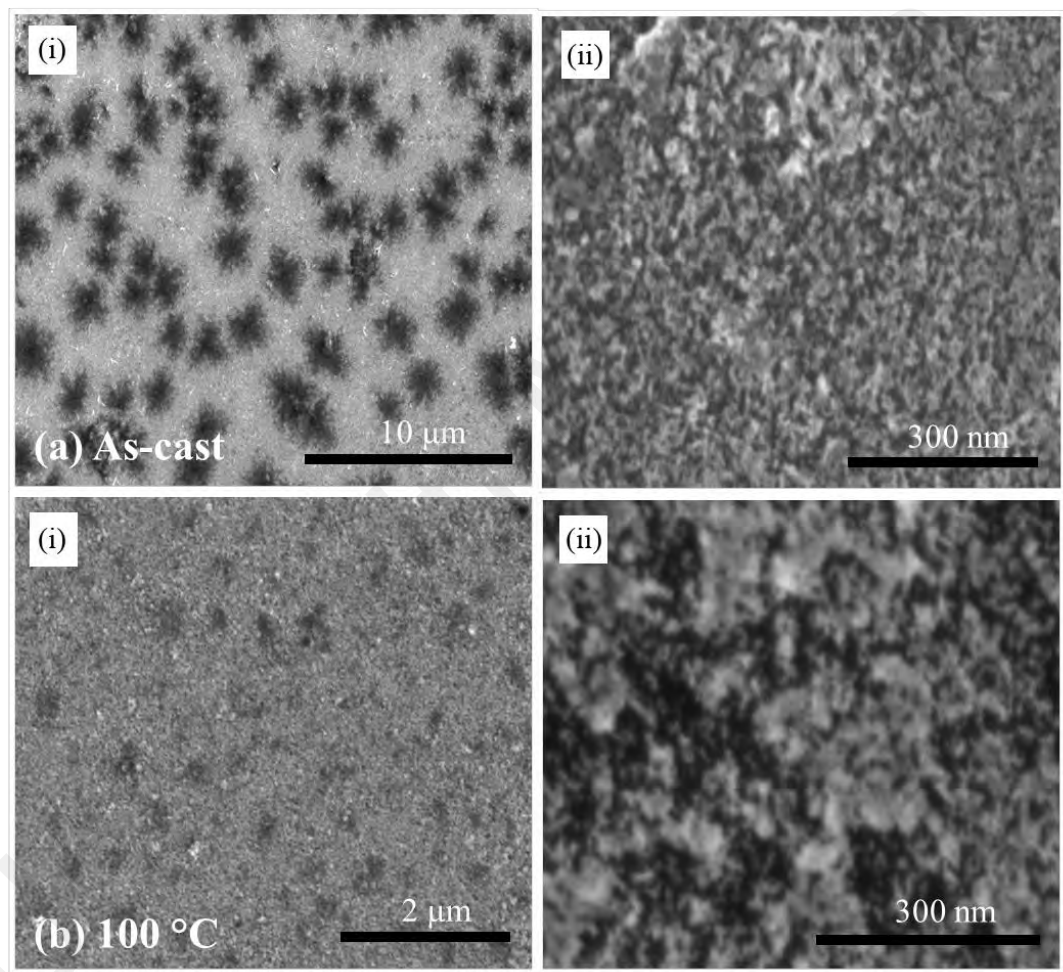
**Figure 4.11: PL spectra of ZnO QDs capped with TEA.**

#### **4.3.4 FESEM and EDX analysis**

FESEM images of the as-cast and annealed ZnO QDs are demonstrated in Figure 4.12. Nearly the same morphology of ZnO QDs at elevated magnification as shown in Figure 4.12(i)(b) and (ii)(b)) has been reported for annealed ZnO QDs prepared by the sol-gel method (Al-Asedy et al., 2016). Al-Asedy (2016) described that the morphology performed through FESEM shows the dot appearance and the distributions are coarsened during the annealing process at the temperature range of 425 °C to 500 °C. The dot distributions became visible with increasing annealing temperatures. The coarsening mechanism is due to the Ostwald



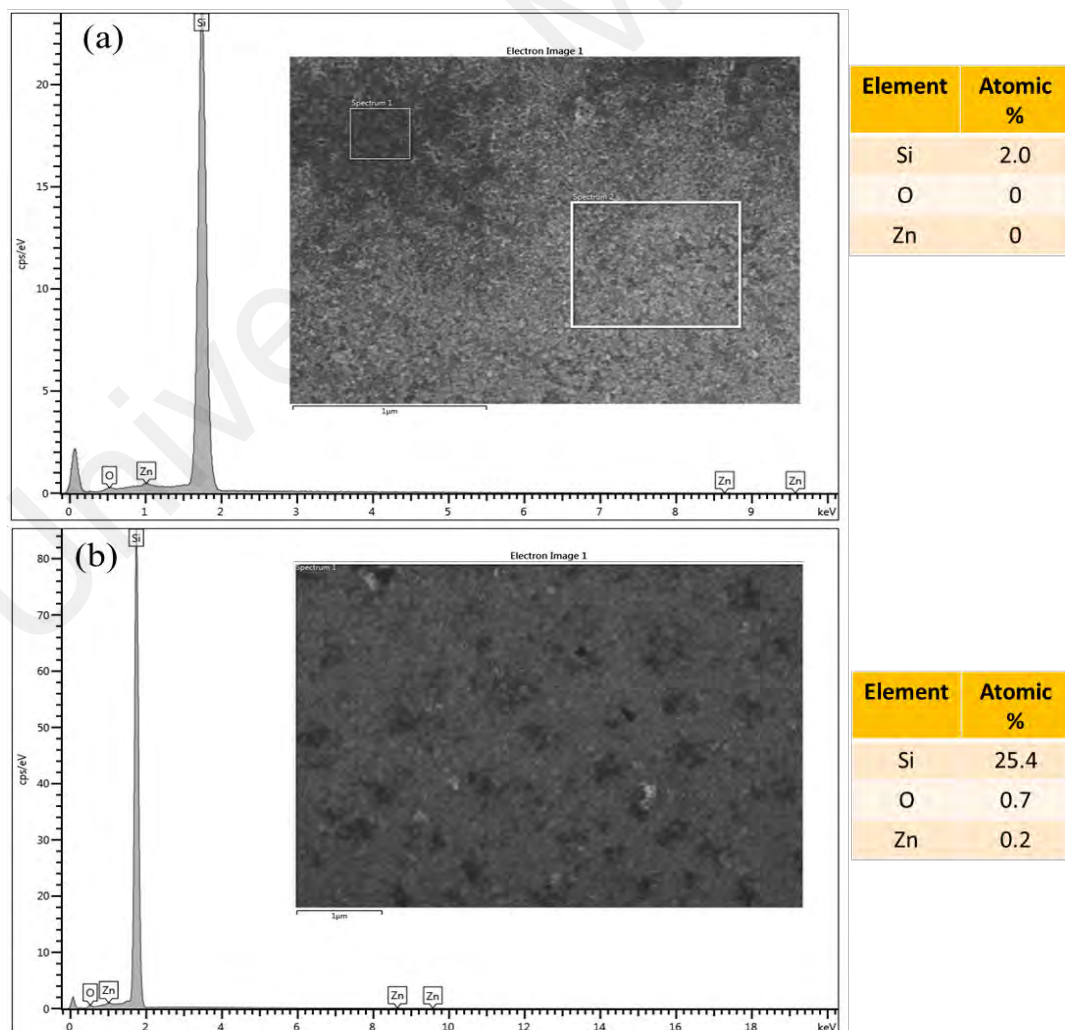
ripening which in turn increases the quantum dots size with increasing temperature. In this present work, the samples of nanocomposites P(VDF-TrFE) / ZnO QDs were subjected to an annealing process at the optimum temperature of 100 °C as the crystallinity is maximum for P(VDF-TrFE). The inclusion of TEA passivated the growth of QDs size. Therefore, the distribution or morphology of the dots is not much different between the as-cast and the annealed ZnO QDs



**Figure 4.12: FESEM images of (i) as-cast ZnO QDs and (ii) anneal ZnO QDs at 100 °C spin coat on Si wafer at different magnification and resolution.**

In order to determine the chemical composition of P(VDF-TrFE) and P(VDF-TrFE) / ZnO QDs nanocomposites (refer to Section 4.4.4), the energy dispersive X-ray (EDX) spectra were recorded. The EDX spectrum of the ZnO quantum dots is illustrated in Figure 4.13. EDX can measure the composition and amount of heavy metal ions of nanoparticles located near or on

the surface of a sample, while elements with an atomic number below 11 are difficult to detect with EDX (Scimeca et al., 2018). The EDX spectrum confirms the presence of ZnO in both the as-synthesised and annealed samples by the elemental mapping images. Al-Asedy et al. (2016) reported that the annealing process decreases the peak intensity of O due to the diffusion of Zn into the Si substrate, which creates more oxygen vacancies. In Figure 4.13, the atomic percentages of O and Zn (insert table) show zero percentages for the as-synthesized ZnO QDs and low percentages of less than 1% for the annealed ZnO QDs. However, the peak intensities of Zn and O in both samples are almost similar. The excess oxygen percentages demonstrate that the Si substrate and Zn are both responsible for the emergence of the O peak in the annealed ZnO QD sample, which has a Zn/O atomic percentage ratio that is greater than 1. Therefore, the ratio of atomic % of Zn to O from EDX cannot be used to conclude the existence of oxygen vacancies in the thin film.



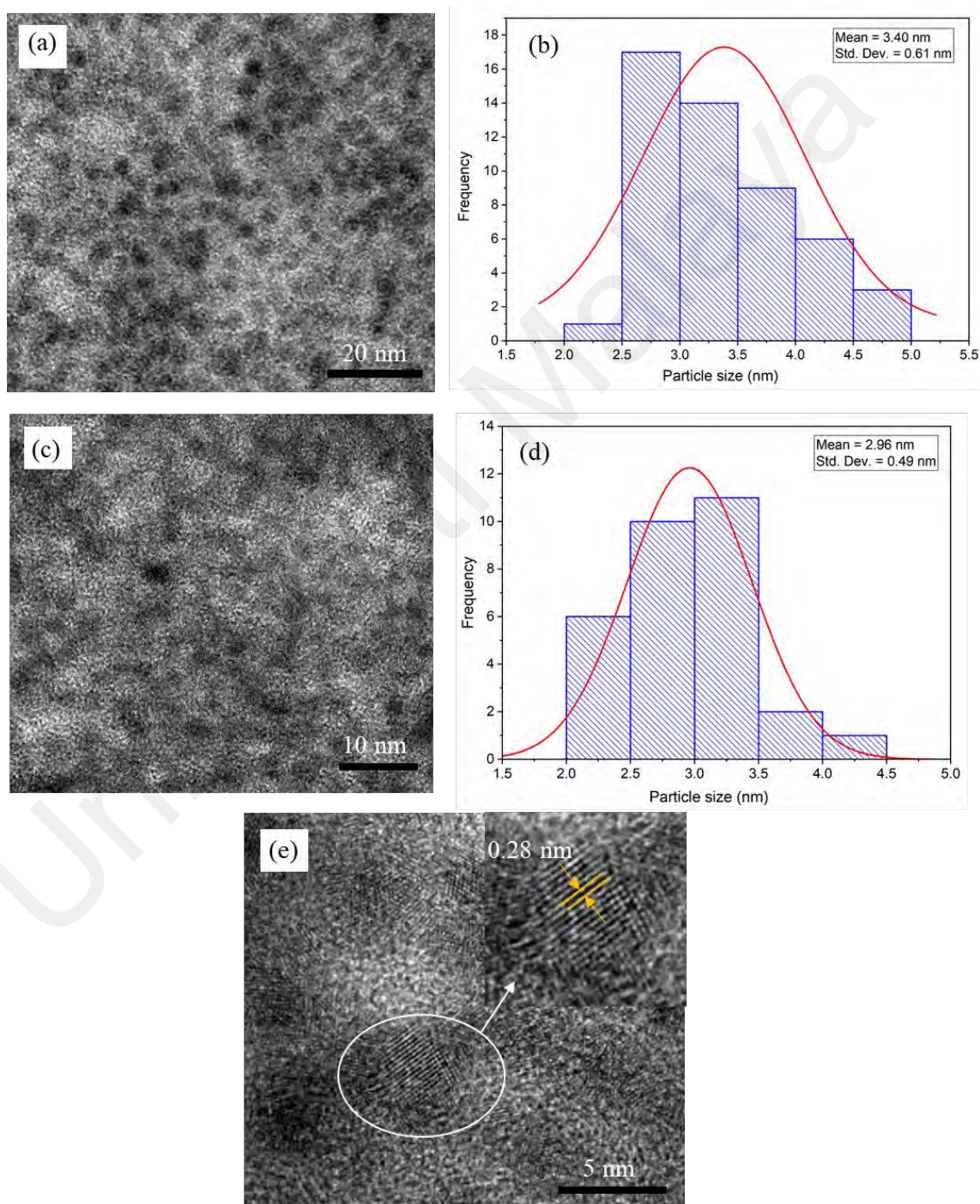
**Figure 4.13: EDX spectra of (a) as-cast ZnO QDs and (ii) anneal ZnO QDs.**

#### 4.3.5 TEM analysis

The corresponding TEM image of ZnO / TEA QDs are in a quasi-spherical shape with a particle distribution of  $3.4 \pm 0.6$  nm and  $3.0 \pm 0.5$  nm as shown in Figure 4.14(a) to (d) together with their histogram distribution, respectively. The HRTEM image (see Figure 4.14(e)) shows lattice fringes with a spacing of  $0.28 \pm 0.03$  nm spacing which corresponds to the (100) plane of the hexagonal wurtzite structure (Adnan et al., 2017). The interplanar spacing deduced from the line profile of the QDs is very close to the spacing of (100) planes in the hexagonal wurtzite structure of ZnO (Adnan et al., 2017; Zhang et al., 2021). The particle size analysis through UV-Vis, XRD and TEM confirmed the QDs size obtained in this work is in the range of 2-3.5 nm. The TEM pattern of ZnO QDs presented in this work shows resemblances with other work on the sol-gel technique (Adnan et al., 2017; Zhang et al., 2021), wet chemistry method (Fonoberov et al., 2006) and spray pyrolysis method (Rajappan-Achary et al., 2011). As an aminoalcohol ligand, TEA can interact with the surface of ZnO QDs via amine ( $-NH$ ) and hydroxy ( $-OH$ ) groups. Because of its large number of hydroxy branches, TEA has a strong steric effect. According to Adnan et al. (2017), the stability of TEA-capped ZnO QDs results from a combination of steric and electronic effects that facilitates the formation of ultrasmall, monodisperse ZnO QDs via a digestive ripening process.

Differences in particle size analyzed using Brus' model from UV-Vis and TEM images may have various causes. While TEM is an experimental method that directly images nanoparticles, Brus' model is usually used to refer to a theoretical model used to estimate the size of nanoparticles based on their optical properties. Here are a few explanations for the differences: TEM physically measured ZnO quantum dots capped with a TEA ligand, therefore the size is greater than the measurement performed by theoretical calculation of the Brus model. Furthermore, ligands may not contribute to the peak absorption in the calculation of the Brus model. As a result, TEM measurements show a slightly larger size. On the other hand, the Brus model makes several assumptions about the nanoparticles, including their spherical shape, uniform composition, and a clearly defined dielectric constant. It also

assumes that the nanoparticles are individual and non-agglomerated. Therefore, comparing the results from various methods can help validate and refine the size measurements of the QDs presented in this work. In addition, the spherical shape of TEM images of as-synthesized ZnO QDs presented in this work are quite blurry possibly due to the instrument's limitation factor. Therefore, it is essential to accurately analyze the particle size at least from two distributions as depicted in Figure 4.14(a) and (c).



**Figure 4.14: TEM micrograph (a) and (c) and histogram (b) and (d) of particle size distribution for ZnO QDs and (e) the lattice fringe of ZnO QDs wurtzite plane.**

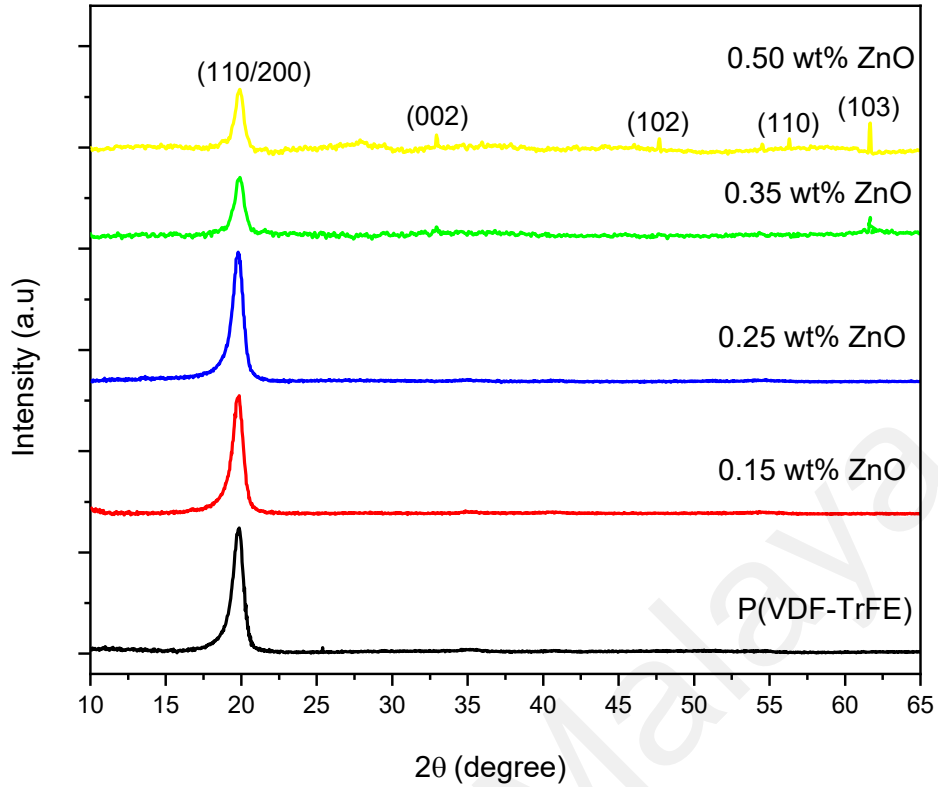
#### 4.4 Nanocomposite films with various weightage percentages of ZnO QDs

The dried solid ZnO QDs were dispersed in polymer solution to form 5 wt% of nanocomposites of P(VDF-TrFE) / ZnO QDs with various weightage percentages; 0, 0.15, 0.25, 0.35 and 0.50. Nanocomposite films were annealed at 100 °C which is close to Curie temperature to form a highly crystalline structured film. Chen et al. (2011) reported that annealing wurtzite ZnO QDs without doping any element in nitrogen, vacuum, and air increased the size of ZnO QDs and a reduction in their photoluminescence. This indicates that the diameter increases of the ZnO QDs after annealing had a larger influence on their emission intensity than the enhancement of their crystallinity (Chen et al., 2011). The structural and morphological studies of nanocomposite films were presented in subsections below.

##### 4.4.1 XRD analysis

Figure 4.15 shows the XRD pattern of the P(VDF-TrFE) / ZnO QDs nanocomposite films with various ZnO QDs concentrations. The characteristic peak at  $2\theta = 19.9^\circ$  represents the crystalline  $\beta$  phase of P(VDF-TrFE) with (110/200) orientation plane. The unit cell of the  $\beta$  phase is orthorhombic which has been explained in detail in an earlier section (refer to Section 4.2.1). With the inclusion of ZnO QDs into the copolymer shifted the peaks slightly to the right, suggesting that the ZnO QDs act as a dopant in the polymer host. Therefore, ZnO QDs changes the polymer interstitial. The characteristic peaks of wurtzite ZnO (002), (102), (110) and (103) are only clearly visible in the nanocomposite films with 0.50 wt% of ZnO QDs (Qiao et al., 2016; Oliva et al., 2015; Jacob et al., 2014). The crystallinity of P (VDF-TrFE), based on the peak intensity at  $19.9^\circ$ , is consistent in nanocomposite films as the concentration of ZnO QDs increases to 0.25 wt%. A further increase in the QDs filler ( $> 0.25$  wt%) deteriorates the crystallinity of the films as referred to the peak intensity of P(VDF-TrFE) and is expected to impair their ferroelectric and pyroelectric properties.



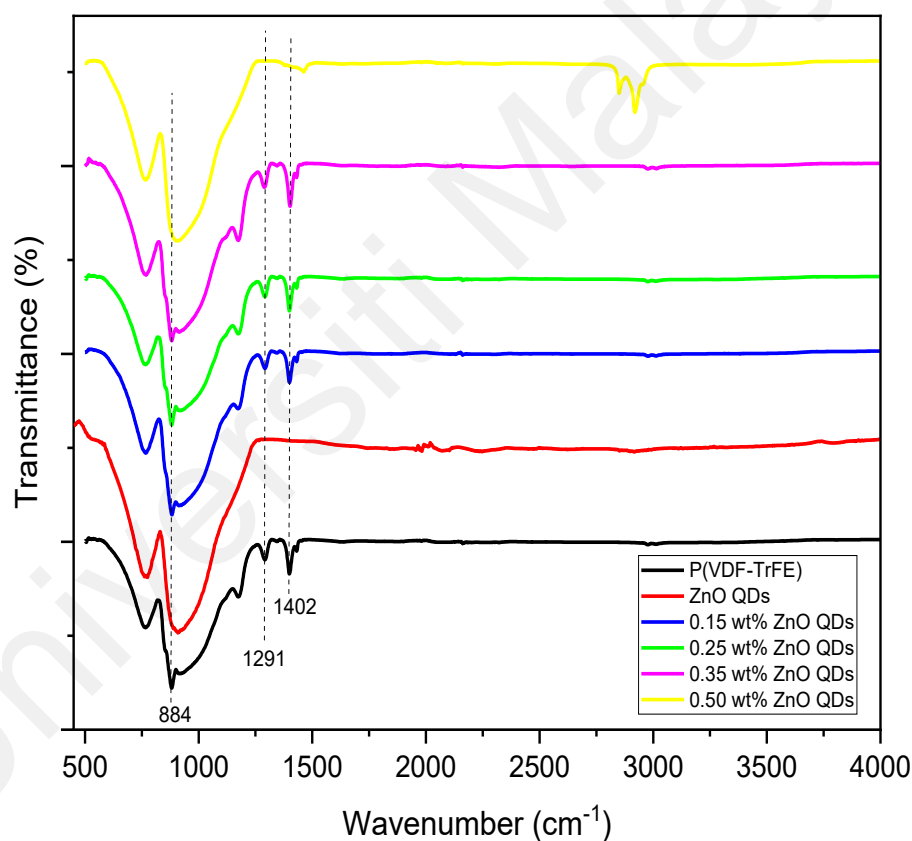


**Figure 4.15: XRD pattern of P(VDF-TrFE) and nanocomposite films with various concentrations of ZnO QDs.**

#### 4.4.2 FTIR analysis

FTIR characterization as depicted in Figure 4.16 was analyzed to explore the functional groups on the surface of the ZnO QDs and the nanocomposite films. The vibrational peaks located at  $1291\text{ cm}^{-1}$  and  $1402\text{ cm}^{-1}$  are corresponding to the  $\beta$  phase of P(VDF-TrFE). The presence of a nonpolar  $\alpha$  phase is responsible for the appearance of a vibration band at  $884\text{ cm}^{-1}$ . The assignment attributed to copolymer peaks was explained earlier in Section 4.2.2. The broad absorption band at  $550\text{ cm}^{-1}$  is due to the stretching mode of hexagonal ZnO. Contrarily, the existence of TEA on the surface of ZnO was not detected by FTIR measurements, as reported by Oliva et al. (2015), in which the TEA-associated bands are centred at  $2926\text{ cm}^{-1}$ ,  $1065\text{ cm}^{-1}$ ,  $893\text{ cm}^{-1}$  and  $613\text{ cm}^{-1}$ . Others reported that the band assigned at  $1410\text{ cm}^{-1}$  is due to asymmetric and symmetric stretching vibrations of the carbonyl group (COO–Zn coordination) (Vidhya et al., 2015). C–H groups' stretching vibration peaks are at

about 2851–2922  $\text{cm}^{-1}$  (Gayathri et al., 2015; Hosseini Largani & Akbarzadeh Pasha, 2017; Kołodziejczak-Radzimska et al., 2012). Moreover, an absorption peak at 470  $\text{cm}^{-1}$ , corresponding to the Zn–O stretching vibrations also cannot be detected due to instrument limitation. No absorption band observed around 550  $\text{cm}^{-1}$  for the nanocomposite P(VDF-TrFE) / ZnO QDs thin films. The results indicate that the incorporation of ZnO QDs into P(VDF-TrFE) with different compositions do not show any significant changes in the phase transition of the initial copolymer. This suggests that ZnO did not affect the structure or crystalline phase of PVDF-TrFE.



**Figure 4.16: FTIR spectra of copolymer P(VDF-TrFE), ZnO QDs and nanocomposite thin films.**

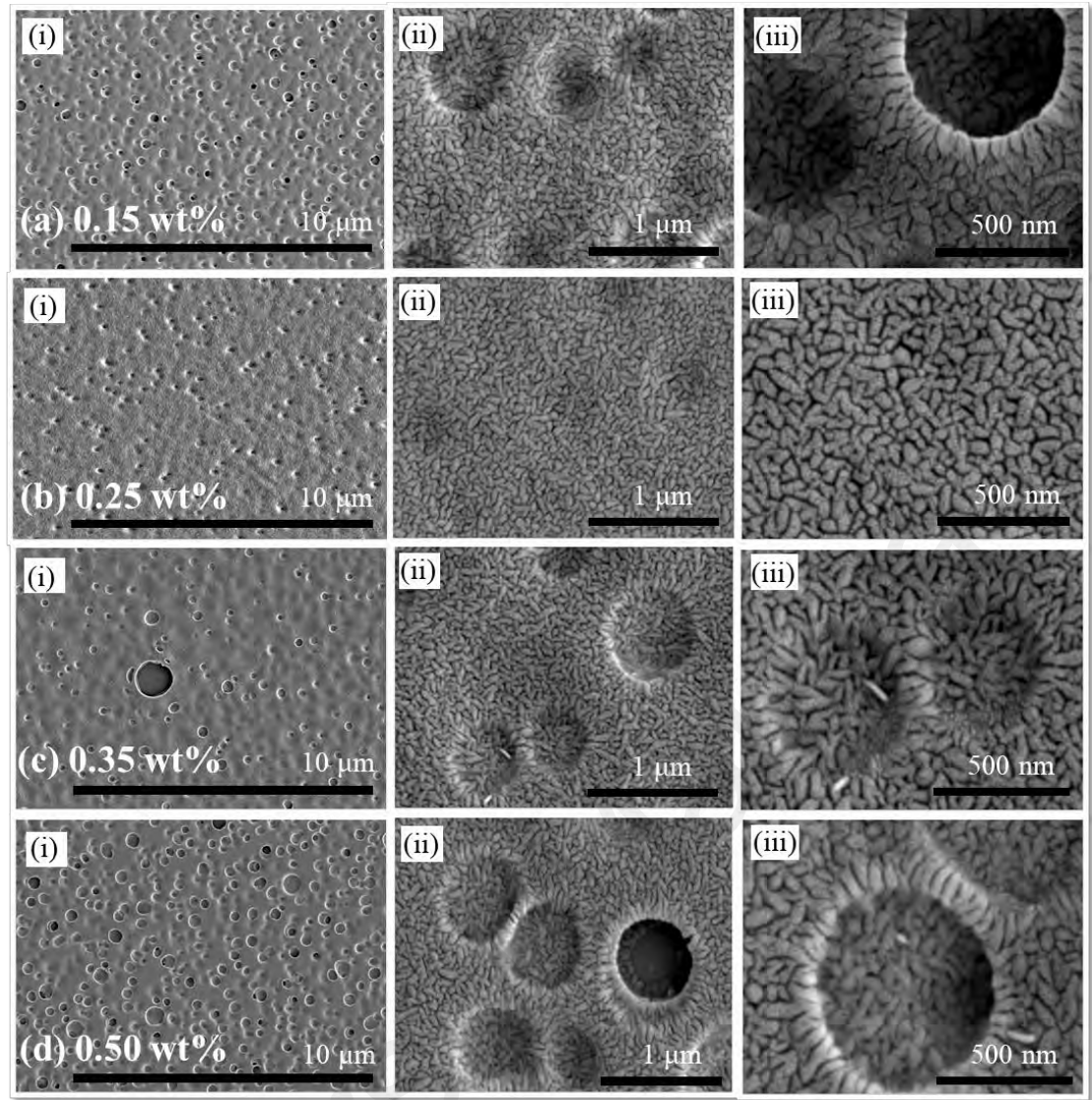
#### 4.4.3 FESEM and EDX analysis

FESEM images of the nanocomposite P(VDF-TrFE) / ZnO QDs films are shown in Figure 4.17. An annealing treatment at 100 °C significantly improves the polarization of copolymer

P(VDF-TrFE) films as indicated in our previous work (Ahmad et al, 2020). Therefore, the composite films were purposely annealed at this temperature in this work to enhance the crystallinity and to achieve a dominant  $\beta$  phase in the films. Surface morphology shows the distribution of spherically shaped crystalline micelles embedded inside the elongated rod-like structures and can be observed in all composite films as shown in Figure 4.17(a)(i)-(d)(i). Similar morphology has been reported by others which investigate the PVDF / ZnO hybrid membranes and the ‘hole’ that appeared in the morphology is called the pores structure of PVDF (Zhang et al., 2014).

As illustrated in Table 4.1, the dimensions of both spherical micelle-like structure and elongated rod-like structure were taken into consideration in findings of the correlation between morphological and polarization aspects for these nanocomposite films. Table 4.1 shows that films of 0.15 wt% assembled with the greatest average length of elongated rod-like structure among all variations of films doped with ZnO QDs. The polarization of composite films which helps in the performance of ferroelectric is most probably proportional to the length dimension of the elongated rod-like structure. The coalescence of crystallite micelle-like structure surrounded with elongated rod-like structure may get saturated at films doped with more than 0.25 wt% of ZnO QDs (see Figure 4.17((c)(i) and (d)(i)). The spherical micelle-like structure becomes a micelle-like hole structure as depicted by Zhang et al. (2014) and Figure 4.17((c)(i) and (d)(ii)) clearly show the micelle-like hole structure on the surface of Si substrate. The distribution of this saturated agglomeration was found to increase with increasing ZnO QD concentration exceeding 0.25 wt%.



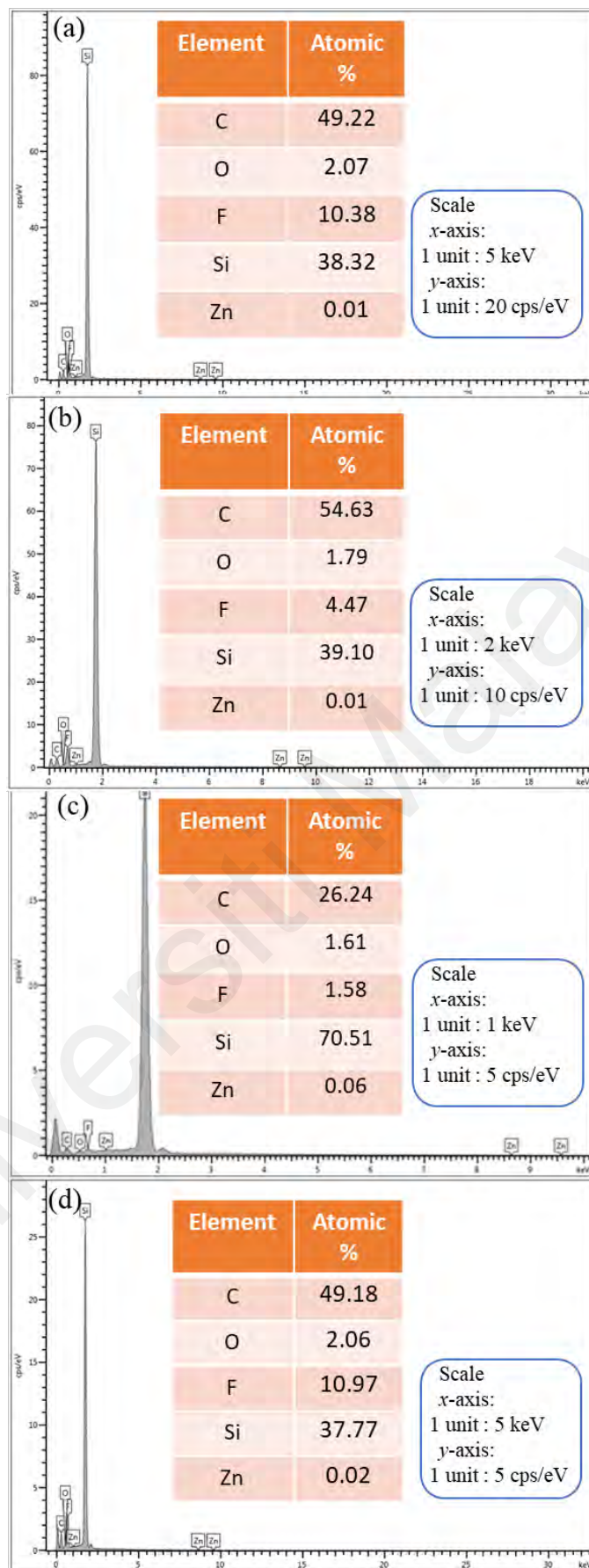


**Figure 4.17: FESEM images of P(VDF-TrFE) / ZnO QDs films anneal at 100 °C spin coat on Si wafer (a) 0.15 wt% (b) 0.25 wt% (c) 0.35 wt% and (d) 0.50 wt% with magnification and resolution of (i) 5 k, 10  $\mu\text{m}$  (ii) 50 k, 1  $\mu\text{m}$  (iii) 100k, 500 nm.**

**Table 4.1. Distribution of structures observed in nanocomposite films of P(VDF-TrFE) / ZnO.**

<b>Morphology (average)</b>	<b>0 wt%</b>	<b>0.15 wt%</b>	<b>0.25 wt%</b>	<b>0.35 wt%</b>	<b>0.50 wt%</b>
Diameter of spherical micelle-like structure ( $\pm 0.01$ )	0.51 $\mu\text{m}$	0.51 $\mu\text{m}$	0.29 $\mu\text{m}$	0.47 $\mu\text{m}$	0.57 $\mu\text{m}$
Length of elongated rod-like structure ( $\pm 0.1$ )	95.1 nm	103.9 nm	86.3 nm	97.9 nm	92.0 nm
Width of elongated rod-like structure ( $\pm 0.1$ )	32.7 nm	37.8 nm	36.5 nm	38.8 nm	40.7 nm

Energy-dispersive X-ray spectroscopy (EDX) was evaluated to determine the elemental composition of the polymer nanocomposite P(VDF-TrFE) / ZnO QDs on the Si substrate. Figure 4.18 shows the EDX spectrum of P(VDF-TrFE) / ZnO nanocomposite, which reveals the strong signals from Zn, O, C and F atoms without any impurity peaks. Furthermore, the presence of Zn, O, C, and F atoms was confirmed by the elemental mapping images and the atomic percentage of each element (insert Table) is also presented in Figure 4.18. The Zn and Si atomic wt % for 0.35 wt% thin film appear to be higher than the rest of the films due to the saturated micelle-like hole structure at which the EDX was probed, which will be explained further in Chapter 6 when surface morphology is analysed and discussed.



**Figure 4.18: EDX spectra of P(VDF-TrFE) / ZnO QDs films at (a) 0.15 wt% (b) 0.25 wt% (c) 0.35 wt% and (d) 0.50 wt%.**

## 4.5 Conclusion

The study of the annealing effect in copolymer films in the first phase of this research work shows that the polarization of copolymer P(VDF-TrFE) thin films is significantly influenced by an annealing treatment in a certain temperature range (from 80 °C to 140 °C), which can therefore contribute to the improvement of electrical performance, such as ferroelectrics, dielectric and pyroelectrics. Spin-coated copolymer P(VDF-TrFE) thin films annealed at 100 °C give the highest percentage of crystallinity (75.3%), which is further confirmed by the existence of the homogeneous micelle-like crystallites embedded on the elongated rod-like crystallites identified by FESEM measurement. The domains belong to the  $\beta$  phase of copolymer P(VDF-TrFE) which is the most dominant ferroelectric phase in the film and is attributed to the all-trans (TTTT) conformation of the polymer chain alignment. The transition phase from ferroelectric to paraelectric phase,  $T_c$  occurs at 116.8 °C. Therefore, further increment of annealing temperature above  $T_c$  which is closer to the melting point, caused the polymer chains to start to rotate and partially align normal to the substrate, hence acicular and needle-like structures were emerged and decreased the spontaneous polarization of the films.

In this study, ZnO quantum dots were incorporated into P(VDF-TrFE) to enhance its ferroelectricity and pyroelectricity. Various analyses of particle size from UV-Vis, XRD and TEM proved the size of wurtzite ZnO quantum dots synthesized in this work in the range of  $\sim 2.5$  to 3 nm. Each zinc ion is surrounded by a tetrahedron of four oxygen ions, and similarly, each oxygen ion is coordinated by a tetrahedron of four zinc ions. The arrangement of this tetrahedral coordination exhibits ZnO as a polar character, giving rise to spontaneous electric polarization,  $P_s$ . The inclusion of ZnO QDs into the polymer matrix is considered to induce local extra dipole moments. These extra local dipoles coupled with parent dipoles could induce ferroelectricity and pyroelectricity. The emergence of spherical micelle-like crystallite embedded with elongated rod-like crystallite at a concentration of ZnO QDs of more than 0.25 wt% appeared to be a micelle-like hole structure and the hole is deepened until the surface of Si substrate as clearly observed in Figure 4.17(c)(i) and (d)(ii). The distribution of this micelle-

like hole structure deteriorates the net polarization of the films and affect the performance of ferroelectric and pyroelectric of composite films, which will be explained further in the Chapter 5.

Universiti Malaya

## CHAPTER 5: FERROELECTRIC PROPERTIES OF COPOLYMER P(VDF-TrFE) AND NANOCOMPOSITE THIN FILMS OF P(VDF-TrFE) / ZnO QDs

### 5.1 Introduction

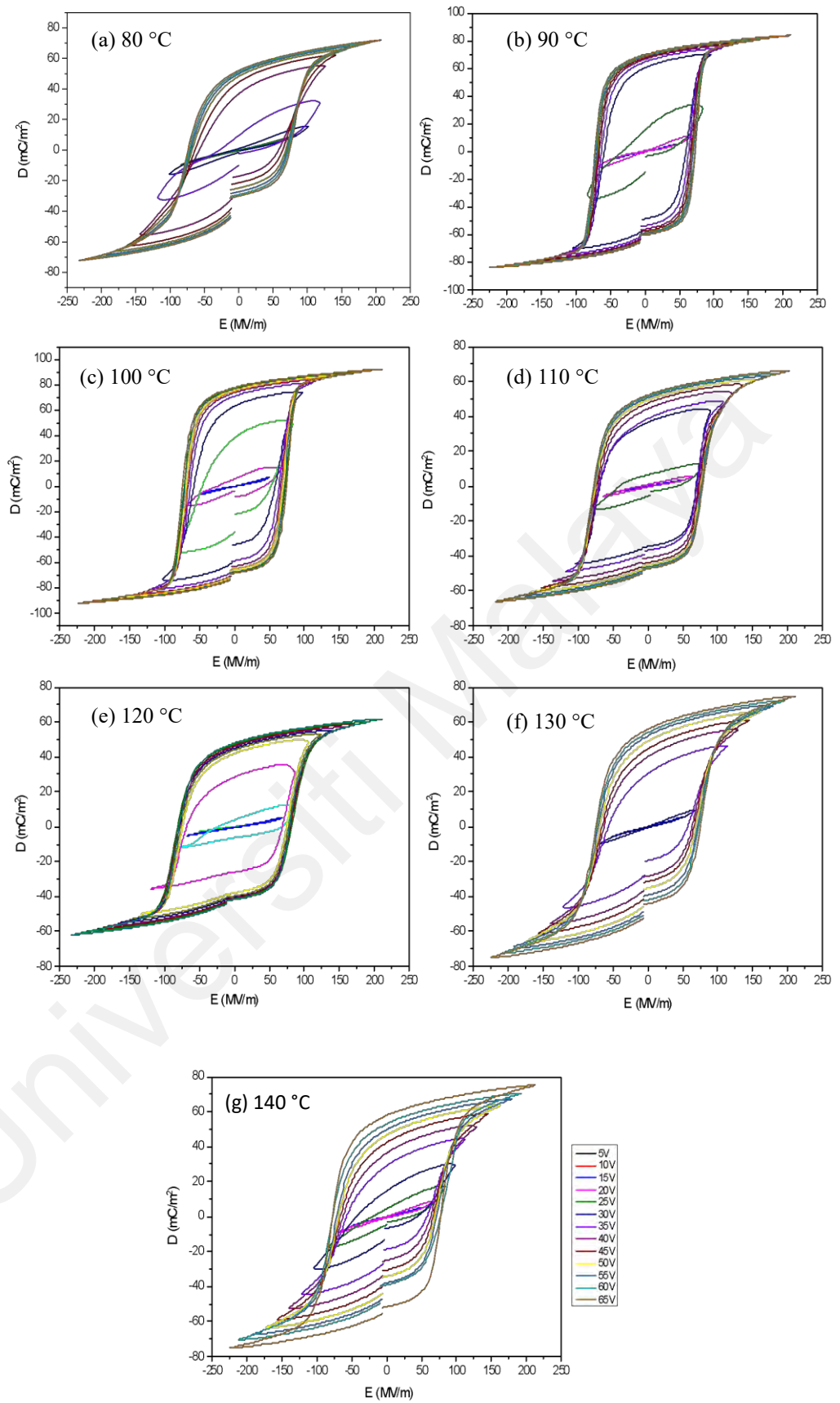
In this chapter, the ferroelectric characterization of the copolymer and composite films of P(VDF-TrFE) / ZnO QDs was presented. The analysis from the polarization hysteresis loop ( $D$ - $E$ ) gives the properties of remnant polarization, coercive field, and orientation of dipoles with the switching of an applied electric field. The obtained results will be discussed in this chapter which would focus on the contribution of the semiconductive filler to enhance the ferroelectric properties of the polymer matrix. Further analysis of ferroelectric loops will determine the potential use of nanocomposites as energy storage devices.

### 5.2 Ferroelectric of P(VDF-TrFE) copolymer at different annealing temperatures

The polarization hysteresis loop is established to characterize ferroelectrics. Figure 5.1 shows the room temperature polarization-electric field ( $D$ - $E$ ) hysteresis loop of the P(VDF-TrFE) films annealed at 80 °C until 140 °C. The sweeping voltage is  $\pm 65$  V and the frequency is 100 Hz. The poling voltage for all annealed films increased from 5 V to 65 V to polarize the dipoles as shown in Figure 5.1. When the applied voltage  $V$  is less than 20 V, the  $D$ - $E$  relationship is almost linear. As  $E$  increases, a squared hysteresis loop rapidly begins to appear. The polarization of the electric field shown in the figure is consistent and stable for all samples annealed from 80 °C to 140 °C. The intercept on the polarization axis gives a remnant polarization ( $P_r$ ) and that on  $E$ -axis gives a coercive field ( $E_c$ ). From the  $D$ - $E$  hysteresis loop, the changes in remnant polarization and coercive field with different annealing temperatures are investigated. The maximum remnant polarization  $P_r$ , 76.7 mC/m<sup>2</sup> with the coercive field  $E_c$ , 74 MV/m is observed for the sample annealed at 100 °C. This is in

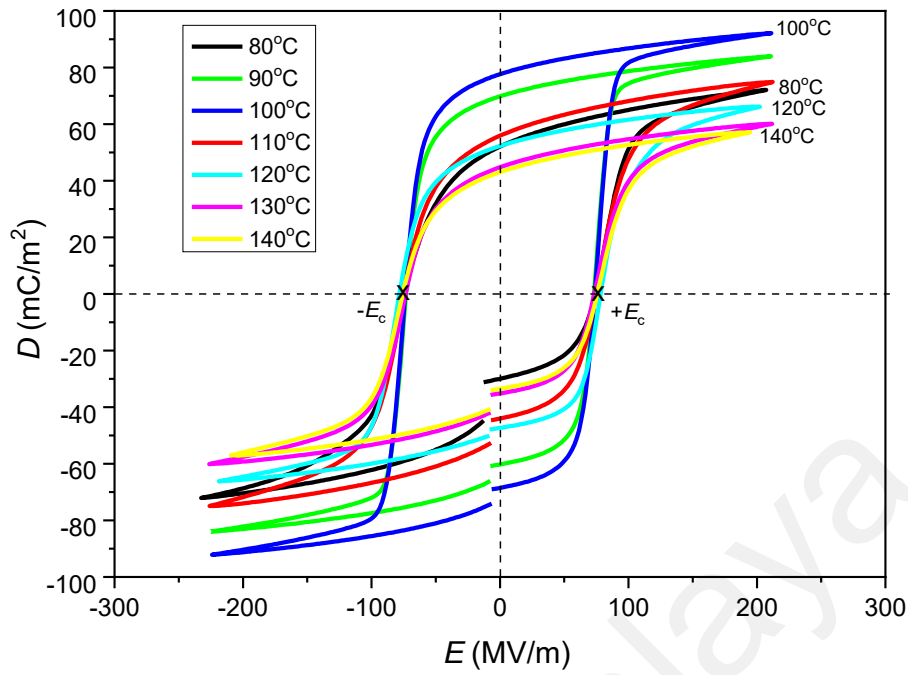
good agreement with the previously reported results for P(VDF-TrFE) (Choi et al., 2011; Choi et al., 2010; Mahdi et al., 2014).

The diagram shown in Figure 5.2 indicates that the thermal treatment enhances the ferroelectric nature of the polymer material due to the increment of the ferroelectric  $\beta$  phase, as the polymer chains ( $c$ -axis) should be aligned parallel to the film substrate since the polarization dipole moment is induced perpendicular ( $b$ -axis) to the substrate or chain axis. As shown by FESEM in morphological studies in Chapter 4, the enhancement of ferroelectric properties is exhibited from the emergence of elongated rod-like crystallite embedded into a micelle-like crystallite structure. Films annealed at 100 °C show the highest remnant polarization with the highest crystalline  $\beta$  phase, which was first proven by X-ray diffraction analysis in the earlier chapter. The hysteresis implies that the orientation of the crystal dipole moment changes with the application of electric fields. Its rotation to the applied electric field leads to a switching of the molecular dipole. The sharp edge observed at the saturation point (top and bottom of the hysteresis loop) indicates the rapid switching or spontaneous polarization of dipoles with the applied electric field (Mai et al., 2019). The  $E_c$  remained almost unchanged within this variation of annealing temperatures.



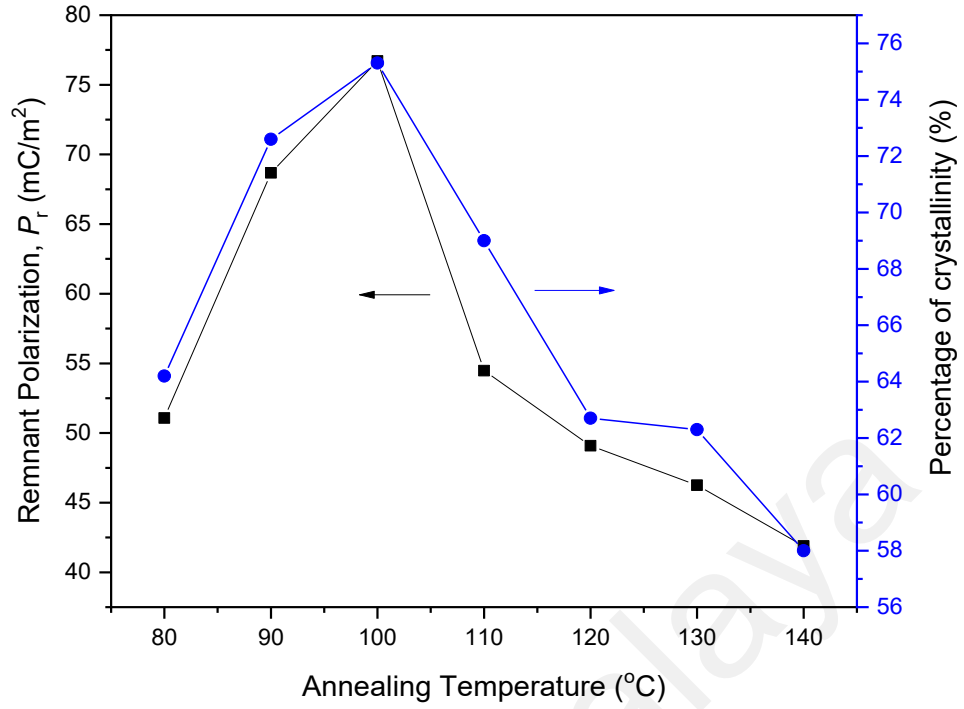
**Figure 5.1: Hysteresis of the polarization of P(VDF-TrFE) copolymer thin films at room temperature as a function of the electric poling field.**





**Figure 5.2:** *D-E* hysteresis loops of P(VDF-TrFE) copolymer thin films as measured at room temperature for various annealing temperatures at 60 V applied voltage.

Remnant polarizations are plotted in Figure 5.3 together with their percentage of crystallinity for copolymer films obtained by XRD against the annealing temperature. The figure shows that both remnant polarization and the percentage of crystallinity of P(VDF-TrFE) films increase in parallel with the increment of annealing temperature. A significant increment of remnant polarization from 49.1 to 76.7 mC/m<sup>2</sup> of the thin films was observed when they were annealed at 80 °C and 100 °C. However,  $P_r$  was dramatically decreased to 41.9 mC/m<sup>2</sup> at 140 °C when the thin film was annealed at a temperature above 100 °C. The result indicates that copolymer films with a higher degree of crystallinity will exhibit higher remnant polarization. Therefore, the pyroelectric coefficient is also expected to be the highest for the film annealed at 100 °C.



**Figure 5.3: Dependence of remnant polarization with the percentage of film's crystallinity on the various annealing temperature.**

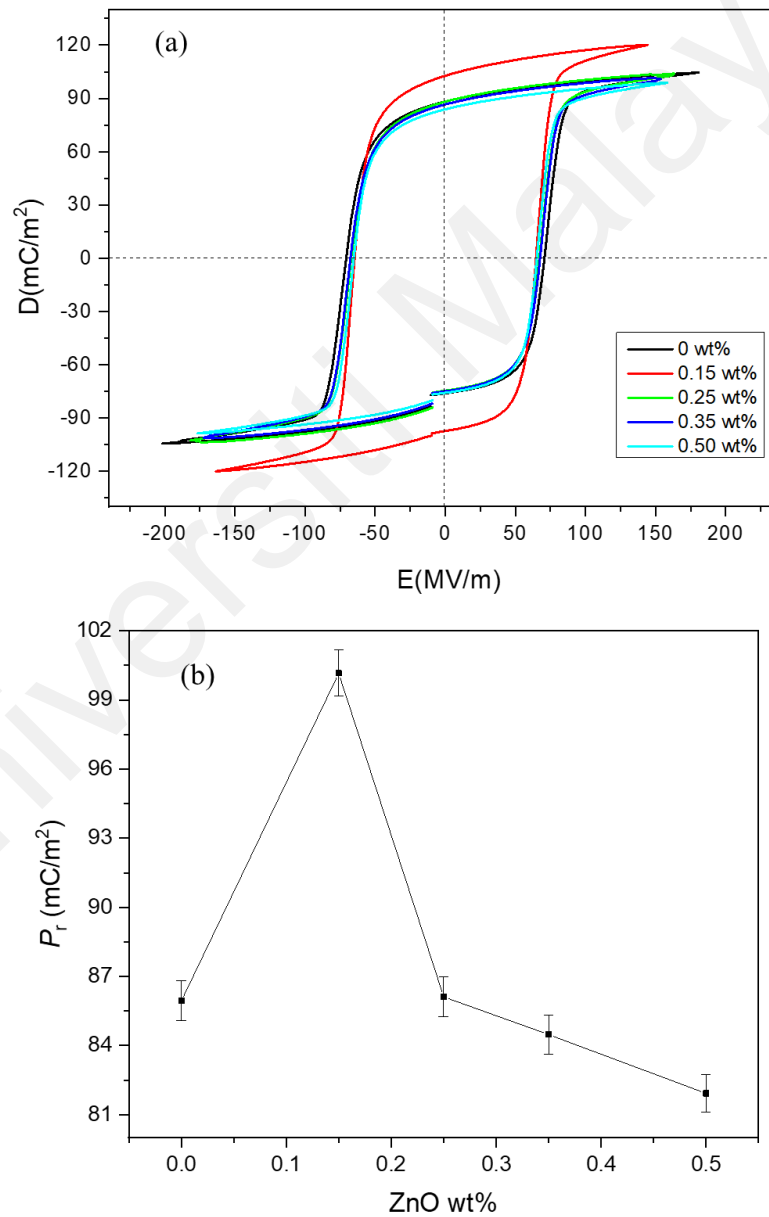
### 5.3 Ferroelectric and energy performance of composite P(VDF-TrFE) / ZnO QDs

Before observing ferroelectric behaviour, all deposited films are initially subjected to poling process. The composite films were immersed in silicon oil and poled using DC voltage at room temperature. The poling process is needed to obtain a greater ferroelectric domain, which is a microscopic area within the material where all-electric dipoles are oriented in the same direction as a result of the applied electric field. Electric dipole moment per unit volume known as polarization ( $P$ ), is related to dielectric displacement  $D$  through the linear expression (Equation 5.1).

$$D = P + \epsilon_0 E \quad (5.1)$$

where  $\epsilon_0$  is the permittivity of free space. The ferroelectric  $D$ - $E$  hysteresis loops measured with the step amplitude of an applied electric field at 100 Hz for all composite films are presented in Figure 5.4(a). The loops are close to rectangular, and 0.15 wt% composite has

the biggest area of loops with the highest remnant polarization,  $10.02 \mu\text{C}/\text{cm}^2$ . The result as depicted in Figure 5.4(b) shows that the incorporation of ZnO quantum dots considerably improves the remnant polarization of the nanocomposites, which the composite films of 0.15 wt% demonstrate an increment of remnant polarization of about 16.5% from the undoped P(VDF-TrFE). ZnO QDs filled in the P(VDF-TrFE) matrix are considered to induce extra dipole moments locally. It is deliberated that these local dipoles couple with polymer dipoles and trigger to induce an enhancement of ferroelectricity.

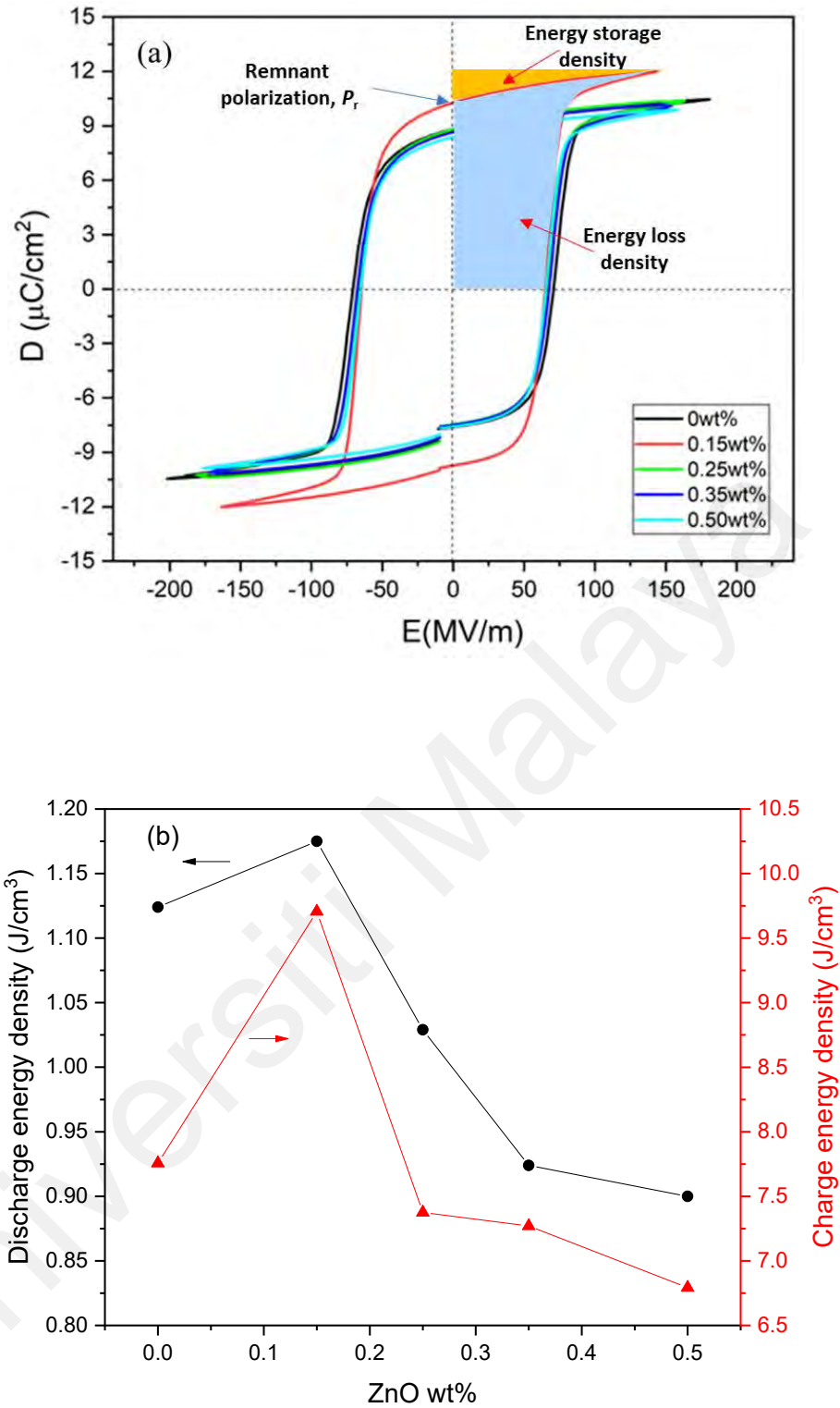


**Figure 5.4: (a)  $D$ - $E$  hysteresis loops at 100 Hz and (b) Remnant polarization,  $P_r$  of P(VDF-TrFE) / ZnO QDs composite films with various compositions.**

Poly (vinylidene fluoride)-based dielectric materials are promising candidates for high-power density electric storage applications because of their ferroelectric nature, high dielectric breakdown strength, and superior workability. The polarization-field hysteresis loops obtained through ferroelectric measurement in Section 5.3 were further investigated for energy storage characteristics, as described by Equation (5.2) (Galdámez-Martinez et al., 2020)

$$U_e = \int E dD \quad (5.2)$$

where  $U_e$  is discharged (stored) electric energy density,  $E$  is the external electric field and  $D$  is the electric displacement. The shaded area in the hysteresis loop in Figure 5.5(a) indicates the energy storage density (orange-shaded) and energy loss density (blue-shaded) calculated using Equation (5.2). The integration of the energy charging and discharging density for each composite film is shown in Figure 5.5(b). The energy storage density is  $1.12 \text{ J/cm}^3$  for pure copolymer P(VDF-TrFE) measured at 100 Hz frequency. According to Tsutsumi et al. (2020), the estimated value for the energy storage density of annealed P(VDF-TrFE) at 150 MV/m, at 100 Hz is equal to  $1 \text{ Jcm}^{-3}$ . The obtained value was approximately comparable to that in another work, which uses the copolymer, P(VDF-TrFE) as the polymer matrix and is presented in Table 6.1, Chapter 6, Section 6.8. Figure 5.5(b) shows that the energy storage and energy loss density for the composite film increases at 0.15 wt% of ZnO QDs compared to that of the copolymer film, reaching a maximum value of  $1.18 \text{ J/cm}^3$  and  $9.71 \text{ J/cm}^3$ , respectively. Further doping of ZnO QDs shows a decrease in remnant polarization, parallel with both the discharge and charge energy density trends, possibly due to the higher conductivity value of the composite film coming from a higher leakage current (refer to Figure 5.6 in Section 5.4).



**Figure 5.5: (a)  $D$ - $E$  hysteresis loops at 100 Hz and (b) Energy discharge and charging density of P(VDF-TrFE) / ZnO QDs composite films with various compositions.**

Nevertheless, the studies on the effect of embedding QDs into the ferroelectric polymer for energy storage and energy harvesting purposes (as listed in Table 5.1) are considered new due to the lack of reported work. Li et al. (Li et al., 2020) demonstrated that CdSe /  $\text{Cd}_{1-x}\text{Zn}_x\text{S}$

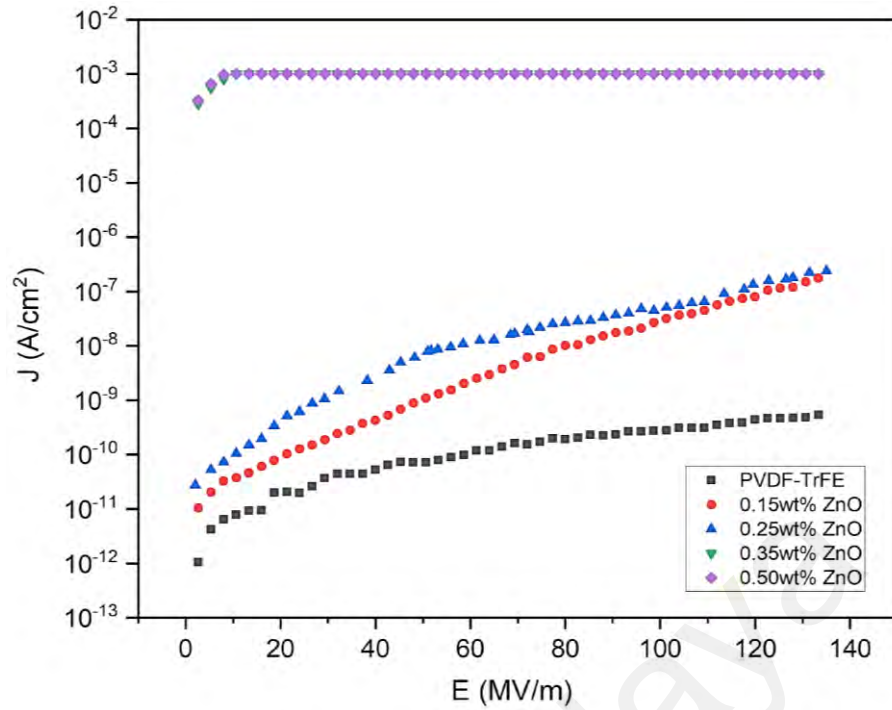
QDs with a wide-bandgap dual-ligand surface structure encapsulated in a fluoropolymer, poly(vinylidene fluoride-co-hexafluoropropylene) (P(VDF-HFP)) exhibit the greatest discharged energy density,  $U_e \sim 21.4 \text{ J/cm}^3$  among the previously reported works in the polymer nanocomposites with low filler contents. The QDs synthesized by Li et al. (2000) were grafted with short mercaptopropionic acid (MPA) ligands and 0.42 mmol 1H,1H,2H,2H-perfluorooctyltriethoxysilane (POTS, 99%) was added in the process, denotes as QDs-M-P. Films of pure P(VDF-HFP) and P(VDF-HFP)/0.82 vol% QDs-M-P nanocomposite were tested for their hysteresis and discharge energy density. The results showed that both  $D$ - $E$  loops of the nanocomposite films exhibited slim hysteresis and a large area of discharge energy density compared to P(VDF-TrFE) with ZnO QDs fillers used in the same study. This makes them some of the most outstanding ferroelectric polymer-based dielectric materials reported so far, with excellent energy storage performance. However, CdSe/Cd<sub>1-x</sub>Zn<sub>x</sub>S QDs may have an environmental issue due to their toxicity and thus ZnO QDs remain an alternative QD to be embedded in a ferroelectric polymer as a poly nanocomposite P(VDF-TrFE) / ZnO QDs for energy harvesting applications due to their nontoxicity, flexibility, moderate energy storage and high display of remnant polarization.

**Table 5.1. Ferroelectric studies of polymer nanocomposite films embedded with quantum dots.**

Material	Method	Energy storage density, $U_e$	Ref.
CdSe QDs/P(VDF-TrFE)	Langmuir-Blodgett	-	(Korlacki et al., 2011)
PMMA/carbon quantum dots (CDs)/PEDOT:PSS	Spin coating	-	(Zhang et al., 2016)
CdSe/ZnS quantum dots/PVC	Solution casting	-	(Ahmed & Morsi, 2017)
Cd <sub>1-x</sub> Zn <sub>x</sub> Se <sub>1-y</sub> S <sub>y</sub> nanodots/ P(VDF-HFP)	Solution casting	$\sim 21.4 \text{ J/cm}^3$	(Li et al., 2020)

#### 5.4 Leakage current analysis of composite films

The leakage current density,  $J$  against the applied electric field,  $E$  is shown in Figure 5.6. The leakage current plays a crucial role in the performance of ferroelectric devices. The leakage current increased with an increasing electric field. The  $J$  of P(VDF-TrFE) is in the range of  $10^{-12}$  to  $10^{-10}$  A/cm<sup>2</sup> with an increasing field up to 140 MV/m. The  $J$  of the composites increased from  $10^{-11}$  to  $10^{-7}$  A/cm<sup>2</sup> when the ZnO quantum dot fillers increased up to 0.25 wt%. This suggests that further increases in the ZnO QDs in PVDF-TrFE deteriorate the ferroelectric properties due to the excessively high leakage current density, which will be a disadvantage for potential applications (Korlacki et al., 2011). Further increments of ZnO QDs greater than 0.25 wt% show that the leakage current density increases to a maximum of approximately  $10^{-3}$  A/cm<sup>2</sup> and saturates above 20 MV/m. It is important to note that the 0.35 wt% graph overlaps with the 0.50 wt%. The poor ferroelectric performance due to the high leakage current density demonstrated by the thin films with ZnO QD nanofillers exceeding 0.25 wt% can be related to the appearance of deep micelle-like hole structures distributed in the polymer nanocomposite, as indicated by FESEM characterization. Hence, the 0.15 wt% P(VDF-TrFE) / ZnO QD device, which exhibits the highest remnant polarization and can store the largest amount of energy, may be useful in an energy harvesting application (elaborated in Chapter 6).



**Figure 5.6:** Leakage current curve of P(VDF-TrFE) / ZnO QD composite films.

### 5.5 Conclusion

An annealing treatment significantly improves the polarization of copolymer P(VDF-TrFE) thin films and therefore helps to improve the ferroelectric properties. Spin-coated thin films of copolymer P(VDF-TrFE) annealed at 100 °C yield the highest remnant polarization (76.7 mC/m<sup>2</sup>) due to the dominance of the ferroelectric beta phase and showed the highest percentage of crystallinity (75.3%), which was revealed by deconvolution technique by XRD in Chapter 4. ZnO quantum dots were added to P(VDF-TrFE) to improve its ferroelectricity. Incorporation of 0.15 wt% ZnO QDs into the polymer host significantly enhanced the remnant polarization ( $P_r = 10.02 \mu\text{C}/\text{cm}^2$ ) compared to the pure P(VDF-TrFE), which is largely composed of homogeneous micelle-like crystallite and the growth of elongated rod-like crystallite. The maximum energy storage density calculated at 100 Hz is 1.18 J/cm<sup>3</sup> obtained from the 0.15 wt% P(VDF-TrFE) / ZnO QD polymer nanocomposite. The incorporation of ZnO QDs as filler into copolymer does not reinforce the energy storage characteristics of the nanocomposite. The poor ferroelectric performance of the thin films with ZnO QDs fillers exceeding 0.25 wt% may be related to the high leakage current density and the occurrence of



micelle-like hole structure and the hole are deep to the surface of the Si substrate as shown by FESEM characterization. The non-centrosymmetric crystal structure of ZnO consists of alternating layers of positive and negative ions that result in spontaneous polarization along the *c*-axis, could induce extra local dipole moments in the films and thus help in the increment of ferroelectric until up to 0.15 wt% composition. The surface morphology and polarization are interrelated and influence the ferroelectric properties of the nanocomposite device.

Universiti Malaysia

## CHAPTER 6: DIELECTRIC AND PYROELECTRIC PROPERTIES OF COPOLYMER P(VDF-TrFE) AND NANOCOMPOSITE THIN FILMS P(VDF-TrFE) / ZnO QDs

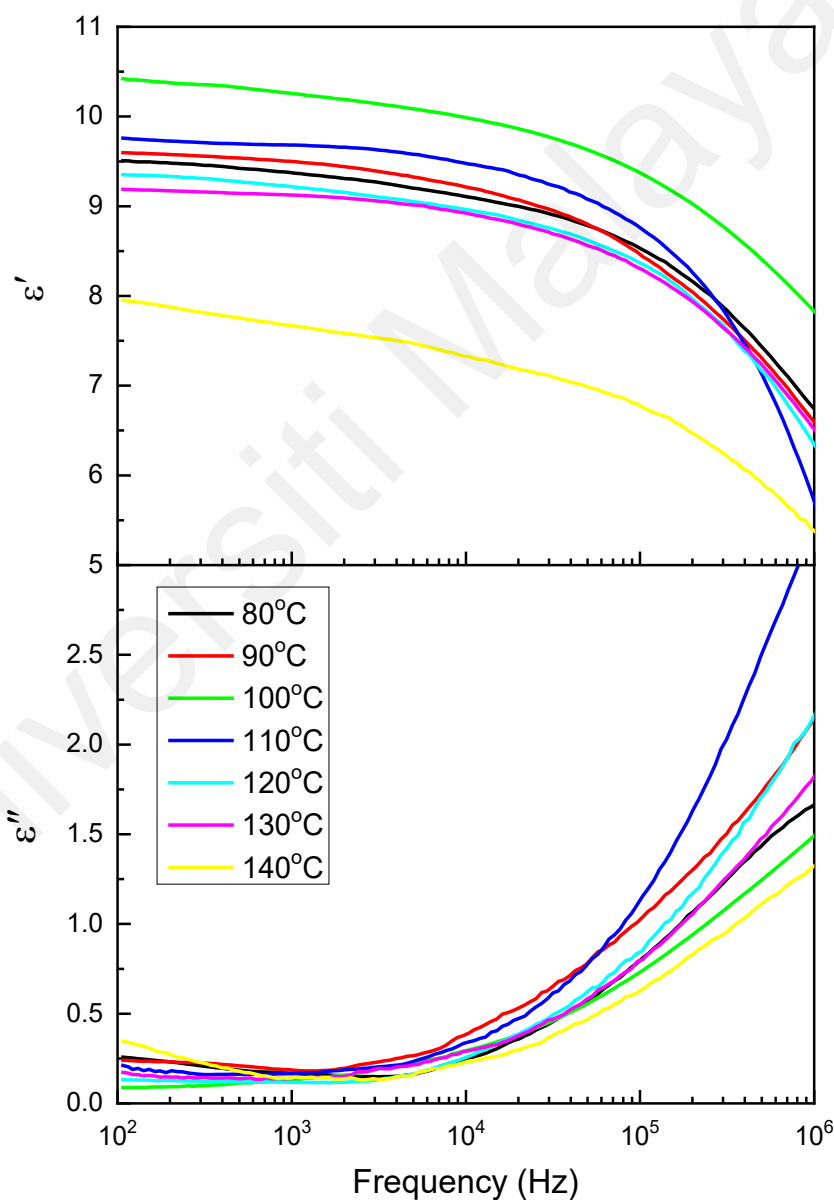
### 6.1 Introduction

The dielectric and pyroelectric characterizations of the fabricated copolymer P(VDF-TrFE) and composite device P(VDF-TrFE) / ZnO QDs were presented. The annealing treatment applied is normally close to Curie temperature,  $T_c$  since the material is in between the ferroelectric phase and the paraelectric phase. The study of polymers as a function of frequency and temperature can be employed to elucidate the effects owing to intermolecular cooperative motions and hindered dielectric rotations. It is expected that improvement in the functional properties can occur when semiconductive ZnO quantum dots are incorporated to that of pure P(VDF-TrFE). The obtained result suggests that the contribution of the ferroelectric nanofiller would enhance the dielectric and pyroelectric properties of the polymer matrix. Further investigation on the energy harvesting performance of composite devices is elaborated in this chapter.

### 6.2 Dielectric of copolymer P(VDF-TrFE) at different annealing temperatures

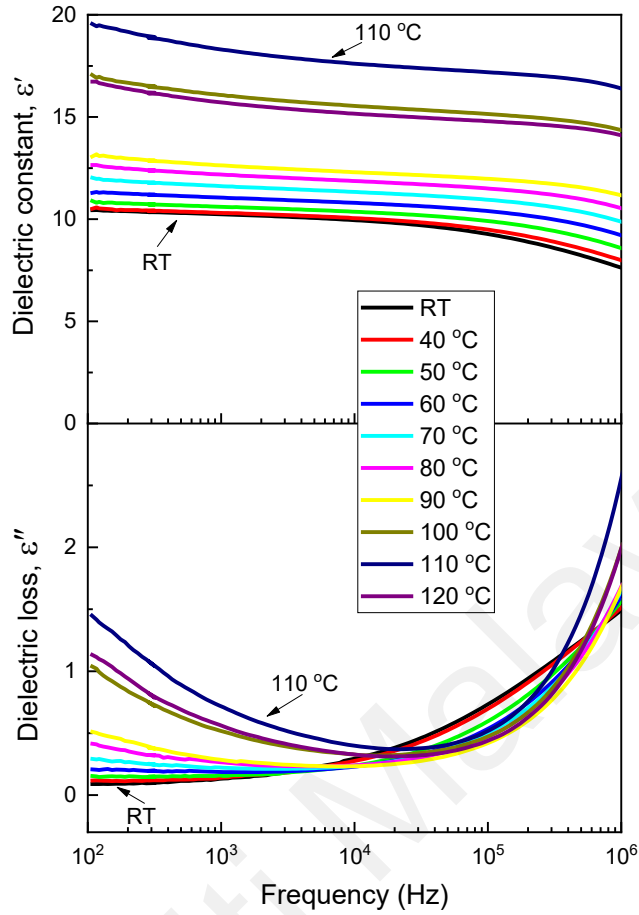
Figure 6.1 shows the room temperature (30 °C) frequency dependence of the real,  $\epsilon'$ , and imaginary,  $\epsilon''$ , parts of the dielectric permittivity for the copolymer P(VDF-TrFE) thin films annealed at 80 °C to 140 °C. The applied frequency ranged from 100 Hz to 1 MHz. The dielectric constant increases from 9.4 to 10.3 as the annealing temperature increases from 80 °C to 100 °C. The dielectric constant of the 100 °C annealed thin film at 1 kHz has the highest value of approximately  $\epsilon' = 10.3$  and the loss is  $\epsilon'' = 0.1$ . The higher degree of crystallinity in the 80 °C to 100 °C annealed copolymer P(VDF-TrFE) thin films, initially confirmed by the XRD (see section 4.2.1), has caused the dipole moments to align in an ordered conformation, contributing to an increase in the dielectric constant. As the annealing temperature reached

100 °C, micelle-like and elongated rod-like crystallites were formed homogeneously on the surface of the copolymer thin films P(VDF-TrFE) as depicted from morphological characterization in Chapter 4 (see section 4.2.4). However, as the annealing temperature was further increased,  $\epsilon'$  began to decrease. This decrease in the dielectric constant is observed for frequencies from  $10^4$  Hz to  $10^6$  Hz (high frequency), above which the value saturates. The film annealed at 140 °C shows the lowest dielectric constant, 7.7 at 1 kHz.

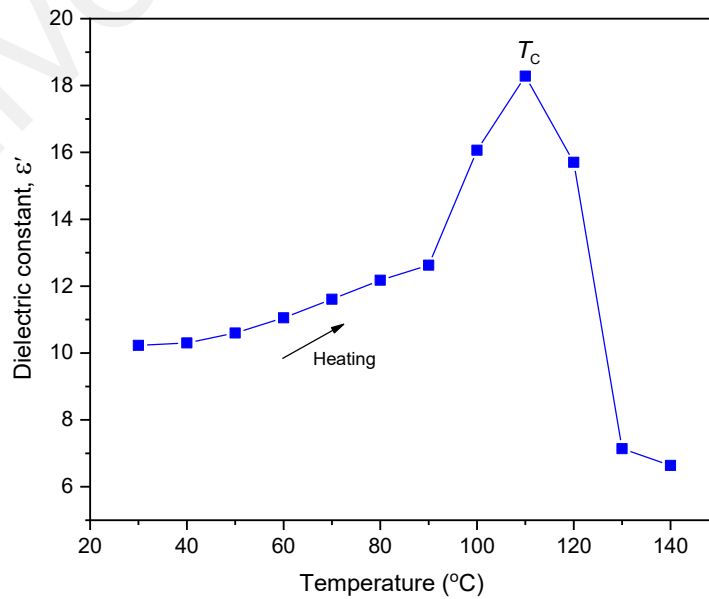


**Figure 6.1: Room temperature dielectric frequency spectra of P(VDF-TrFE) films at various annealing temperatures.**

The thin film annealed at 100 °C, which exhibits the highest dielectric constant as measured at room temperature, was then subjected to a frequency dependence measurement and the spectrum is shown in Figure 6.2. The dielectric constant  $\epsilon'$  of the 100 °C annealed films increase significantly from room temperature until 110 °C. The rapid increase in  $\epsilon'$  between 90 °C and 110 °C is attributed to the onset of cooperative dipolar motions, leading to an FE-PE transition, as mentioned by Furukawa (Takeo Furukawa, 1997). The dielectric constant,  $\epsilon'$  is related to the ability of molecular dipoles of the polymer chains to oscillate in an alternating field. With increasing temperature, the thermal oscillations intensify and dipoles follow the alternating field more freely, which leads to an increase in the dielectric constant. The spectrum of dielectric constant temperature dependence measurement in Figure 6.3 at 1 kHz frequency is extracted from frequency dependence spectra of film annealed at 100 °C in Figure 6.2. Further heating (above 110 °C) causes the dipoles to lose their cooperativity, and as a result, the dielectric constant  $\epsilon'$  decreases to 6.6 at 140 °C. The temperature at which the dielectric constant,  $\epsilon'$ , is the highest is correlated to the Curie temperature,  $T_c$ . The  $T_c$  peak (at approximately 110 °C) observed in the dielectric constant  $\epsilon'$  temperature dependence spectrum is in good agreement with the corresponding TSC data (as discussed in Chapter 7), which is attributed to the dipolar relaxation mode in the crystalline phase (Arifin & Ruan, 2018; Sutani et al., 2021). The coalescence of the micelle-like and elongated rod-like crystallites formed into acicular grains with some smaller needle-like crystallites inside the grains at film structure annealed above 100 °C is the major factor in the deterioration of dielectric constant of copolymer thin films annealed at temperatures above  $T_c$  as the copolymer experience phase changes from the ferroelectric to the paraelectric phase.



**Figure 6.2:** Dielectric frequency spectra for the P(VDF-TrFE) thin film annealed at 100 °C and measured at a temperature step size of 10 °C from room temperature (RT) to 120 °C.



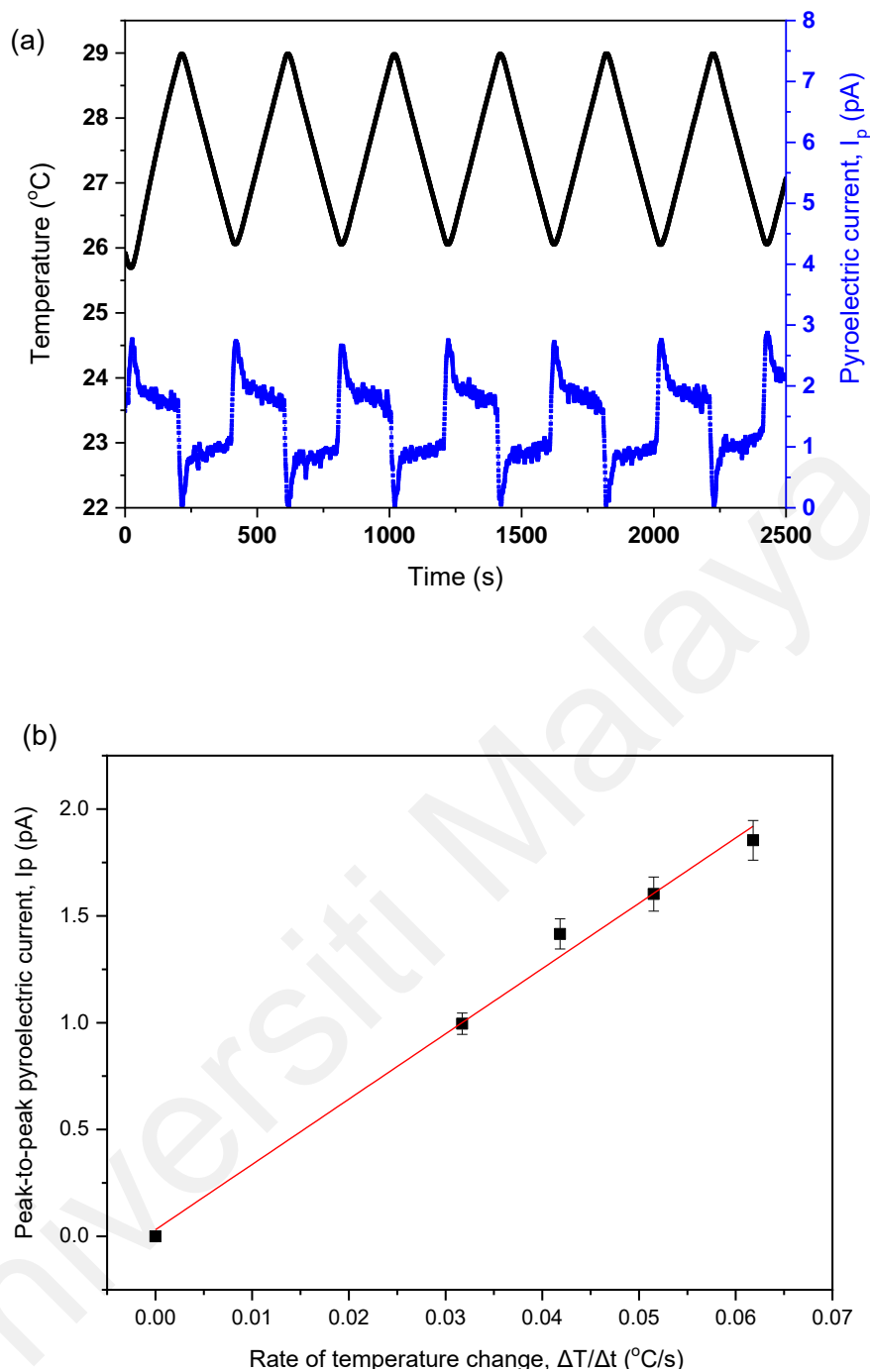
**Figure 6.3:** Dielectric constant of P(VDF-TrFE) film annealed at 100 °C as a function of temperature with a step size of 10 °C.

### 6.3 Pyroelectric coefficient of copolymer P(VDF-TrFE) at different annealing temperatures

In this study, the pyroelectric coefficient,  $P_i$  of the P(VDF-TrFE) copolymer thin film was measured using the quasi-static measurement method. The pyroelectric coefficient,  $P_i$ , was obtained by measuring the pyroelectric current  $I_p$  induced during the heating of the sample from 26 °C to 29 °C, with an effective area of 1 mm<sup>2</sup> for all samples. The heating rates used in this experiment were 0.015 °Cs<sup>-1</sup>, 0.02 °Cs<sup>-1</sup>, 0.025 °Cs<sup>-1</sup> and 0.03 °Cs<sup>-1</sup>. A rectangular waveform of pyroelectric current was obtained when a triangular temperature waveform was applied to the P(VDF-TrFE) thin films, with different annealing temperatures, as shown in Figure 6.4(a), which depicts the pyroelectric coefficients of the thin film annealed at different annealing temperatures. Equation (6.1) describes the relationship between the pyroelectric coefficient ( $P_i$ ), generated pyroelectric current ( $I_p$ ), rate of temperature change ( $dT/dt$ ) and surface area ( $A$ ) of the element (Bowen et al., 2015; G. Chen & Majid, 2006; Li & Ohigashi, 1992).

$$P_i = \frac{I_p}{A \left( \frac{dT}{dt} \right)} \quad (6.1)$$

When the temperature gradient changes from heating to cooling or vice versa, C-F dipoles in the PVDF unit cell are orientated to a slightly disordered state. The disordered state of the dipoles reduces the spontaneous polarisation of the samples and changes the bound charge on the material surface. The free charges at the aluminium electrodes were then redistributed themselves to compensate for the change in the bound charges, causing the pyroelectric current to flow. Plotting the  $I_p$  versus  $\Delta T/\Delta t$  graph (see Figure 6.4(b)) allows the pyroelectric coefficients of the poled P(VDF-TrFE) films to be determined. Therefore, the pyroelectric coefficients of poled P(VDF-TrFE) copolymer thin films annealed at different temperatures were evaluated.

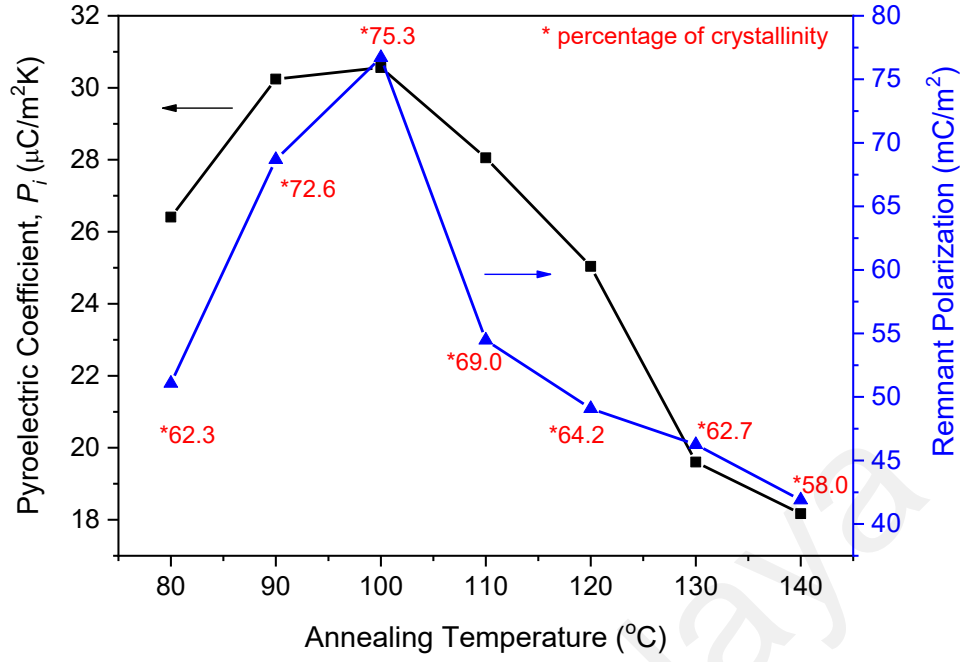


**Figure 6.4: (a) Change in pyroelectric current with time and temperature of the P(VDF-TrFE) thin film and (b) graph of  $I_p$  versus rate of temperature change,  $dT/dt$  for poled P(VDF-TrFE) thin film annealed at 100 °C.**

The dependences of the pyroelectric coefficient, remnant polarization and degree of crystallinity of the copolymer thin films on the annealing temperature were plotted and are shown in Figure 6.5. The annealing temperature of 100 °C is the optimum temperature, with a pyroelectric coefficient of 31  $\mu\text{C}/\text{m}^2\text{K}$ . Above the optimum annealing temperature, the

pyroelectric coefficients for the copolymer thin films deteriorate. The pyroelectric coefficient for the thin film annealed at 140 °C is reduced to 18  $\mu\text{C}/\text{m}^2\text{K}$ . The higher the percentage of crystallinity is, the better the pyroelectric performance, as illustrated in Figure 6.5. At the optimum annealing temperature of 100 °C, the pyroelectric coefficient, remnant polarization and percentage of crystallinity all give maximum values of 31  $\mu\text{C}/\text{m}^2\text{K}$ , 76.7  $\text{mC}/\text{m}^2$  and 75.3%, respectively. The degree of crystallinity in the  $\beta$  phase of the copolymer decreases dramatically at higher annealing temperatures above 100 °C (in the paraelectric phase), as the polymer molecular chains tend to align normally to the substrate, which will decrease the polarization of the copolymer thin film. The poor pyroelectric performance exhibited by the thin films annealed above 100 °C can be related to the low percentage of crystalline  $\beta$  phase, as thoroughly shown in the XRD, FTIR and ferroelectric results in Chapter 4. The micelle-like crystallites coalesce with the elongated rod-like crystallites to form acicular grains with small needle-like structures inside the grain, which may cause the copolymer thin film to lose some of its ferroelectric and pyroelectric properties. The C-F bonds in the P(VDF-TrFE) copolymer are highly polar, with a large dipole moment,  $D$ , of  $6.4 \times 10^{-30}$  Cm (Navid & Pilon, 2011). If the crystalline structure of the copolymer thin film is non-centrosymmetric, then the polarization of the dipoles can be spontaneous and temperature dependent. Therefore, the copolymer was also investigated for its pyroelectric effect (Joshi & Dawar, 1982; Lang, 2005; Navid et al., 2010).





**Figure 6.5: Pyroelectric coefficient ( $P_i$ ) of P(VDF-TrFE) thin films plotted together with their respective remnant polarization and percentage crystalline for various annealing temperatures.**

#### 6.4 Energy harvesting and sensor Figure of Merit (FOM) of copolymer films

Figures of merit (FOMs) can be used to assess the performance of pyroelectric devices for thermal or infrared sensor and energy harvesting applications. FOMs are numerical values for measuring the efficiency and performance of a transducer and a sensor. For better performance of pyroelectric materials, the thermal conductivity and specific heat capacity should be low to enhance their figures of merit (Jayalakshmy & Philip, 2015). Here, two types of FOM can be used to quantify the performance of a pyroelectric material for thermal sensing and energy harvesting. The first type of FOM is the detectivity without division of the specific heat capacity,  $F_D$  (Gan & Majid, 2015), which is normally used for thermal sensors. The expression is stated as:

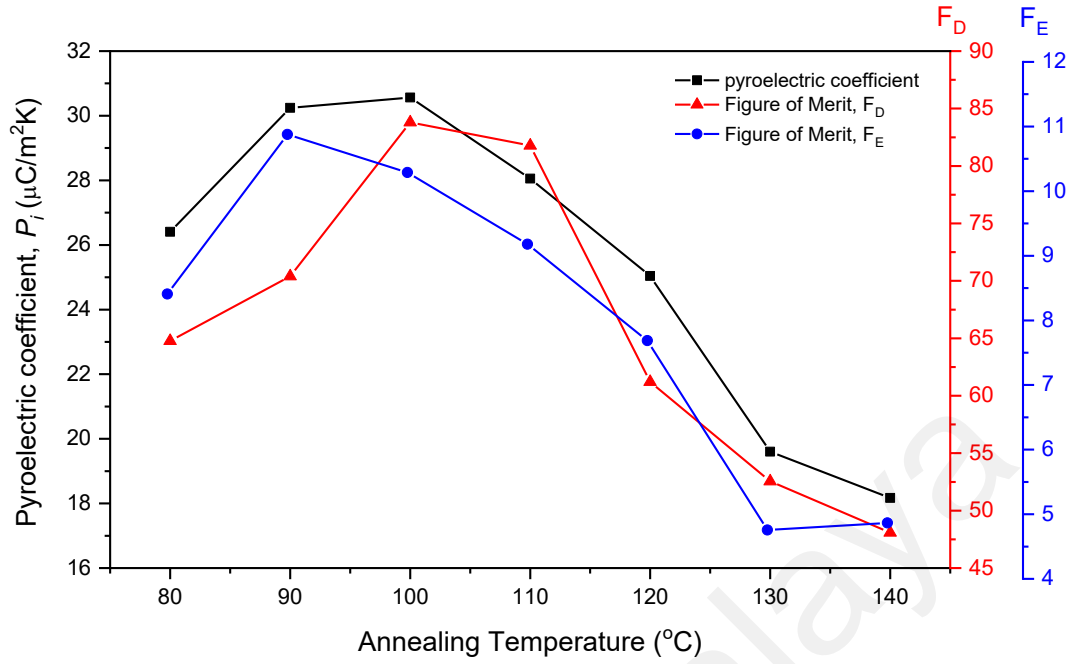
$$F_D = \frac{P_i}{\sqrt{\varepsilon' \tan \delta}} \quad (6.2)$$

where  $P_i$ ,  $\varepsilon'$  and  $\tan \delta$  are the pyroelectric coefficient, dielectric constant and tangent loss, respectively. The values of  $\varepsilon'$  and  $\tan \delta$  were measured at 1 kHz, 10 kHz and 100 kHz. The second FOM,  $F_E$ , is used for energy harvesting and represents the amount of electrical power that can be harvested from the hot source of a pyroelectric material, and it can be defined as:

$$F_E = \frac{P_i^2}{\varepsilon_o \varepsilon_r} \quad (6.3)$$

where  $\varepsilon_o$  is the vacuum permittivity ( $8.854 \times 10^{-12} \text{ Fm}^{-1}$ ) and  $\varepsilon_r$  is the permittivity of the pyroelectric material (Navid & Pilon, 2011; Yamanaka et al., 2017).

The spectra of  $F_D$  and  $F_E$  calculated at 1 kHz are shown in Figure 6.6.  $F_D$  increases from 61 to 84  $\mu\text{C}/\text{m}^2\text{K}$  when the annealing temperature of the P(VDF-TrFE) thin films is increased from 80 °C to 100 °C. The variations in  $F_D$  and  $F_E$  at the higher frequencies of 10 kHz and 100 kHz are similar to those at 1 kHz and thus are not reproduced here.  $F_D$  starts to decrease at annealing temperatures above 100 °C up to 140 °C until the value reaches 48  $\mu\text{C}/\text{m}^2\text{K}$ . The maximum  $F_E$  calculated at 1 kHz is 10.9  $\text{Jm}^{-3}\text{K}^2$ , obtained from P(VDF-TrFE) thin films annealed at 90 °C, and it decreases to 10.3  $\text{Jm}^{-3}\text{K}^2$  for 100 °C annealed films. Although  $F_E$  is highest at an annealing temperature of 90 °C, the percentage difference is only 5.7% for  $F_E$  annealed at 100 °C compared to the large difference in  $F_D$  at these two annealing temperatures. Therefore, based on the spectra in Figure 6.6, P(VDF-TrFE) thin films annealed at 100 °C are still the optimum films for use in both sensor and energy harvesting applications.



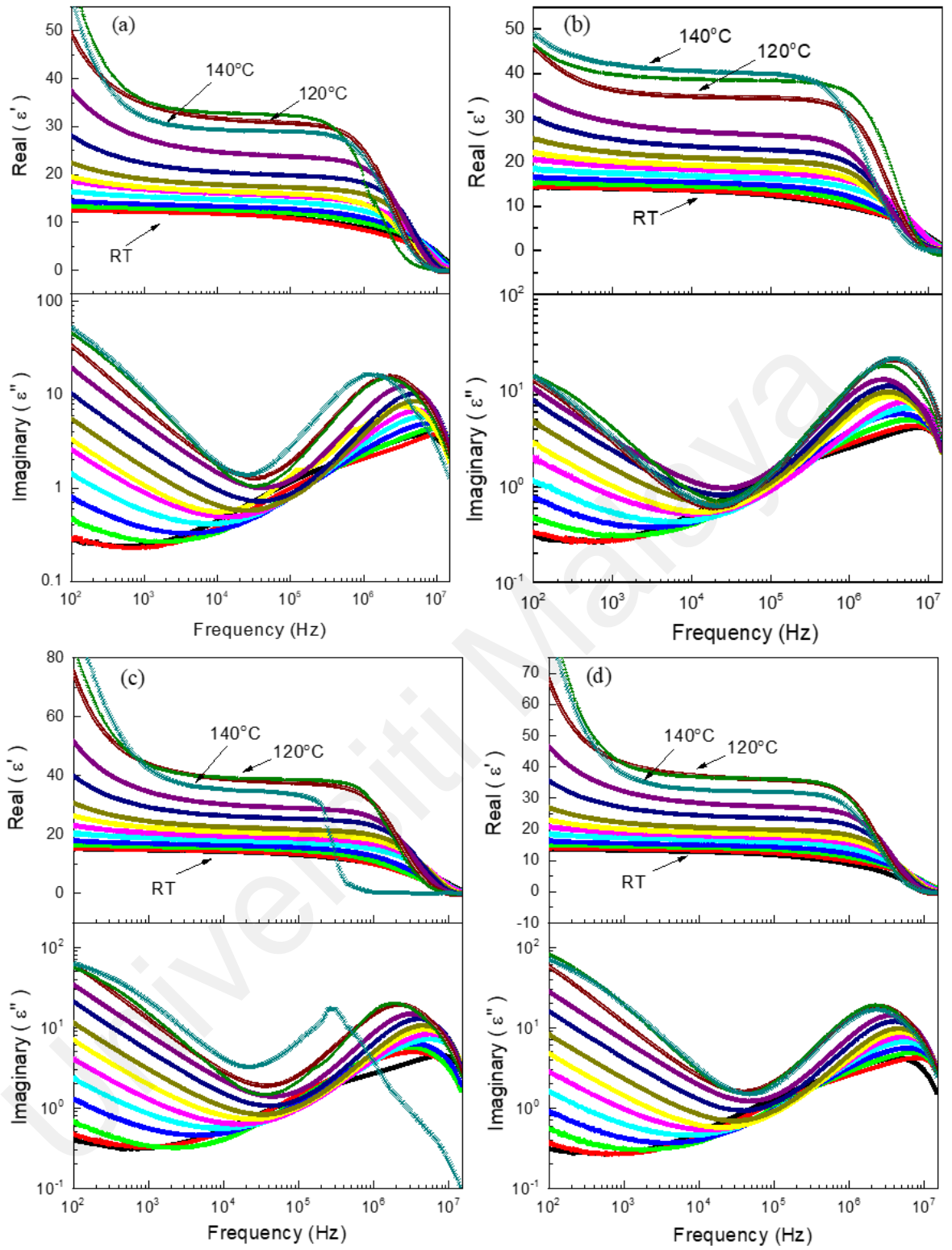
**Figure 6.6: Dependence of pyroelectric coefficient ( $P_i$ ) with two figures of merit (FOMs),  $F_D$  and  $F_E$  on various annealing temperatures of P(VDF-TrFE) thin films.**

### 6.5 Dielectric of composite P(VDF-TrFE) / ZnO QDs

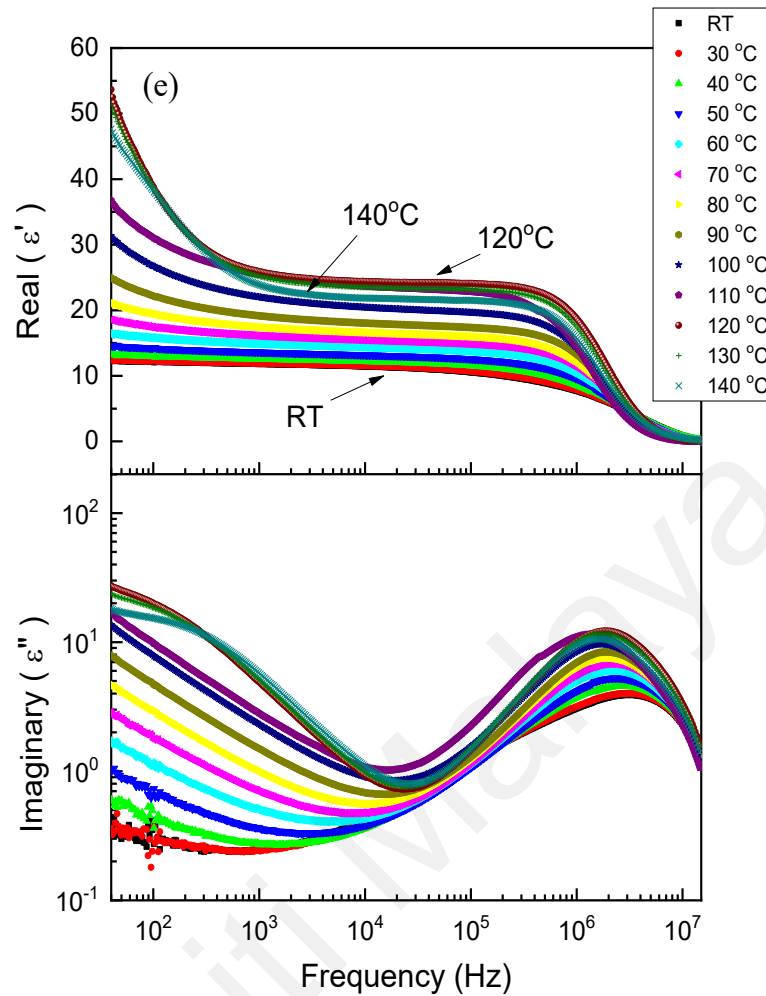
The dielectric spectra of copolymers without ZnO QDs are shown in Figure 6.7(a). The incorporation of ZnO QDs into the PVDF-TrFE matrix amends the dielectric spectra with the increasing temperature from room temperature (RT) to 140 °C as depicted in Figure 6.7(b)-(e). At low frequency, both  $\varepsilon'$  and  $\varepsilon''$  of nanocomposites thin films increases for all composition until up to 100 °C. The enhancement in the dielectric constant dielectric loss values at low frequencies can be ascribed to Maxwell–Wagner–Sillars polarization arising from charge carriers accumulated at the interphase between amorphous and crystalline regions (P. Xu & Zhang, 2011). The increasing trend of dielectric loss in the frequency range 10 kHz to 1 MHz is convincing evidence of the dielectric relaxation peak corresponding to  $\beta$  relaxation induced by the micro-Brownian motion of non-crystalline chain segments in P(VDF-TrFE) (Mahdi & Majid, 2016). The increase in the real permittivity of the composite up to 0.25 wt% ZnO QDs is attributed to the large permittivity of ZnO which enhanced the

polarization from dipole-dipole interaction of closely packed nanoparticles and may be due to interfacial polarization which increases the polarizability of the samples at the interface. Dipole-dipole interactions arise from the alignment of permanent dipoles within the molecules or atoms of the material. The molecules with permanent dipoles attract each other electrostatically; the positive end of one molecule attracts the negative end of another molecule, and so on, leading to an alignment of the molecules (Moeller, 2012). When the dipoles are aligned with an applied electric field, they increase the polarization of the material and increase its dielectric constant. The material responds to the electric field by generating its own dipole moments. On the other hand, interfacial polarization mechanism also known as Maxwell-Wagner gives rise to the increase in the dielectric permittivity at low frequencies. Toor (2017) reported that the ligand coating on the nanoparticle surface provides local electrical resistance, so these nanoparticles could still be incorporated at a high-volume ratio in the polymer scaffold without compromising the breakdown strength and causing an increase in the dielectric loss of the polymer nanocomposite. The interfacial ligand/surface functionalization layer can restrict electron transfer between the nanoparticles, resulting in a more gradual increase in dielectric permittivity with increasing nanoparticle concentration. The dielectric loss,  $\epsilon''$  increases due to the increment of conductivity of ZnO QD itself. The dielectric loss distortion in Figure 6.7(e) for 0.50 wt% composite films at room temperature to 50 °C is probably caused by a problem with the aluminium electrode attached to the sample.

Few studies reported that the dielectric properties of ZnO may be attributed to the hybridization between the Zn 3*d*-electron and the O 2*p*-electron based on the first principle (Albertsson et al., 1989; Dal Corso et al., 1994; Onodera & Takesada, 2012). One of the theoretical studies also includes DFT based study of ZnO nanostructure adopting Local Density Approximation (LDA) and Generalized Gradient Approximation (GGA) correlation function.

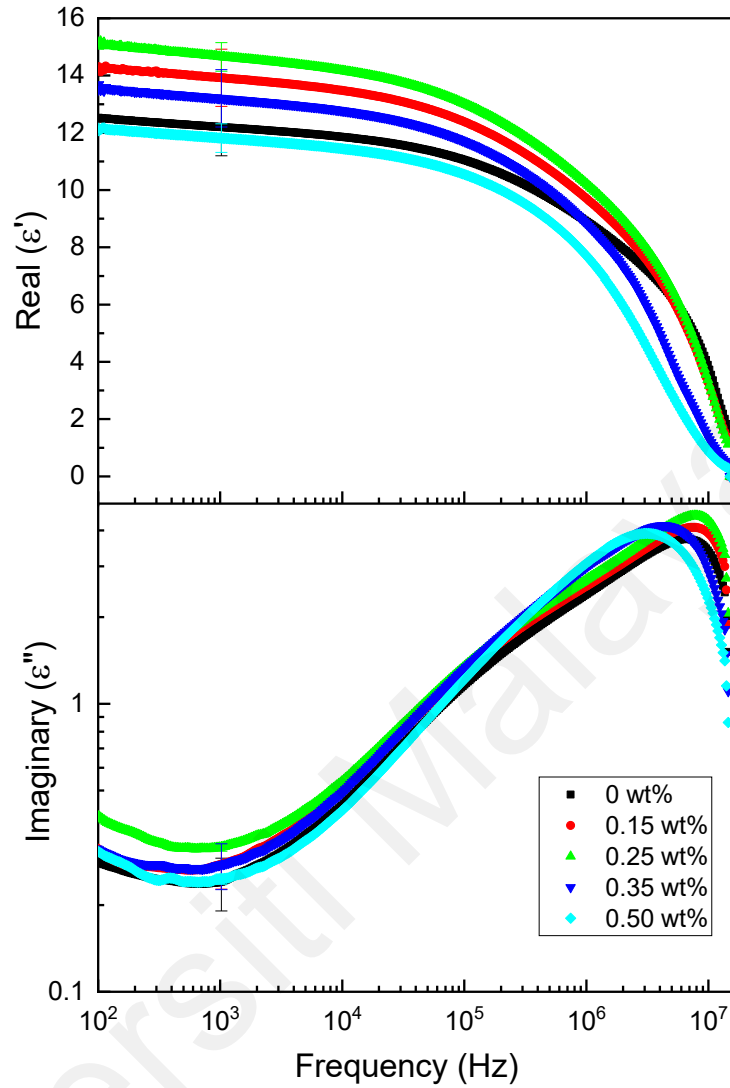


**Figure 6.7: Real ( $\epsilon'$ ) and imaginary ( $\epsilon''$ ) dielectric spectra of P(VDF-TrFE) / ZnO QDs (a) 0 wt% (b) 0.15 wt% (c) 0.25 wt% (d) 0.35 wt% and (e) 0.50 wt%.**



**Figure 6.7, continued.**

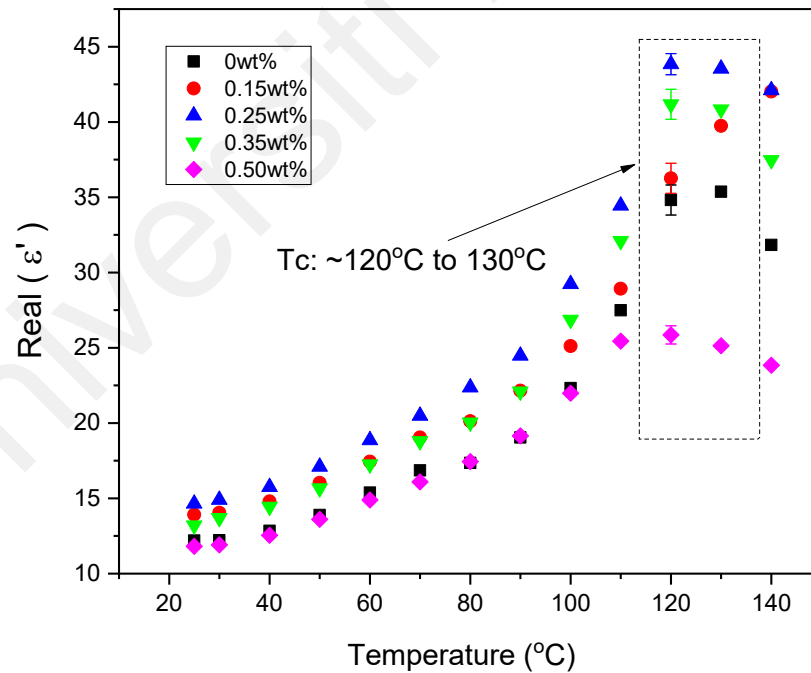
Figure 6.8 shows the temperature dependence of  $\epsilon'$  and  $\epsilon''$  for various wt% of ZnO at 1 kHz. It is observed that  $\epsilon'$  and  $\epsilon''$  increase with the increase of ZnO wt% in composite up to 0.25 wt% ZnO QDs. The increase in the real permittivity of the polymer nanocomposite is attributed to the polarization from dipole-dipole interaction of closely packed nanoparticles and may also be due to interfacial polarization which increases the polarizability of the samples at the interface (Tan et al., 2014). As ZnO quantum dots have a high surface area/volume ratio, the interface becomes larger with the increase of ZnO content. Meanwhile, the dielectric loss,  $\epsilon''$  was shifted to lower frequencies as the nanofiller content increased. Although composite films of 0.25 wt% have the highest dielectric constant, they also result in the highest dielectric loss, hence the optimized composite films are more suitable for device operation at 0.15 wt%.



**Figure 6.8: Frequency dependence of dielectric spectra, real ( $\epsilon'$ ) and imaginary ( $\epsilon''$ ) of P(VDF-TrFE) / ZnO QDs composites with different filler contents at room temperature.**

The increase in  $\epsilon'$  and  $\epsilon''$  for the P(VDF-TrFE) / ZnO QD polymer nanocomposite thin films in the low-frequency range (Figure 6.8) is due to the inclusion of ZnO QDs with higher conductivity, embedded in the polymer matrix. In polymer nanocomposites with conductive fillers, the polarization properties of the matrix molecule, the conductive filler, and their interface, together play a decisive role in the dielectric properties. The high dielectric relaxations occurring at low frequencies referred to as Maxwell-Wagner relaxations are normally generated due to the interfacial effects between the fillers and the polymer matrix (Parangusan et al., 2018). According to percolation theory and the Maxwell-Wagner-Sillars

interfacial polarization effect, the charge carriers in the composites depend on the transport of the polymer matrix to the conductive fillers, which leads to the accumulation of space charge polarization at their interface. Meanwhile, the dielectric constant decreases with increasing frequency. A similar pattern was observed and reported in reference (Gao et al., 2019; Halim & Halim, 2018; Han et al., 2019; Wu et al., 2022; Xu et al., 2018). The dipoles struggled to align in the direction of the applied field at higher frequencies, but at lower frequencies, the dipoles had enough time to align with the applied field. Therefore, the reduction in the dielectric constant at higher frequencies is due to the gradual decrease in the speed of movement of the charges in response to the applied electric field (Han et al., 2019). The Curie temperature is increased by approximately 10 °C with the addition of ZnO QDs compared to that of the pure copolymer as shown in Figure 6.9 which indicates that the semiconductor filler enhanced the ferroelectric phase of a nanocomposite device.



**Figure 6.9: Temperature dependence of real ( $\epsilon'$ ) of dielectric spectra for various wt% of ZnO at 1 kHz.**



## 6.6 Room temperature dielectric models

The nanocomposite films can be modelled by a two-phase dispersion system consisting of a polymer matrix P(VDF-TrFE) and semiconductive inclusions (ZnO QDs). To predict the effective dielectric constant of the P(VDF-TrFE) / ZnO nanocomposites, a set of theoretical models were applied to the dielectric experimental results. Figure 6.10 shows the comparison of Vo-Shi, EMT, Claussius-Mossoti, Maxwell-Wagner and Furukawa model predictions with experimental data of the P(VDF-TrFE) / ZnO QD nanocomposite at room temperature with various weight percentages of ZnO QDs as measured at 10 kHz. From the theoretical models employed above, it is seen in Figure 6.10 that the Vo-Shi and EMT models gave the best-fit parameters. The experimental value fits well with the Vo-Shi up to 0.25 wt% ZnO QDs because this model assumes that the effective dielectric constant of the polymer/filler composite depends on the interfacial region between the polymer and the filler as well as depends on the size of the filler (Vo & Shi, 2002). Vo and Shi calculated the effective dielectric constant of a three-component system consisting of polymer, interphase and filler:

$$\varepsilon_c = \frac{h+2l}{h-l} \quad (6.4)$$

where  $h$  and  $l$  are given by:

$$h = 1 + 2 \frac{(\varepsilon_1 - \varepsilon_3)(\varepsilon_3 - \varepsilon_2)}{(2\varepsilon_1 + \varepsilon_3)(2\varepsilon_3 + \varepsilon_2)} \frac{a^3}{b^3} - 2 \frac{(\varepsilon_1 - 1)(\varepsilon_1 - \varepsilon_3)}{(\varepsilon_1 + 2)(2\varepsilon_1 + \varepsilon_3)} \frac{b^3}{c^3} - 2 \frac{(\varepsilon_1 - 1)(\varepsilon_1 + 2\varepsilon_3)(\varepsilon_3 - \varepsilon_2)}{(\varepsilon_1 + 2)(2\varepsilon_1 + \varepsilon_3)(2\varepsilon_3 + \varepsilon_2)} \frac{a^3}{c^3} \quad (6.5)$$

$$l = \frac{(\varepsilon_1 - 1)}{(\varepsilon_1 + 2)} j - \frac{(2\varepsilon_1 + 1)m}{(\varepsilon_1 + 2)(2\varepsilon_1 + \varepsilon_3)} \frac{b^3}{c^3} \quad (6.6)$$

where  $j$  and  $m$  are given by:

$$j = 1 + 2 \frac{(\varepsilon_1 - \varepsilon_3)(\varepsilon_3 - \varepsilon_2)}{(2\varepsilon_1 + \varepsilon_3)(2\varepsilon_3 + \varepsilon_2)} \frac{a^3}{b^3} \quad (6.7)$$

$$m = (\varepsilon_1 - \varepsilon_3) + \frac{(\varepsilon_1 + 2\varepsilon_3)(\varepsilon_3 - \varepsilon_2)}{(2\varepsilon_3 + \varepsilon_2)} \frac{a^3}{b^3} \quad (6.8)$$

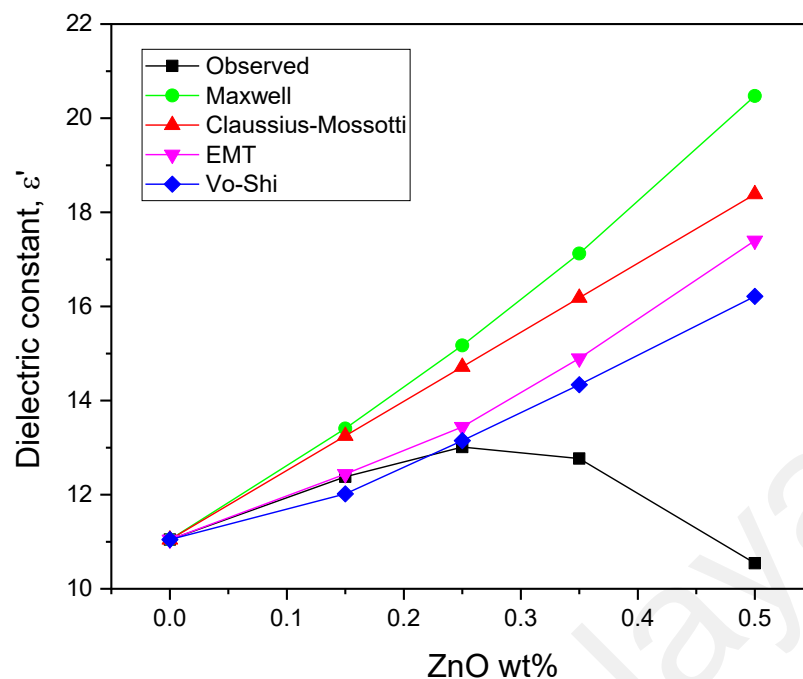
In Equations 6.7 and 6.8,  $\varepsilon_1$ ,  $\varepsilon_2$ , and  $\varepsilon_3$  are the dielectric constants of polymer, filler and interphase composite respectively, and  $a$  is the radius of filler,  $(b-a)$  is the thickness of the interphase region and  $c$  is the radius of the equivalent composite as shown in Figure 6.11.  $a^3/b^3$ ,  $b^3/c^3$  and  $a^3/c^3$  are given respectively by:

$$\frac{a^3}{b^3} = \frac{1+k\phi}{1+k} \quad (6.9)$$

$$\frac{b^3}{c^3} = \phi \left[ 1 + k \frac{(1-\phi)}{(1+k\phi)} \right] \quad (6.10)$$

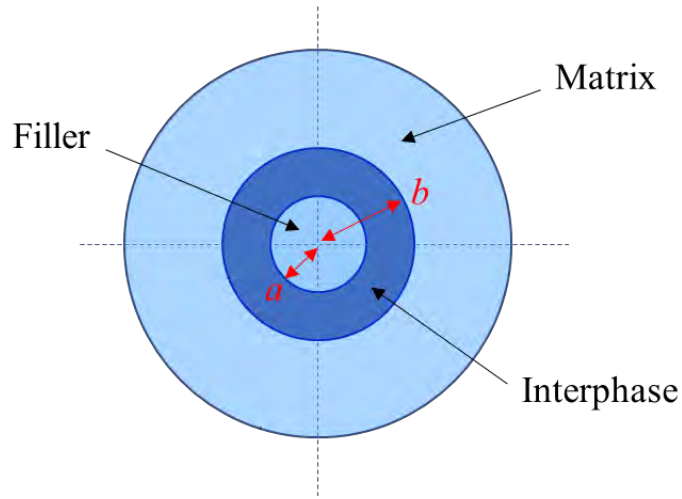
$$\frac{a^3}{c^3} = \phi \quad (6.11)$$

where  $k$  is a parameter related to the size of the filler and  $\phi$  is the volume fraction of the filler. Moreover, the value of  $k$  also reflects the matrix/filler interaction strength. All parameters mentioned above are known, except for  $k$  and  $\varepsilon_3$ , which need to be fitted. The known parameters obtained from the experimental results are  $\varepsilon_1 = 11.05$  and  $\varepsilon_2 = 35.6$  at 10 kHz. The Vo-Shi model fits the experimental data well, with  $k = 55$  and  $\varepsilon_3 = 10$  giving the best fit.



**Figure 6.10: Various models of the effective dielectric permittivity ( $\epsilon'$ ) as a function of the weightage of ZnO QDs, wt% at room temperature and 1 kHz.**

The high  $k$  values propose a strong interaction between the functional groups of the polymer and the surface of the filler which cannot be detected through FTIR results. Figure 6.11 shows the schematic diagram of polymer/filler composite materials consisting of filler particles, interphase and polymer matrix. Therefore, the obtained effective dielectric constant could be attributed to the size of the filler used in this work. For a given volume fraction of filler, smaller particle size has a larger fraction of the interphase volume, that is the area between the filler and the polymer matrix which indicates more polarization in the interphase surface (Nioua et al., 2017; Tan et al., 2014).



**Figure 6.11: Schematic diagram of polymer / filler composite materials consisting of filler particle, interphase and matrix (Vo & Shi, 2002).**

The effective medium theory (EMT) model has been established by taking into consideration the morphology of the inclusions. The effective dielectric response of the EMT model is given by;

$$\varepsilon = \varepsilon_1 \left[ 1 + \frac{\phi(\varepsilon_2 - \varepsilon_1)}{\varepsilon_1 + n(\varepsilon_2 - \varepsilon_1)(1 - \phi)} \right] \quad (6.12)$$

where  $n$  is the morphology fitting constant, corresponds to the shape of the ellipsoidal particle and their orientation with composite film surface material. The value of  $n$  is greatly affected by the change in the morphology factor. The experimental values were found to fit this model with the shape parameter  $n = 0.9$ . A high value of  $n$  indicates largely non-spherical particles, which is inconsistent with the picture of ZnO quantum dots shown by nearly spherical TEM results. Therefore, the prediction of a near-spherical filler shape in the nanocomposite P(VDF-TrFE) / ZnO QDs that contribute to the improvement of the dielectric is not supported in the present work. Moreover, when more than 0.25 deteriorates are doped into the copolymer P(VDF-TrFE), both Vo-Shi and EMT models no longer fit the experimental data due to the high leakage current (see Figure 5.6) and the appearance of micelle-like hole structures as shown by FESEM in Figure 4.18 which deteriorates the functional properties of composite devices.

A model developed by Clausius Mossotti (Thomas et al., 2010), was used to predict the effective dielectric constant using the following equation:

$$\varepsilon = \varepsilon_1 \left[ 1 + 3\phi \frac{(\varepsilon_2 - \varepsilon_1)}{(\varepsilon_2 + 2\varepsilon_1)} \right] \quad (6.13)$$

where  $\varepsilon_1$ ,  $\varepsilon_2$  and  $\phi$  refer to the dielectric constants of the polymer matrix and filler and the volume fraction of the filler, respectively. However, the predicted effective dielectric constant from this model deviates from the experimental value.

The Maxwell-Wagner model is also used to fit the experimental result. This model assumes that the equal-sized spherical fillers are isolated from each other and will not experience a field induced by other spherical fillers. The formula is given by (Thomas et al., 2010):

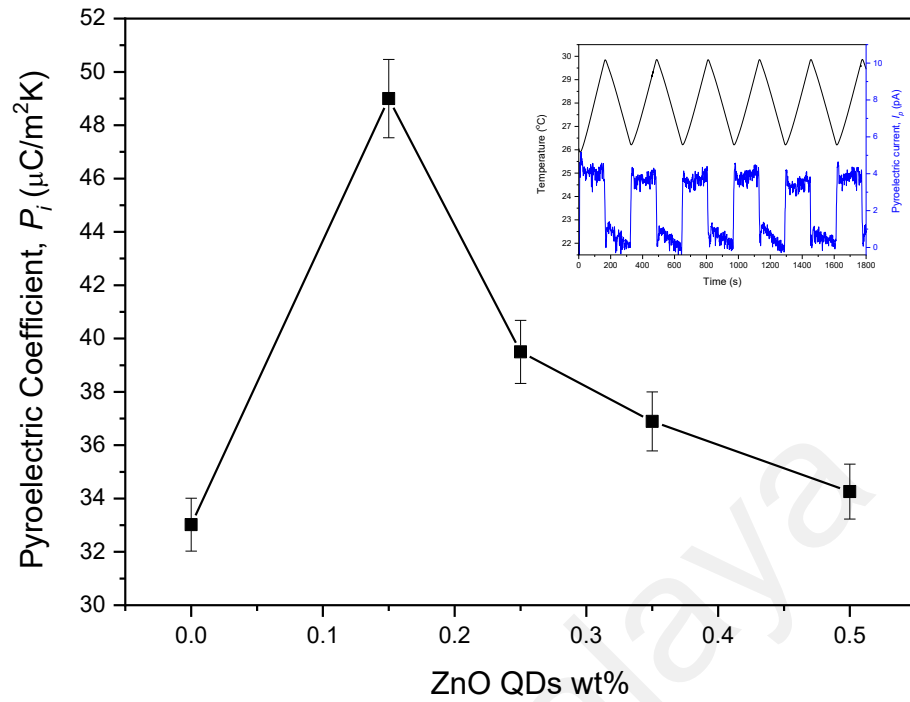
$$\varepsilon = \frac{\varepsilon_1 \left[ 1 + 3\phi \frac{(\varepsilon_2 - \varepsilon_1)}{(\varepsilon_2 + 2\varepsilon_1)} \right]}{(1-\phi) \left( \frac{2}{3} + \frac{\varepsilon_2}{3\varepsilon_1} \right) + \phi} \quad (6.14)$$

where  $\varepsilon_1$ ,  $\varepsilon_2$  and  $\phi$  refer to the dielectric constants of the polymer matrix and filler and the volume fraction of the filler, respectively. However, the predicted values from this model, however, appear to deviate by large orders of magnitude from the observed experimental data for filler volume fractions greater than 0.25 wt%. The experimental data cannot fit well into Claussius-Mossotti and Maxwell-Wagner because these models do not consider the presence of interphase, which exists between the polymer and filler.

## 6.7 Pyroelectric activity of P(VDF-TrFE) / ZnO QDs nanocomposite thin film

The pyroelectric coefficient of the P(VDF-TrFE) / ZnO QDs nanocomposite thin films was measured using the quasi-static measurement method. The experimental procedures mentioned in the earlier section (Section 6.3) including the temperature range and equation for the pyroelectric coefficient are followed. Triangular temperature waveforms with six heating rates utilized in this experiment by a Lakeshore 331 temperature controller were 0.02 °Cs<sup>-1</sup>, 0.025 °Cs<sup>-1</sup>, 0.03 °Cs<sup>-1</sup>, 0.035 °Cs<sup>-1</sup>, 0.04 °Cs<sup>-1</sup> and 0.05 °Cs<sup>-1</sup>. Pyroelectric materials respond to changes in temperature which cause internal strain and in turn, result in

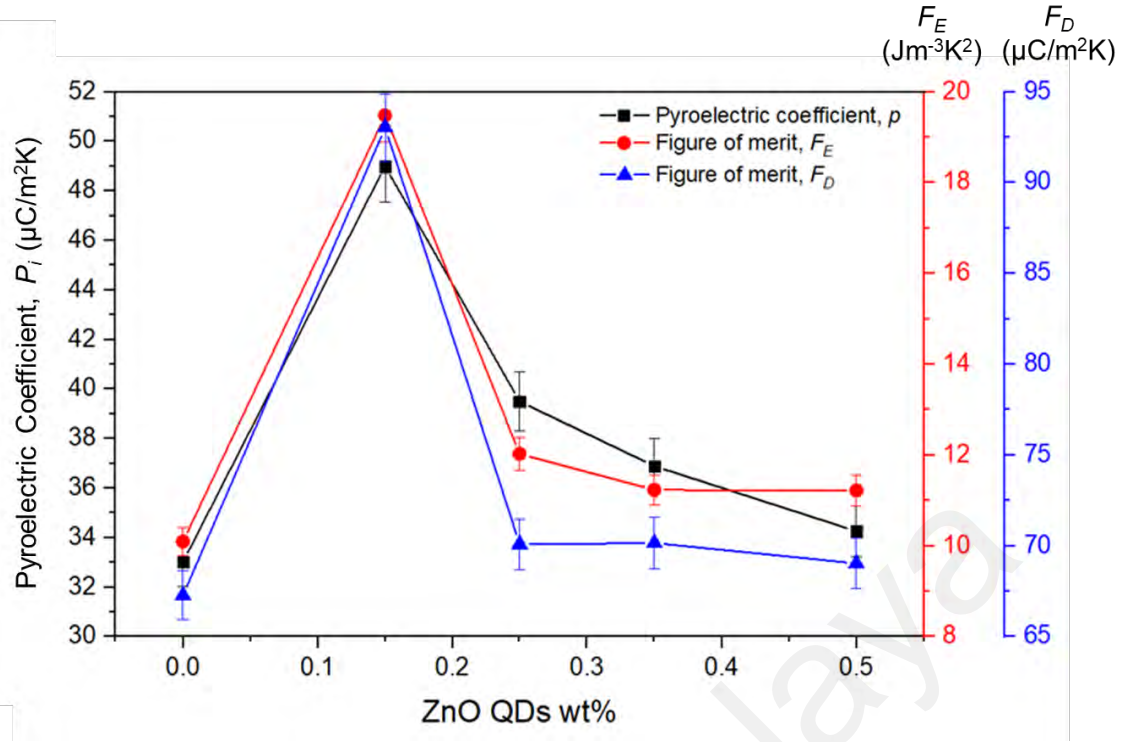
an electrical charge on the material surface. Figure 6.12 shows that the pyroelectric coefficient improved by 50% from pure PVDF-TrFE from 31 to 49  $\mu\text{C}/\text{m}^2\text{K}$  at 0.15 wt% P(VDF-TrFE) / ZnO QDs. The inset figure shows the pyroelectric signal observed in all composite films. Galsin (Galsin, 2019) reported that the ZnO wurtzite structure has non-centrosymmetric and anisotropic crystalline which may contribute to piezoelectric and pyroelectric. The wurtzite structure was formed by tetrahedral unit cells where the zinc atom is located at the centre and the oxygen atoms at the four corners. All the tetrahedral units are stacked and oriented in one direction, assembling the wurtzite hexagonal symmetry which is known as the non-central symmetric crystal structures of wurtzite ZnO (Sadeghi et al., 2020). Besides that, the polar surfaces of ZnO itself where the oppositely charged ions produced positively charged  $\text{Zn}^+$  and negatively charged  $\text{O}^-$  surfaces, which result in a normal dipole moment and spontaneous polarization along the axis (Huang et al., 2021). The interfacial polarization may arise from the interaction between the nanofiller and polymer matrix through poling process and may contribute to the increment of remnant polarization and pyroelectric coefficient obtained in this work. Tan et al. (Tan et al., 2014) suggested that the addition of ZnO nanoparticles in the nanocomposite thin films enhances the local electric field during the poling process in the polymer matrix at the boundary of the ZnO nanoparticle. The above-mentioned paper reported that doping a pure PVDF thin film with a higher wt% ZnO did not increase the pyroelectric coefficient of the nanocomposite thin film but caused the thin film to deteriorate due to the increase in DC conductivity during the poling process. When the weight percentage of the ZnO QD was greater than 0.15 by weight, it was found that its pyroelectric coefficient deteriorated which is paralleled to that of ferroelectric properties.



**Figure 6.12:** The pyroelectric coefficient ( $P_i$ ) with a respective filler content of nanocomposite films. The inset figure shows the pyroelectric current waveform.

### 6.8 Energy harvesting and sensor Figure of Merit (FOM) of nanocomposite films P(VDF-TrFE) / ZnO QDs

The results obtained by pyroelectric measurement were further analyzed for potential energy harvesting applications. The figure of merit (FOM),  $F_E$  is an indicator used to perceive the energy harvesting performance of a pyroelectric device which is expressed in Equation (6.3) in Section 6.3.1. The spectrum of  $F_E$  calculated at 1 kHz is shown in Figure 6.13 below. The maximum  $F_E$  calculated at 1 kHz is  $19.5 \text{ Jm}^{-3}\text{K}^2$ , obtained from P(VDF-TrFE) / ZnO QDs composite film at 0.15 wt%, and it decreases to  $11.2 \text{ Jm}^{-3}\text{K}^2$  for 0.50 wt%.  $F_D$  reaches a maximum of  $93 \text{ } \mu\text{C}/\text{m}^2\text{K}$  at 0.15 wt% of ZnO QDs. The inclusions of ZnO QDs significantly improved the energy harvesting performance and thermal sensing of nanocomposite devices and were optimum for the films incorporated with 0.15 wt% of ZnO QDs (Navid et al., 2010).



**Figure 6.13: Dependence of pyroelectric coefficient ( $P_i$ ) with energy harvesting figure of merit ( $F_E$ ) and detectivity figure of merit ( $F_D$ ) on various of P(VDF-TrFE) / ZnO QDs nanocomposite films.**

The performance of the developed P(VDF-TrFE) / ZnO QDs nanocomposite compared with other reported works is presented in Table 6.1. The calculated discharged energy density for the polymer matrix using P(VDF-TrFE) in this work (elaborated in Chapter 5) is comparable with other reported work. This study indicates that a device made with P(VDF-TrFE) / ZnO QDs showed good functionality with less than 1% ZnO QDs in the P(VDF-TrFE) copolymer.



**Table 6.1. The PVDF and P(VDF-TrFE) based composite systems**

Polymer matrix	Filler	$P_r$ (mC/m <sup>2</sup> )	$E_c$ (MV/m)	$P_i$ ( $\mu$ C/m <sup>2</sup> K)	FOM, $F_E$ (Jm <sup>-3</sup> K <sup>2</sup> )	Discharge energy density (J/cm <sup>3</sup> )	Ref.
PVDF	ZnO	-	-	29	-	-	(Tan et al., 2014)
PVDF	La <sub>2</sub> O <sub>3</sub>	84	300	42	-	-	(Gan & Majid, 2015)
PVDF-TrFE	Ca-doped ZnO	6.04	41	-	-	1.19	(Sahoo et al., 2020)
PVDF-TrFE	BNT-CeO <sub>2</sub>	166	55	43	-	-	(Halim & Halim, 2018)
PVDF-TrFE	BNT-BKT-BT	130	70	90	-	1.25	(Mahdi et al., 2018)
PVDF-TrFE	ZnO QDs	102	64	49	19.5	1.18	This work

## 6.9 Conclusion

In this study, 2–3.5 nm ZnO quantum dots were embedded into P (VDF-TrFE) to enhance their dielectric and pyroelectricity. By monitoring the pyroelectric current in response to the applied temperature, the pyroelectric coefficient of P(VDF-TrFE) and its nanocomposite films were extracted based on Equation 6.1. The incorporation of 0.15 wt% ZnO QDs into the polymer host significantly enhanced the dielectric constant ( $\epsilon' = 13.9$ ) and pyroelectric coefficient (49  $\mu$ C/m<sup>2</sup>K) compared to those of pure P(VDF-TrFE) due to the greater distribution of micelle-like crystallites and the growth of elongated rod-like crystallites. The maximum  $F_E$  and  $F_D$  calculated at 1 kHz obtained from P(VDF-TrFE) / ZnO QDs composite film at 0.15 wt% are 19.5 Jm<sup>-3</sup>K<sup>2</sup> and 93  $\mu$ C/m<sup>2</sup>K, respectively. The polarization of the noncentrosymmetric crystal structure of ZnO interacts synergistically with the P(VDF-TrFE) polymer host which contributes to the increase in ferroelectric and pyroelectric properties up to 0.15 wt% composition. As with the ferroelectric observation, the poor pyroelectric performance exhibited by the thin films with ZnO QD fillers above 0.25 wt% may also be related to the high leakage current density and the occurrence and distribution of a micelle-

like hole structure, as indicated by FESEM characterization. The surface morphology and polarization are interrelated and influence the ferroelectric (refer to Chapter 5) and pyroelectric properties of the nanocomposite device. The new advanced materials developed in this research can be exploited to design a pertinent device that is suitable for energy storage and energy harvesting applications.

Universiti Malaya

## **CHAPTER 7: THERMALLY STIMULATED CURRENT (TSC) OF COPOLYMER P(VDF-TrFE) AND COMPOSITE FILMS**

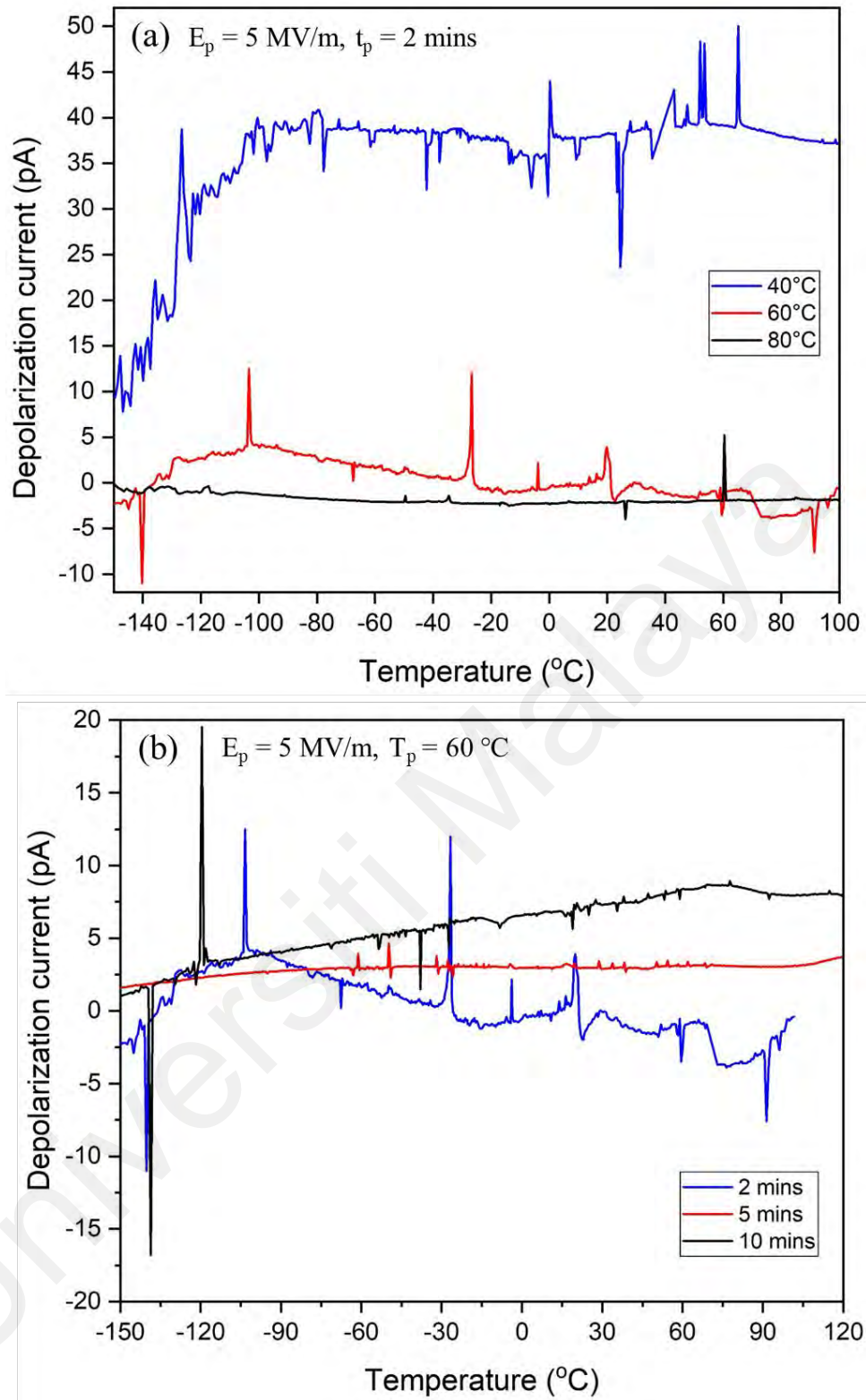
### **7.1 Introduction**

Thermally stimulated current (TSC) studies are carried out on cast and annealed samples of P(VDF-TrFE) copolymers and P(VDF-TrFE) / ZnO QDs nanocomposite films as the final goals of this research work. Basic evaluations on TSC thermograms of P(VDF-TrFE) are performed by comparing the results with those from the DSC technique. The preliminary analysis in this chapter is also very important to demonstrate the sensitivity and reliability of the TSC technique. TSC results from an electric current observed during heating caused by the thermally initiated relaxation of the frozen electric polarization of a sample. TSC is commonly performed to provide information about molecular mobility in the solid state and as a result to characterize phase transitions related to thermal transitions in the crystalline and amorphous phases. Therefore, it is crucial to investigate possible relaxation spectra and activation energies and other thermal features in the thermogram of P(VDF-TrFE) and nanocomposite P(VDF-TrFE) / ZnO QDs films to find the correlation with the thermal transition, morphological and other properties.

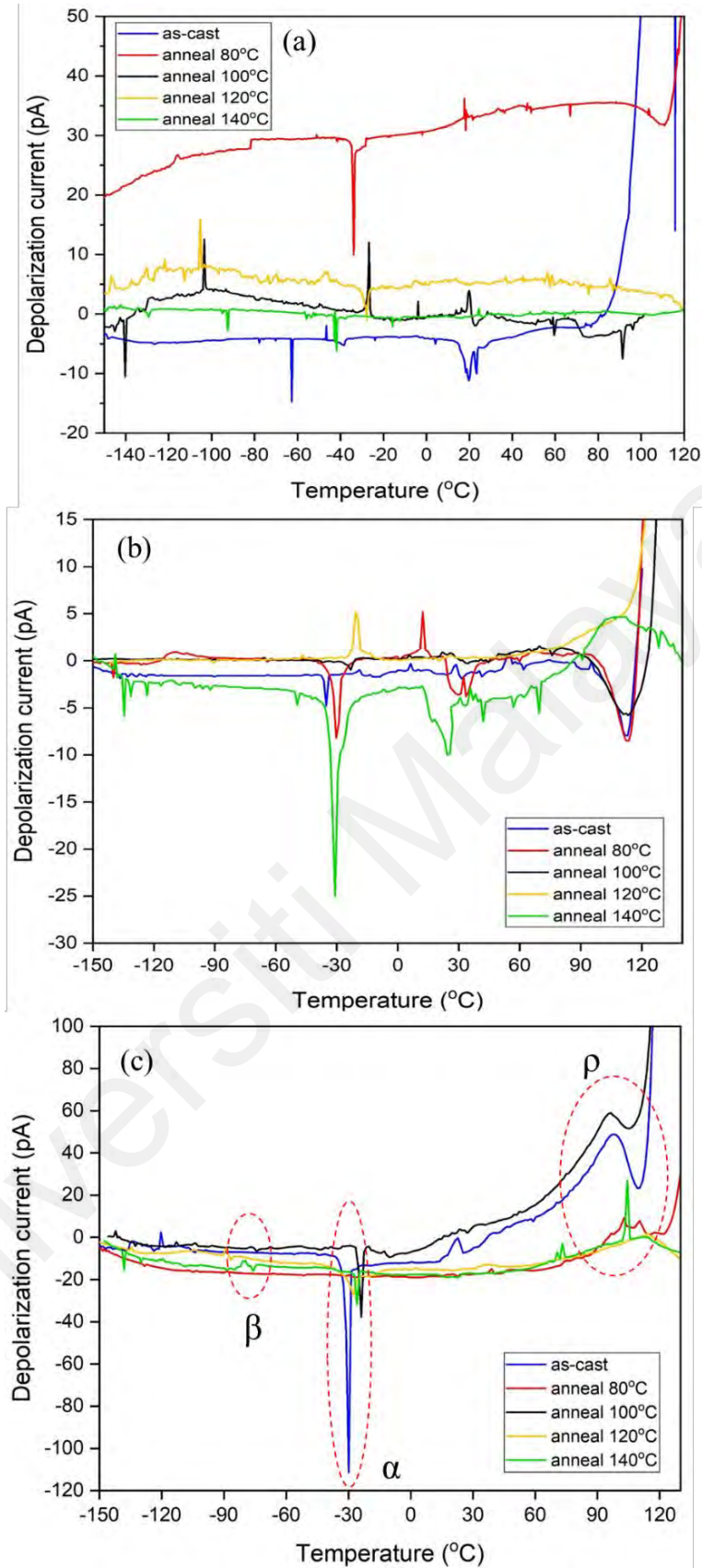
### **7.2 TSC analysis of copolymer P(VDF-TrFE) at different annealing temperatures**

The measurement procedure and settings were explained in detail in Section 3.5.4. Many attempts at TSC measurement have been made to find optimized setting parameters for P(VDF-TrFE) films as illustrated in Figure 7.1 and Figure 7.2. The annealed films at 100 °C were subjected to TSC measurement for a preliminary test at selected poling temperatures,  $T_p$ ; 40 °C, 60 °C and 80 °C as shown in Figure 7.1(a). The sample is subjected to a static electric field of about 5 MV/m at the selected polarization temperature for a poling time of  $t_p = 2$  mins which allows the orientation of the dipolar units of P(VDF-TrFE) (Menegotto et al., 1999).

The depolarized current gives the best spectrum (TSC peaks appear with greater intensity and emerged at possible relaxation peaks as reported by Teyssedre et al.(1993a) with the same mol ratio of P(VDF-TrFE)) at a poling temperature of 60 °C. Therefore, the measurements were continued to find the optimal poling time at  $T_p = 60$  °C and an electric field of 5 MV/m (see Figure 7.1(b)). However, it seems that 10 minutes (for Figure 7.1(b)) and 5 MV/m electric fields for the depolarization process of P(VDF-TrFE) were not sufficient to give the best appearance of  $T_g$  and  $T_c$  peaks. All samples were then subjected to various TSC measurement conditions as shown in Figure 7.2 to observe the relaxation behaviour, particularly around  $T_g$  and  $T_c$  peaks. The TSC spectrum for all samples as indicated in Figure 7.2(a) were observed at setting parameters;  $T_p = 60$  °C,  $t_p = 2$  min,  $E = 5$  MV/m and heating rate 5 °C/min. Figure 7.2(b) is the TSC spectrum for P(VDF-TrFE) with setting parameters;  $T_p = 60$  °C,  $t_p = 10$  min,  $E = 10$  MV/m and heating rate 5 °C/min. The spectrum could show  $T_g$  and  $T_c$  relaxation peaks for all samples, but since the coercivity field of ferroelectric polymers is typically higher than 50 MV/m, the poling time was increased to 20 minutes and the poling field to 20 MV/m, which far below the coercive field (refer to Figure 7.2(c)) (Bai et al., 2003). Various dipoles and space charges relaxations of as-cast and annealed semi-crystalline copolymer P(VDF-TrFE) films were observed in the optimized TSC complex spectrum as shown in Figure 7.2(c), with the appearance of  $\beta$ ,  $\alpha$  and  $\rho$  peaks.



**Figure 7.1: TSC complex spectrum of P(VDF-TrFE) 72/25 for 100 °C anneal films at (a) vary poling temperatures (b) varied times of poling.**



**Figure 7.2** TSC complex spectrum of P(VDF-TrFE) 72/25 for as-cast film and all anneal films at various setting parameters (a)  $T_p = 60^\circ\text{C}$ ,  $t_p = 2$  min,  $E = 5$  MV/m (b)  $T_p = 60^\circ\text{C}$ ,  $t_p = 10$  min,  $E = 10$  MV/m and (c)  $T_p = 60^\circ\text{C}$ ,  $t_p = 20$  min,  $E = 20$  MV/m.

The obtained peaks of depolarization current from Figure 7.2(c) are compared with other works and tabulated in Table 7.1. The  $\alpha$ -PVDF and  $\beta$ -PVDF films with poling temperature of 80 °C observed by Teyssedre et al. (1993b) show no depolarization peak below  $T_g$  ( $T_g$  labeled as  $\alpha_1$  peak in Table 7.1). Teyssedre et al. (1993b) reported a broadening of the  $\alpha_1$  peak (glass transition temperature) and a decrease in its intensity observed for  $\beta$ -PVDF compared to  $\alpha$ -PVDF which is due to the increase in the crystallinity phase of  $\beta$ -PVDF after stretching. This phenomenon is observed in the TSC spectrum of annealed P(VDF-TrFE) as depicted in Figure 7.2(a)-(c). The annealing process affected the intensity of the TSC peak at  $T_g$  due to the increment of crystalline phase in the samples. The  $\alpha_2$  relaxation peak for both  $\alpha$ -PVDF and  $\beta$ -PVDF observed by Teyssedre et al. suggests that the molecular motions at the surface of the crystalline lamellae might be preferentially oriented perpendicularly to the films. With the addition of TrFE into PVDF, it shows that the  $T_g$  or  $\alpha_1$  peak shifted to the higher temperature and the Curie peak  $T_c$  or  $\rho$  emerged at  $\sim 100$  °C. The reported glass transition temperature value,  $T_g$  for P(VDF-TrFE) is  $\sim -39$  °C (Furukawa, 1997). The TSC setting parameters of the present work were equivalent to the work reported by Bai et al. (2003). However, this work managed to observe the lower temperature relaxation peaks ( $\beta$  and  $\alpha_1$ ) and the higher temperature relaxation peaks ( $\alpha_2$  and  $\rho$ ) that occurred at lower temperatures compared to that reported by Bai et al.(2003). The relaxation peaks are of  $\beta$ ,  $\alpha_1$ ,  $\alpha_2$  and  $\rho$  of this work is equivalent to the work reported by Teyssedre & Lacabanne (1993) using the same molar ratio of the copolymer P(VDF-TrFE). The TSC relaxation peaks in Table 7.1 shift to higher temperatures as the molar content of TrFE increases for as-cast P(VDF-TrFE) films by Teyssedre et al. (Teyssedre et al., 1993a) and Capsal (Capsal et al , 2013).

**Table 7.1: TSC parameters of copolymer films**

P(VDF) & Mol Ratio of P(VDF-TrFE)	Poling Temp. (°C)	Poling Field (MV/m)	Poling Time (min)	Peak Position (°C)				Ref.
				$\beta$	$\alpha_1$ ( $T_g$ )	$\alpha_2$	$\rho$ (Curie)	
$\alpha$ -PVDF $\beta$ -PVDF	80	5	2	- -	-50 -50	50 50	- -	(Teyssedre et al., 1993b)
70/30 P(VDF-TrFE) As-cast	110	3	*	-	-24	-	103	(Capsal, et al., 2013)
75/25 P(VDF-TrFE) As-cast	100	5	2	-	-34	50	-	(Teyssedre et al., 1993a)
75/25 P(VDF-TrFE) Anneal 140 °C				-80	-34	102	100	
70/30 P(VDF-TrFE) Anneal 125-130 °C	60	20	20	*	*	63	113	(Bai et al., 2003)
65/35 P(VDF-TrFE) Ascast	40	5	2	-120	-33	35	110	(Menegotto et al., 1999)
75/25 P(VDF-TrFE) As-cast	60	20	20	-	-29.8	21.9	97.3	Present work
75/25 P(VDF-TrFE) Anneal 100 °C				-75.5	-23.8	27.4	96.3	

\* no information

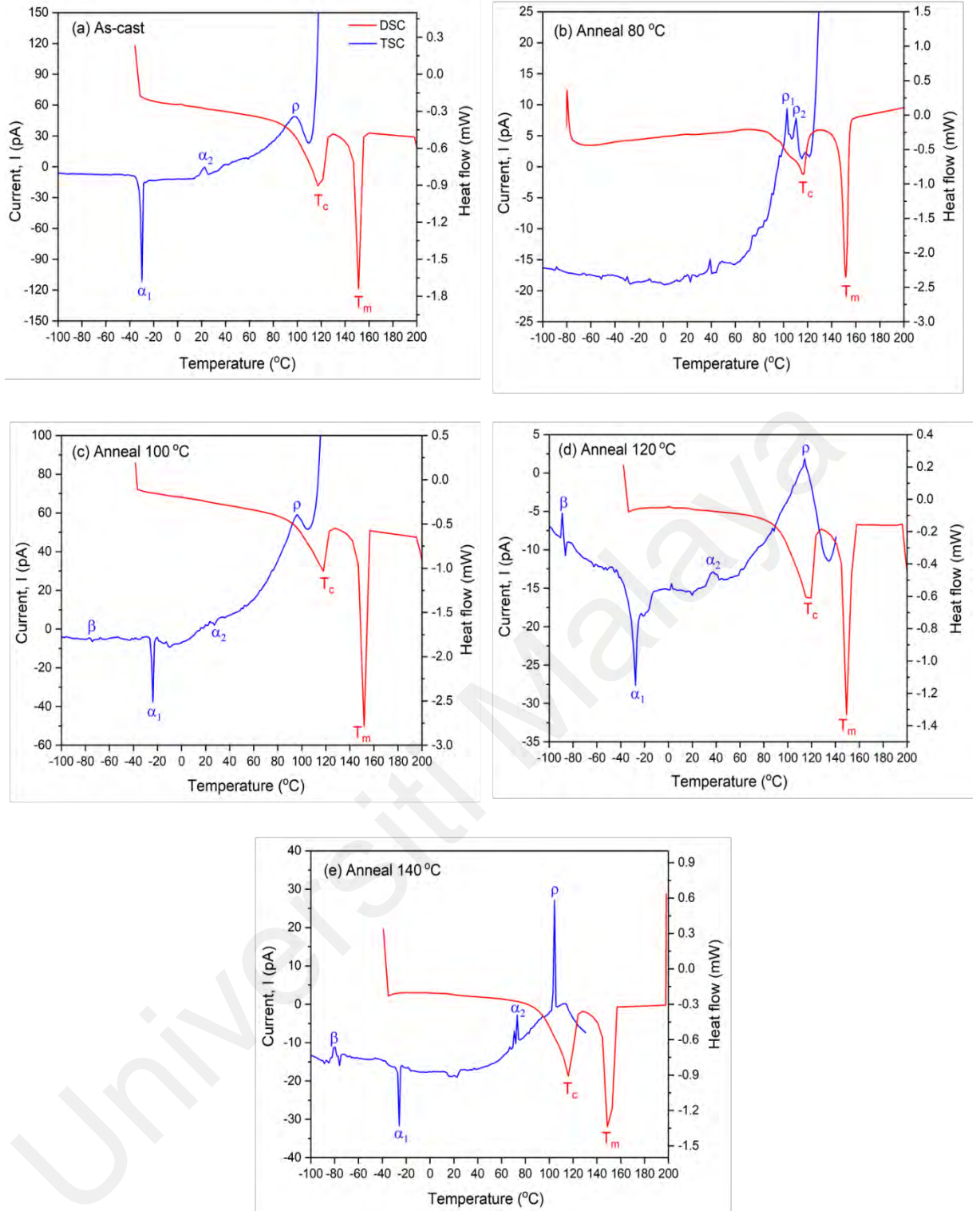
The DSC and the complex TSC thermograms of P(VDF-TrFE) were plotted in the same graph as shown in Figure 7.3(a)-(e) which constituted from the thermal behaviour of both crystalline and amorphous phase with poling temperature of 60 °C and poling field of 20 MV/m. No thermal transition was observed within the range of known  $T_g$  (-40 °C to -0 °C) for all samples in the DSC spectrum, which depicted as  $\alpha$  peak or related to the amorphous region of P(VDF-TrFE). The DSC scan for all films was discussed earlier in section 4.2.3 in Chapter 4 (see Figure 4.7). For the as-cast copolymer film, with no preheat or annealing history, three relaxation modes appeared in the TSC spectrum as shown in Figure 7.3(a). The  $\alpha_1$ ,  $\alpha_2$  and  $\rho$  relaxations are centred at -29.8 °C, 21.9 °C and 97.3 °C respectively. The  $\alpha_1$  mode



corresponds to the glass rubber transition attributed to dipolar relaxation in the amorphous phase. This peak is in good agreement with the same molar ratio copolymer film as reported by Teyssedre et al. (Teyssedre et al., 1993a). TSC measurement is capable of revealing glass transition temperature,  $T_g$  which was initially undetected from DSC spectra. In the high-temperature range, a broad peak around 100 °C is depicted as  $\rho$  peak. This mode is associated with Curie transition (from ferroelectric to paraelectric transition) due to dipolar relaxation in the crystalline phase of the copolymer. A shoulder appears at 21.9 °C known as  $\alpha_2$  which is ascribed as the upper component of the amorphous phase constrained by crystallites (Teyssedre et al., 1993a). Upon annealing at 100 °C,  $\beta$  peak emerged at a lower temperature region of  $\sim -80$  °C as shown in Figure 7.3(c). Moreover, the magnitude of  $T_g$  at -25 °C (from TSC) decreases whilst that of  $T_c$  increases. This phenomenon is due to enhancement of crystallinity of the film. Benrekaa et al. (Benrekaa et al, 2004) observed that the higher annealing temperature applied to the polyethylene terephthalate (PET) films have caused the reduction of peak intensity due to the amorphous phase ( $\alpha$  relaxation mode) and the emergence of a secondary peak corresponding to semi-crystalline phase. All other annealed films were consistently showing a  $T_g$  peak of  $\sim -30$  °C except for the film annealed at 80 °C where the peak seems to vanish from the spectrum. Further, at a higher heating temperature, the Curie mode for the film annealed at 80 °C was separated into two peaks of  $\rho_1$  and  $\rho_2$ . A similar trend is observed in the DSC thermogram for the sample. Broaden peaks of  $\beta$ ,  $\alpha_1$ ,  $\alpha_2$  and  $\rho$  are observed for the film annealed at 120 °C as shown in Figure 7.3(d). This is the annealing temperature at which, the molecule structure of P(VDF-TrFE) was in transition from ferroelectric to paraelectric phase. It can be observed that the mode of  $\alpha_2$  is shifted to a higher temperature and the Curie peak becomes sharper at 104 °C when the film was annealed above 100 °C as shown by the TSC spectrum in Figure 7.3(d) and (e). The temperature shift is probably due to the increment of  $\alpha$  phase (trans-gauche conformation) of PVDF (Mizutani et al., 1981) of the copolymer.

The  $\alpha_1$  peak representing the glass transition of the copolymer in the TSC complex spectrum for all samples appears in the direction of negative depolarization current while Curie peaks are on the positive sides of the depolarization current for all the copolymer samples. This phenomenon is probably due to polarity reversal which indicates the polarization-switching characteristics of P(VDF-TrFE) at a specific temperature. This is the first TSC spectrum of copolymer P(VDF-TrFE) which reveals this unique feature.

Universiti Malaya



**Figure 7.3: DSC (endothermic process) and TSC measurements for the (a) as-cast and, (b)-(e) Anneal P(VDF-TrFE) films.**

### 7.3 Decomposition on TSC peaks of As-cast and Anneal P(VDF-TrFE) at 100 °C

TSC peaks shown in Figure 7.2 were decomposed using the first-order kinetic theory to determine the type of relaxation processes that participated in the formation of TSC peaks (Sature et al., 1971). The equation used is stated below:

$$I(T) = I_m \exp \left[ 1 + \left( \frac{E}{kT} \right) \frac{(T - T_{max})}{T_{max}} - \frac{T^2}{T_{max}^2} \times \exp \left( \frac{E}{kT} \right) \frac{(T - T_{max})}{T_{max}} (1 - \Delta) - \Delta_{max} \right] \quad (7.1)$$

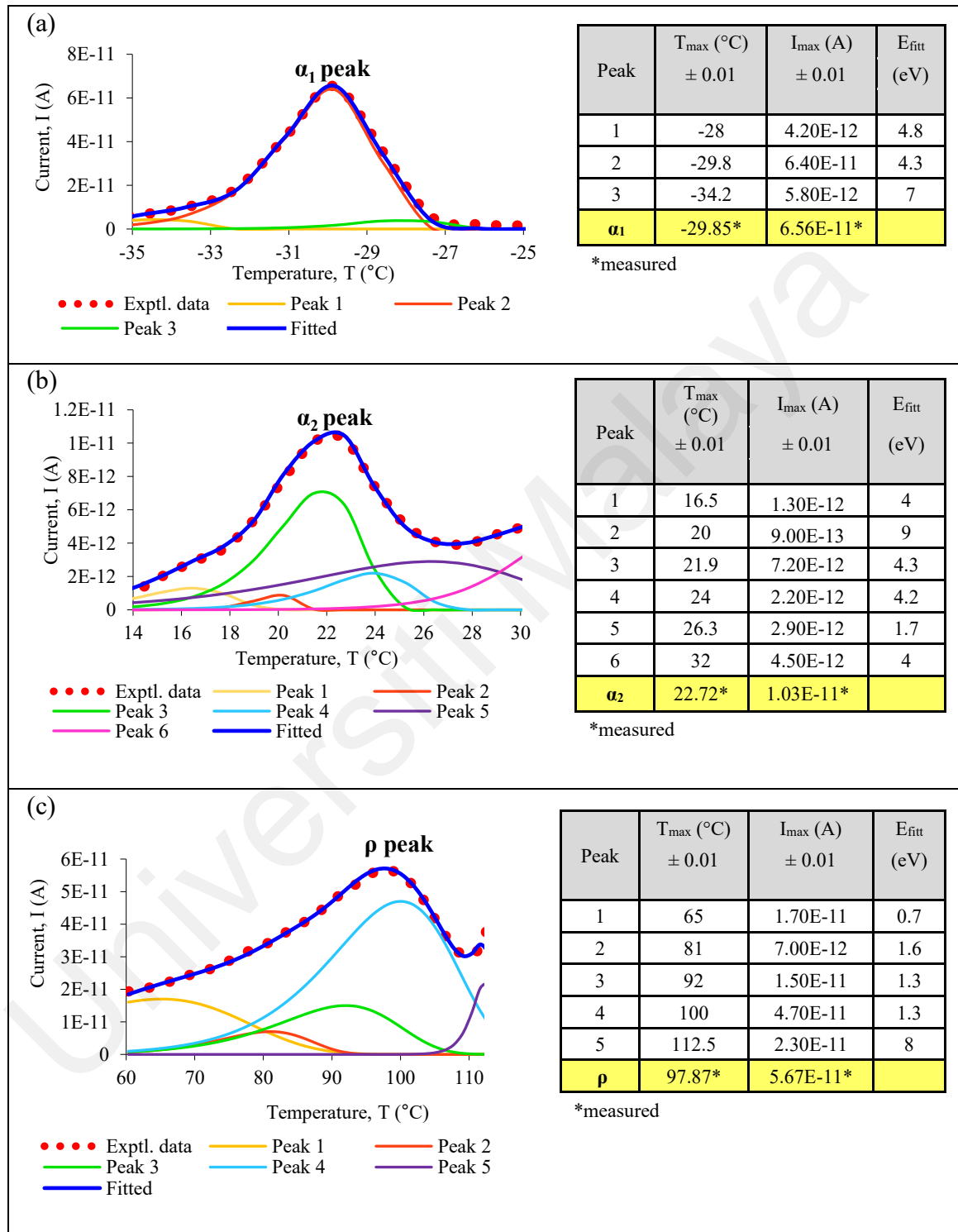
where  $I_m$ ,  $E$ ,  $k$ ,  $T$ ,  $T_{max}$  are the maximum current, activation energy, Boltzmann constant, temperature, maximum temperature and  $\Delta = 2kT/E$ ,  $\Delta_{max} = 2kT_{max}/E$ , respectively (Poulsen & Ducharme, 2010). This fitting method requires the utilisation of the temperature ( $T$ ) from TSC experimental data along with appropriate values for the activation energy ( $E$ ), the maximum current ( $I_m$ ) and the maximum temperature ( $T_{max}$ ) to generate a peak. Simultaneously monitoring the sum of current, ( $T$ ) values from the peaks to fit the TSC current,  $I$ . The activation energy ( $E$ ) is known as the amount of energy needed for a pair of positive and negative charges to rotate during the depolarization process, which for the copolymer film corresponds to hydrogen and fluorine as positive and negative charges to the carbon atom. Dipoles with low activation energies will disorient at low temperatures, while those polarized dipoles with high activation energies will disorient at relatively high temperatures.

The TSC complex spectrum for copolymer films is necessary to undergo baseline subtraction and shifting of the negative peaks to the positive sides as part of the peak deconvolution procedure. Only the as-cast and film annealed at 100 °C were deconvoluted since these two films gave a consistent TSC spectrum. The  $\alpha_1$ ,  $\alpha_2$  and Curie peaks for the as-cast film are centered at -29.8 °C, 21.9 °C and 97.3 °C respectively. Data fitting in Figure 7.4(a) to (c) shows the experimental peaks, decomposed peaks and summation of the peaks for the as-cast copolymer film. As the TSC heating process crosses their  $T_g(\alpha_1)$ , the segmental molecules receive enough thermal energy to assist the mobility of polarized and frozen main chains to depolarize and then randomize. This process involves the motion of about 40 to 50 carbon atoms on polymer backbones. However, the observed peak is sharp and intense, with a relatively high activation energy around 4.3 to 7 eV which is in contrast with that reported by (Capsal et al., 2013)(Teyssedre et al., 1993). This is probably due to the contribution of

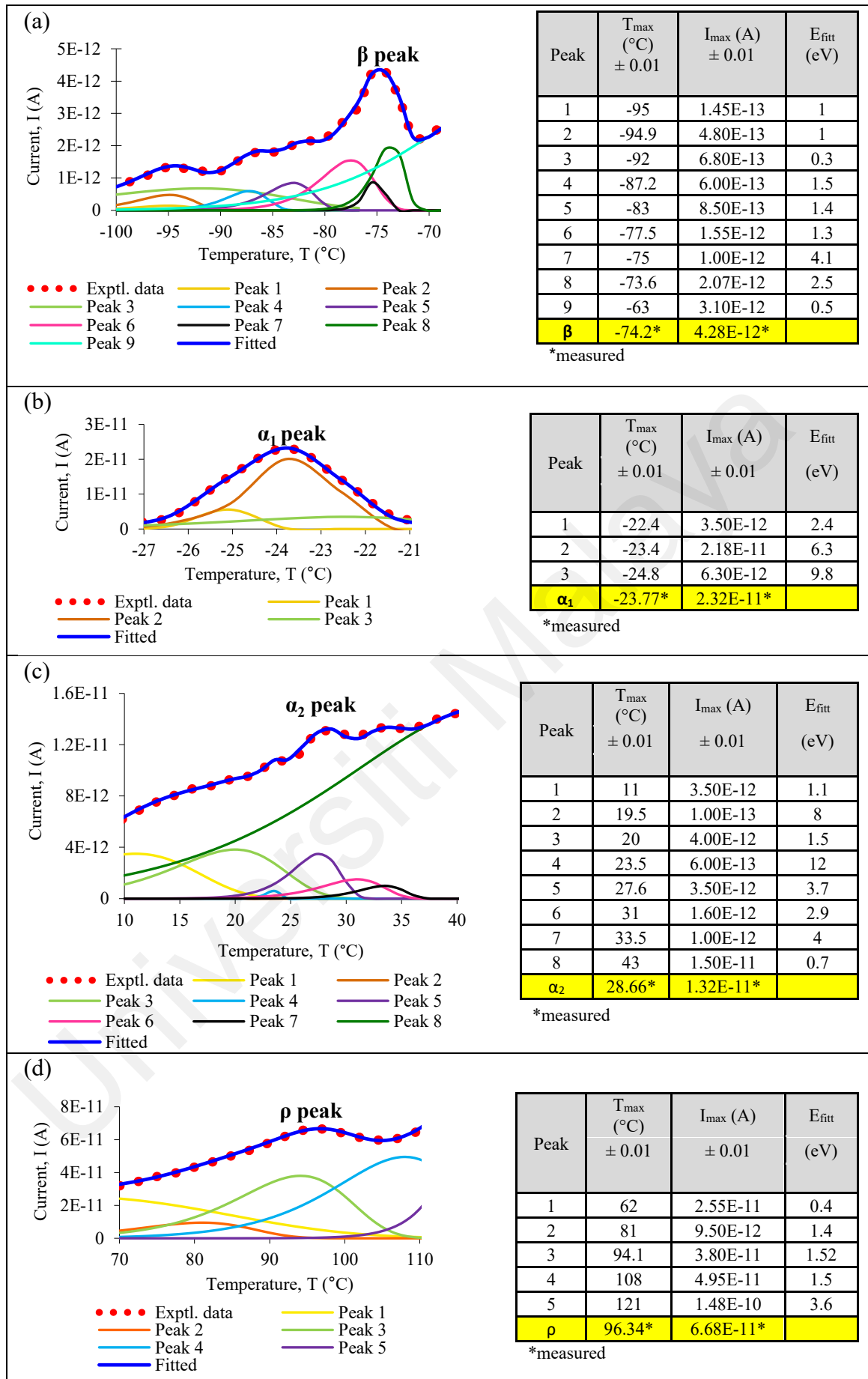
space charges injected at the sample-electrodes interfaces during the TSC poling process. The space charges are trapped within localized polarization in the polymers (Indolia & Gaur, 2013) or trapped along the chains or at the crystalline-amorphous boundaries (Eliasson, 1985). Further heating to 21.9 °C exhibits a peak known as  $\alpha_2$  peak. According to Teyssendre et al., this peak represents the molecular mobility of amorphous domains constrained by crystallites (Teyssendre et al., 1993). An increment in the heat supply gives enough activation energy around 1.7 to 9 eV for the polarized space charges to be released in the process. The sensitivity of the TSC system due to the temperature change enables it to reveal a transition called Curie mode ( $\rho$  peak), as also shown in the corresponding DSC spectrum. The activation energies of the decomposed peaks in this temperature region are around 0.7 to 8 eV. At this transition temperature, the activation energy involves the rotational motion of the molecules within the paraelectric crystalline phase (Napolitano, 2015).

The decomposed TSC peaks of the copolymer of P(VDF-TrFE) annealed at 100 °C are shown in Figure 7.5(a) to (d). There is a low intense peak observed at -75.5 °C which is around 52 °C below the glass transition temperature,  $T_g$ , for the film annealed at 100 °C as shown in Figure 7.5(a). This peak is identified as  $\beta$  peak. It is associated with the relaxation of side chains on the polymer backbone of the amorphous phase (Diogo & Ramos, 2008; Mzabi et al., 2009). This peak is contributed by nine decomposed peaks with various activation energies. The data fitting also demonstrates that the dipoles of the annealed film with frozen backbone chains have low activation energies around 0.3 eV to 4.1 eV. The values correspond to the energy movement needed for the localized polarization of the copolymer side chains. The relaxation mode of  $\alpha_1$  can be fitted from three decomposed peaks with activation energies in the range of 2.4 to 9.8 eV. The activation energy calculated is higher compared to that of as-cast film. It is because of the high crystallinity of the annealed copolymer used in this work. Further heating above  $T_g$  reveals the second relaxation peak,  $\alpha_2$  as shown in Figure 7.5(b), but with a very low intensity peak and the energy is around 0.7 to 8 eV. The molecular motion of the polarized dipole moments together with the injected space

charge at Curie mode,  $\rho$  is shown in Figure 7.5(d). The maximum activation energy for the  $\rho$  peak calculated is 3.6 eV.



**Figure 7.4: Decomposition of the TSC spectrum of the as-cast P(VDF-TrFE) film for  $\alpha_1$ ,  $\alpha_2$  and  $\rho$  relaxation peaks.**

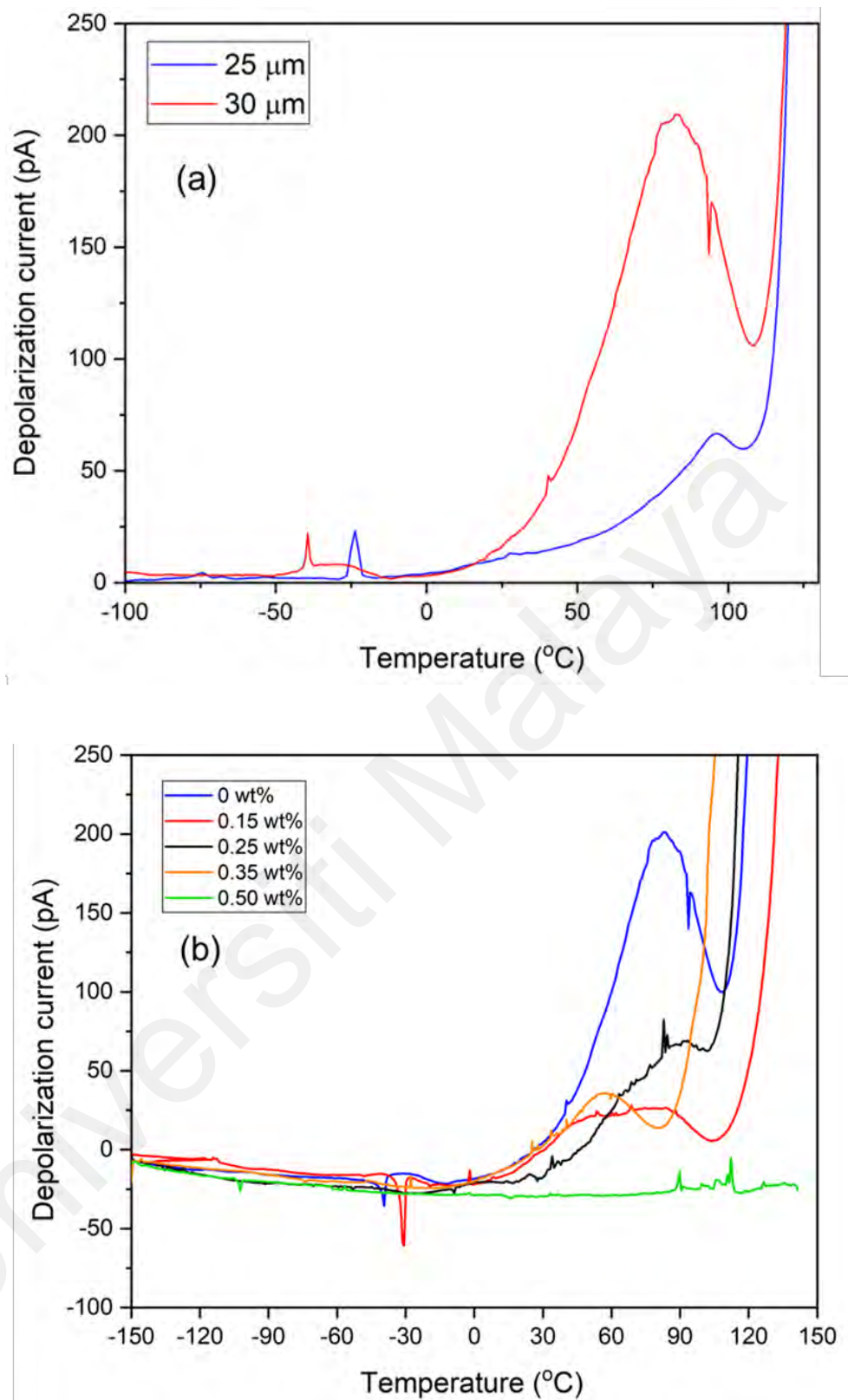


**Figure 7.5: Decomposition of the TSC spectrum of the annealed P(VDF-TrFE) at 100 °C for  $\beta$ ,  $\alpha_1$ ,  $\alpha_2$  and  $\rho$  relaxation peaks.**

#### 7.4 TSC analysis of composite P(VDF-TrFE) / ZnO QDs

TSC measurements of nanocomposite P(VDF-TrFE) / ZnO QDs films at 0, 0.15, 0.25, 0.35 and 0.50 wt% were performed at a poling temperature,  $T_p = 60\text{ }^{\circ}\text{C}$ , subjected to a static electric field of about 20 MV/m for a poling time,  $t_p = 20\text{ min}$ . The TSC complex spectra of the P(VDF-TrFE) / ZnO QDs films are presented in Figure 7.6(b). Sharp and intense peaks of  $T_g$  were observed for copolymer P(VDF-TrFE) and 0.15 wt% P(VDF-TrFE) / ZnO QDs films, at  $-39.4\text{ }^{\circ}\text{C}$  and  $-30.9\text{ }^{\circ}\text{C}$ , respectively. The glass transition peak,  $T_g$  is shifted to a higher temperature with higher intensity by the addition of ZnO QDs. However, the  $T_g$  peak seems to vanish with higher content of ZnO QDs, of more than 0.15 wt%. The thickness of the composite film series was 5  $\mu\text{m}$  thicker compared to the annealed film series (as presented in Section 7.2). The TSC spectrum of copolymer P(VDF-TrFE) prepared during the annealing series and composite series (commonly written as 0 wt%) was presented in Figure 7.6(a). The  $T_g$  and Curie peaks shifted to lower temperatures with the increase in the film thickness. The  $T_g$  intensity is similar for both films, but the 30  $\mu\text{m}$  film is closer to the reported  $T_g \sim -39\text{ }^{\circ}\text{C}$  (Furukawa, 1997). In addition, the Curie peak emerged at a greater intensity of the depolarization current for the 30  $\mu\text{m}$  film of P(VDF-TrFE). Therefore, the TSC of composite films (0.15, 0.25, 0.35 and 0.50 wt%) P(VDF-TrFE) / ZnO QDs were measured at an average thickness of 30  $\mu\text{m}$ ,  $T_p = 60\text{ }^{\circ}\text{C}$ ,  $E_p = 20\text{ MV/m}$  and  $t_p = 20\text{ min}$ . Similar TSC settings were used by Yang et al. for biaxially oriented PVDF (Yang et al., 2015). These TSC setting parameters ( $T_p$ ,  $E_p$  and  $t_p$ ) for the composite films are used for all the annealed composite thin films.





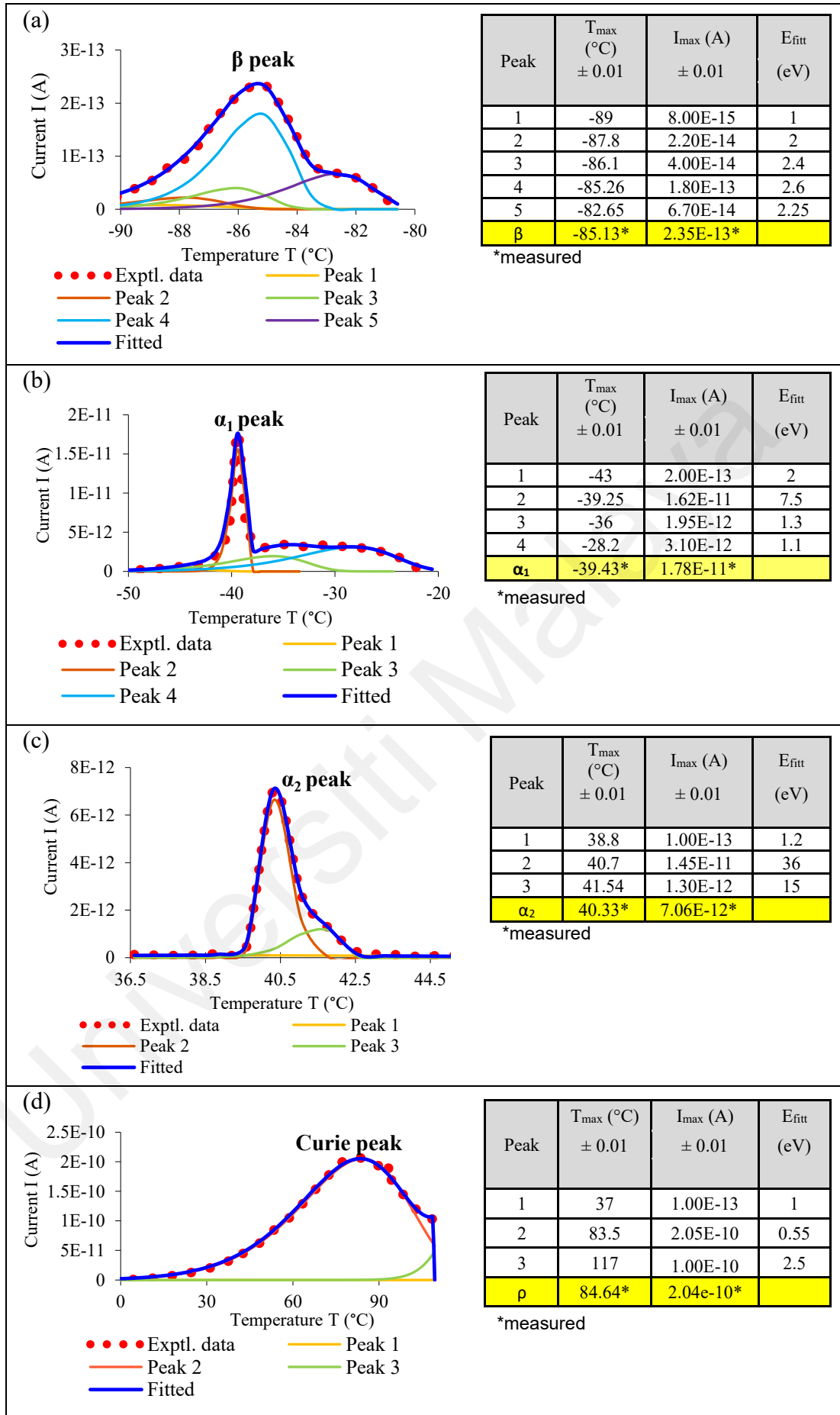
**Figure 7.6: TSC complex spectrum of (a) copolymer P(VDF-TrFE) at different thickness and (b) nanocomposite P(VDF-TrFE) / ZnO QDs of 30  $\mu\text{m}$  thickness.**

## 7.5 Decomposition of composite P(VDF-TrFE) / ZnO QDs films

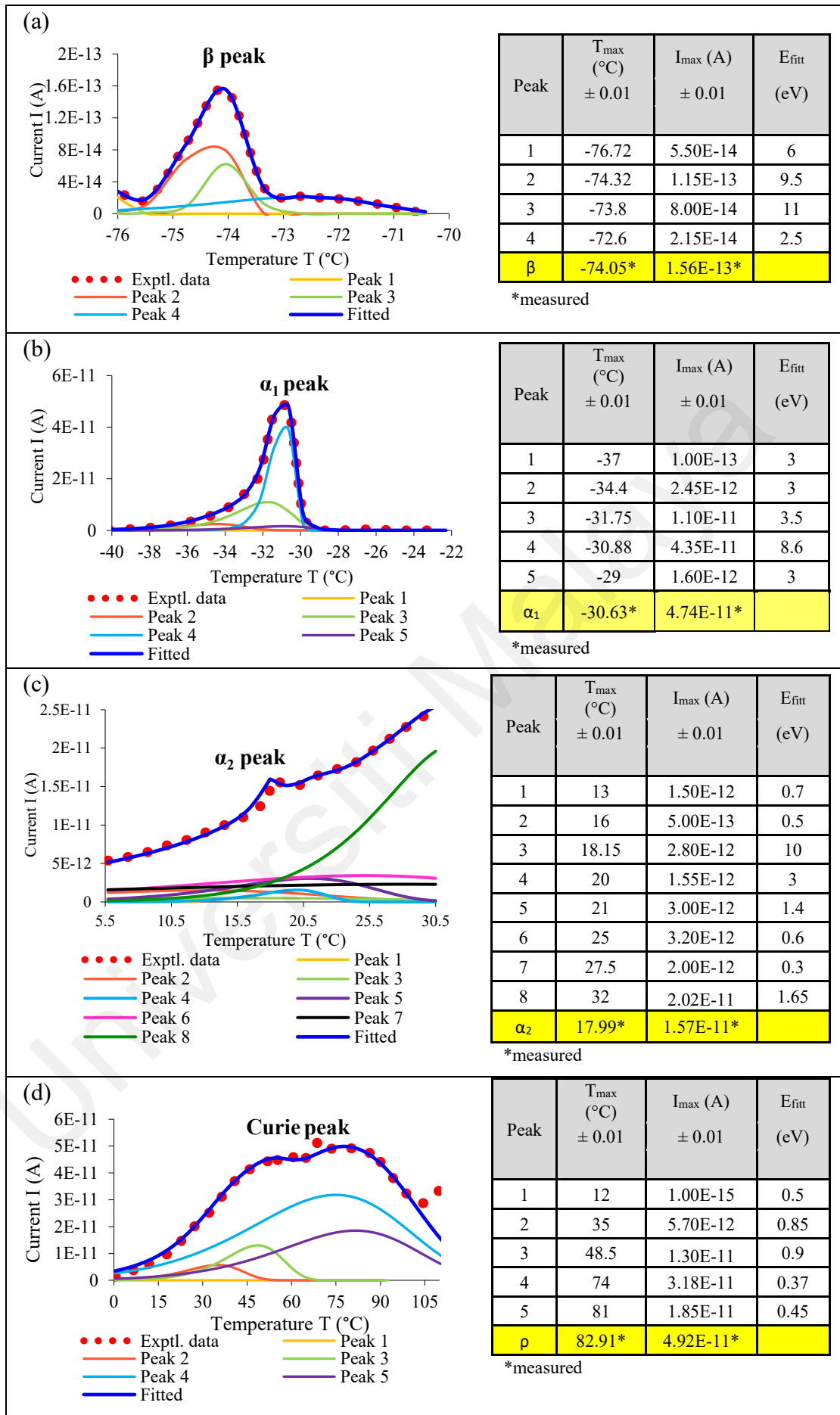
The decomposition analysis of nanocomposite films of P(VDF-TrFE) / ZnO QDs was constructed using Equation (7.1) (refer to Section 7.3) and presented in Figure 7.7-7.11. The TSC peak positions and activation energy of composite films P(VDF-TrFE) / ZnO QDs (0–0.50 wt%) through the decomposition technique are presented in Table 7.2.

As explained earlier in Section 7.3, the  $\beta$  peak observed through decomposition analysis is attributed to the relaxation of side chains on the polymer P(VDF-TrFE) backbone of the amorphous phase meanwhile the glass transition ( $\alpha_1$  relaxation) peak is associated with the segmental molecules for the mobility of polarized and frozen main chains to depolarize and then randomize. The rotational motion of the molecules within the paraelectric crystalline phase attributed to Curie peak ( $\rho$  relaxation) is observed at elevated temperatures. In between  $\alpha_1$  and  $\rho$  relaxation, the emergence of the  $\alpha_2$  peak represents the molecular mobility of amorphous domains constrained by crystallites. However, there are two relaxations of  $\alpha_2$  (named  $\alpha_{2-1}$  and  $\alpha_{2-2}$ ) observed in the composite films of P(VDF-TrFE) / ZnO QDs during decomposition analysis.

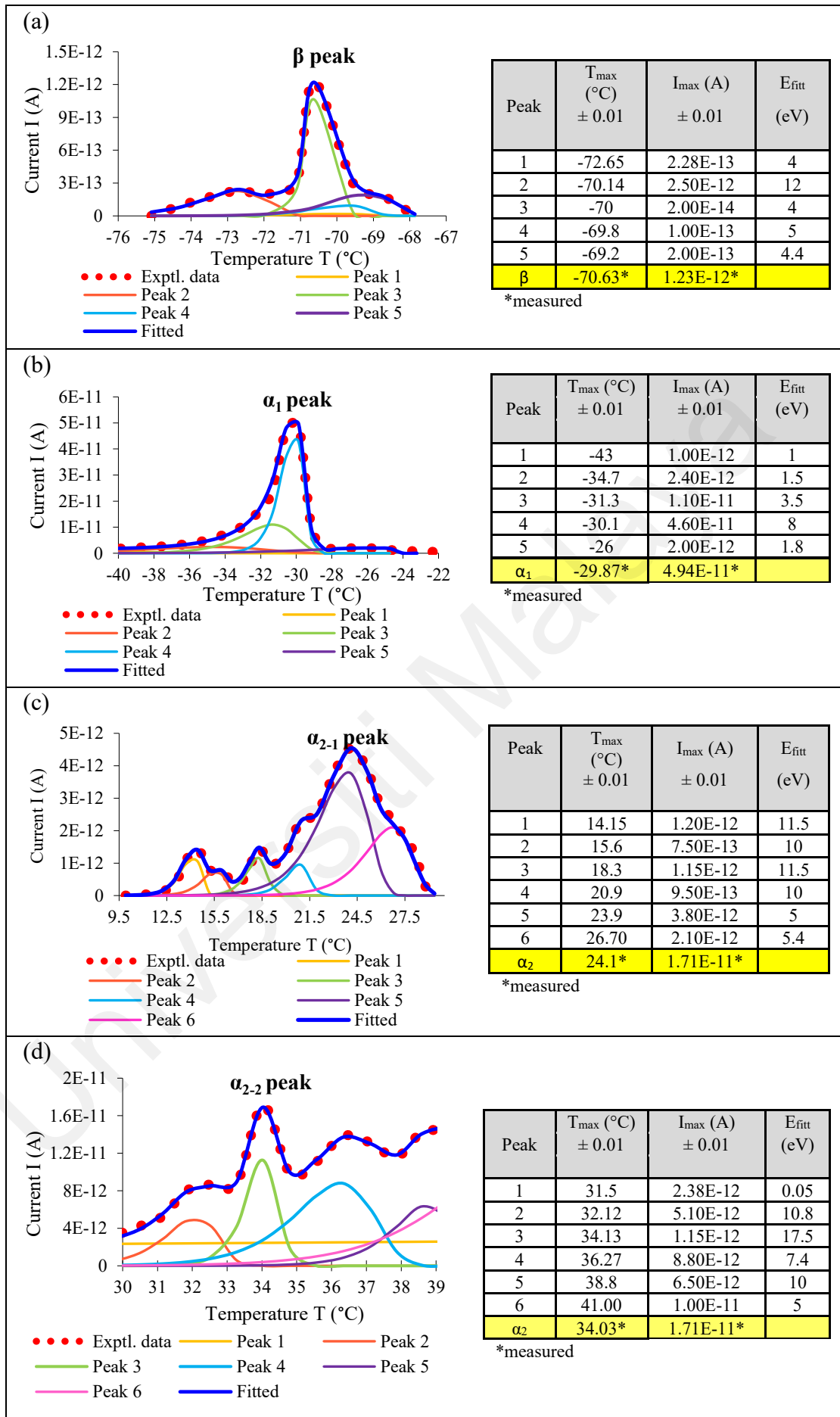
The addition of ZnO QDs into polymer matrix P(VDF-TrFE) significantly increases the activation energy of the decomposed peaks at all relaxation ( $\beta$ ,  $\alpha_1$ ,  $\alpha_{2-1}$ ,  $\alpha_{2-2}$  and  $\rho$ ) peaks. The  $\beta$  peak is shifted to a lower temperature until 0.25 wt% of ZnO and emerged at a higher temperature for 0.35 wt% and 0.50 wt% ZnO films. The trend is quite similar to the  $\alpha_1$  relaxation peak for composite films.  $\alpha_{2-1}$  relaxation peak is shifted to higher temperature with the addition of ZnO QDs and the peak seems diminished for 0.50 wt% of ZnO films. A wide range of  $\alpha_{2-2}$  and  $\rho$  relaxation peaks are observed in the composite P(VDF-TrFE) / ZnO QDs films. The increase of the leakage current is responsible for the elevated activation energy observed in 0.35 wt% and 0.50 wt% P(VDF-TrFE) / ZnO QDs films. From the literature review, no research on zinc oxide QDs acting as a nanofiller in a ferroelectric copolymer P(VDF-TrFE) host has been reported so far, with a focus on the Thermally Stimulated Current of polymer nanocomposite.



**Figure 7.7: Decomposition of the TSC spectrum of the 0 wt% P(VDF-TrFE) / ZnO QDs films.**



**Figure 7.8: Decomposition of the TSC spectrum of the 0.15 wt% P(VDF-TrFE) / ZnO QDs films.**



**Figure 7.9: Decomposition of the TSC spectrum of the 0.25 wt% P(VDF-TrFE) / ZnO QDs films .**

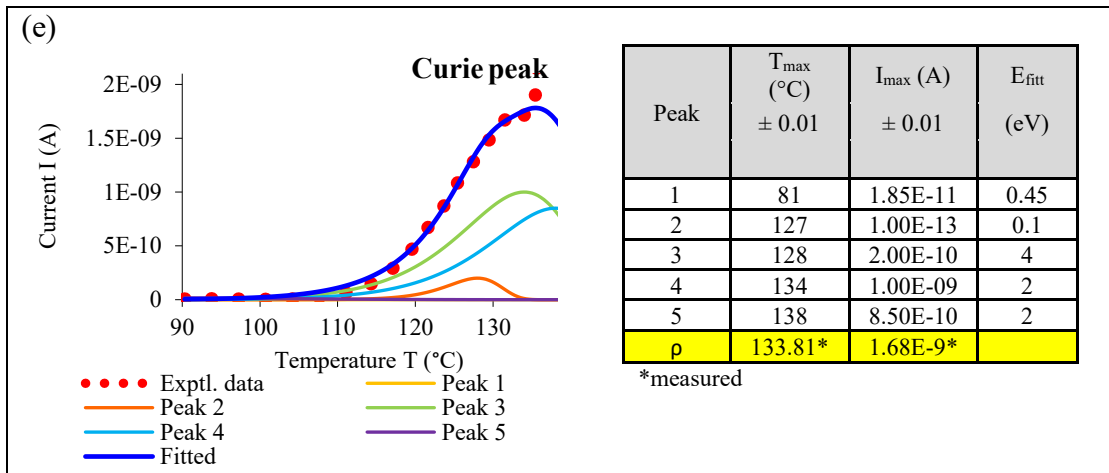


Figure 7.9, continued

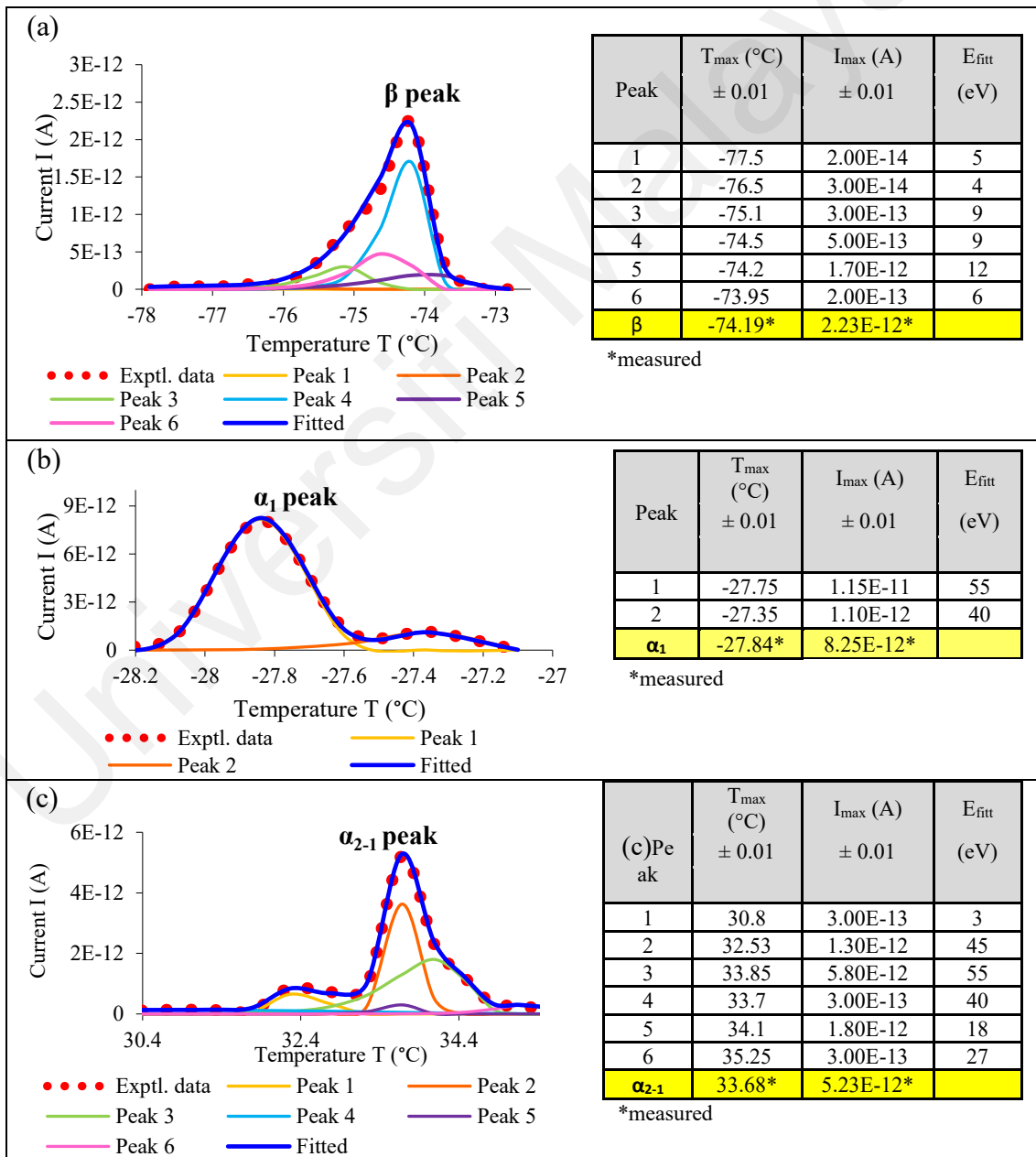


Figure 7.10: Decomposition of the TSC spectrum of the 0.35 wt% P(VDF-TrFE) / ZnO QDs films.

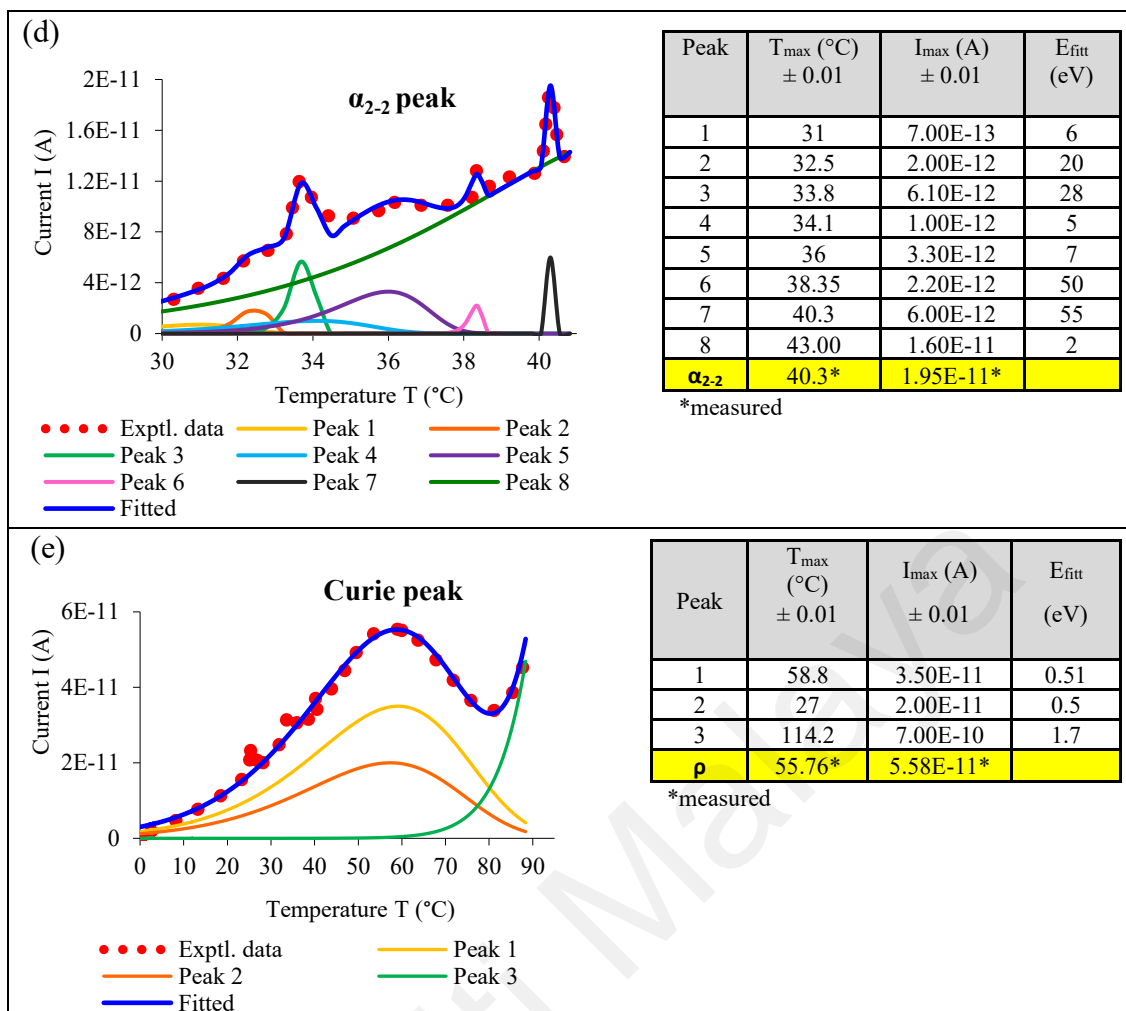
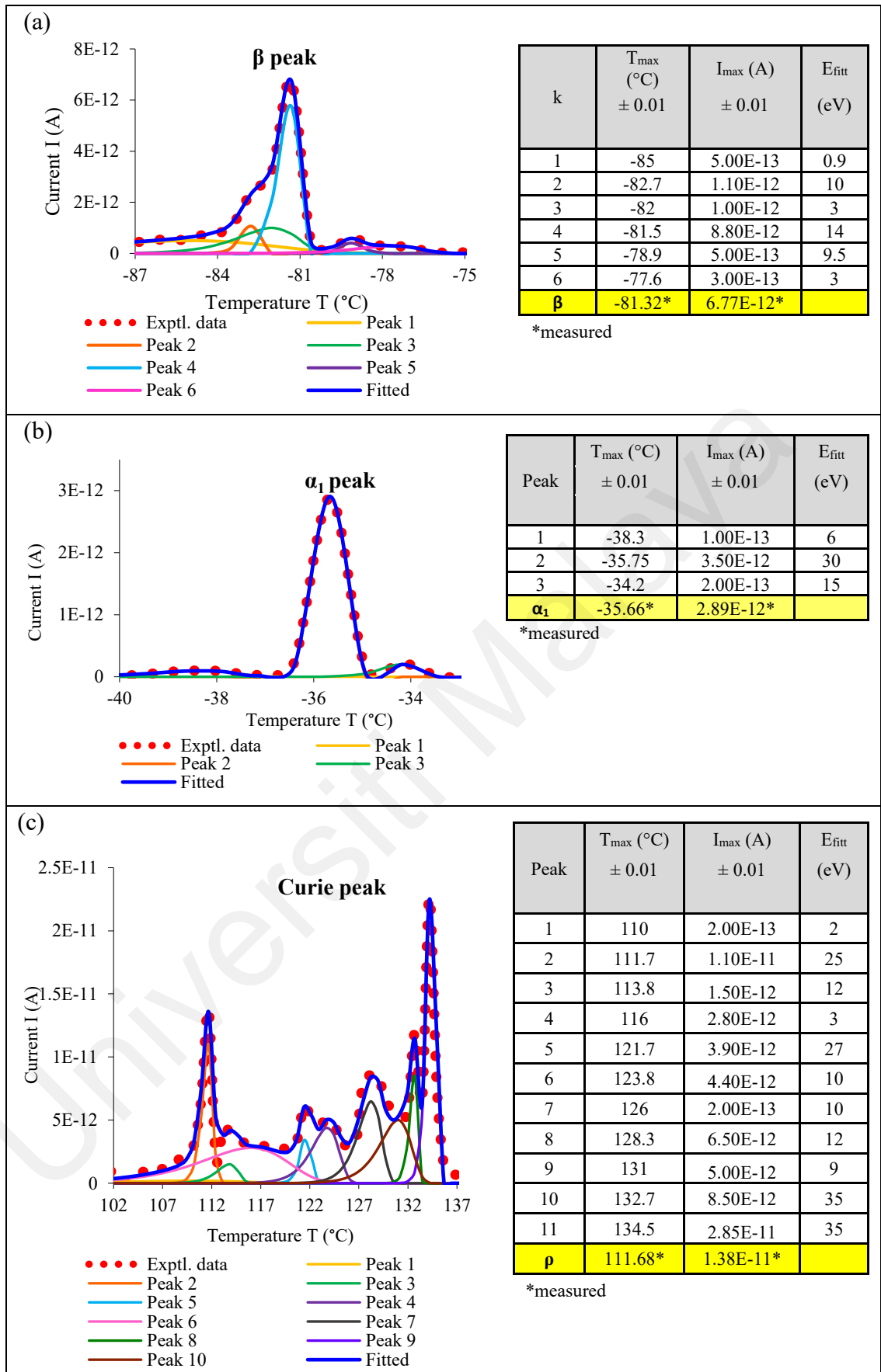


Figure 7.10, continued



**Figure 7.11: Decomposition of the TSC spectrum of the 0.50 wt% P(VDF-TrFE) / ZnO QDs films.**



**Table 7.2: TSC peak positions and activation energy of copolymer and composite films through the decomposition technique presented in this work.**

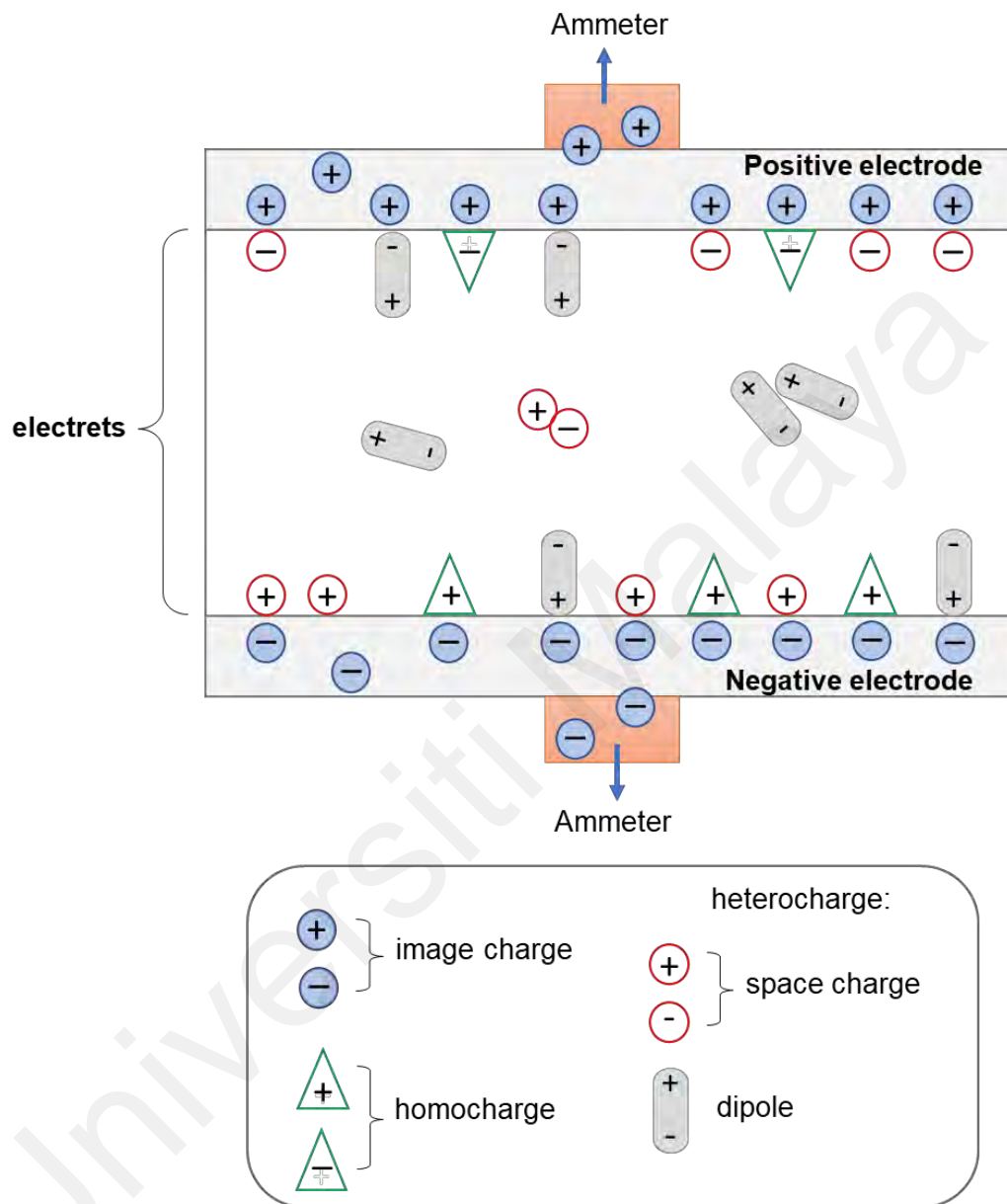
Sample	Peak Position (°C) [Activation energy, $E$ (eV)]				
	$\beta$	$\alpha_1$	$\alpha_{2-1}$	$\alpha_{2-2}$	$\rho$
P(VDF-TrFE) <b>As-cast</b>	-	-29.8 [4.3 – 7]	21.9 [1.7 – 9]	-	97.3 [0.7 – 8]
P(VDF-TrFE) <b>Anneal 100 °C</b>	-75.5 [0.3 – 4.1]	-23.8 [2.4 – 9.8]	27.4 [0.7 – 8]	-	96.3 [0.4 – 3.6]
<b>0 wt%</b> P(VDF-TrFE) / ZnO QDs <b>Anneal 100 °C</b>	-85.13 [1 – 2.6]	-39.43 [1.1 – 7.5]	-	40.33 [1.2 – 36]	84.64 [0.55 – 2.5]
<b>0.15 wt%</b> P(VDF-TrFE) / ZnO QDs <b>Anneal 100 °C</b>	-74.05 [2.5 – 11]	-30.63 [3 – 8.6]	17.99 [0.3 – 10]	-	82.91 [0.37 – 0.9]
<b>0.25 wt%</b> P(VDF-TrFE) / ZnO QDs <b>Anneal 100 °C</b>	-70.63 [4 – 12]	-29.87 [1 – 8]	24.1 [5 – 11.5]	34.03 [0.05 – 17.5]	133.81 [0.1 – 4]
<b>0.35 wt%</b> P(VDF-TrFE) / ZnO QDs <b>Anneal 100 °C</b>	-74.19 [4 – 12]	-27.84 [40 – 55]	33.68 [3 – 55]	40.3 [2 – 55]	55.76 [0.5 – 1.7]
<b>0.50 wt%</b> P(VDF-TrFE) / ZnO QDs <b>Anneal 100 °C</b>	-81.32 [0.9 – 14]	-35.66 [6 – 30]	-	-	111.68 [2 – 35]

The high activation energy ( $> 3$  eV) observed at almost all the decomposed peaks is probably due to the contribution of space charges injected at the sample-electrodes interfaces during the TSC poling process. The space charges are trapped within localized polarization in the polymers (Indolia & Gaur, 2013). The relaxation modes of  $\beta$ ,  $\alpha_1$ ,  $\alpha_2$  and  $\rho$  can also be associated with deep traps due to the highly polar molecular structure of P(VDF-TrFE) and the trapping of charge carriers on the surface region of the copolymer (Indolia & Gaur, 2013). Thermal stimulated discharged current (TSDC) behaviour of PVDF / ZnO at poling condition

(5 MV/m, 60 °C) studied by Indolia & Gaur (2013) suggested that the peaks were contributed from both the interfacial phenomena as well as space charge properties. TSDC peak current of the PVDF / ZnO nanocomposite increased and shifted toward the higher temperature side as the ZnO content in the nanocomposites was increased. However, the trend is not similar for P(VDF-TrFE) / ZnO QDs presented in this work. Indolia & Gaur suggest that the charge carriers tend to be trapped on top surface of the polymer after the addition of ZnO nanofiller. If these trapped carriers induce homocharge layers near the electrodes, space charge formation would be enhanced. This explains the fact that the amount of charge in nanocomposites with a suitable dispersion of ZnO nanoparticles is higher than in pure PVDF (Indolia & Gaur, 2013).

As elaborated in Chapter 2 (Section 2.6), TSC measurement involves the emergence of thermoelectrets which usually originate from both dipole polarization and space charges. An electret could also be formed as carriers transferred through the dielectric in a molecular or domain structure. In theory, the existence of electrets as a permanently polarized dielectric was predicted as early as 1892 by the British physicist Heaviside. The electrets can be obtained by applying high electric fields to polar dielectrics. Polarization induces the alignment of dipoles; thus, heterocharges are formed on the surface (Kestelman et al., 2000). Moreover, space charge polarization is observed when charge carriers are accumulated at the interface and grain boundaries in dielectrics with heterogeneous structures. Therefore, the current observed in TSC is generally described as the result of polarized chain mobility and space charges released. Figure 7.12 shows schematically the current generated from the flows of initially induced image charges by injected charge (homocharges) as well as by dipole and space charge (heterocharges) in an electret. These induced charges leave both electrodes in the direction of an electrometer. The flows take place due to the release of image charges. It occurs after the release of trapped charge or the disorientation of dipoles which has taken place to restore charge neutrality within the electrets (Abdul Halim, 2010; Van Turnhout, 2005). The dipole reorientation is believed to involve the rotations of a coupled pair of positive

and negative charges. It, therefore, requires a certain amount of energy for depolarization, which can be up to a few eV in the case of solids (Sessler & Shahi, 1980).



**Figure 7.12: Schematic representation of the image charges on electrodes released by depolarization of dipoles, space charges and homocharges within the electrets (Abdul Halim, 2010; Van Turnhout, 1971).**

The process of phase change of the copolymer P(VDF-TrFE) from glassy to rubbery state ( $T_g$ ) may lead to the release of trapped space charges when their polymer chains (main chain) loosen, thus contributing to the large amount of activation energy observed at  $T_g$  relaxation peaks and onwards ( $\alpha_1$ ,  $\alpha_{2-1}$  and  $\alpha_{2-2}$ ) for nanocomposite P(VDF-TrFE) / ZnO QDs as

presented in Table 7.2. Heterocharges within polymer electrets can be either ionic which comes from impurities within a polymer or electrons and holes (Fleming, 1999; Taraskin & Henn, 2008). These electronic charges are non-uniformly distributed and are often located near the electrodes which are believed to be trapped in localized traps (Abdul Halim, 2010).

The molecular-ion model proposed by Duke and Fabish probably can support the occurrence of high activation energy of decomposed peaks around  $> 3$  eV, which indicates the existence of a molecular-ion deep trap (Duke & Fabish, 1976; Fabish & Duke, 1977). The model was employed to demonstrate the presence of an electronic acceptor (or donor) state in polymers. The model suggested that if there were proper acceptors or donors present within a polymer, then the injected electronic carriers can create molecular-ions with them (Cui et al., 2009; Mellinger et al., 2004). The charge acceptors or donors could be in the form of polar and pendant groups. High energy deep trap is equivalent to the ionization energy  $E_g$  implies the formations of molecular ions within the materials during the polarization process. These molecular ions could have trapped charge carriers, which turned them into localized traps with high activation energy inside the electret materials. However, no work reported on molecular ion traps of P(VDF-TrFE) in TSC. Meanwhile, Thermally stimulated discharge conductivity study of zinc oxide thermoelectrets by Sangawar et al. explained that the ZnO crystals exhibit strong n-type conductivity due to intrinsic defects (oxygen vacancy and interstitial zinc atoms). These defects introduce donor states in the forbidden band slightly below the conduction band and hence result in the conducting behaviour of ZnO (Sangawar & Golchha, 2014). It was found that the activation energy of ZnO thermoelectrets increases with increasing polarization field.

Gaur et al. reported TSC of nanocomposite (5% ZnO-filled polycarbonate (PC)) at poling field  $10 \text{ MVm}^{-1}$  (Gaur et al., 2010). It has been observed that the increment of depolarization current of TSC nanocomposite at the high charging field and temperature is due to the formation of a charge-transfer complex (CTC) between inorganic and organic molecules. The CTC is an interaction between two or more molecules or different parts of a very large

molecule, in which the attraction between the molecules (or parts) is generated by an electronic/ionic transition to an excited state, transferring charge friction (e.g., ions) between molecules. Since ZnO nanoparticles introduce ionic species into the PC matrix, which contribute ionic charge carriers. Therefore, work reported by Gaur et al. may suggest that the ionization process takes place during the TSC measurements. These friction charges rapidly tunnel from the inorganic phase to the organic phase and are responsible for leakage or breakdown current (Gaur et al., 2010). TSC studies by Wang et al. reported that the introduction of ZnO nanoparticles into epoxy resin will introduce a large number of interface traps and its high surface energy will limit the movement of polymer molecular segments. With the increase of nanoparticles, since agglomeration occurs between particles, nanoparticles will introduce a large number of traps as impurities. In addition, the increase in nanoparticles rapidly increases the volume of the internal interface of the material, which allows the capture of a large number of space charges and the formation of a large number of traps (Wang et al., 2019).

Therefore, it may conclude that the high activation energies observed at all compositions of P(VDF-TrFE) / ZnO QDs may involve space charges injection at the polymer/semiconductor interface and molecular-ions deep traps. At more than 0.25 wt% ZnO QDs fillers, the leakage current takes place based on the extreme activation energy at almost all decomposition peaks and possibly due to the appearance of a micelle-like hole structure as observed in the FESEM measurement.

## **7.6 Conclusion**

Decomposition analysis using first-order kinetic theory to determine the type of relaxation processes involved in the formation of TSC peaks, as follows; the  $\beta$  peak is attributed to the relaxation of side chains on the polymer P(VDF-TrFE) backbone of the amorphous phase, while glass transition ( $\alpha_1$  relaxation) peak is associated by the segmental molecules for the mobility of polarized and frozen main chains and at elevated temperature, a rotational motion

of the molecules within the paraelectric crystalline phase is observed, which is attributed to Curie peak ( $\rho$  relaxation). In between  $\alpha_1$  and  $\rho$  relaxation, the emergence of the  $\alpha_2$  peak represents the molecular mobility of amorphous domains constrained by crystallites. The relaxation peak of the TSC spectrum showed the phenomenon of spontaneous polarization or switching characteristics of P(VDF-TrFE) observed at a specific temperature of  $T_g$  and Curie mode. The elevated activation energies for as-cast and annealed film at 100 °C from the deconvolution process is probably due to the high electronegativity between carbon, hydrogen and fluorine atoms of P(VDF-TrFE) and may also be due to the injection of trapping charge carriers of the copolymer thin film which is mostly covered by homogeneous micelle-like crystallites surrounded by elongated rod-like crystallites.

Doping of ZnO QDs in P(VDF-TrFE) revealed two relaxations of  $\alpha_2$  (named  $\alpha_{2-1}$  and  $\alpha_{2-2}$ ) instead of just one relaxation,  $\alpha_2$ , of P(VDF-TrFE) during decomposition analysis. The interaction of semiconducting ZnO QDs with carbonate groups of copolymers during the poling process can result in heterocharges (space charges and dipoles) being trapped in localized traps due to ionization and thus decomposed with high activation energy ( $> 3$  eV) at most relaxation peaks of P(VDF-TrFE) / ZnO QDs. So far, no study on ZnO quantum dots in the Thermally Stimulated Current measurements has been reported, which makes it quite difficult to discuss the high activation energy observed in this work.

## CHAPTER 8: CONCLUSION

### 8.1 Conclusion

The goal of this research is to develop a new polymer nanocomposite device consisting of a zero-dimensional nanofiller in a ferroelectric polymer host that acts as a nanogenerator for energy harvesting. The research shows that it is possible to improve the multifunctional properties of the copolymer P(VDF-TrFE) and conduct a thorough investigation of novel polymer-nanocomposite devices in terms of both physical and electrical properties.

The study is mainly divided into two parts; annealing series of copolymer P(VDF-TrFE) and a polymer nanocomposite of P(VDF-TrFE) embedded with ZnO quantum dots. The first part focused on the preparation and analysis of the physical (structural and morphological) and electrical (ferroelectric, pyroelectric and TSC) properties of P(VDF-TrFE) at various annealing temperatures. The optimum annealed sample with the best physical and electrical properties was found and employed as the polymer matrix in the nanocomposite films in the second part of the study.

The spin-coated P(VDF-TrFE) film with the highest degree of crystallinity corresponds to all trans (TTTT) conformation of the copolymer chain alignment or known as  $\beta$  phase, achieved at an annealing temperature of 100 °C using the XRD spectra deconvolution technique. A thermal annealing treatment on P(VDF-TrFE) films was applied between 80 °C to 140 °C, which is in the range of the Curie temperature,  $T_c$  and the melting point,  $T_m$  of the material. The films were annealed between the ferroelectric and paraelectric phases. The annealing temperature close to the Curie point induces the crystallization of the  $\beta$  phase, which leads to the largest spontaneous polarization,  $P_s$  in the unit cell of the copolymer. The surface morphology of the as-cast and the film of P(VDF-TrFE) annealed at 80 °C and 100 °C was covered by homogeneous spherical crystalline micelles embedded in the elongated rod-shaped structures and it can be observed that the micelle-like crystallites expand and grow as a function of the temperature of the heat treatment. A larger domain of  $\beta$  phase and micelle-like

crystallites with the elongated rod structures of the annealed copolymer are the important properties which contribute to a higher remnant polarization and pyroelectric coefficient observed in ferroelectric and pyroelectric measurements, respectively. Copolymer P(VDF-TrFE) annealed at 100 °C gives the highest remnant polarization = 76.7 mC/m<sup>2</sup>, the highest value of the dielectric constant of about  $\epsilon' = 10.3$  and the loss of  $\epsilon'' = 0.1$  at 1 kHz and the highest pyroelectric coefficient of 31  $\mu\text{C}/\text{m}^2\text{K}$  together with the maximum energy harvesting FOM,  $F_E = 10.3 \text{ Jm}^{-3}\text{K}^2$  calculated at 1 kHz. When the copolymer thin film is annealed at 120 °C which is above Curie point, the micelle-like crystallite disappears and the acicular crystallite is observed. The transformation of morphology from micelle-like crystallite with elongated rod into acicular crystallite structure is due to the phase transition from ferroelectric to paraelectric phase. Simultaneously, the remnant polarization, dielectric constant and pyroelectric coefficient were decreased due to this phase transition.

Subsequently, the TSC technique was carried out to investigate the molecular motions of the crystalline copolymer P(VDF-TrFE). The relaxation peaks of the TSC spectrum revealed the phenomenon of spontaneous polarization or a switching characteristic of P(VDF-TrFE) observed at a specific temperature of  $T_g$  and the Curie mode. The elevated activation energies obtained from the deconvolution process for the as-cast film and film annealed at 100 °C are due to the high electronegativity between the carbon, hydrogen and fluorine atoms of P(VDF-TrFE) and may also be due to the injection and trapping of charge carriers in the copolymer thin film, which is mostly covered by homogeneous micelle-like crystallites surrounded by elongated rod-like crystallites. Therefore, the crystallinity, surface morphology, molecular chain orientation and polarization are interrelated and influence the ferroelectric and pyroelectric properties of the copolymer thin films that may be used in sensor and energy harvesting applications.

In the second part of this work, non-toxic ZnO QDs stabilized with TEA were synthesized using the sol-gel method and embedded into a copolymer matrix, P(VDF-TrFE) to investigate the functional properties of the novel polymer nanocomposite in terms of energy harvesting



nanogenerator purposes. Various particle size analyses from UV-Vis, XRD and TEM proved that the size of the wurtzite-ZnO quantum dots synthesized in this work is in the range from ~2.5 to 3 nm. Encapsulation between TEA ligands with the surface of ZnO leads to smaller size QDs. A smaller particle size has a larger fraction of the interphase volume, i.e., the region between the filler and the polymer matrix, which implies more polarization in the interphase surface. A significant improvement in ferroelectric, dielectric and pyroelectric properties was demonstrated when 0.15 wt% ZnO QDs were dispersed in copolymer P(VDF-TrFE). Since quantum dots have a high surface area to volume ratio, only a few weight per cent additions is required to intensify the properties of the polymer. The maximum energy storage density calculated at 100 Hz of the ferroelectric hysteresis loop is 1.18 J/cm<sup>3</sup> for the 0.15 wt% P(VDF-TrFE) / ZnO QD polymer nanocomposite. Again, the incorporation of 0.15 wt% ZnO QDs into the polymer host significantly enhanced the dielectric constant and pyroelectric coefficient together with their  $F_E$  and  $F_D$  compared to those of pure P(VDF-TrFE) due to the greater distribution of micelle-like crystallites and the growth of elongated rod-like crystallites. The polarization of the non-centrosymmetric crystal structure of ZnO interacts synergistically with the P(VDF-TrFE) polymer host which contributes to the increase in ferroelectric and pyroelectric properties up to 0.15 wt% composition. The experimental value in dielectric measurement fits well with the Vo-Shi up to 0.25 wt% ZnO QDs because this model assumes that the effective dielectric constant of the polymer/filler composite depends on the interfacial region between the polymer and the filler as well as the size of the filler. The value of  $k$  also reflects the matrix/filler interaction strength. The Vo-Shi model matches the experimental data well, with the best-fit  $k = 55$  and  $\varepsilon_3 = 10$ .

The poor ferroelectric performance of thin films containing more than 0.25 wt% ZnO QDs fillers may be attributed to the high leakage current density which is related to the presence of micelle-like hole structures that are deep to the Si substrate's surface. The involvement of space charges injection at the polymer/semiconductor interface and molecular-ions deep traps

during the poling process of TSC can result in the decomposition the of TSC spectrum with high activation energy at most relaxation peaks of P(VDF-TrFE) / ZnO QDs.

## 8.2 Future work

ZnO QDs are synthesized on a very small scale utilizing the sol-gel process to form polymer nanocomposite. For industry, an optimization of the manufacturing process for mass production is necessary. The P(VDF-TrFE) / ZnO QDs nanogenerator demonstrated the best ferroelectric and pyroelectric properties at 0.15 wt%. The pyroelectric smart device or nanogenerator developed in this work is a recent paradigm in nanotechnology that is crucial for sensing and energy harvesting purposes. The ZnO quantum dots with particle size in the range of 2.5 – 3 nm significantly contribute to the enhancement of energy storage and energy harvesting figure of merits from ferroelectric and pyroelectric characterizations of P(VDF-TrFE) / ZnO QDs. It is important to investigate the particle size effect (at different size ranges) of ZnO QDs in P(VDF-TrFE) to discover the highest ferroelectric and pyroelectric properties. Harvesting electrical energy from the human body waste heat like thermoelectric generators (TEGs) to power portable electronic devices is an inspiration of current researchers. However, further improvement is still possible, in particular, to improve the pyroelectric properties by varying the poling method or varying the particle size of the nanofiller. As ZnO QDs mixed into ferroelectric polymers, they form interfacial interactions between the polymer chains and quantum dots. More research is needed to understand the effect of nanofiller addition on dielectric and TSC relaxation of polymer composite, which will contribute to knowledge advancement and better characterization in the future.

The determination of electrical and mechanical properties plays an essential role in the characterization of the piezoelectric material. Since ZnO is often cited as a promising candidate for piezoelectric materials, it is good to also explore the potential of P(VDF-TrFE) / ZnO QDs as piezoelectric nanogenerators. For this suggestion, the samples can be prepared

in a thick film with proper electrodes evaporated on both sides of the film and therefore can be analyzed using the piezoelectric resonance method.

Universiti Malaya

## REFERENCES

- Abdul Halim, N. (2010). *Thermo-electrical and mechanical studies on polymer-organically modified montmorillonite composites*. (Doctoral dissertation). University of Malaya, Kuala Lumpur, Malaysia. Retrieved on 1 November 2018 from <https://studentsrepo.um.edu.my>.
- Abubakar, S., Tan, S. T., Liew, J. Y. C., Talib, Z. A., Sivasubramanian, R., Vaithilingam, C. A., ... & Paiman, S. (2023). Controlled Growth of Semiconducting ZnO Nanorods for Piezoelectric Energy Harvesting-Based Nanogenerators. *Nanomaterials*, 13(6), Article#1025.
- Adnan, M. M., Dalod, A. R., Balci, M. H., Glaum, J., & Einarsrud, M.-A. J. P. (2018). In situ synthesis of hybrid inorganic–polymer nanocomposites. *Polymers*, 10(10), Article#1129.
- Adnan, R. H., Woon, K. L., Chanlek, N., Nakajima, H., & Majid, W. H. A. (2017). Ligand-Stabilized ZnO Quantum Dots: Molecular Dynamics and Experimental Study. *Australian Journal of Chemistry*, 70(10), 1110-1117.
- Ahmad, N., Majid, W. A., & Halim, N. (2020). Thermally Stimulated Current Study and Relaxation Behaviour of Annealed Copolymer P (VDF-TrFE) Films for Potential Pyroelectric Energy Harvesting. *Journal of Electronic Materials*, 49(9), 5585-5599.
- Ahmed, R., & Morsi, R. (2017). Polymer nanocomposite dielectric and electrical properties with quantum dots nanofiller. *Modern Physics Letters B*, 31(30), Article#1750278.
- Albertsson, J., Abrahams, S., & Kvik, Å. (1989). Atomic displacement, anharmonic thermal vibration, expansivity and pyroelectric coefficient thermal dependences in ZnO. *Acta Crystallographica Section B: Structural Science*, 45(1), 34-40.
- Alim, K. A., Fonoberov, V. A., Shamsa, M., & Balandin, A. A. (2005). Micro-Raman investigation of optical phonons in ZnO nanocrystals. *Journal of Applied Physics*, 97(12), Article#124313.
- Alkan, C., Günther, E., Hiebler, S., Ensari, Ö. F., & Kahraman, D. (2012). Polyurethanes as solid–solid phase change materials for thermal energy storage. *Solar Energy*, 86(6), 1761-1769.
- Arifin, D. E. S., & Ruan, D. J. (2018). Study on the curie transition of P(VDF-TrFE) copolymer. *Materials Science and Engineering*, (p. 012056), IOP Conference Series 299.
- Arshad, A., Wahid, M., Rusop, M., Majid, W., Subban, R., & Rozana, M. (2019). Dielectric and Structural Properties of Poly (vinylidene fluoride)(PVDF) and Poly (vinylidene

fluoride-trifluoroethylene)(PVDF-TrFE) Filled with Magnesium Oxide Nanofillers. *Journal of Nanomaterials*, Article# 5961563.

Askeland, D. R. (1996). Electrical Behaviour of Materials. In *The Science and Engineering of Materials* (pp. 618-671). Boston, MA: Springer.

Asok, A., Gandhi, M. N., & Kulkarni, A. (2012). Enhanced visible photoluminescence in ZnO quantum dots by promotion of oxygen vacancy formation. *Nanoscale*, 4(16), 4943-4946.

Bai, B., Zhang, X., Peng, Z., Chan, H. L., & Choy, C. L. (2003). Thermally stimulated depolarization current in ferroelectric blends of copolymers of vinylidene fluoride with trifluoroethylene. *Ferroelectrics*, 297(1), 75-81.

Batra, A. K., & Aggarwal, M. D. (2013). *Pyroelectric materials: infrared detectors, particle accelerators and energy harvesters*. Bellingham, USA: SPIE Press.

Belana, J., Pujal, M., Colomer, P., & Montserrat, S. (1988). Cold crystallization effect on  $\alpha$  and  $\rho$  amorphous poly (ethylene terephthalate) relaxations by thermally stimulated discharge currents. *Polymer*, 29(10), 1738-1744.

Benrekaa, N., Gourari, A., Bendaoud, M., & Ait-Hamouda, K. (2004). Analysis of thermally stimulated current and effect of rubbery annealing around glass-rubber transition temperature in polyethylene terephthalate. *Thermochimica Acta*, 413(1-2), 39-46.

Berger, L. I. (1996). *Semiconductor materials*. CRC press.

Bergman Jr, J., McFee, J., & Crane, G. (1971). Pyroelectricity and optical second harmonic generation in polyvinylidene fluoride films. *Applied Physics Letters*, 18(5), 203-205.

Bhadwal, N., Ben Mrad, R., & Behdinin, K. (2023). Review of Zinc Oxide Piezoelectric Nanogenerators: Piezoelectric Properties, Composite Structures and Power Output. *Sensors*, 23(8), 3859.

Bowen, C., Taylor, J., Le Boulbar, E., Zabek, D., & Topolov, V. Y. (2015). A modified figure of merit for pyroelectric energy harvesting. *Materials Letters*, 138, 243-246.

Bowen, C. R., Taylor, J., LeBoulbar, E., Zabek, D., Chauhan, A., & Vaish, R. (2014). Pyroelectric materials and devices for energy harvesting applications. *Energy & Environmental Science*, 7(12), 3836-3856.

Brazel, C. S., & Rosen, S. L. (2012). *Fundamental principles of polymeric materials – Third edition*. New Jersey: John Wiley & Sons.

- Capsal, J. F., Dantras, E., & Lacabanne, C. (2013). Molecular mobility interpretation of the dielectric relaxor behavior in fluorinated copolymers and terpolymers. *Journal of Non-Crystalline Solids*, 363, 20-25.
- Chen, G. W., & Majid, W. H. A. (2006). Pyroelectric Properties of Polyvinylidene Fluoride (PVDF) by Quasi Static Method. In 2006 *IEEE International Conference on Semiconductor Electronics* (pp. 468-471). IEEE.
- Chen, Z., Li, X. X., Du, G., Chen, N., & Suen, A. Y. (2011). A sol–gel method for preparing ZnO quantum dots with strong blue emission. *Journal of Luminescence*, 131(10), 2072-2077.
- Cheon, S., Kang, H., Kim, H., Son, Y., Lee, J. Y., Shin, H. J., . . . Cho, J. H. (2018). High-Performance Triboelectric Nanogenerators Based on Electrospun Polyvinylidene Fluoride–Silver Nanowire Composite Nanofibers. *Advanced Functional Materials*, 28(2), Article#1703778.
- Choi, J., Borca, C., Dowben, P. A., Bune, A., Poulsen, M., Pebley, S., . . . Fridkin, V. (2000). Phase transition in the surface structure in copolymer films of vinylidene fluoride (70%) with trifluoroethylene (30%). *Physical Review B*, 61(8), 5760.
- Choi, Y.-Y., Hong, J., Leem, D.-S., Park, M., Song, H., Sung, T.-H., & No, K. (2011). Spin-coated ultrathin poly (vinylidene fluoride-co-trifluoroethylene) films for flexible and transparent electronics. *Journal of Materials Chemistry*, 21(13), 5057-5061.
- Choi, Y. Y., Hong, J., Hong, S., Song, H., Cheong, D. S., & No, K. (2010). Nanoscale piezoresponse of 70 nm poly (vinylidene fluoride-trifluoro-ethylene) films annealed at different temperatures. *Physica Status Solidi (RRL)–Rapid Research Letters*, 4(3-4), 94-96.
- Consonni, V., & Lord, A. M. (2021). Polarity in ZnO nanowires: A critical issue for piezotronic and piezoelectric devices. *Nano Energy*, 83, Article#105789.
- Cui, L., Song, M., Kong, Y., Cheng, L., Wang, D., Xiao, Y., & Jiang, J. (2009). The comparative studies of charge storage stabilities among three PP/porous PTFE/PP electret. *Journal of Electrostatics*, 67(2-3), 412-416.
- Dai, Z., Feng, Z., Feng, C., Meng, L., Li, C., Wang, C., . . . Bai, Y. (2021). Thermoplastic polyurethane elastomer induced shear piezoelectric coefficient enhancement in bismuth sodium titanate–PVDF composite films. *Journal of Applied Polymer Science*, 138(6), 49818.
- Dal Corso, A., Posternak, M., Resta, R., & Baldereschi, A. (1994). Ab initio study of piezoelectricity and spontaneous polarization in ZnO. *Physical Review B*, 50(15), 10715.

- Das Gupta, D. K., & Doughty, K. (1977). Changes in x-ray diffraction patterns of polyvinylidene fluoride due to corona charging. *Applied Physics Letters*, 31(9), 585-587.
- Davis, G. T., McKinney, J. E., Broadhurst, M. G., & Roth, S. (1978). Electric-field-induced phase changes in poly (vinylidene fluoride). *Journal of Applied Physics*, 49(10), 4998-5002.
- Devadas, B., & Imae, T. (2018). Effect of carbon dots on conducting polymers for energy storage applications. *ACS Sustainable Chemistry & Engineering*, 6(1), 127-134.
- Dias, C., & Das-Gupta, D. (1996). Inorganic ceramic/polymer ferroelectric composite electrets. *IEEE Transactions on dielectrics and electrical insulation*, 3(5), 706-734.
- Diogo, H. P., & Ramos, J. J. M. (2008). Slow molecular mobility in the crystalline and amorphous solid states of glucose as studied by thermally stimulated depolarization currents (TSDC). *Carbohydrate research*, 343(16), 2797-2803.
- Doll, W., & Lando, J. (1970). Polymorphism of poly (vinylidene fluoride). III. The crystal structure of phase II. *Journal of Macromolecular Science, Part B: Physics*, 4(2), 309-329.
- Duke, C., & Fabish, T. (1976). Charge-induced relaxation in polymers. *Physical Review Letters*, 37(16), 1075.
- Ekimov, A. I., & Onushchenko, A. A. (1981). Quantum size effect in three-dimensional microscopic semiconductor crystals. *Journal of Experimental and Theoretical Physics Letters*, 34(6), 345-349.
- Eliasson, S. (1985). On TSD in PVDF in the temperature range -60 degrees C to 165 degrees C. I. *Journal of Physics D: Applied Physics*, 18(2), 275.
- El-Hami, K., Hara, M., Yamada, H., & Matsushige, K. (2001). The use of nanotechnology to fabricate ultra-high density molecular memory in P (VDF/TRFE) copolymer: data storage. *Annales de Chimie Science des Matériaux*, 26(1), 217-220.
- Fabish, T. J., & Duke, C. B. (1977). Molecular charge states and contact charge exchange in polymers. *Journal of Applied Physics*, 48(10), 4256-4266.
- Farzana, R., Rajarao, R., Behera, P. R., Hassan, K., & Sahajwalla, V. (2018). Zinc oxide nanoparticles from waste Zn-C battery via thermal route: characterization and properties. *Nanomaterials*, 8(9), 717.

- Fleming, R. J. (1999). Space charge in polymers, particularly polyethylene. *Brazilian Journal of Physics*, 29, 280-294.
- Fu, Y. S., Du, X. W., Kulinich, S. A., Qiu, J. S., Qin, W. J., Li, R., . . . Liu, J. (2007). Stable aqueous dispersion of ZnO quantum dots with strong blue emission via simple solution route. *Journal of the American Chemical Society*, 129(51), 16029-16033.
- Fu, Z., Xia, W., Chen, W., Weng, J., Zhang, J., Zhang, J., . . . Zhu, G. (2016). Improved thermal stability of ferroelectric phase in epitaxially grown P(VDF-TrFE) thin films. *Macromolecules*, 49(10), 3818-3825.
- Fukada, E. (1989). Introduction: Early studies in piezoelectricity, pyroelectricity, and ferroelectricity in polymers. *Phase Transitions: A Multinational Journal*, 18(3-4), 135-141.
- Furukawa, T. (1989). Ferroelectric properties of vinylidene fluoride copolymers. *Phase Transitions: A Multinational Journal*, 18(3-4), 143-211.
- Furukawa, T. (1997). Structure and functional properties of ferroelectric polymers. *Advances in Colloid and Interface Science*, 71, 183-208.
- Furukawa, T., & Johnson, G. (1981). Dielectric relaxations in a copolymer of vinylidene fluoride and trifluoroethylene. *Journal of Applied Physics*, 52(2), 940-943.
- Furukawa, T., Nakajima, T., & Takahashi, Y. (2006). Factors governing ferroelectric switching characteristics of thin VDF/TrFE copolymer films. *IEEE transactions on dielectrics and electrical insulation*, 13(5), 1120-1131.
- Furukawa, T., Wen, J. X., Suzuki, K., Takashina, Y., & Date, M. (1984). Piezoelectricity and pyroelectricity in vinylidene fluoride/trifluoroethylene copolymers. *Journal of Applied Physics*, 56(3), 829-834.
- Galdámez-Martínez, A., Santana, G., Güell, F., Martínez-Alanis, P. R., & Dutt, A. (2020). Photoluminescence of ZnO nanowires: a review. *Nanomaterials*, 10(5), 857.
- Galsin, J. S. (2019). *Solid State Physics: An Introduction to Theory*: Academic Press.
- Gan, W. C., & Majid, W. H. A. (2015). Enhancing pyroelectric and ferroelectric properties of PVDF composite thin films by dispersing a non-ferroelectric inclusion La<sub>2</sub>O<sub>3</sub> for application in sensors. *Organic Electronics*, 26, 121-128.



- Gao, R., Qin, X., Zhang, Q., Xu, Z., Wang, Z., Fu, C., . . . Cai, W. (2019). Enhancement of magnetoelectric properties of  $(1-x) \text{Mn}_{0.5}\text{Zn}_{0.5}\text{Fe}_2\text{O}_4\text{-}x\text{Ba}_{0.85}\text{Sr}_{0.15}\text{Ti}_{0.9}\text{Hf}_{0.1}\text{O}_3$  composite ceramics. *Journal of Alloys and Compounds*, 795, 501-512.
- Garlick, G., & Gibson, A. (1948). The electron trap mechanism of luminescence in sulphide and silicate phosphors. *Proceedings of the physical society*, 60(6), 574.
- Gaur, M., Rathore, B., Singh, P., Indolia, A., Awasthi, A., & Bhardwaj, S. (2010). Thermally stimulated current and differential scanning calorimetry spectroscopy for the study of polymer nanocomposites. *Journal of Thermal Analysis and Calorimetry*, 101(1), 315-321.
- Gayathri, S., Ghosh, O. N., Sathishkumar, S., Sudhakara, S., Jayaramudu, J., Ray, S. S., & Viswanath, A. K. (2015). Investigation of physicochemical properties of Ag doped ZnO nanoparticles prepared by chemical route. *Applied Science Letters*, 1(1), 8-13.
- Geurts, J. (2010). Crystal Structure, Chemical Binding, and Lattice Properties. In Zinc Oxide. Springer Series in Materials Science (Vol. 120, pp 7-37). Berlin, Heidelberg: Springer.
- Guggilla, P., & Batra, A. K. (2011). Novel electroceramic: polymer composites-preparation, properties and applications. In *Nanocomposites and Polymers with Analytical Methods* (pp. 287-308), IntechOpen. Retrieved on 5 October 2022 from <https://www.researchgate.net>.
- Halim, N. A., & Halim, A. (2018). *Ferroelectric, piezoelectric and pyroelectric properties of sol-gel derived sodium bismuth titanate and ceramic powder-polymer composite*. (Doctoral dissertation). Retrieved on 27 May 2020 from <https://studentsrepo.um.edu.my>.
- Han, J., Li, D., Zhao, C., Wang, X., Li, J., & Wu, X. (2019). Highly sensitive impact sensor based on PVDF-TrFE/Nano-ZnO composite thin film. *Sensors*, 19(4), 830.
- He, Q., Li, X., Zhang, J., Zhang, H., & Briscoe, J. (2021). P-N junction-based ZnO wearable textile nanogenerator for biomechanical energy harvesting. *Nano Energy*, 85, Article#105938.
- Hosseini Largani, S., & Akbarzadeh Pasha, M. (2017). The effect of concentration ratio and type of functional group on synthesis of CNT-ZnO hybrid nanomaterial by an in situ sol-gel process. *International Nano Letters*, 7, 25-33.
- Huang, Z., Hao, J., Blackburn, J. L., & Beard, M. C. (2021). Pyroelectricity of Lead Sulfide (PbS) Quantum Dot Films Induced by Janus-Ligand Shells. *ACS Nano*, 15(9), 14965-14971.

- Indolia, A. P., & Gaur, M. (2013). Investigation of structural and thermal characteristics of PVDF/ZnO nanocomposites. *Journal of Thermal Analysis and Calorimetry*, 113(2), 821-830.
- Ito, D., & Nakakita, T. (1980). Thermally stimulated current and thermoluminescence due to electron detrapping by local molecular motions in polyethylene-terephthalate. *Journal of Applied Physics*, 51(6), 3273-3277.
- Iwamoto, M., & Taguchi, D. (2018). Research trend in thermally stimulated current method for development of materials and devices in Japan. *Japanese Journal of Applied Physics*, 57(3S2), Article#03EA04.
- Jacob, N. M., & Thomas, T. (2014). Digestive ripening and green synthesis of ultra-small ( $r < 2$  nm) stable ZnO quantum dots. 40(9), 13945-13952.
- Jalali, N., Briscoe, J., Woolliams, P., Stewart, M., Weaver, P. M., Cain, M., & Dunn, S. (2013). Passivation of zinc oxide nanowires for improved piezoelectric energy harvesting devices. In *Journal of Physics: Conference Series* (Vol. 476, p. 012131), IOP Publishing.
- Jayalakshmy, M., & Philip, J. (2015). Pyroelectricity in strontium barium niobate/polyurethane nanocomposites for thermal/infrared detection. *Composites Science and Technology*, 109, 6-11.
- Jia, N., He, Q., Sun, J., Xia, G., & Song, R. (2017). Crystallization behavior and electroactive properties of PVDF, P (VDF-TrFE) and their blend films. *Polymer Testing*, 57, 302-306.
- Joshi, J., & Dawar, A. (1982). Pyroelectric materials, their properties and applications. *Physica Status Solidi. A, Applied Research*, 70(2), 353-369.
- Jurczuk, K., Galeski, A., Mackey, M., Hiltner, A., & Baer, E. (2015). Orientation of PVDF  $\alpha$  and  $\gamma$  crystals in nanolayered films. *Colloid and polymer science*, 293, 1289-1297.
- Kamruzzaman, M. (2020). The effect of ZnO/ZnSe core/shell nanorod arrays photoelectrodes on PbS quantum dot sensitized solar cell performance. *Nanoscale Advances*, 2(1), 286-295.
- Kao, K. C. (2004). *Dielectric phenomena in solids*. USA: Elsevier Academic Press.
- Kawai, H. (1969). The piezoelectricity of poly (vinylidene fluoride). *Japanese Journal of Applied Physics*, 8(7), 975.
- Kestelman, V. N., Pinchuk, L. S., & Goldade, V. A. (2000). *Electrets in engineering: fundamentals and applications*. USA: Springer Science & Business Media.

- Khoon-Keat, C., Swee-Leong, K., & Kok-Tee, L. (2018). Design and characterization of piezoelectric P (VDF-TrFE) thick film on flexible substrate for energy harvesting. *Journal of Telecommunication, Electronic and Computer Engineering (JTEC)*, 10(1), 63-68.
- Kishore, R. A., & Priya, S. (2018). A review on low-grade thermal energy harvesting: Materials, methods and devices. *Materials*, 11(8), 1433.
- Kitis, G., Gomez-Ros, J., & Tuyn, J. (1998). Thermoluminescence glow-curve deconvolution functions for first, second and general orders of kinetics. *Journal of Physics D: Applied Physics*, 31(19), 2636.
- Kołodziejczak-Radzimska, A., Markiewicz, E., & Jesionowski, T. (2012). Structural characterisation of ZnO particles obtained by the emulsion precipitation method. *Journal of Nanomaterials*, 2012, Article# 656353.
- Korlacki, R., Saraf, R. F., & Ducharme, S. (2011). Electrical control of photoluminescence wavelength from semiconductor quantum dots in a ferroelectric polymer matrix. *Applied Physics Letters*, 99(15), Article#153112.
- Kremer, F., & Schönhal, A. (2002). *Broadband dielectric spectroscopy*. Berlin, Heidelberg: Springer-Verlag Berlin Heidelberg.
- Kumar, S. N., & Kumar, P. (2013). Dielectric and Pyroelectric Properties of Ferroelectric SBN–PVDF Composites Prepared by Hot-Uniaxial Press. *International Journal of Applied Ceramic Technology*, 10, E11-E17.
- Lando, J. B., & Doll, W. W. (1968). The polymorphism of poly (vinylidene fluoride). I. The effect of head-to-head structure. *Journal of Macromolecular Science, Part B: Physics*, 2(2), 205-218.
- Lang, S. B. (1974). *Sourcebook of Pyroelectricity (Vol. 2)*. New York: Science Publishers.
- Lang, S. B. (2005). Pyroelectricity: from ancient curiosity to modern imaging tool. *Physics Today*, 58(8), 31.
- Lau, K., Liu, Y., Chen, H., & Withers, R. (2013). Effect of annealing temperature on the morphology and piezoresponse characterisation of poly (vinylidene fluoride-trifluoroethylene) films via scanning probe microscopy. *Advances in Condensed Matter Physics*, Article#435938.
- Lee, Y. H., Shabbir, I., Yoo, K. H., & Kim, T. W. (2021). Significant enhancement of output performance of piezoelectric nanogenerators based on CsPbBr<sub>3</sub> quantum dots-NOA63 nanocomposites. *Nano Energy*, 85, Article#105975.

- Li, G. R., & Ohigashi, H. (1992). Pyroelectric coefficient and heat capacity of a ferroelectric copolymer of vinylidene fluoride and trifluoroethylene at low temperatures. *Japanese journal of applied physics*, 31(8R), Article#2495.
- Li, L., Cheng, J., Cheng, Y., Han, T., Liang, X., Zhao, Y., . . . Dong, L. (2020). Polymer dielectrics exhibiting an anomalously improved dielectric constant simultaneously achieved high energy density and efficiency enabled by CdSe/Cd 1– x Zn x S quantum dots. *Journal of Materials Chemistry A*, 8(27), 13659-13670.
- Li, Q., Wang, Q. (2016). Ferroelectric polymers and their energy-related applications. *Macromolecular Chemistry and Physics*, 217(11), 1228-1244.
- Li, Q., Zhao, J., He, B., & Hu, Z. (2021). Solution processable poly (vinylidene fluoride)-based ferroelectric polymers for flexible electronics. *APL Materials*, 9(1), Article#010902.
- Li T, Li YT, Qin WW, Zhang PP, Chen XQ, Hu XF, Zhang W. Piezoelectric size effects in a zinc oxide micropillar. *Nanoscale Res Lett* 2015; 10: 1-7.
- Li, W., Wang, G., Chen, C., Liao, J., & Li, Z. (2017). Enhanced visible light photocatalytic activity of ZnO nanowires doped with Mn<sup>2+</sup> and Co<sup>2+</sup> ions. *Nanomaterials*, 7(1), 20.
- Li, X., Lu, S.-G., Qian, X., Lin, M., & Zhang, Q. (2014). Electrocaloric Polymers. In *Electrocaloric Materials* (pp. 107-124), New York: Springer Heidelberg.
- Liu, S., Cui, Z., Fu, P., Liu, M., Zhang, L., Li, Z., & Zhao, Q. (2014). Ferroelectric behavior and polarization mechanism in odd-odd polyamide 11, 11. *Journal of Polymer Science Part B: Polymer Physics*, 52(16), 1094-1099.
- Lovinger, A. J. (1983). Ferroelectric polymers. *Science*, 220(4602), 1115-1121.
- Ma, S., Ye, T., Zhang, T., Wang, Z., Li, K., Chen, M., . . . Wei, L. (2018). Highly Oriented Electrospun P (VDF-TrFE) Fibers via Mechanical Stretching for Wearable Motion Sensing. *Advanced Materials Technologies*, 3(7), Article#1800033.
- Mahdi, R., Gan, W., & Majid, W. (2014). Hot plate annealing at a low temperature of a thin ferroelectric P (VDF-TrFE) film with an improved crystalline structure for sensors and actuators. *Sensors*, 14(10), 19115-19127.
- Mahdi, R., & Majid, W. A. (2016). Piezoelectric and pyroelectric properties of BNT-base ternary lead-free ceramic–polymer nanocomposites under different poling conditions. *RSC Advances*, 6(84), 81296-81309.

- Mahdi, R. I., Gan, W. C., Abd Majid, W. H., Mukri, N. I., & Furukawa, T. (2018). Ferroelectric polarization and pyroelectric activity of functionalized P (VDF-TrFE) thin film lead free nanocomposites. *Polymer*, *141*, 184-193.
- Mai, M., Ke, S., Lin, P., & Zeng, X. (2015). Ferroelectric polymer thin films for organic electronics. *Journal of Nanomaterials*, *16*(1), 181.
- Mai, M., Liu, G., Zhu, C., & Ma, X. (2019). Switching current characteristics of ferroelectric P (VDF-TrFE) copolymer films. *Ferroelectrics*, *550*(1), 127-135.
- Majid, W. A., Richardson, T., Lacey, D., & Topacli, A. (2000). Qualitative evaluation of pyroelectric mechanisms in Langmuir–Blodgett films containing a cyclic polysiloxane substituted with aliphatic side chains using Fourier transform infrared (FTIR) spectroscopy. *Thin Solid Films*, *376*(1-2), 225-231.
- Matsushige, K., Nagata, K., Imada, S., & Takemura, T. (1980). The II-I crystal transformation of poly (vinylidene fluoride) under tensile and compressional stresses. *Polymer*, *21*(12), 1391-1397.
- Mellinger, A., González, F. C., & Gerhard-Multhaupt, R. (2004). Photostimulated discharge in electret polymers: an alternative approach for investigating deep traps. *IEEE transactions on dielectrics and electrical insulation*, *11*(2), 218-226.
- Mena-Garcia, J., Dursun, S., Tsuji, K., Bang, S. H., Fan, Z., Ndayishimiye, A., & Randall, C. (2022). Integration and characterization of a ferroelectric polymer PVDF-TrFE into the grain boundary structure of ZnO via cold sintering. *Journal of the European Ceramic Society*, *42*(6), 2789-2797.
- Menegotto, J., Ibos, L., Bernes, A., Demont, P., & Lacabanne, C. (1999). Dielectric relaxation spectra in ferroelectric P (VDF-TrFE) copolymers. *Ferroelectrics*, *228*(1), 1-22.
- Mizutani, T., Yamada, T., & Ieda, M. (1981). Thermally stimulated currents in polyvinylidene fluoride. I. Unstretched alpha-form PVDF. *Journal of Physics D: Applied Physics*, *14*(6), 1139.
- Möbus, G. (2003). Structure Determination by Quantitative High-Resolution Transmission Electron Microscopy. In *High-Resolution Imaging and Spectrometry of Materials* (pp. 69-118): Springer.
- Moeller, T. (2012). *Chemistry: with inorganic qualitative analysis*. Elsevier.
- Mohamed, W. A., Abd El-Gawad, H. H., Mekkey, S. D., Galal, H. R., & Labib, A. A. (2021). Zinc oxide quantum dots: Confinement size, photophysical and tuning optical properties

effect on photodecontamination of industrial organic pollutants. *Optical Materials*, 118, Article#111242.

Morkoç, H., & Özgür, Ü. (2008). *Zinc oxide: fundamentals, materials and device technology*: John Wiley & Sons.

Mudarra, M., Belana, J., Canadas, J., & Diego, J. (1998). Polarization time effect on PMMA space-charge relaxation by TSDC. *Journal of Polymer Science Part B: Polymer Physics*, 36(11), 1971-1980.

Murata, Y., Tsunashima, K., Koizumi, N., Ogami, K., Hosokawa, F., & Yokoyama, K. Y. K. (1993). Ferroelectric properties in polyamides of m-xylylenediamine and dicarboxylic acids. *Japanese Journal of Applied Physics*, 32(6B), L849.

Mzabi, N., Smaoui, H., Guermazi, H., Mlik, Y., Agnel, S., & Toureille, A. (2009). Heating effects on structural and electrical properties of polyetherimide. *American Journal of Engineering and Applied Sciences*, 2(1), 120-126.

Napolitano, S. (2015). *Non-equilibrium Phenomena in Confined Soft Matter. Soft and Biological Matter*. Springer Cham.

Navid, A., Lynch, C. S., & Pilon, L. (2010). Purified and porous poly (vinylidene fluoride-trifluoroethylene) thin films for pyroelectric infrared sensing and energy harvesting. *Smart Materials and Structures*, 19(5), Article#055006.

Navid, A., & Pilon, L. (2011). Pyroelectric energy harvesting using Olsen cycles in purified and porous poly (vinylidene fluoride-trifluoroethylene)[P (VDF-TrFE)] thin films. *Smart Materials and Structures*, 20(2), Article#025012.

Nioua, Y., El Bouazzaoui, S., Achour, M. E., & Costa, L. C. (2017). Modeling microwave dielectric properties of polymer composites using the interphase approach. *Journal of Electromagnetic Waves and Applications*, 31(14), 1343-1352.

Obreja, P., Cristea, D., Dinescu, A., & Romanițan, C. (2019). Influence of surface substrates on the properties of ZnO nanowires synthesized by hydrothermal method. *Applied Surface Science*, 463, 1117-1123.

Ojha, D. P., Joshi, B., Samuel, E., Khadka, A., Aldalbahi, A., Periyasami, G., ... & Yoon, S. S. (2023). Supersonically Sprayed Flexible ZnO/PVDF Composite Films with Enhanced Piezoelectricity for Energy Harvesting and Storage. *International Journal of Energy Research*, Article#3074782.

- Oliva, J., Diaz-Torres, L., Torres-Castro, A., Salas, P., Perez-Mayen, L., & De la Rosa, E. (2015). Effect of TEA on the blue emission of ZnO quantum dots with high quantum yield. *Optical Materials Express*, 5(5), 1109-1121.
- Onodera, A., & Takesada, M. (2012). Electronic ferroelectricity in II-VI semiconductor ZnO. *Advances in Ferroelectrics*, 231-255.
- Oskam, G., Hu, Z., Penn, R. L., Pesika, N., & Searson, P. C. (2002). Coarsening of metal oxide nanoparticles. *Physical Review E*, 66(1), Article#011403.
- Özgür, Ü., Alivov, Y. I., Liu, C., Teke, A., Reshchikov, M., Doğan, S., . . . Morkoç. (2005). A comprehensive review of ZnO materials and devices. *Journal of Applied Physics*, 98(4), Article#041301.
- Panigrahy, B., Aslam, M., & Bahadur, D. (2012). Effect of Fe doping concentration on optical and magnetic properties of ZnO nanorods. *Nanotechnology*, 23(11), Article#115601.
- Parangusan, H., Ponnamm, D., & Al-Maadeed, M. A. A. (2018). Stretchable electrospun PVDF-HFP/Co-ZnO nanofibers as piezoelectric nanogenerators. *Scientific Reports*, 8(1), Article#754.
- Park, D. Y., Lim, J. H., Ha, M. Y., & Moon, D. G. (2020). High efficiency quantum dot light-emitting diode by solution printing of zinc oxide nanoparticles. *Journal of Nanoscience and Nanotechnology*, 20(7), 4454-4457.
- Poulsen, M., & Ducharme, S. (2010). Why ferroelectric polyvinylidene fluoride is special. *IEEE Transactions on Dielectrics and Electrical Insulation*, 17(4), 1028-1035.
- Rahman, F. (2019). Zinc oxide light-emitting diodes: a review. *Optical Engineering*, 58(1), Article#010901.
- Ramalingam, G., Kathirgamanathan, P., Ravi, G., Elangovan, T., Manivannan, N., & Kasinathan, K. (2020). Quantum Confinement Effect of 2D Nanomaterials. In *Quantum Dots-Fundamental and Applications*: IntechOpen.
- Ren, X., Meng, N., Zhang, H., Wu, J., Abrahams, I., Yan, H., ... & Reece, M. J. (2020). Giant energy storage density in PVDF with internal stress engineered polar nanostructures. *Nano Energy*, 72, Article#104662.
- Roggero, A., Dantras, E., & Lacabanne, C. (2017). Poling influence on the mechanical properties and molecular mobility of highly piezoelectric P(VDF-TrFE) copolymer. *Journal of Polymer Science Part B: Polymer Physics*, 55(18), 1414-1422.

- Sadeghi, S., Jalali, H. B., Srivastava, S. B., Melikov, R., Baylam, I., Sennaroglu, A., & Nizamoglu, S. (2020). High-performance, large-area, and ecofriendly luminescent solar concentrators using copper-doped InP quantum dots. *Iscience*, 23(7), Article#101272.
- Sahoo, R., Mishra, S., Ramadoss, A., Mohanty, S., Mahapatra, S., & Nayak, S. K. (2020). An approach towards the fabrication of energy harvesting device using Ca-doped ZnO/PVDF-TrFE composite film. *Polymer*, 205, Article#122869.
- Sahu, M. K. (2019). Semiconductor nanoparticles theory and applications. *International Journal of Applied Engineering Research*, 14(2), 491-494.
- Sánchez-Godoy, H. E., Salim, K. M., Rodríguez-Rojas, R., Zarazúa, I., & Masi, S. (2022). In Situ Ethanolamine ZnO Nanoparticle Passivation for Perovskite Interface Stability and Highly Efficient Solar Cells. *Nanomaterials*, 12(5), Article#823.
- Sangawar, V. S., & Golchha, M. C. (2014). Thermally stimulated discharge conductivity study of zinc oxide thermoelectrets. *Bulletin of Materials Science*, 37, 1497-1501.
- Sature, K., Patil, B., Dahiwal, S., Bhoraskar, V., & Dhole, S. (2017). Development of computer code for deconvolution of thermoluminescence glow curve and DFT simulation. *Journal of Luminescence*, 192, 486-495.
- Scimeca, M., Bischetti, S., Lamsira, H. K., Bonfiglio, R., & Bonanno, E. (2018). Energy Dispersive X-ray (EDX) microanalysis: A powerful tool in biomedical research and diagnosis. *European journal of histochemistry: EJH*, 62(1), Article#2841.
- Schoenhalz, A. L., Arantes, J. T., Fazzio, A., & Dalpian, G. M. (2010). Surface and quantum confinement effects in ZnO nanocrystals. *The Journal of Physical Chemistry C*, 114(43), 18293-18297.
- Sessler, G. M., & Shahi, K. (1980). Electrets, topics in applied physics. *Journal of The Electrochemical Society*, 127(12), 530C.
- Shang, Y., & Ning, Z. (2017). Colloidal quantum-dots surface and device structure engineering for high-performance light-emitting diodes. *National Science Review*, 4(2), 170-183.
- Shepelin, N. A., Glushenkov, A. M., Lussini, V. C., Fox, P. J., Dicinoski, G. W., Shapter, J. G., & Ellis, A. V. (2019). New developments in composites, copolymer technologies and processing techniques for flexible fluoropolymer piezoelectric generators for efficient energy harvesting. *Energy & Environmental Science*, 12(4), 1143-1176.



- Shi, H. Q., Li, W. N., Sun, L. W., Liu, Y., Xiao, H. M., & Fu, S. Y. (2011). Synthesis of silane surface modified ZnO quantum dots with ultrastable, strong and tunable luminescence. *Chemical Communications*, 47(43), 11921-11923.
- Singh, A., & Vishwakarma, H. (2015). Study of structural, morphological, optical and electroluminescent properties of undoped ZnO nanorods grown by a simple chemical precipitation. *Materials Science-Poland*, 33(4), 751-759.
- Singh, A. K., Pal, P., Gupta, V., Yadav, T. P., Gupta, V., & Singh, S. P. (2018). Green synthesis, characterization and antimicrobial activity of zinc oxide quantum dots using *Eclipta alba*. *Materials Chemistry and Physics*, 203, 40-48.
- Spampinato, N., Maiz, J., Portale, G., Maglione, M., Hadziioannou, G., & Pavlopoulou, E. (2018). Enhancing the ferroelectric performance of P(VDF-co-TrFE) through modulation of crystallinity and polymorphism. *Polymer*, 149, 66-72.
- Sutani, Y., Koshiba, Y., Fukushima, T., & Ishida, K. (2021). Formation mechanism of ferroelectric poly (vinylidene fluoride-trifluoroethylene) copolymers with in-plane dipole alignment under low electric field from melt and its SPR based pyroelectric sensor. *Polymer*, 228, Article#123904.
- Tan, K., Gan, W., Velayutham, T., & Majid, W. A. (2014). Pyroelectricity enhancement of PVDF nanocomposite thin films doped with ZnO nanoparticles. *Smart Materials and Structures*, 23(12), Article#125006.
- Taraskin, S., & Henn, F. (2008). Depolarization current density within the symmetric double-well potential model for solid ionic conductors. *Physical Review B*, 77(13), Article#134306.
- Tasaka, S., Shouko, T., Asami, K. I. A. K. I., & Inagaki, N. I. N. (1994). Ferroelectric behavior in aliphatic polyurethanes. *Japanese Journal of Applied Physics*, 33(3R), Article#1376.
- Tasaka, S., Shouko, T. S. T., & Inagaki, N. I. N. (1992). Ferroelectric polarization reversal in polyureas with odd number of CH<sub>2</sub> groups. *Japanese Journal of Applied Physics*, 31(8A), Article#L1086.
- Teyssedre, G., Bernes, A., & Lacabanne, C. (1993a). DSC and TSC study of a VDF/TrFE copolymer. *Thermochimica Acta*, 226, 65-75.
- Teyssedre, G., Bernes, A., & Lacabanne, C. (1993b). Influence of the crystalline phase on the molecular mobility of PVDF. *Journal of Polymer Science Part B: Polymer Physics*, 31(13), 2027-2034.

- Teyssedre, G., & Lacabanne, C. (1995). Study of the thermal and dielectric behavior of P (VDF-TrFE) copolymers in relation with their electroactive properties. *Ferroelectrics*, 171(1), 125-144.
- Thomas, P., Varughese, K., Dwarakanath, K., & Varma, K. (2010). Dielectric properties of poly (vinylidene fluoride)/CaCu<sub>3</sub>Ti<sub>4</sub>O<sub>12</sub> composites. *Composites Science and Technology*, 70(3), 539-545.
- Tichý, J., Erhart, J. r., Kittinger, E., & Přívratská, J. (2010). *Fundamentals of piezoelectric sensorics: mechanical, dielectric, and thermodynamical properties of piezoelectric materials*: Springer Science & Business Media.
- Toor, A. (2017). *Polymer Nanocomposite Materials with High Dielectric Permittivity and Low Dielectric Loss Properties*. (Doctoral dissertation). University of California, Berkeley. Retrieved on 12 December 2022 from <https://www.proquest.com>.
- Tsutsumi, N., Tanaka, R., Kinashi, K., & Sakai, W. (2020). Re-evaluation of the Energy Density Properties of VDF Ferroelectric Thin-Film Capacitors. *ACS omega*, 5(47), 30468-30477.
- Valiyaneerilakkal, U., Singh, A., Subash, C., Singh, K., Abbas, S., & Varghese, S. (2017). Preparation and characterization of poly (vinylidene fluoride-trifluoroethylene)/barium titanate polymer nanocomposite for ferroelectric applications. *Polymer Composites*, 38(8), 1655-1661.
- Van Turnhout, J. (1971). Thermally stimulated discharge of polymer electrets. *Polymer Journal*, 2(2), 173-191.
- Van Turnhout, J. (1980). Thermally stimulated discharge of electrets. *Electrets*, 81-215.
- Vanderschueren, J., & Gasiot, J. (1979). Field-induced thermally stimulated currents. In: Bräunlich, P. (Eds), *Thermally Stimulated Relaxation in Solids*. In *Thermally stimulated relaxation in solids* (pp. 135-223). Berlin, Heidelberg: Springer.
- Vanderschueren, J., Linkens, A., Gasiot, J., Fillard, J., & Parot, P. (1980). Simulation of field-induced thermally stimulated currents in dielectrics. Application to the dipolar case in polymeric systems. *Journal of Applied Physics*, 51(9), 4967-4975.
- Viola, F. A., Spanu, A., Ricci, P. C., Bonfiglio, A., & Cosseddu, P. (2018). Ultrathin, flexible and multimodal tactile sensors based on organic field-effect transistors. *Scientific Reports*, 8(1), 1-8.

- Vo, H. T., & Shi, F. G. (2002). Towards model-based engineering of optoelectronic packaging materials: dielectric constant modeling. *Microelectronics Journal*, 33(5-6), 409-415.
- Wagner, A. M., Knipe, J. M., Orive, G., & Peppas, N. A. (2019). Quantum dots in biomedical applications. *Acta Biomaterialia*, 94, 44-63.
- Wang, R., Xie, C., Luo, S., Gou, B., Xu, H., & Zeng, L. (2019). The influence mechanism of nanoparticles on the dielectric properties of epoxy resin. *RSC Advances*, 9(34), 19648-19656.
- WC, G., & Majid, W. H. A. (2009). The effect of gases on pyroelectric properties of PVDF/TiO<sub>2</sub> treated by plasma etcher. *Transactions of the Materials Research Society of Japan*, 34(1), 67-71.
- Weber, N., Lee, Y. S., Shanmugasundaram, S., Jaffe, M., & Arinzeh, T. L. (2010). Characterization and in vitro cytocompatibility of piezoelectric electrospun scaffolds. *Acta Biomaterialia*, 6(9), 3550-3556.
- Wu, H., Li, W., Ao, H., Zeng, Z., Qin, X., Xing, S., . . . Cai, W. (2022). Effect of holding time on microstructure, ferroelectric and energy-storage properties of Pb<sub>0.925</sub>La<sub>0.05</sub>Zr<sub>0.95</sub>Ti<sub>0.05</sub>O<sub>3</sub>@SiO<sub>2</sub> ceramics. *Journal of Alloys and Compounds*, 896, 162932.
- Wu, J., Sun, X., Zhu, S., Bai, J., Zhu, X., Dai, J., . . . Sun, Y. (2020). Magnetic field induced formation of ferroelectric  $\beta$  phase of poly (vinylidene fluoride). *Applied Physics A*, 126(8), 1-6.
- Xu, P., & Zhang, X. (2011). Investigation of MWS polarization and dc conductivity in polyamide 610 using dielectric relaxation spectroscopy. *European polymer journal*, 47(5), 1031-1038.
- Xu, R., Wang, Z., Gao, R., Zhang, S., Zhang, Q., Li, Z., . . . Cai, W. (2018). Effect of molar ratio on the microstructure, dielectric and multiferroic properties of Ni<sub>0.5</sub>Zn<sub>0.5</sub>Fe<sub>2</sub>O<sub>4</sub>-Pb<sub>0.8</sub>Zr<sub>0.2</sub>TiO<sub>3</sub> nanocomposite. *Journal of Materials Science: Materials in Electronics*, 29, 16226-16237.
- Xu, Y. (2013). *Ferroelectric materials and their applications*: Elsevier.
- Yamada, T., Mizutani, T., & Ieda, M. (1982). Thermally stimulated currents in polyvinylidene fluoride. II. Effects of stretching. *Journal of Physics D: Applied Physics*, 15(2), 289.
- Yamanaka, S., Kim, J., Nakajima, A., Katou, T., Kim, Y., Fukuda, T., . . . Yamada, N. (2017). Relationship Between the Material Properties and Pyroelectric-Generating Performance of PZTs. *Advanced Sustainable Systems*, 1(3-4), Article#1600020.

- Yanaka, A., Sakai, W., Kinashi, K., & Tsutsumi, N. (2020). Ferroelectric performance of nylons 6-12, 10-12, 11-12, and 12-12. *RSC Advances*, 10(27), 15740-15750.
- Yang, L., Ho, J., Allahyarov, E., Mu, R., & Zhu, L. (2015). Semicrystalline structure–dielectric property relationship and electrical conduction in a biaxially oriented poly (vinylidene fluoride) film under high electric fields and high temperatures. *ACS Applied Materials & Interfaces*, 7(36), 19894-19905.
- Yang, Y., Guo, W., Pradel, K. C., Zhu, G., Zhou, Y., Zhang, Y., . . . Wang, Z. L. (2012). Pyroelectric Nanogenerators for Harvesting Thermoelectric Energy. *Nano Letters*, 12(6), 2833-2838.
- Zhang, W., Wu, G., Zeng, H., Li, Z., Wu, W., Jiang, H., ... & Lei, Z. (2023). The Preparation, Structural Design, and Application of Electroactive Poly (vinylidene fluoride)-Based Materials for Wearable Sensors and Human Energy Harvesters. *Polymers*, 15(13), Article#2766.
- Zhang, X., Xu, J., Shi, S., Wang, X., Zhao, X., Zhou, P., ... & Li, L. (2016). Ferroelectric-like hysteresis effect observed in carbon quantum dots sandwiched between PMMA and PEDOT: PSS hybrid film. *RSC Advances*, 6(63), 58733-58739.
- Zhang, Y., Xie, M., Roscow, J., Bao, Y., Zhou, K., Zhang, D., & Bowen, C. R. (2017). Enhanced pyroelectric and piezoelectric properties of PZT with aligned porosity for energy harvesting applications. *Journal of Materials Chemistry A*, 5(14), 6569-6580.
- Zhu, G., Zeng, Z., Zhang, L., & Yan, X. (2008). Piezoelectricity in  $\beta$ -phase PVDF crystals: A molecular simulation study. *Computational Materials Science*, 44(2), 224-229.
- Zhu, L., & Wang, Q. (2012). Novel ferroelectric polymers for high energy density and low loss dielectrics. *Macromolecules*, 45(7), 2937-2954.